UNIVERSITÀ DEGLI STUDI DI PAVIA

DOTTORATO IN SCIENZE CHIMICHE E FARMACEUTICHE E INNOVAZIONE INDUSTRIALE
(XXXVI Ciclo)

Coordinatore: Chiar.mo Prof. Giorgio Colombo

Design of CNFs-supported self-standing cathodes for Sodium-ion batteries with enhanced performance at high C-rate

Tesi di Dottorato di
Debora Maria Conti

AA 2023/2024

Tutor
Chiar.ma Prof.ssa Doretta Capsoni

Doretta Capsoni

A mia figlia Linda:
che tu possa essere sempre così desiderosa
di conoscere, esplorare, provare ed
ascoltare con il cuore aperto e la mente viva.

''I believe that energy, not the dollar, is the currency of the world.
It is the joule that drives every economy and gives people a way out of poverty.''

Nathan S. Lewis, 'Powering the Planet', MRS Bulletin, 32, 2007

List of pubblications

- Conti, D.M.; Urru, C.; Bruni, G.; Galinetto, P.; Albini, B.; Berbenni, V.; Capsoni, D. High C-Rate Performant Electrospun $LiFePO_4$/Carbon Nanofiber Self-Standing Cathodes for Lithium-Ion Batteries. *Electrochem* **2024**, *5*, 223-242. https://doi.org/10.3390/electrochem5020014

- Conti, D.M.; Urru, C.; Bruni, G.; Galinetto, P.; Albini, B.; Berbenni, V.; Girella, A.; Capsoni, D. $Na_3MnTi(PO_4)_3$/C Nanofiber Free-Standing Electrode for Long-Cycling-Life Sodium-Ion Batteries. *Nanomaterials* **2024**, *14*, 804. https://doi.org/10.3390/nano14090804.

- Conti, D.M.; Urru, C.; Bruni, G.; Galinetto, P.; Albini, B.; Milanese, C.; Pisani, S.; Berbenni, V.; Capsoni, D. Design of $Na_3MnZr(PO_4)_3$/Carbon Nanofiber Free-Standing Cathodes for Sodium-Ion Batteries with Enhanced Electrochemical Performances through Different Electrospinning Approaches. *Molecules* **2024**, 29, 1885. https://doi.org/10.3390/molecules29081885.

- Conti, D.M.; Fusaro, C.; Bruni, G.; Galinetto, P.; Albini, B.; Milanese, C.; Berbenni, V.; Capsoni, D. ZnS–rGO/CNF Free-Standing Anodes for SIBs: Improved Electrochemical Performance at High C-Rate. *Nanomaterials* **2023**, *13*, 1160. https://doi.org/10.3390/nano13071160.

- Friuli, V.; Urru, C.; Ferrara, C.; Conti, D.M.; Bruni, G.; Maggi, L.; Capsoni, D. Design of Etched- and Functionalized-Halloysite/Meloxicam Hybrids: A Tool for Enhancing Drug Solubility and Dissolution Rate. *Pharmaceutics* **2024**, *16*, 338. https://doi.org/10.3390/pharmaceutics16030338.

- Maggi, L.; Urru, C.; Friuli, V.; Ferrara, C.; Conti, D.M.; Bruni, G.; Capsoni, D. Synthesis and Characterization of Carvedilol-Etched Halloysite Nanotubes Composites with Enhanced Drug Solubility and Dissolution Rate. *Molecules* **2023**, *28*, 3405. https://doi.org/10.3390/molecules28083405.

- Capsoni, D.; Lucini, P.; Conti, D.M.; Bianchi, M.; Maraschi, F.; De Felice, B.; Bruni, G.; Abdolrahimi, M.; Peddis, D.; Parolini, M.; et al. Fe_3O_4-Halloysite Nanotube Composites as Sustainable Adsorbents: Efficiency in Ofloxacin Removal from Polluted Waters and Ecotoxicity. *Nanomaterials* **2022**, *12*, 4330. https://doi.org/10.3390/nano12234330.

Riassunto

In questa tesi di dottorato si sono studiati diversi approcci per produrre elettrodi self-standing caratterizzati da alta densità di energia e di potenza, ottenuti con una matrice di nanofibre di carbonio (CNF) e materiali ad alto voltaggio e/o alta capacità. Sono stati effettuati dei test preliminari sui composti $Na_3MnZr(PO_4)_3$, $Na_3MnTi(PO_4)_3$ e ZnS-GO per batterie a ioni sodio (SIBs), preparati con metodo tradizionale (tape-casted), e sulla singola matrice di CNFs elettrodepositata. Dopo aver realizzato un catodo self-standing utilizzando il ben noto materiale catodico per le batterie al Litio $LiFePO_4$ per valutare l'influenza delle CNFs sulla prestazione elettrochimica, i materiali attivi scelti per le SIBs sono stati caricati nelle nanofibre di carbonio per preparare i nuovi elettrodi self-standing. Le prestazioni elettrochimiche ottenute sono molto promettenti per la buona capacità ad alte C-rate, ciclabilità della cella e densità di potenza, grazie alla matrice di CNF che migliora la conducibilità elettronica e il contatto elettrodo/elettrolita.

Abstract

In this Ph.D thesis, we investigate different approaches to prepare high energy and power density self-standing electrodes, based on high voltage/capacity active materials and carbon nanofibers (CNFs). First, the characterization and electrochemical investigation was carried out on conventional tape-casted electrodes with the $Na_3MnZr(PO_4)_3$, $Na_3MnTi(PO_4)_3$ and ZnS-GO active materials for sodium-ion batteries (SIBs), and on the only electrospun CNFs matrix. Thereafter, a self–standing cathode was synthesized, based on CNFs and the well-known $LiFePO_4$ active material for lithium-ion batteries (LIBs), to investigate the role of CNFs on the electrochemical performance. Finally, the active materials for SIBs are loaded into CNFs, to prepare the new self-standing electrodes. The results are very promising in terms of enhanced capacity at high C-rate, cell lifespan, and power density (high cycling rate), thanks to the CNFs matrix, which improves the electronic conductivity and the electrode/electrolyte contact.

Table of contents

Chapter 1. Introduction

Nathan Lewis reported that '"Energy is the most important technological problem in the world" in 2007 during the Materials Research Society Spring meeting in San Francisco [1]. Indeed, since the industrial revolution the demand of energy in our societies kept increasing. Nowadays, energy powers most of our activities such as industry, communication, and transport. The main energy sources are fossil fuels such as coal, crude oil, and natural gas [2], see Figure 1.1: they are easy to transport and store, and they provide a high energy to volume ratio. Nevertheless, they present significant drawbacks:

- They are all pollutants because they naturally release toxic substances in the atmosphere, such as the sulfur dioxide responsible for acid rains;
- They are not renewable resources, that is the deposits of fossil fuels are subjected to progressive depletion.
- Their usage increases the emission of CO_2 into the atmosphere, as their consumption to produce energy requires their combustion as fuels. Carbon dioxide along with methane CH_4 and nitrous oxide N_2O contribute to the greenhouse effect and climate change.

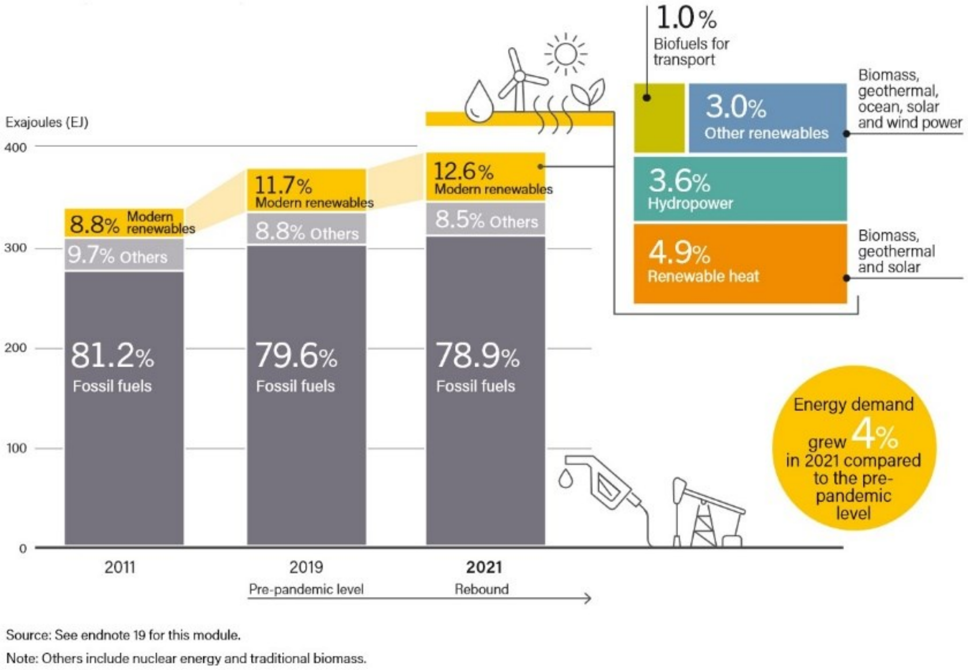

Figure 1.1: Final energy consumption of sources 2011, 2019 and 2021 (taken from [2]).

The greenhouse gases (GHGs) capture the reflected sun rays that would otherwise return into space, causing the increment of earth average temperature. The European commission has established that human-induced global warming is increasing at an average rate of 0.2°C per decade [3,4]. To name but a few, the consequences of increasing temperatures are drought, forest fires, more frequent floods, and drastic negative impact on biodiversity and sea environment. A complete list is reported in refs. [3–5].

One method to reduce the GHG emissions is to replace fossil fuels with renewable resources (RRs) that produce renewable energy (RE) such as solar, wind, hydroelectric and marine, biomass, and geothermal energy [4,6]. They present unbounded deposits which could meet the increasing global demand of world energy consumption. Their use will enable the world energy transition, satisfying the global energy consumption without bringing about the climate change.

Most renewable resources do, however, present one critical downside, namely their intermittence. Indeed, solar, wind, and hydroelectric power plants cannot produce energy on demand, as they depend on weather and environment conditions. To overcome this limit, the energy produced by renewable resource must be stored onto different devices and with different technologies, briefly described in the Subsection 1. A deep and complete review about RRs, RE and GHGs is reported in refs. [1–6].

Section 1. Storage systems

Subsection 1 Electro-mechanical storage system

Pumped Hydroelectric Storage (PHS)

The PHS is the most used energy storage system today, because it allows to reserve large amount of energy. By pumping water from a reservoir placed at lower to a higher one, we consume energy provided by the grid and store it in the form of gravitational potential energy of the water between the two levels. The stored energy is proportional to water mass and altitude between the two reservoirs. Whenever the energy grid demands more power, water is released back into the lower reservoir thus producing energy via an electric turbine. PHS's principal feature is that the stored energy is available after few hours of idle inactivity without losses, so it has a very low self-discharge rate. Its main application is the energy time-shifting while the principal disadvantage is the need of specific topographic sites [6,9,10].

Compressed Air Energy Storage (CAES)

CAES is an electro-mechanical storage system and, as for PHS, the turbines are used to store energy, but in this case the energy is stored in the form of compressed air into underground tanks. The quantity of stored energy depends on dimension of cavern, air pressure and temperature. As PHS, the principal app is the energy time-shifting. Finally, the necessity of caverns or underground tanks is a disadvantage for realizing big and inexpensive systems [6,9,10].

Flywheel Energy Storage

In the case of Flywheel, the energy is stored in form of rotational inertia thanks to the rotation of a big mass. The energy can be added or drained from the storage interrupting the mechanism with an electric engine. The energy retention is influenced by the initial and final energy ratio, while the amount of energy depends on the speed and weight of the rotating mass. The flywheel advantages are fast charge/discharge capability, quick response, and good lifespan, while its critical aspect is the safety, because it can cause damage to the enclosing environment. These features make the flywheel usable for fast response like frequency regulation and power buffering [9,10].

Subsection 2 Thermal Energy Storage (TES)

For TES the energy is stored in form of a medium's heat. Three are the type of medium used: sensitive, latent, or chemical. The sensible heat medium storage is the most used for TES and consists of reserving energy increasing temperature of a medium featured by high heat capacity. The medium could be solid or liquid such as brick, sand, aluminum, iron or engine oil, water, butane, propane. This type of TES is used in solar field where the medium is hated by the sun, storing the energy. When the medium is cooled, it produces energy following the principle of heat engine.

In the case of latent medium heat, the material phase transitions are exploited to generate heat at a constant temperature.

Finally, for chemical medium heat, the chemical exothermic and reversible reaction is used to produce heat as by-product. In this last case the molten salt and the water-based method are the principal technologies.
For all TES, the working principle is quite simple, but the cost is high and the self-discharge depends on medium's isolation from the surrounding external environment [6,9,10].

Subsection 3 Chemical Energy Storage (ECS)

Chemical storage system generates and stores energy through chemical reactions.

Hydrogen-Based Energy Storage

Hydrogen production is based on the reaction of water hydrolysis:

$$H_2 + \frac{1}{2}O_2 \rightleftharpoons H_2O.$$

Eq. 1.1

The hydrogen produced by water electrolysis reaction can be stored in different forms such as compressed gas, liquid or cryo-compressed hydrogen. It is important to choose the way of storage based on the features of the end-use application. For instance, storage volume and weight are critical factors for vehicle apps but are important characteristics for the forklift or marine employments. Hence, it is extremely important to choose the most efficient way to store hydrogen at the right temperature and pressure for the end-use applications. This aspect together with the flammability safety remain critical aspects or downsides of hydrogen storage.
Today the most common way to store hydrogen is the compressed gas form at different pressure. The release of compressed hydrogen happens using a fuel cell composed by two electrodes divided by an electrolyte. The release involves two reactions at anode and cathode, respectively:

$$H_2 \rightleftharpoons 2H^+ + 2e^- \ (anode)$$

Eq. 1.2

$$and\ \frac{1}{2}O_2 + H_2O + 2e^- \rightleftharpoons 2OH^- \ (cathode)$$

Eq. 1.3

This type of release is fundamental for vehicle application where the principal functions of hydrogen storage are receiving hydrogen during the refueling, containing hydrogen until the gas is requested back, and releasing hydrogen to make the vehicle working. One downside is that the efficiency of the device is 65% at room temperature, but the upside is the easy storage of hydrogen for long period. The overall efficiency is about 42%. [6,9,10].

Section 2. Electrochemical Energy Storage and the electrochemical cell

The electrochemical energy storage (EES) or the battery energy storage (BES) are systems based on reduction and oxidation taking place in an electrochemical cell. The electrochemical cell is a device able to convert the chemical energy in electrical one and vice versa. It is composed by two half-cells: one is the positive electrode known also as cathode and the other one is a negative element called anode. The two half-cells are divided by a membrane drenched with a solid/liquid ionic conductor, known as electrolyte. The electrical energy derives from the redox reactions and is stored in chemical form, electrons are generated at one electrode and are drained from the other one. The three main families of this EES are electrolytic cells, primary galvanic and secondary galvanic cells. In the electrolytic cells the electrical energy is supplied to promote the chemical reaction. In the primary galvanic cell, the chemical reaction is irreversible, and the chemical energy is transformed into electrical one; once the chemical process is complete, the cell is no longer usable. In the secondary galvanic cells, the red-ox reaction is reversible. Once the cell is discharged, it is possible to invert the process in order to recharge it. To recharge the cell, it is necessary a source of electrical energy. The electrical energy converts to the chemical one, and it is stored into the secondary cell or rechargeable battery (RB). This work is focused on studying the secondary galvanic cells based on alkaline ions such as lithium and sodium, but we report examples for both type of galvanic cell.

Alkaline Batteries

The alkaline batteries belongs to the primary galvanic cells . The main technologies in alkaline batteries are Cadmium-nickel oxide and metal hydride-nickel oxide cells. For Cadmium-nickel oxide battery the reaction is:

$$Cd(s) + 2NiO(OH)(s) + 2H_2O(l) \rightleftharpoons Cd(OH)_2 + 2Ni(OH)_2(s)$$

Eq. 1.4

The semireactions at the positive and negative electrodes are:

$$2NiO(OH)(s) + 2H_2O + 2e^- \rightleftharpoons 2Ni(OH)_2(s) + 2OH^-(aq)$$

Eq. 1.5

$$Cd(s) + 2OH^-(aq) \rightleftharpoons Cd(OH)_2(s) + 2e^-$$

Eq. 1.6

In the case of hydride-nickel oxide cells, a different reaction occurs at the negative electrode, involving the formation of metal hydride from metal:

$$M(s) + H_2O(l) + e^- \rightleftharpoons MH(s) + OH^-(aq).$$

Eq. 1.7

This cell is safer and displays higher capacity values than the lead-acid one, and these features make it preferable for portable apps.

Lead-acid batteries

The lead-acid batteries have been firstly introduced in the nineteen century and are secondary batteries. In this type of battery the electrolyte (sulphuric acid) has an active role and is not only used as ion conductor [9,11]. The complete reaction is

$$Pb(s) + PbO_2(s) + 2H_2SO_4 \rightleftharpoons 2PbSO_4(s) + 2H_2O(l)$$

Eq. 1.8

Some drawbacks are envisaged for these batteries: the reaction generates gaseous oxygen and hydrogen as byproducts. Therefore, it is required to keep the environment well-ventilated to avoid the pressure increase of highly flammable gases. Moreover, the lifespan of the battery is negatively affected by the evaporation of the electrolyte. The advantage of this technology is the low price compared to other secondary batteries.

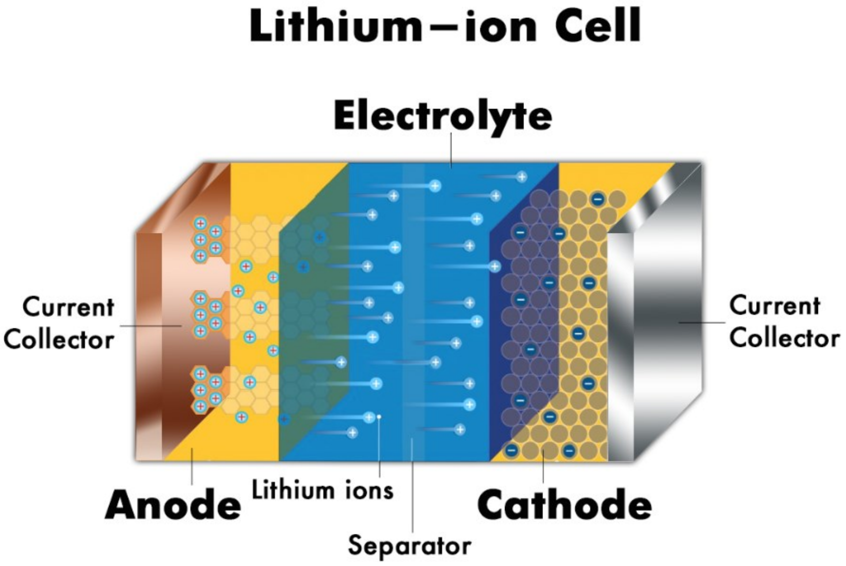

Figure 1.2: Representation of a Li-ions cell.

The scientific research in Lithium-ion battery (LIB) started in the mid-1960s simultaneously to the Sodium-ion battery (SIB). In the pioneering investigations, Sodium (Na) showed worse electrochemical performance, and the Lithium's advantages were considered more interesting to start the fabrication and commercialization of rechargeable batteries (RB), also known as accumulators or *secondary batteries*. Indeed, the RBs are still appealing for their use in a lot of applications as power grid, computer, digital cameras, tablet, and possible electrical vehicles.
What is an accumulator or a secondary battery? It is a *rechargeable system* capable of converting energy released by spontaneous chemical reactions into electrical energy. The cell is a single unit of a rechargeable battery (RB). One single cell is built following the concept of *''Rocking-chair''* [12,13].
Introduced first in 1970, the model involves the use of two different intercalation compounds for both the negative electrode (anode) and the positive one (cathode), along with an electrolyte which drenches a porous dielectric separator (Figure 1.2).
The intercalation compounds, called active materials, are made up of different crystalline layered structures, and ions rock from one electrode to the other. The active materials are combined with carbon and a binder. The former is used to enhance electronic conductivity and the latter, usually Polyvinylidene fluoride (PVdF), is added to ensure a close connection between the materials. Moreover, the carbon creates a conductive path for electrons which move back and forth electrode's active sites passing through the current collector and the external circuit. The current collector, typically a metal foil such as Aluminum or Copper, acts as support for the active material mixture and guarantees the electron transport.
This system permits the insertion/deinsertion of positive charges to guarantee an efficient and stable charge and discharge. The consequence of the continuous insertion/deisertion of alkali ions is the conversion of chemical energy into electrical one and vice versa. During the discharge process, ions are extracted from anode and intercalate into the cathode. When the ions are intercalated into active sites, the ions are stored in the electrode and the red-ox takes place at the interface between electrolyte and the electrode. The mole of electrons and ions changes in cathode/anode materials over time. For this reason, there is different stoichiometry at any different moment of cycling. The ions insertion /deinsertion process of both anode and cathode may occur following different reaction mechanisms:

$$MS_x + yA^+ \rightarrow A_yMS_x \qquad \text{Intercalation}$$

Eq. 1.9

$$A_yMS_x + (2x - y)A^+ \rightarrow M + xA_2S \qquad \text{Conversion}$$
Eq. 1.10

$$M + zA^+ \rightarrow A_zM \qquad \text{Alloying}$$
Eq. 1.11

$$A^+ + e^- \rightarrow A \qquad \text{Plating}$$
Eq. 1.12

where A is an alkaline element, M is a transition metal and S is an anion such as O, S, and F.

In an ideal intercalation reaction (Eq. 1.9), the crystal structure of active material is stable and does not chemically change during the cycling process. Usually, these structures display tunelled, layered or 3D networks, which permit to easily intercalate/deintercalate the alkaline ions. These active materials provide stable interfaces but have low volumetric capacity density. In the conversion reaction mechanism (Eq. 1.10), for each removed ion-electron couple a new substance is formed. These active materials have high-capacity density but low electronic conductivity and instability due to the structural changes during cycling. In the alloying process (Eq. 1.11), an alloy is obtained by the metal and the alkaline ions reaction, and in some cases different phases are formed. The chemical nature of the active material is preserved, and it exhibits a good interface stability. In this case more alkaline ions are inserted into initial electrode, so the result is a higher capacity. The disadvantage is the volume expansion and mechanical stress, which negatively affect the electrochemical performance of the active material. In the last plating mechanism, the alkaline ions make a self-alloy with the metal electrode made up of the same material. However, differently from the previous alloying system, in the plating mechanism phase transitions do not occur. as ions plate on themselves and we have only metallic element. In this case we obtain high-capacity values, but at the same time, complex structures such as dendrites could form. The bigger the dendrites are, the higher is the possibility to short-circuit the two electrodes of the cell.

The electrodes are composed not only by the active material but also by other components. It consists of two layers. The first includes the active material mixed with conducive carbon and binder, and the second is the current collector. So, the internal cell resistance is composed by two parts: the first from the current collector, and the second originate at the interface of the active material mix and the current collector. This last resistance is caused by the path from active sites to collector and is a function of the battery's state-of-charge (SOC) [9].

The ions transport is sustained by the electrolyte which is a reservoir of free ions available for reactions. It is electrically neutral and it could be liquid or solid. Whereas the former is less safe, it is preferred to the solid one, which implies a more complex interface with the electrode. The liquid electrolyte is responsible for ionic conductivity; the most commonly used for SIBs and LIBs are composed of a mixture of organic carbonate solvents and a Li-salt/Na-salt. It allows to reach high voltage without generating volatile by-products, compared to the other secondary batteries. The electrolyte guarantees to shuttle the ions between the two electrodes preserving the local electro-neutrality. The electrolyte must be highly resistive and electrically insulating to enforce the electron flow outside of the cell. Otherwise, a steady current flows through the cell causing it to self-discharge during both operating and resting time. Moreover, it is important to control the chemical stability of the electrolyte to make the ions reacting only through one controlled chemical reaction, as for the single electrons path. It is necessary because if the electrolyte reacts with ions forming composites, the cell capacity decreases [9].

At the electrolyte-electrode interface some adverse reactions may occur. The reaction between carbon and organic electrolytes forms composites, causing the decrease of ions amount and the cell capacity. Finally, the by-products could accumulate on the electrode surface forming a layer between electrode and electrolyte, called solid electrolyte interphase (SEI). An electrode self-passivation occurs, which plays a favorable role as it prevents the parasitic reaction to consume all ions. The SEI must ensure ion diffusion [9].

Section 3. Lithium vs sodium

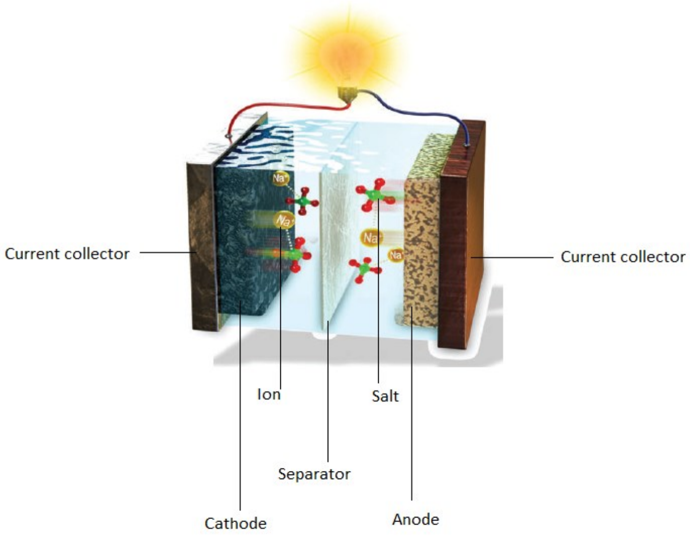

Figure 1.3: Schematic view of a Na cell (taken from [14]).

In 1970 during the oil crisis, the production of lithium-ion batteries starts. First, M. Stanley Whittingham started to work on new technology to produce fossil fuel-free energy. He discovered a new energy-rich material which becomes the first cathode of lithium-ion batteries, the titanium disulfide. Hence, the first lithium cell was built with TiS_2 and metallic lithium as anode, and although this combination showed a potential of 2 V, the risk of explosion due to the presence of metallic lithium can be envisaged. In the 1980 there was the second important turning point which brought to the development of the lithium-ion batteries. The scientist John Goodenough discovered the cobalt layered oxide $LiCoO_2$ as a promising intercalation cathode which delivers as much as 4 V, leading to a more powerful battery. In 1985 Akira Yoshino proposed the use of a carbon material as petroleum coke which intercalates Li ions and is safer than metallic lithium. Thanks to these three turning points, the first prototype of lithium-ion batteries was developed. It was based on $LiCoO_2$ as cathode and carbon material as anode, and it was lightweight. It was robust and featured by the possibility to be cycled hundreds of times before the deterioration of its performances. In 2019 M. Stanley Whittingham, John B. Goodenough, and Akira Yoshino, won the Nobel Prize in Chemistry “for the development of lithium-ion batteries”. All these information are found in ref. [15].

In 1991, Sony Energy Tech Corporation commercialized the first Lithium-ion battery (LIB) built with layered lithium-cobalt oxide $LiCoO_2$ (LCO), graphitic carbon and propylene carbonate (PC): ethylene carbonate (EC) solvent with lithium hexafluorophosphate ($LiPF_6$) as cathode, anode, and electrolyte, respectively (Figure 1.3). The cathode was prepared as lithium-source while the anode as lithium-sink, that is the Li-ions are injected during the first cycle to initiate the negative electrode. The first battery reactions are

$$Li_{1-x}CoO_2 + xLi^+ + xe^- \longrightarrow LiCoO_2,$$

Eq. 1.13

$$Li_xC_6 \longrightarrow xLi^+ + xe^- + 6C,$$

Eq. 1.14

Whereas the entire red-ox is

$$Li_xC_6 + Li_{(1-x)}CoO_2 \longrightarrow +6C + LiCoO_2$$

Eq. 1.15

The main advantages of these cells are: high volumetric energy density of approx. 250W hL^{-1}, high Li diffusion (≈$10^{-9}cm^2s^{-1}$), high open-circuit voltage of 3.7 V, high coulombic efficiency and long cycle life [16]. This active material is still nowadays very relevant in the market of mobile applications, such as smartphones, PCs and tablets.

In the following years, the LIBs scientific research focused on improving the properties of accumulators to increase the capacity, the working voltage and lifespan. The works comprehend all the LIBs components: a safer anode with higher specific capacity and rate capability such as graphite, a cathode with a better crystallinity, different percentage of Co, and higher working voltage, a binder which can provide a better positive electrode adhesion, and an electrolyte with high oxidation resistance up to 4.5 V, for example organic carbonates and a salt with high purity and state of dryness [17,18] (see Section 2 in 0 for further information on LIBs typical composition). Today, LIBs are fabricated with the same rules and concepts, but changing the active material of the cathode to enhance the energy storage. For instance, Lithium-Nickel-Cobalt-Aluminum oxide (NCA), Lithium-Nickel-Manganese-Cobalt oxide (NMC), Lithium-Iron-Phosphate (LFP) or other lithium layered oxides (LMOs) are now exploited as positive electrodes in secondary batteries [19,20]. NMC and LFP are the most commercially available. The former includes cobalt different percentages with respect to LCO, finds application in the electric vehicles field and shows high energy density, as it guarantees a good battery lifespan. The latter is poor of cobalt and ensures excellent performance, despite its low electronic conduction and diffusion of Lithium. LFP is, particularly, of large employment in the market of residential energy storage.

However, to choose the right active material we must consider not only the technical behavior and performance, but also the social and economic aspects such as natural abundance, low cost, no competition with other possible applications, eco-friendly nature for usage and possibility of material recycling [18,21]. In this section we concentrate our attention on the environmental aspects of the LIBs sources, to explain why the scientific community starts to search for an alternative to LIBs technology using ions such as magnesium, potassium and especially the principal candidate, sodium. To choose a starting material for the storage devices, sustainability, renewability, green chemistry of material's sources must firstly be taken into account, and secondly, the type and volume of the markets in which the storage system will be applied. To discuss the former topic we report the distribution of principal reserves around the world of the crucial elements used in LIBs for lithium (Table 1.1), cobalt (Table 1.2) and graphite (Table 1.3).

The term *reserve* means "that part of the reserve base which could be economically extracted or produced at the time of determination. Reserves include only recoverable materials; thus, terms such as 'extractable reserve' and 'recoverable reserves' are redundant and are not a part of this classification system" as reported in refs. [22,23].

Cobalt is defined as a critical element, namely its reserves are poor, non-uniform distributed and restricted. The Co reserves are principally localized in the Democratic Republic of Congo (DRC) (see Table 1.2). This uneven distribution is settled in an economic and political unstable country as DRC, and it makes the permanent production and export of the raw material[1] difficult. Indeed, the market price has been continuously fluctuating and it is not possible to assure a constant Co supply to the worldwide production facilities [24]. Moreover, the Li reserves have recently risen serious global concerns on abundance and distribution. Even though the Lithium resources are rather uniformly spread, and they are concentrated mainly in no-problematic countries as South America and Australia (see Table 1.1), the Lithium request has brusquely increased due to the introduction of electric vehicles and stationary applications. Indeed, these employments of Li sources require considerable and huge accumulators which lead to an increment in Lithium demand. This aspect bring us to talk about the latter important aspect when choosing a starting material: its type of market and market volume. It is estimated that the amount of lithium's reserves are sufficient if they are involved in portable device market, but they

---

[1] Raw material: basic material from which a product is made.

Table 1.1: Lithium reserves worldwide distribution in Tons (taken from [22])

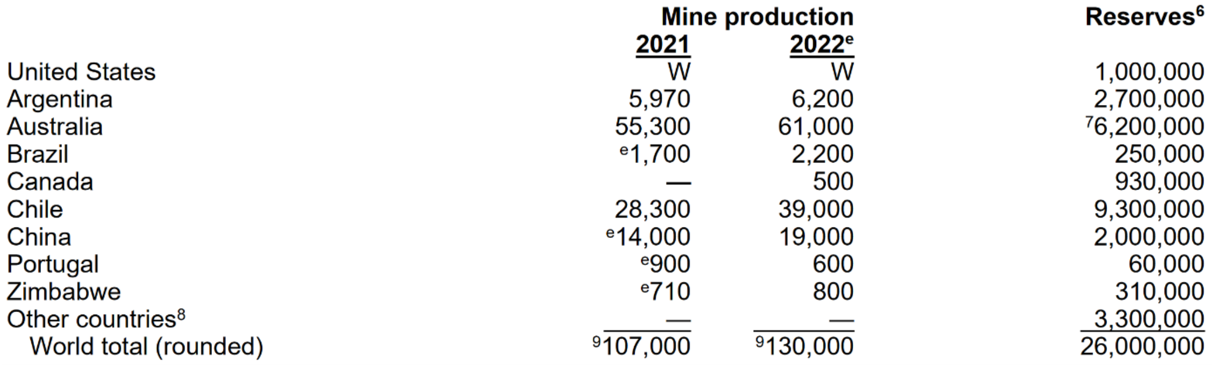

	Mine production		Reserves[6]
	2021	2022^{e}	
United States	W	W	1,000,000
Argentina	5,970	6,200	2,700,000
Australia	55,300	61,000	[7]6,200,000
Brazil	^{e}1,700	2,200	250,000
Canada	—	500	930,000
Chile	28,300	39,000	9,300,000
China	^{e}14,000	19,000	2,000,000
Portugal	^{e}900	600	60,000
Zimbabwe	^{e}710	800	310,000
Other countries[8]	—	—	3,300,000
World total (rounded)	[9]107,000	[9]130,000	26,000,000

Table 1.2: Cobalt’s reserves worldwide distribution in Tons (taken from [22])

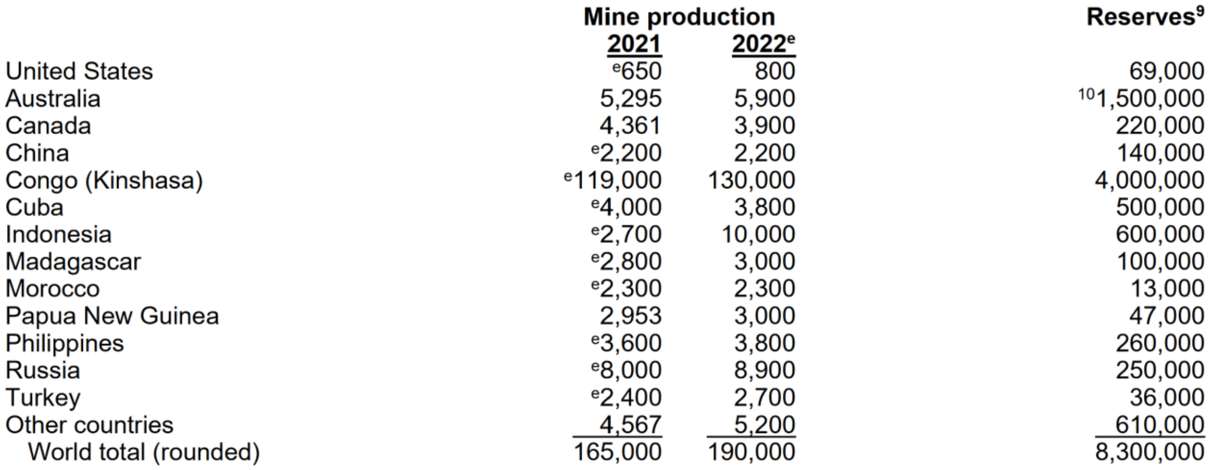

	Mine production		Reserves[9]
	2021	2022^{e}	
United States	^{e}650	800	69,000
Australia	5,295	5,900	[10]1,500,000
Canada	4,361	3,900	220,000
China	^{e}2,200	2,200	140,000
Congo (Kinshasa)	^{e}119,000	130,000	4,000,000
Cuba	^{e}4,000	3,800	500,000
Indonesia	^{e}2,700	10,000	600,000
Madagascar	^{e}2,800	3,000	100,000
Morocco	^{e}2,300	2,300	13,000
Papua New Guinea	2,953	3,000	47,000
Philippines	^{e}3,600	3,800	260,000
Russia	^{e}8,000	8,900	250,000
Turkey	^{e}2,400	2,700	36,000
Other countries	4,567	5,200	610,000
World total (rounded)	165,000	190,000	8,300,000

Table 1.3: Graphite’s reserves worldwide distribution in Tons (taken from [22])

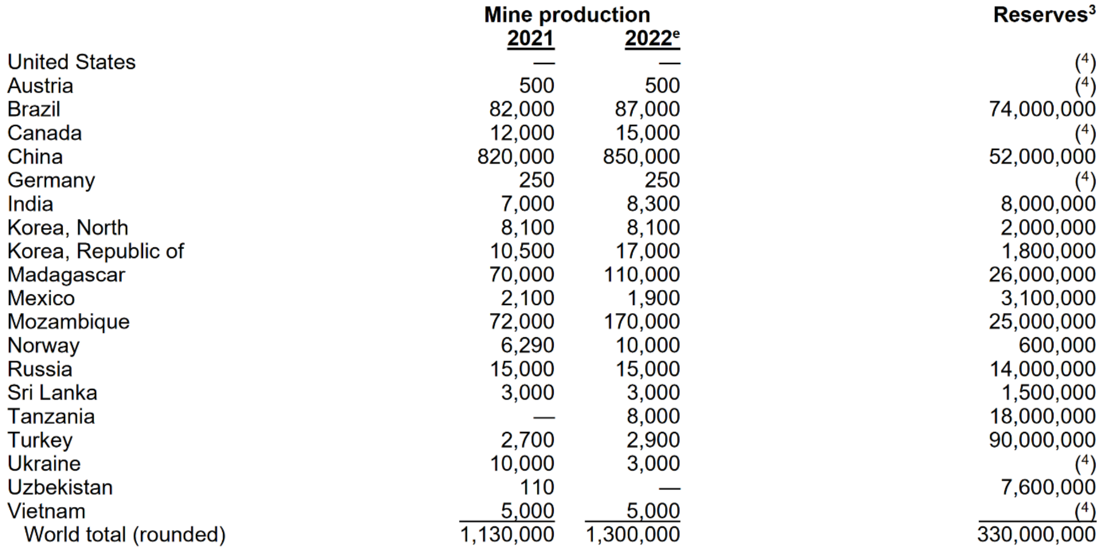

	Mine production		Reserves[3]
	2021	2022^{e}	
United States	—	—	(4)
Austria	500	500	(4)
Brazil	82,000	87,000	74,000,000
Canada	12,000	15,000	(4)
China	820,000	850,000	52,000,000
Germany	250	250	(4)
India	7,000	8,300	8,000,000
Korea, North	8,100	8,100	2,000,000
Korea, Republic of	10,500	17,000	1,800,000
Madagascar	70,000	110,000	26,000,000
Mexico	2,100	1,900	3,100,000
Mozambique	72,000	170,000	25,000,000
Norway	6,290	10,000	600,000
Russia	15,000	15,000	14,000,000
Sri Lanka	3,000	3,000	1,500,000
Tanzania	—	8,000	18,000,000
Turkey	2,700	2,900	90,000,000
Ukraine	10,000	3,000	(4)
Uzbekistan	110	—	7,600,000
Vietnam	5,000	5,000	(4)
World total (rounded)	1,130,000	1,300,000	330,000,000

will not be already sufficient when the electric vehicles and power grid markets are included [25–27]. This is one of the principal reasons why scientific community invests its time into searching for alternative chemistries to Li. The restatement choice is carried out on the base of the raw material's percentage around the world, its uniform distribution, the extraction, and refinement methods costs. Among them the sodium chemistry results to be the most promising for it features similar to the lithium one. In the Subsection 5 a complete description of sodium chemistry is reported.

Subsection 5 Properties and applications of SIBs

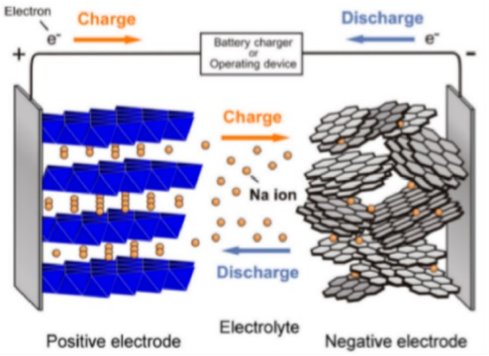

Figure 1.4: the interface in Sodium-ion battery with layered oxides (taken from [28]).

The research about Na and Sodium-ion batteries began in 1980 with the starting study on the sodium-cobalt layered oxide ($NaCoO_2$) as cathode material. However, some adverse Na features and the lack of a suitable negative electrode for SIB has discouraged more developments, until the 21th century when the increasing demand of electrochemical energy storage (EES) stimulated the researchers to test other storage systems. In 2000, a new anode material for SIBs demonstrating great electrochemical properties close to the graphite for LIBs was developed. The tested material was hard-carbon as Na host structure anode: it exhibits a reversible capacity of 300 mAhg^{-1}[29]. Thereafter, the second turning point is made by Okada and co-workers in 2006 [30], which report the use of $NaFeO_2$ as possible cathode for SIBs. It is a O-type layered oxide like the $LiCoO_2$ used into LIBs, and it presents similar intercalation/ deintercalation mechanisms. The Figure 1.4 shows the first sodium cells composed by a layered oxide as cathode and hard carbon as anode.

Today, the SIBs are composed by a liquid electrolyte, a current collector and two intercalation compounds used for both electrodes. The electrolyte is typically composed by a salt such as $NaClO_4$ or $NaPF_6$ mixed with aprotic organic carbonate solvents (e.g. polyethylene carbonate and diethylcarbonate, or polyethylene carbonate) and additives such as fluoroethylene carbonate (FEC). This additive is employed to broaden the electrochemical stability window (ESW) . The current collector is made of Aluminum for both electrodes, which is less expensive than Copper. The cathode is usually a layered oxide or a polyanionic compound like phosphates or pyrophosphates. Whereas, the anode is typically based on hard carbon, tin oxides, metal alloys or phosphorous [14,28,31,32].

Lithium-ion and sodium-ion battery performance is strongly affected by the properties of the Li and Na elements, respectively. Sodium is an alkali-metal with ionic radius of 1.07 Å, molar mass of 22.98 g mol^{-1} and a red-ox potential (*vs.* SHE) of −2.71 V. These values are higher than Lithium's ones (Table 1.4). The larger ionic radius and the higher mass of Na atom limit the electrochemical performance of Sodium-based cells. Indeed, both volumetric and gravimetric reversible capacity decrease of about 14% in $NaCoO_2$-hard carbon cells compared to $LiCoO_2$-graphite ones (Table 1.4) [28]. In addition, the greater volume of Na ions restrains the use of typical anode materials, e.g. graphite. It is generally accepted that sodium insertion into graphitic carbons is minimal, unless under high pressures [33]. However, hard carbon is adequate thanks to its huge voids and disordered structure where Sodium can intercalate during electrochemical reactions [29].

On the other hand, the Na element as alkali ion in SIB presents several benefits [34–36]. First of all, the large dimension of Na ensures a weak solvation energy in aprotic polar solvents in contrast to Li's one. This Sodium feature implies an easier diffusion and better conductivity of Na ions from bulk electrolyte to the electrode interface and a low charge density around ions. This also implies a favored alkali-ion insertion process and a fast reaction at the electrode. In fact, $NaClO_4$ in propylene carbonate (PC) is

10% to 20% better than $LiClO_4$ in the same organic solvent [37]. Another fundamental advantage of sodium is the cost reduction against the lithium which is an expensive and critical raw material. In fact, it is demonstrated that the abundant resource reserves permit a low-cost manufacturing, and make the SIBs technology the most promising alternative product to the LIBs [20,38,39].

Based on the abovementioned properties of Na ion, it can be summarized that sodium-ion batteries are low-cost and until today they storage lower energy density. Hence, in the near term the principal applications for SIBs are the stationary applications energy storage such as power grid. These energy storage systems help in enhancing the flexibility, minimizing the power fluctuations and making the integration of renewable power generation easier. In the power grid field, the SIBs can really be a good alternative to LIBs: an adequate value of energy storage is achieved by assembling several cells, as in these systems the high weight is not a problem. While the properties, including battery global weight of SIBs, make the production of portable devices difficult, field where LIBs technology is already dominant [40].

The electrode materials for SIBs are divided in groups based on their crystalline structure. In the following, we summarize and describe the anode and cathode materials exhibiting better energy capacity, and structural and cycling stability.

Table 1.4: Lithium and Sodium ion properties (table taken from [28]). Ionic radii data are taken from [41], de-solvation energy from [34], and molar conductivity from [37].

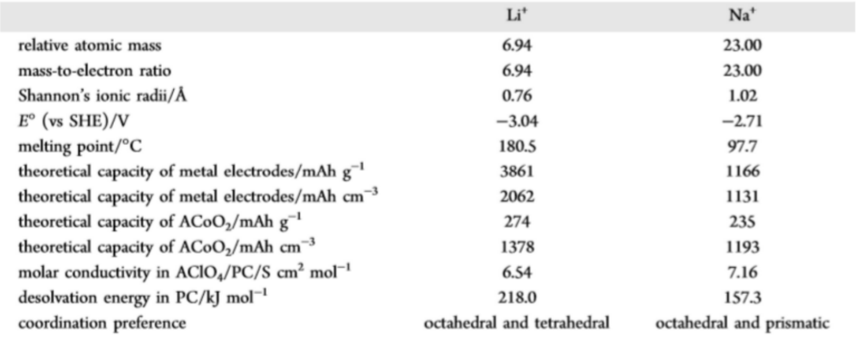

	Li^+	Na^+
relative atomic mass	6.94	23.00
mass-to-electron ratio	6.94	23.00
Shannon's ionic radii/Å	0.76	1.02
E° (vs SHE)/V	−3.04	−2.71
melting point/°C	180.5	97.7
theoretical capacity of metal electrodes/mAh g^{-1}	3861	1166
theoretical capacity of metal electrodes/mAh cm^{-3}	2062	1131
theoretical capacity of $ACoO_2$/mAh g^{-1}	274	235
theoretical capacity of $ACoO_2$/mAh cm^{-3}	1378	1193
molar conductivity in $AClO_4$/PC/S cm^2 mol^{-1}	6.54	7.16
desolvation energy in PC/kJ mol^{-1}	218.0	157.3
coordination preference	octahedral and tetrahedral	octahedral and prismatic

Subsection 6 Brief overview on cathodes for SIBs

In the present work, we synthesize and characterize two cathodic materials that belong to the polyanionic compound family. For the sake of completeness, we also introduce two other main cathodic structures for SIBs, layered-oxides and Prussian-blue-type. The layered oxides are the first cathodes studied for SIBs because of their successful application as cathodes for LIBs with $LiCoO_2$. However, they reveal to be particularly unstable at air and undergo structural transition during cycling for SIBs. A complete review on this topic is reported in refs. [14,32,42–44].

Layered Oxides

The general formula of layered oxides is A_xMO_2 where *A* is either Li or Na ions whereas *M* is a transition metal such as Ti, V, Co, Mn, Cr, Fe, or Ni. These compounds are divided into groups *O3, O'3, P2, P'2, P3, P'3,* or *T1* where:

- the letters O, P, and T refer to the Na coordination: octahedral, prismatic, and tetrahedral, respectively,
- the number indicate the number of stacking layers,
- the superscript symbol ' or '' the inferior symmetry of the structure [45].

The layered oxide structures are characterized by channels which allow intercalation of Na ions [46–48], as shown in Figure 1.5. However, the A_xMO_2 compounds exhibit irreversible phase transition during the cycling and instability at air [49–51]. A benchmark cathode for SIBs is the manganese oxide $NaMnO_2$, which exhibits high specific capacity of 200 mAh/g in the voltage range of 2V-4V [49,52,53].

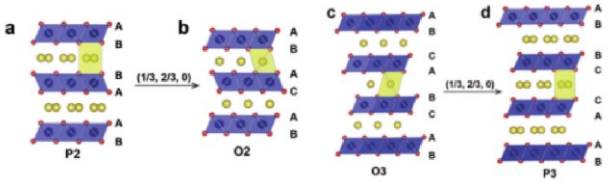

Figure 1.5: Crystal structure of the selected layered oxide in ion-batteries (taken from [49]).

Polyanionic Compounds

The polyanionic compounds exhibit strong covalent bonds among the polyanionic units $(XO_4)^{n-}$, where X is S, P or Si [54]. Contrary to layered oxides, the covalent bonds of these structures assure a more stable crystalline structure without phase transitions and a good mechanical stability. However, these strong bonds negatively affect the material as well. Indeed, they lower the cathode electronic conductivity and the overall cell performance. A strategy to decrease the electrical resistance is mixing the active material powder with conductive carbon. Yet, it increases the electrode's weight while being electrochemical inactive, thus decreasing the gravimetric and volumetric energy density. The families of polyanionic compounds include Sodium (Na) Super Ionic Conductors (*NaSICON)* [55,56], Olivine [57,58], Pyrophosphates [59,60], Mixed Phosphates [61,62], Metaphosphates [63,64], Fluorophosphates [65,66] and alluaudite [67,68]. The *NaSICON* structure will be discussed in detail in the Section 4, as the SIBs cathodes synthesized and characterized in this PhD work belong to this family of polyanionic compounds.

Prussian Blue and Analogues

They are characterized by the $[Fe(CN)_6]$ group, and the most famous for Na-ion batteries is $Na_xM[Fe(CN)_6]$ where M is Co, Fe, Ni, Cu and Ti. Prussian Blue Analogues (PBAs) exhibit large channels suitable for reversible Na intercalation, but some structural instability during cycling as irreversible phase transition and thermal degradation may occur [69–72].

Subsection 7 Brief overview on anodes for SIBs

The absence of a good anode materials for SIBs is the bottleneck which makes the large-scale production of SIBs difficult. Hence, the scientific research is actively working to test and discover new anodic materials. Among the anodes fo SIBs, in this PhD study we investigate ZnS, belonging to the conversion/conversion-alloying materials family, but we also report some features of carbon based and alloying materials anodes for SIBs. Further information can be found in refs. [44,73–76].

Carbon-based materials

The use of graphite as anode for SIBs is delayed due to the exfoliation of graphite structure during the insertion/extraction of Na ions, and weak interaction between Na ions and graphite [33,77]. For this reason, the carbon-based materials such as expanded graphite [78,79], carbon nanomaterial [80–84], non-graphitic carbon [85,86] and metal organic framework (MOFs) [87,88] become the first choice as SIBs anodes.

The carbon-based materials exhibit low voltage vs. sodium and are thermally and chemically stable. Among them, the carbon nanomaterials such as carbon nanotubes (CNTs), carbon nanofibers and graphene oxides became popular thanks to their extraordinary strength and electronic conductivity [73]. Notably, they can be used as anode themselves [81] (see Section 1 in Chapter 3) or as a carbonaceous support for an active material anode [74] (see Section 5 in Chapter 3). In both cases, they provide great advantages, such as electrode flexibility, "buffering" of the active material's crystal volume changes upon sodium intercalation/deintercalation, and good electrolyte permeation. The use of carbonaceous nanomaterials as support are one of the topics of this work and further literature data are given in Section 7, while the results are reported and discussed in in Chapter 3.

Conversion/conversion-alloying materials

The typical conversion/conversion alloying anode materials for SIBs are oxides [75,89], sulfides [74,90–94], selenides [95,96], phosphides [97,98] and MOFs [99,100]. In these materials the Na insertion/deinsertion mechanism involves the chemical transformation of metal oxide into a new chemical compound. In some cases, the conversion takes place along with the alloying reaction, depending on the metal oxide involved. The conversion/conversion alloying anode materials enable to store more than one Na ion; as a consequence, huge volume changes occur upon cycling, which can negatively affect the electrode performance [73]. The problem of volume expansion/contraction is usually minimized either incorporating a carbon material which “buffers” the volume changes, or changing the electrolyte to form a stable SEI. In this work, we investigate and evaluate the electrochemical performance of zinc sulfide properly supported into carbon nanofibers (CNFs), both to obtain self-standing electrodes and to benefit of the buffering action of CNFs. Further details are given in ref. [74], and Section 5 of Chapter 3.

Alloying

The family of alloying anodes for SIBs includes all that elements which can form an alloy with sodium, such as Pb, Bi, Sn, P, and Sb [14,101–105]. One single atom of the aforementioned elements form an alloy with more than one sodium ions at a voltage < 1 V vs Na/Na$^+$. The alloying materials exhibit a high theoretical capacity and a huge volume change. For this reason, tin, phosphorus and antimuonium are the most widely analyzed, as bismuth and lead give volume changes of 150% and 364%, respectively [73].

Section 4. *NaSICON* state of the art

NaSICON-structured materials belong to the polyanionic compounds family, and are discovered and studied for the first time by H. Y-P. Hong, J.B. Goodenough and J.A. Kafalas in 1975 as solid electrolyte. Only in the recent years the *NaSICON* compounds with appealing physico-chemical properties, such as thermal, kinetic, and structural stability in air, high ionic conductivity, and chemical flexibility, were regarded as promising cathode and anode materials in both Sodium and Lithium batteries and in many other electrochemical devices. However, the *NASICON* materials have also a few drawbacks, and the most relevant is the poor electronic conductivity, which can be enhanced by using approaches such as carbon coating, metal doping, and nanostructuring [106,107]. This section focuses on the employment of *NaSICON* in SIBs, which are the main issue of this thesis. Hence, we report a state of art on the *NaSICON* research, and specifically on the two *NaSICON* structures studied in this work: $Na_3MnZr(PO_4)_3$ and $Na_3MnTi(PO_4)_3$.

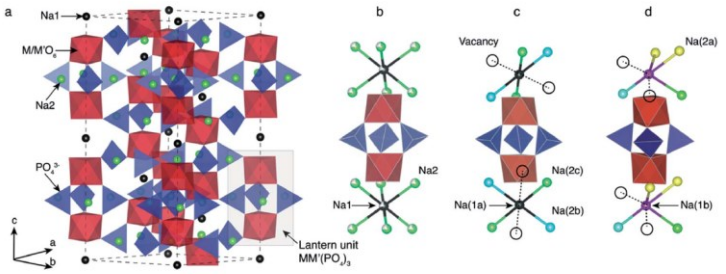

Figure 1.6: a) The general and the most common $Na_4MM'(PO_4)_3$ rhombohedral structure where the Na ion sites are the black Na1 and the green Na2, the MO_6 and $M'O_6$ octahedra are red while the tetrahedra PO_4^{3-} are blue; b) Lantern unit representation with Na disordering in the $Na_3MM'(PO_4)_3$ polymorph; c) local ordering of Na ions in the monoclinic $Na_3MM'(PO_4)_3$ phase; d) local Na1b violet and Na2a yellow environment in monoclinic phase (taken from [108]).

The general formula of a polyanionic compound is $A_yMM'(TO_4)_3$ where A are alkali ions, Na in our case, M and M' are transition metals (TMs), mainly Ti, V, Cr, Mn, Fe, Co, and Ni, y indicates the amount of Na ions into the formula which are intercalated/deintercalated in the structure, and T is the anion such as P, Si, S or P, which is the most commonly used in *NaSICON* structures [108]. The polyanionic units TO_4^{n-} ensure alkali ions migration and provide structure stability during the charge/discharge process, the MO_6 or $M'O_6$ charge compensation body garantees the polyhedra connectivity, the inductive effect, the d-splitting orbitals, and TMs coordination determines the high working voltage of polyanionic compounds. The M-O bond is covalent and the weaker is the covalent bond, the smaller will be the repulsion between bonding and antibonding orbitals. This reduces the antibonding orbitals away from Fermi energy level, increasing consequently the working potential. Moreover, the higher is the coordination number, the stronger is the polyanionic unit electronegativity making the M-O bond weaker. So, for polyanionic compounds the voltage features follow a regularity silicate<phosphate<pyrophosphate<sulfate [109]. A variety of TMs can be selected to prepare *NaSICON* structures, and a wide range of chemical compositions can be explored: this leads to the fabrication of several cathode and anodes with different high-capacity density and impressive voltage working window. Notably, by choosing M and M' with +2 and +3 oxidation state respectively, and giving to M and M' the possibility to accommodate multiple red-ox active states, it is possible to intercalate/deintercalate up of 4 Na^+ ions [108]. High working voltage is accessed by cathodes such as $Na_3V_2(PO_4)_3$ [110,110,111,111,112], $Na_3MnZr(PO_4)_3$ [56,113], $Na_3MnTi(PO_4)_3$ [114–116], $Na_3Cr_2(PO_4)_3$ [117–119], and low working voltage by anodes such as $NaTi_2(PO_4)_3$ [120–122], $NaZr_2(PO_4)_3$ [123–125], $Na_3MnTi(PO_4)_3$, $NaSn_2(PO_4)_3$ [126–128]; notably, the NaSICON structure is suitable to fabricate symmetric cells. The typical working potentials are about 2 V, 3.2 V, 3.6 V and 4.1/4.5 V, and depend on the chemical composition and the structure of the host material [21,106–108,129].

The $A_yMM'(TO_4)_3$ structure ($Na_4MM'(TO_4)_3$ in our case) consists of PO_4 tetrahedral and MO_6 or $M'O_6$ octahedral units connecting to form a 3D open framework, shown in Figure 1.6. Usually the $A_yMM'(TO_4)_3$ compounds exhibit monoclinic (*2C/2* S.G.), triclinic (*P1 S*.G.) or rhombohedral ($R\bar{3}c$ S.G.) structure, depending on the oxidation state of TMs. The rhombohedral structure is the most common. As an example, $Na_4V^{+2}V^{+3}(PO_4)_3$ exhibits the rhombohedral structure, while $Na_3Ti^{+3}Ti^{+3}(PO_4)_3$ displays the monoclinic form. In the rhombohedral phase, three tetrahedral and two octahedral units connects via corners to form the ''lantern units'', which provide an excellent phase stability during the red-ox process. Two types of Na intercalation sites (Na1 and Na2) are formed by assembling lantern units in the 3D $MM'(PO_4)_3$ open framework. There is one Na1 site per formula unit (f.u.), it is six-coordinated and located between two octahedra, whereas there are three Na2 sites per f.u. and they are eight-coordinated to tetrahedra via Oxygen atoms. When y < 1, the Na ions occupy the Na1 site, whereas for y>1 the Na ions are randomly distributed on both the Na1 and Na2 sites. When y=4, the Na1 and Na2 sites are fully occupied, resulting in $A_4MM'(TO_4)_{3,}$ and the structure is rhombohedral, whereas for y=3 several *NaSICON* compounds adopt the monoclinic structure. In the former the high symmetry results in six equivalent Na1-O distances. In the latter displaying a lower symmetry, Na1 splits into two different sites Na1a and Na2b, and Na2 into five: Na2a, Na2b, and Na2c are occupied, Na2d and Na2e are vacant (see Figure 1.7). The Na2 coordination with O atoms is more complicated [108,129]. The Na ions in Na1 site usually are not involved in the intercalation/deintercalation process, as the Na-O bonds are strong (237.8pm), indicating a good stability of Na ions in Na1. While, the Na ions in the Na2 sites actively participate to red-ox reaction, are responsible for the ions' migration into the structure, and exhibit a Na-O bond of 252.1pm (weaker than the Na1 site) [107].

Due to the y wide range of the alkali metal component A_y with 0<y<4, the 3D open framework $MM'(TO_4)_3$ can be considered the structural block for *NaSICON* structures: it is shown in Figure 1.7. Interestingly, the $MM'(TO_4)_3$ can accept M, M' and T of different relative size while maintaining the high rhombohedral symmetry and without distorting the tetrahedra and the octahedra. The study of Maxim Avdeev [129] demonstrates that the distortion or symmetry lowering are not dependent on M, M' and T size, but they are driven by interionic interactions due to the M, M' and T oxidation states, by geometrical mismatch of 3D open framework $MM'(TO_4)_3$ and Na cations, and electronic effects such as Jahn Teller distortion. When one of the abovementioned phenomena occur, the octahedra and tetrahedra tilt and distort from their ideal positions.

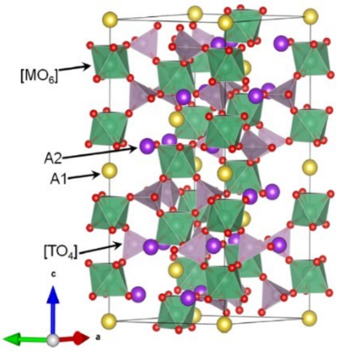

Figure 1.7: The general representation of $A_yMM'(TO_4)_3$ (taken from [129]).

The Na^+ ions storage capacity depends on the reversible intercalation/deintercalation of alkali metal ions into the 3D open framework $MM'(PO_4)_3$, and follows the equation:

$$Na_zMM'(PO_4)_3 + (y-z)Na^+ + (y-z)e^- \rightleftharpoons Na_yMM'(PO_4)_3$$

Eq. 1.16

where z and y are the initial and final atomic *Na* amount in the *NaSICON* structure [107,108]. To understand the electrochemical behavior of *NaSICON* it is crucial to know the Sodium-ion migration mechanism and pathway, the local environment of ion intercalation, the aforementioned structural features, and the pathway involving the lower energy barrier [107]. Since the crystal structure has been already discussed above, now we focus on ionic transport and conductivity in the *NaSICON* structures. In both rhombohedral and monoclinic symmetry, the ionic transport depends on the framework geometry and *Na* content. The former plays a key role in in the *Na* migration, because if it is too small it becomes the bottleneck of *Na* migration and diffusion in the crystal structure. The latter has two important roles, firstly carrying the carriers' concentration and secondly the *Na-Na* motion influences the ionic conductivity. There are three principal migration mechanisms of Na-ions into the *NaSICON* structure, studied especially for rhombohedral $Na_3V_2(PO_4)_3$ ($R\overline{3}c$ S.G.) [107,130,131]. The mechanism A is reported in Figure 1.8a: the Na ion migration, occurring along the x direction, is hosted by the channel between tetrahedra. The mechanism B involves migration along the y direction (Figure 1.8b), and the Na ions move through the voids located between the XO_4^{3-} tetrahedra and the MO_6 or $M'O_6$ octahedra. Finally, in the Figure 1.8c, it is reported the mechanism C where the Na ions move along the z direction close to the octahedra. The mechanism C has an energy barrier >200eV, so it is energetically unfavored with respect to mechanism A and B with energy barrier of 0.0904 eV and 0.11774 eV, respectively [107,130]. Moreover, other two possible mechanisms for the Na motion in NaSICON structure are reported by Wang et al. [131]: Na2⟶Na2 and Na1⟶Na2⟶Na1 (Figure 1.9). The direct motion of Na ions occurs through a small space between MO_6 or $M'O_6$ octahedra and three XO_4^{3-} tetrahedra. To transit in the small space, the length of Na-O bond needs to be shorted, thus inducing strain into the lattice. Consequently, in order to move the ions following this mechanism, the migration

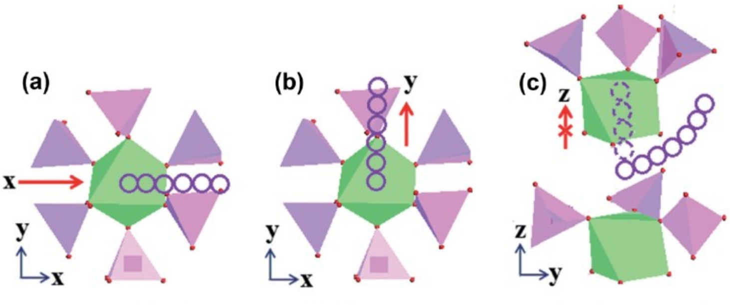

Mechanism A Mechanism B Mechanism C

Figure 1.8: Different mechanism of Na ion migration in *NaSICON* structure; the Na diffusion pathway is also represented (taken from [130]).

process must overcome a high energy barrier which makes the Na2⟶Na2 forbidden. Instead, in the two-step mechanism Na1⟶Na2⟶Na1, the ions firstly jump from Na1 to Na2 vacant site, leaving the Na1 site empty, and subsequently the Na ions migrate from Na2 to Na1 sites. This second mechanism is preferred with respect to the first one because the sum of energy barriers of the two step results in a lower value than the single step process [107,131].

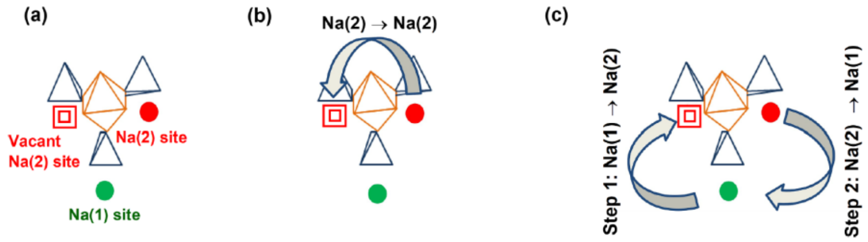

Figure 1.9: a) Arrangement of *Na1* and *Na2* sites in Rhombohedral symmetry; b) The diffusion mechanism of *Na* ions from *Na2*-to-Na2 sites; c) Mechanism from *Na1* to *Na2* and from *Na2* to *Na1* (taken from [131]).

Another possibility for Na motion is when the Na ions move from Na1 to Na2 sites through two triangular bottlenecks called T1 and T2 showed in Figure 1.10 [129]. It is required that the T1 and T2 are larger than the sum of Na and O ionic radii to ensure the ionic transport and guarantee a good ionic conductivity in the structure [129,132–134]. In particular, Maxim Avdeev [129] demonstrates that high ionic conductivity can be achieved only when the M and M' size is smaller than the T one. In fact, by decreasing T and increasing M or M', the factional subspace volume of Na sites decreases, and the ionic conductivity too. Finally, experiments on diffusion Na pathway in *NaSICON* structure are conducted, and it is difficult to understand which is the preferred one. However, it is possible to conclude that the ion transport occurs employing both sites Na1 and Na2.

As abovementioned, the crucial disadvantage of *NaSICON* structure is its poor electronic conductivity, which is an important aspect as well as ion diffusion in order to fully using the charge capacity of electrochemical active materials, especially at high C-rate. The low electronic conductivity could cause a sluggish kinetics of the diffusion process and an important restriction of the rate performance and cycling stability [107]. There are different methods to improve the electronic conductivity such as (i) the ionic [135,136] and heteroatom doping [137,138], (ii) the usage of additive conductive carbon or carbon coating [139,140] or carbonaceous matrix [74,141–146], or (iii) the exploitation of different synthetic approaches to obtain nanostructured materials with peculiar morphologies, as the particles size and shape influence the electrochemical performance.

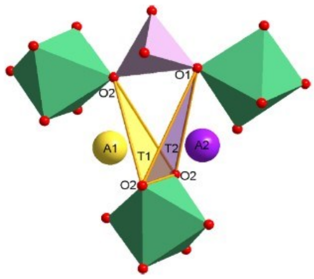

Figure 1.10: Two triangular bottlenecks T1 and T2 when Na ions pass from Na1(A1) to Na2(A2) sites (taken from [129]).

To implement the ionic doping, different metallic ions with different valence state and size are introduced in the *NaSICON* structure, such as Ti^{4+}, Fe^{3+} and Mg^{2+}. The cations are introduced to partially substitute the M o M' TMs or alkali metal, and to improve the electronic conductivity. The higher valence cation doping generates Na vacancies which compensate the defects and enhance the alkali metal ions diffusion in the material. While, by lower valance cations addition, few holes are produced within the structure and the electronic conductivity increases. It is also important to control the size and the number of ions doping. Indeed, in the case the ion is too large, and the amount of element doping is in excess and not uniform, the crystal structure is damaged, and the structural stability is destroyed. Finally, using non-toxic and cheap elements it is possible to reduce the cost of SIBs and make them safer. The introduction of heteroatoms such as N, P, S and B tailors the electronic structure too, and N is the most common. Usually, they are inserted in the carbon framework of the *NaSICON* structure or as anion substituting T already present. Adding them permits to create additional active sites and extrinsic defects which enhance the structural *NaSICON* stability and reversibility [107].

Adding conductive carbon is the most common strategy to enhance the electronic conductivity. The carbon-based materials are chosen for their numerous advantages: low cost, high conductivity, high surface area, and chemical stability. There are two methods to add conductive carbon: in-situ carbon and ex-situ carbon modifications. The former results in adding carbon sources as citric acid, sucrose, dopamine, and glucose into the precursors of the materials synthesis to create a carbon coating, or in the slurry preparation. The choice of carbon sources and the thermal treatment influence the electrochemical performances. In the case of carbon coating, the added source is successively carbonized in the inert atmosphere at high calcination temperature. In this way, a thin and homogeneous carbon layer is formed on the particles, producing an electron-conducting network which increments the electronic conductivity. This thin layer prevents from the agglomeration of particles, and avoids the excessive growth of particles, favoring the formation of nanoparticles and diminishing the Na ions diffusion length. Finally, the thin carbon layer also plays the key role of "buffer", as it allows for the volume change accommodation, which results in better mechanical electrode integrity and long lifespan. So, the in-situ carbon has several advantages and enhances the electronic conductivity, but it does not satisfy the electrochemical performances of high-power applications developed in the last years. It is due to the pyrolysis temperature below 1000°C of active materials does not completely graphitize the carbon coating, the temperature brings to micrometric particles with a large electrode polarization, and, in addition, the carbon coating improves the electronic conductivity of single particles and it does not assure a fast electronic transport [107]. However, the latter ex-situ approach can satisfy the requirements creating new electron pathways, which electrically connect the active particles at high C-rate too. It involves the use of carbon-sources such as amorphous carbon [144], graphene [147], carbon nanotubes (CNTs) [148], carbon nanofibers (CNFs) as carbon porous framework [74,145,146,149,150], mesoporous carbon materials [151], to prepare composite with the active materials. These ex-situ carbons can be doped by heteroatoms that help in enhancing the electronic conductivity and in increasing the carbon surface wettability from the electrolyte, because they make the carbon more apolar: these features are beneficial for achieving a higher Na storage. The carbon composite consists of carbon additives as external conducive matrix and small particles of active materials, *NaSICON* in our case, which are crystalline and embedded. The carbon framework firstly avoids the active material particles agglomeration and secondly forms a conducive bridge to guarantee an electrical intimate connection of active particles. Moreover, the matrix is also composed by huge and well-connected pores which enable a fast ion and electrons diffusion. It plays the key role of buffer, controlling the volume changes during cycling, which produce structure strain negatively affecting the cell lifespan [107].

Last but not least, the synthesis methods can significantly influence the active material particles, and so the electrochemical performance of the cell. *NaSICON* synthesis has to be low cost, simple process with high yield, safety, have to guarantee power production with homogeneous chemical composition, small particles size, high purity, and large active surface area, and need the facile availability of precursors. The synthesis temperature, precursors, concentrations, time, and solvent are fundamental to handle the particle size and shape, the pore size, and the level of porosity. These physical properties can influence the electrochemical mechanism and performance. Indeed, to obtain a superior capacity retention and a good stability during cycling, it is important to guarantee nanoscale morphology and significant porosity, which enhance surface area. The nanostructure allows to increase the charge-transfer reaction at solid-liquid interface and diminishes the electrode polarization resistances. In addition, the diffusion path decreases, and consequently the diffusion time too. The significant porosity helps the ions diffusion and a better permeation of liquid electrolyte, making the ion transport easier during red-ox, fundamental to make the cell functioning at high rate (see Figure 1.11). Moreover, the porous electrode guarantees extra voids which restrict the volume change during the intercalation/deintercalation of *Na* into the structure making the cell lifespan longer [107].

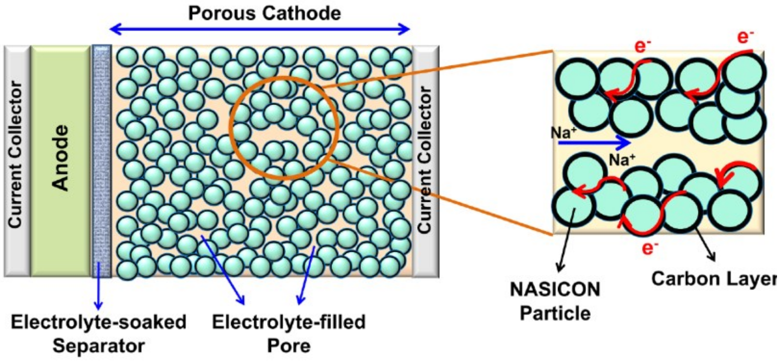

Figure 1.11: Na ions diffusion path in porous electrode (taken from [107]).

There are two categories of synthetic approaches to fabricate electrodes with right features, the first is the powered synthesis of *NaSICON* structures and the second is the fabrication of 3D structures [152–154]. The former includes different types of procedures: solid state [155], sol-gel [56,145,146,155,156], hydrothermal [157] and solvothermal [158], combustion [159], electrospinning [145,160], freeze-drying [161], solution evaporation [162], spray drying [163] and rheological phase reaction [164]. These methodologies affect several particles features such as size, distribution, morphology, and chemical distribution. In this work we choose to use the sol-gel synthesis for the *NaSICON* structures $Na_3MnZr(PO_4)_3$ and $Na_3MnTi(PO_4)_3$ because it is simple, low-cost, fast, and permits to control the particle size and the formation of carbon coating around the particles. The latter includes the preparation of 3D electrodes with interconnected pores in which the active particle could be embedded or synthesized. The 3D architecture not only guarantees efficient charge transport, excellent stability as in the case of 1D and 2D electrode materials, but also prevents severe particle aggregation and so provides good ion and electron diffusion kinetic into the electrode at high C-rate. The matrix is a continuous electron path and a robust buffer which improves electrochemical performance. It could contain three possible pores or a combination of them: macropores with pore size >50nm, mesopores with pore size in the range of 2nm-50nm, and micropores with pore size <2nm. Nowadays, the principal techniques used to fabricate these hierarchical electrodes are the spray drying, aerosol spray, pyrolysis, and electrospinning [107].

Subsection 8 Mn-based cathodes for Sodium-ion batteries

As aforementioned in Subsection 5 the abundant resources and low-cost of Sodium-ion batteries create high expectations on SIBs usage in large-scale applications such as large-scale energy storage and low-speed or low-end electronic products. In this case the cathode plays a key role in determining electrochemical performance and controlling the cost of the battery. So in the last years the research attention is focused on Mn-based polyanionic materials which combine greenness, abundant resources, performance and low price [109].
The compensation charge body MO_6 or $M'O_6$ could be composed by a huge variety of TMs which influence the working voltage of polyanionic compounds, but only Fe e Mn are the principal potential candidates for environmental and price motivations. In the case of Iron-based cathodes for SIBs, the polyanionic compounds such as $Na_4Fe_3(PO_4)_2P_2O_7$ [165] and $NaFePO_4$ [166,167] achieve high theoretical capacity values of about 129 mAh/g and 154 mAh/g, but the working potential of about 3.2 V for Fe(II)/Fe(III) red-ox pair is low, losing the energy density advantage. On the contrary, for Mn-based compounds such as $Na_4Mn_3(PO_4)_2P_2O_7$ or $Na_3MnTi(PO_4)_3$, it is possible not only to achieve high capacity of about 170 mAh/g, but also activate both Mn(II)/Mn(III) and Mn(III)/Mn(IV) red-ox pairs reaching the work potential of 3.9 V and 4.2 V, respectively [114,168]. So, the advantages of these compounds are the use of 4 Na ions during charge/discharge cycling and the relevant energy density because of the high working voltage, low-cost and good cycling performance. However, the Mn-based materials are

characterized also by two main disadvantages which weakens their functionality, namely the *Jahn Teller effect (JT)* of Manganese (III), and the dissolution of Mn^{2+} into organic liquid electrolyte caused by the disproportion reaction of surface manganese $2Mn^{3+} \rightleftharpoons Mn^{2+} + Mn^{4+}$ [56,109,169]. The *JT* effect leads the Mn-based cathode to structural disorder, large volume change and irreversible phase transition which negatively affects the electrochemical performance. Among the first efforts to limit the *JT* effect there is the doping with Mg, Hf and Zr, which stabilize the *NaSICON* structure due to the bond-length deviation created by the large-ionic mismatch. The presence of doping element such as Hf with 5d orbitals can enforce the structure presenting a small volume change and can stabilize the local environment of the Mn-O bonds during cycling. It reveals a cooperative *JT* effect present for the Mn(II)/Mn(III) red-ox pair, but a recovery of the MnO_6 octahedra symmetry for the Mn(III)/Mn(IV) red-ox couple [169].

Finally, phosphates are the principal class of Mn-based polyanionic compounds, and the first one is $NaMnPO_4$ exhibiting the crystal forms of olivine and maricite [170,171]. The former is thermodynamically unstable and electrochemically active, the latter is thermodynamically stable but not red-ox active. However, today the research attention is focused on *NaSICON* phosphates as, among phosphates, seem to be the most promising for SIBs, due to their open skeleton structure described in Section 4. They are $Na_3V_2(PO_4)_3$ derivatives completely replacing the Vanadium with Manganese metal transition $Na_3Mn_2(PO_4)_3$, employing electroneutrality as basic principle [109,172]. Other mainstay Mn-based *NaSICON* structures include the partial substitution of Mn with another TMs such as Chromium, Aluminum, Zirconium, and Titanium, creating the respective compounds $Na_4MnCr(PO_4)_3$ [173], $Na_4MnAl(PO_4)_3$ [174], $Na_3MnZr(PO_4)_3$ [56,113,145,175–177], and $Na_3MnTi(PO_4)_3$ [114–116,146,178–185]. Among these structures, this work discusses below and investigates in the following chapters the $Na_3MnZr(PO_4)_3$ and $Na_3MnTi(PO_4)_3$ phosphates, due to their electrochemical performances and their environmentally friend elements.

$Na_3MnZr(PO_4)_3$

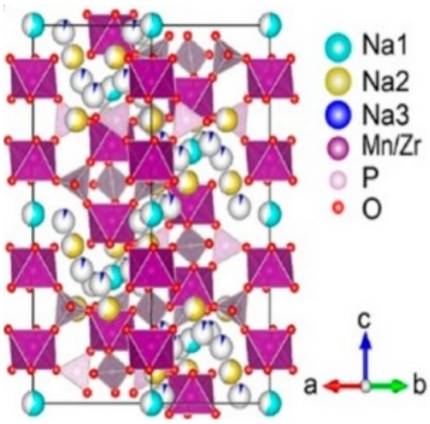

Figure 1.12: $Na_3MnZr(PO_4)_3$ crystal structure (taken from [56]).

$Na_3MnZr(PO_4)_3$ is a *NaSICON*-structured compound characterized by rhombohedral symmetry with space group $R\bar{3}c$. Its structure is displayed in Figure 1.12. It is formed by MnO_6 and ZrO_6 octahedra as charge compensation units and PO_4 tetrahedra as polyanionic units. Octahedra and tetrahedra are connected through corner-sharing, creating a framework which include three different interstitial sites to accommodate Na ions: Na1, Na2, and Na3. Na1 exhibits a 6-fold coordination, Na2 is 8-fold coordinated, while the Na3 sites are 4-fold coordinated and are located between Na1 and Na2. This material presents a theoretical capacity of 107 mAh/g, obtained by both Mn(II)/Mn(III) and Mn(III)/Mn(IV) red-ox pairs during insertion and extraction of two Na ions per formula unit, respectively. Indeed, the cathode shows two red-ox peaks at about 3.6 V and 4.1 V. The former is due to the Mn(II)/Mn(III) red-ox couple and the latter is caused by the Mn(III)/Mn(IV) red-ox pair, followed by two phase reversible transformations [56,145]:

$$at\ 3.6V \quad Na_3Mn^{2+}Zr(PO_4)_3 \rightleftharpoons Na_2Mn^{3+}Zr(PO_4)_3 + Na^+ + e^-,$$
Eq. 1.17

$$at\ 4.1V \quad Na_2Mn^{3+}Zr(PO_4)_3 \rightleftharpoons NaMn^{4+}Zr(PO_4)_3 + Na^+ + e^-.$$
Eq. 1.18

The activation energy of $Na_3MnZr(PO_4)_3$ rhombohedral structure is about 0.38 eV, similar to other *NaSICON* structures reported in literature, and it is lower than the monoclinic phase of other *NaSICON* materials such as $Na_3V_2(PO_4)_3$ (about 0.87 eV). This makes the $Na_3MnZr(PO_4)_3$ crystal structure promising as possible SIBs cathode. Moreover, this cathode material is composed of Zirconium in order to limit the presence of both *JT* effect of Mn(III) and the possible disproportion reaction into liquid electrolyte. The typical synthesis, reported also in literature, is the sol-gel route, which forecasts the formation of carbon coating of the active material's particles, to provide electron tunnelling on Na ions surface followed by the oxidation of Mn(II) to Mn(III) and then to Mn(IV) [56,113]. After this brief overview on the structure, we report in detail the insertion/extraction of *Na* ions with the subsequent $Na_3MnZr(PO_4)_3$ structural evolution, and the $Na_3MnZr(PO_4)_3$ conductivity.

Gao et al. in [56] report a theoretical study on the desodiation mechanism of $Na_3MnZr(PO_4)_3$ computed by *Density functional theory* (*DFT*). The Figure 1.13a reports the convex hull obtained by DTF calculations which shows, per formula unit, the formation energy E_{form} of the phases $Na_xMnZr(PO_4)_3$ relative to composition x=3 with E_{Na3} and to x=1 with E_{Na1}. Following the formula, the E_{form} is:

$$E_{form} = E_{Nax} - \frac{1}{2}(x-1)E_{Na3} - \frac{1}{2}(x-3)E_{Na1}.$$
Eq. 1.19

The $Na_2MnZr(PO_4)_3$ phase is in the mid of the hull and it is stable, while the phases with x=1.5 and x=2.5 are metastable/unstable.

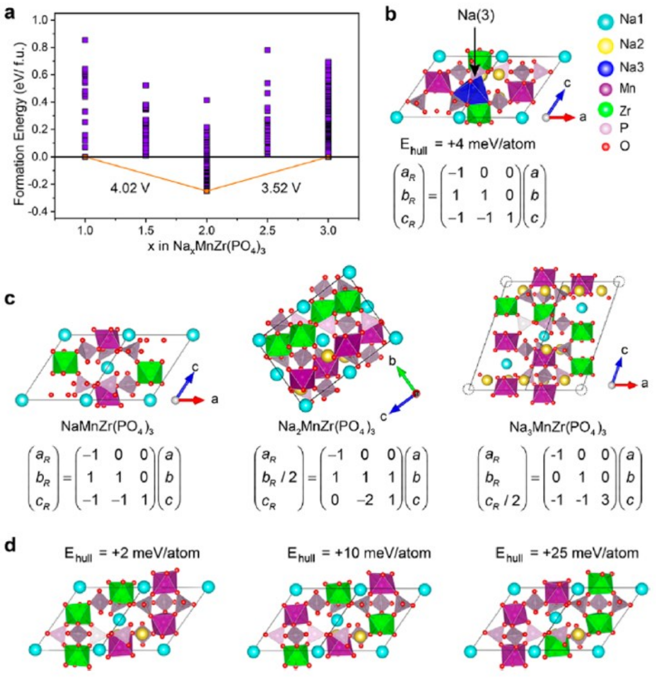

Figure 1.13: a)Convex hull obtained by the *DFT* calculations; b) $Na_3MnZr(PO_4)_3$ relaxed structure with Na ions in Na3 sites; c) Structures of $Na_xMnZr(PO_4)_3$ lowest energy phase and relation among *DFT* cell parameter (a, b, c) and $R\bar{3}c$ cell parameter (a_R,b_R, c_R), dashed circles are Na1 vacancies; d) $Na_2MnZr(PO_4)_3$ structure optimized by *DTF* with Mn/Zr in different orders (taken from [56]).

According to the study, the lowest energy phase $Na_3MnZr(PO_4)_3$ presents a significant disorder of the Mn and Zr sites which leads to three different Na1 positions showed in Figure 1.13c, namely the occupied MnO_6-Na1-MnO_6 and MnO_6-Na1-ZrO_6 sites, and the vacant ZrO_6-Na1-ZrO_6 positions. All the Na1 sites are connected to the Mn and Zr octahedra through face-sharing. The ZrO_6-Na1-ZrO_6 positions are empty because of the Zr^{4+} and Na^+ unfavorable electrostatic interaction which leads to Na1 site destabilization. In $Na_3MnZr(PO_4)_3$, the Na ions principally occupy the Na2 positions face-shared with MnO_6-Na2-MnO_6 and MnO_6-Na2-ZrO_6 sites due to the smaller electrostatic repulsion between Zr^{4+} and Na^+ or Mn^{2+} and Na^+. Due to the random distribution of Mn/Zr ions, 1/12 of the MnO_6-Na2-ZrO_6 and 1/3 of the ZrO_6-Na2-ZrO_6 high energy configuration preferentially remain vacant for the electrostatic repulsion and the analysis of lowest energy structure. A long-range Na order is precluded in $Na_3MnZr(PO_4)_3$ because of the Mn/Zr random distribution and the high energy of MnO_6-Na2-ZrO_6 positions. The $Na_2MnZr(PO_4)_3$ phase shows a weak preference for Mn^{3+}/Zr^{4+} order, reported in Figure 1.13d. The lowest energy $Na_2MnZr(PO_4)_3$ reports full occupation of Na1 positions, but principally in MnO_6-Na1-MnO_6 configuration, because the other ones (ZrO_6-Na1-ZrO_6 and MnO_6-Na1-ZrO_6) are less stable and present vacant Na1 sites. Na ions are located in 1/3 of Na2 positions in the preferred MnO_6-Na2-MnO_6. Finally, the $NaMnZr(PO_4)_3$ shows Manganese sites completely oxidized to Mn^{4+} and, at the lowest energy configuration, the Na1 positions are totally occupied, while the Na2 ones are vacant. Following this DFT analysis, the tentative desodiation mechanism forecasts the initial extraction of the Na ion from MnO_6-Na2-ZrO_6 to go from $Na_3Mn^{2+}Zr(PO_4)_3$ to $Na_2Mn^{3+}Zr(PO_4)_3$ at 3.6V, while the Na2 sites in MnO_6-Na2-MnO_6 remained totally occupied with both x=3 and x=2. Instead, the ZrO_6-Na1-ZrO_6 occupied positions increase with desodiation to x=2 because the Na1 ions displace to Na3 site for the growing Na2 vacancies. Finally, the desodiation process from $Na_2Mn^{3+}Zr(PO_4)_3$ to $NaMn^{4+}Zr(PO_4)_3$ implies the full occupation of the Na1 site and the complete Na2 desodiation [56].

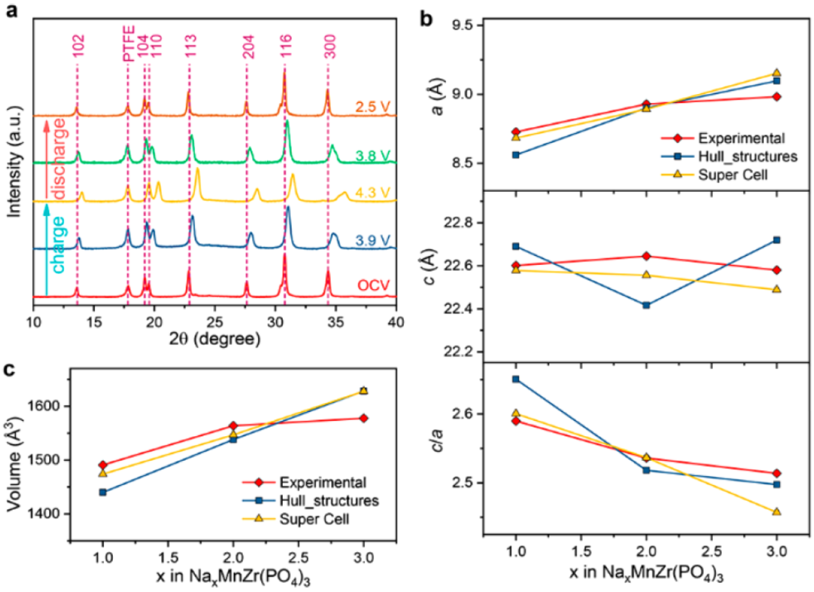

Figure 1.14: a) $Na_3MnZr(PO_4)_3$ patterns at different states during cycling; b) lattice parameters variation; c) volume change (taken from [56]).

The structural evolution caused by desodiation mechanisms consists of two reversible phase transitions as reported in Eq. 1.17 and Eq. 1.18, and the Figure 1.14 displays the patterns and lattice parameter variations during the cycling of $Na_3MnZr(PO_4)_3$. The transition from $Na_3MnZr(PO_4)_3$ to $Na_2MnZr(PO_4)_3$ is followed by the cell parameter variation, particularly the expansion of *c* values, linked to the increased desodiation and the Na1 and Na2 sites occupation (see Figure 1.14b). In $Na_3MnZr(PO_4)_3$ the Na1 sites between two ZrO_6 octahedra are vacant, and during the desodiation mechanism to $Na_2MnZr(PO_4)_3$ the Na ions occupy the Na3 site, close to the empty Na1 positions in ZrO_6-Na1-ZrO_6 configurations. In the following desodiation process from $Na_2MnZr(PO_4)_3$ to $NaMnZr(PO_4)_3$, *c* increases for the higher repulsion of TMs along c-axis, which causes the increasing and expansion of Na1 site occupation. The small increase of the *c* lattice parameter during the two-phase transitions is followed by the small decrease of the *a* value and the increase of the *c/a* ratio. The variation of the *a* parameter is related to the decrease of Na2 occupation and the decrease of TMs ionic radius during the oxidation process of Mn^{2+} to Mn^{3+} and Mn^{4+} (0.83 Å, 0.645 Å, and 0.53Å, respectively). The *a* and *c* variation are smaller compared to the other *NaSICON* structures reported in the literature, which means a smaller volume change. It is desirable for a better long-term cycling stability of the $Na_3MnZr(PO_4)_3$ cathode [56].

Seeing as the NaSICON compounds are good ion conductors, we report a brief overview on the conductivity of $Na_3MnZr(PO_4)_3$ material, discussed in different papers in literature [175–177]. The ionic conductivity of $Na_3MnZr(PO_4)_3$ is $1.8x10^{-6}$ $\Omega^{-1}cm^{-1}$ at room temperature [175] and the ionic conductivity mechanism is similar for all the three forms ($Na_3MnZr(PO_4)_3$, $Na_2MnZr(PO_4)_3$ and $NaMnZr(PO_4)_3$) discussed above [176]. The ionic conductivity value increases as the Na ion concentration increases. Notably, the Na mobility enhancement is related to the Na ions which occupy the Na2 sites, participating to the ionic conductivity. While the Na1 sites do not give contribution to ion conduction but have an effect on the skeleton structure stability. The growing Na concentration in Na2 leads to an increase of Na-O bond which suggests an easier mobility of Na ion and higher ionic conductivity in Na2 positions. To conclude, in literature it is demonstrated that Na occupancy and Na-O bond increase monotonically with the *x* content of Na into the structures [176].

$Na_3MnTi(PO_4)_3$

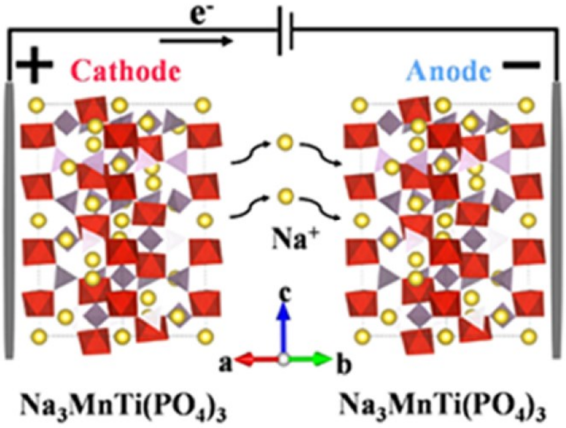

Figure 1.15: Structure of $Na_3MnTi(PO_4)_3$, where MnO_6 and TiO_6 octahedra are red, the PO_4 tetrahedra are pink and Na ion sites are yellow (taken from [55]).

$Na_3MnTi(PO_4)_3$ is a suitable *NaSICON* structure as both cathode and anode for rocking chair batteries, due to the presence of both electrochemically active elements Manganese (Mn) and Titanium (Ti) [182,186]: this paves the way to fabricate symmetric Sodium cells with the same active material for both anode and cathode [55,114]. Among the other advantages of this compound there are the non-critical composition, the low-cost, the high working potential up to 4.2 V, and the high theoretical capacity of about 176 mAh/g. While the main problem is the poor electronic conductivity and the limit in the temperature synthesis. Usually, the former is solved by carbon coating or adding an electron conducting matrix [179,180,184]. Instead, synthesis temperatures higher than 650°C led to a cell volume shrinkage probably caused by the oxidation of small amounts of Mn(II) to Mn(III) (ionic radii: of 0.83 Å and 0.64 Å, respectively). It can negatively affect the electrochemical performance for the Manganese red-ox couples [146,187]. The typical synthesis is the sol-gel method [55,180,182,186–188], but spray-drying [183,184] and solid state [189] processes are also suitable to obtain the compound.

$Na_3MnTi(PO_4)_3$ crystallizes in the rhombohedral structure with $R\overline{3}c$ space group, and consists of a MnO_6 and TiO_6 octahedra (red) and PO_4 tetrahedra (pink) skeleton, shown in Figure 1.15. The Mn and Ti are randomly distributed on the transition metal octahedral sites, which are connected to tetrahedra by corner-sharing, creating a large open channel among the two polyhedron types, accessible for the easier Na ion diffusion. The tetrahedra consist of strong covalent bonds, which give good structural stability and safety at high working voltage. Typically, there are two Na ion sites (yellow) in the structure, Na1 and Na2. The Na1-Sodium ions are not mobile, while the Na2 position undergoes to occupancy variation during cycling [186].

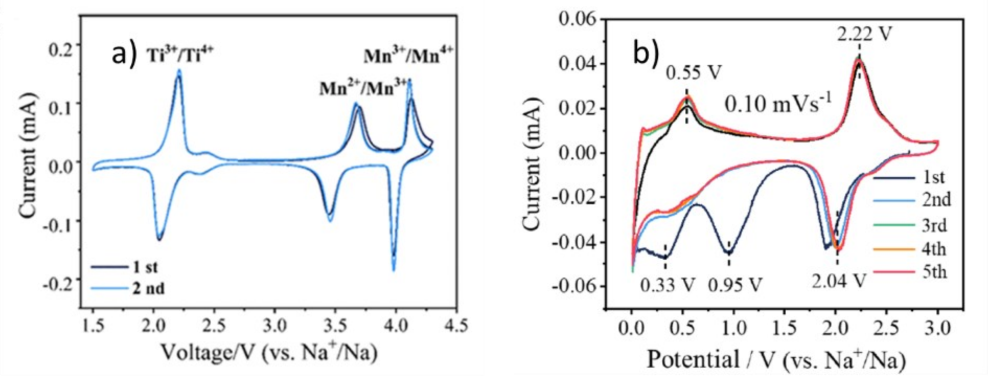

Figure 1.16: Electrochemical activity of $Na_3MnTi(PO_4)_3$: a) as cathode (taken by [55]), b) as anode (taken by [182]).

As cathode, the electrochemical activity is dominated by three-electron reactions due to the Ti(III)/Ti(IV), Mn(II)/Mn(III) and Mn(III)/Mn(IV) red-ox couples at 2.1V, 3.6V and 4.1V vs Na/Na^+, respectively (Figure 1.16a). The redox mechanism involves a multielectron process during the Na^+ extraction/insertion. It includes a two-electron transfer for Mn^{2+}/Mn^{3+} and Mn^{3+}/Mn^{4+} and one electron process in the case of Ti^{3+}/Ti^{4+}; an ex situ X-ray diffraction investigation demonstrates the sodiation/desodiation process involves both solid–solution and two-phase reactions [55,183] Equation Eq. 1.20 summarize the charge/discharge process:

$$Na_4MnTi(PO_4)_3 \overset{2.1V}{\longleftrightarrow} Na_3MnTi(PO_4)_3 \overset{3.6V}{\longleftrightarrow} Na_2MnTi(PO_4)_3 \overset{4.1V}{\longleftrightarrow} Na_1MnTi(PO_4)_3$$

Eq. 1.20

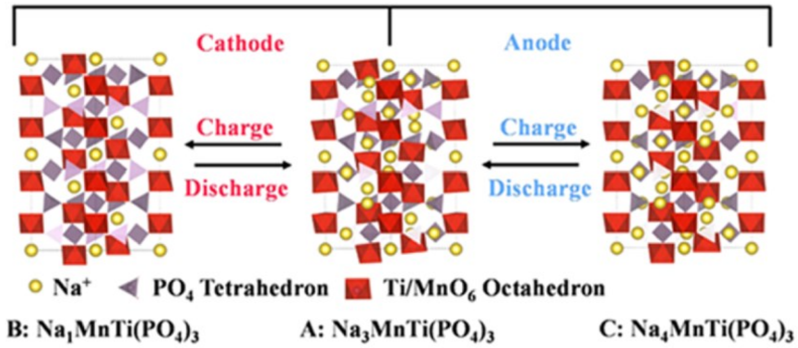

Figure 1.17: Scheme of the three-electron reaction (taken from [55]).

As reported by Gao et al. in [186], all these structures maintain the rhombohedral symmetry, the volume change is about 4.8%, lower than other *NaSICON* structures. Moreover, the phase transition leads to the decrease of the *a* lattice parameter and the increase of the *c/a* ratio. Manganese also implies possible cooperative *JT* effect, as the voltage difference between the two red-ox Manganese couples is about 0.5V. It confirms the presence of the localized-electron Mn(III) with the t^3e^1 configuration in $Na_2MnTi(PO_4)_3$ structure [186].

Usually, the red-ox peak at 2.1 V is used as both anode and cathode, as shown in Figure 1.16b, displaying the anode electrochemical activity. The anode activity is not only characterized by the peak at 2.1 V but also by the peak at 0.5 V caused by the reduction of Ti(III) to Ti(II), while the peak at 0.95 V is irreversible and due to the decomposition of electrolyte followed by the formation of SEI [182]. In this case, the *NaSICON* structure passes from $Na_3MnTi(PO_4)_3$ at 2.1V to $Na_4MnTi(PO_4)_3$ at 0.5V during discharge process and insertion of one Na ion (Figure 1.17), according to the equation:

$$Na_3MnTi(PO_4)_3 + Na^+ + e^- \rightleftharpoons Na_4MnTi(PO_4)_3[55].$$

Eq. 1.21

In this work we study the $Na_3MnTi(PO_4)_3$ material as cathode, and we report a theoretical study on the Na ion storage [55]. The study assumes that all possible Na sites are completely occupied, and it classifies the positions in five groups based on symmetry and thermal stability (Figure 1.18b). Na1 is the most favorable position for Na ions, and it is fully occupied. There, ions do not move during cycling, due to the favorable energy, and so Na1 sites guarantee the framework stability. Instead, the Na ions are inserted/disinserted in/from Na2, Na3, Na4 and Na5 to storage electrochemical energy. Among these sites, the Na5 position is the less stable, so it is not taken into account in the theoretical study reported by Zhou et al. [55]. According to the investigation, the $Na_3MnTi(PO_4)_3$ material shows three different voltage plateaus at 4.1V, 3.6V and 2.1V vs Na/Na^+ during the discharge process (Figure 1.18c), which starts from $Na_1MnTi(PO_4)_3$ and goes to $Na_4MnTi(PO_4)_3$. Beginning from x=1, the Na ions occupy first the Na2 sites, followed by Na3 and Na4 positions. This theoretical order of occupation implies the formation of three voltage plateaus shown with black dotted lines in Figure 1.18c.

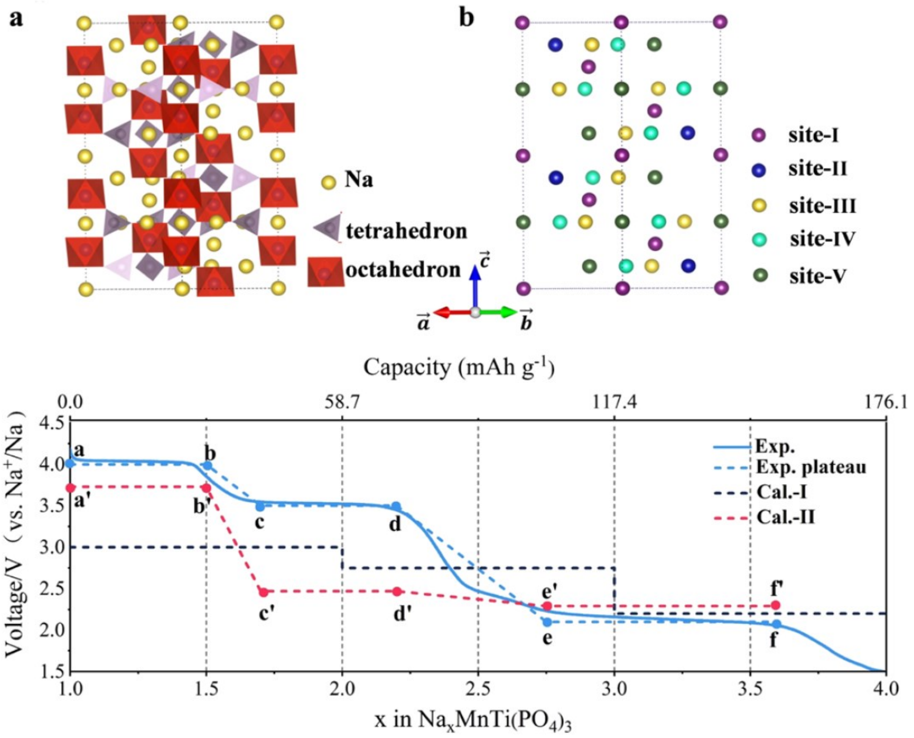

Figure 1.18: a) Atomic structure of the supercell $Na_xMnTi(PO_4)_3$ where x is the number of Na ions inserted/deinserted during cycling; b) Five group of Sodium sites distinguished with different color and called Na1 (site-I), Na2 (site-II), Na3 (site-III), Na4 (site-IIII), and Na5 (site-IIIII); c) The voltage profile obtained by theoretical calculations (red and black dotted lines) is compared to the experimental one (blue solid and dotted lines). Black lines is related to the fully Na1, Na2, Na3 and Na4 occupied sites, while the red profile is obtained with the experimental occupation rate values for every plateau (taken from [55]).

The experimental trend (blue solid line) deviates from the calculated prediction: when Na ions starts to occupy one sites group, the voltage shifts to the following plateau and the change from one voltage plateau to another occurs gradually. In the intermediate region, the Na ions occupy positions which are the dynamic average of the two occupied sites of the two different plateaus, while from theoretical calculation the Na ions occupy positions with diverse on-site energies [55]. Finally, the theoretical dotted red line in Figure 1.18c, fits better the experimental one, as is re-simulated using the experimental x value for each voltage plateau. The voltage plateau depends on the real value of x in $Na_xMnTi(PO_4)_3$. One Sodium and half is inserted/disinserted at 4.1V for Mn(III)/Mn(IV) red-ox couple, only one Na ion is intercalated/deintercalated at 3.6V for Mn(II)/Mn(III) red-ox pair, and finally another Sodium ion is sodiated/desodiated at 2.1V for Ti(III)/Ti(IV) red-ox reaction. The last part of Na ions is inserted/disinserted during the intermediate regions among the plateaus following the most favorable on-site energy.

Section 5. Metal sulfides: state of the art

Among the anodes family, the metal sulfides group is particularly interesting for high theoretical specific capacity values, and easy control of particles morphology [76]. The metal sulfides compounds (MS_x), belong to the conversion/conversion-alloying family of SIBs anodes. The formula is MS_x where M is Cu [190–192], Zn [74,90–92,193–199], Ti [200,201], Sn [202–205], V [206,207], Mo [208,209], W [210,211], Mn [212,213], Fe [93,214,215], Co [216,217], and Ni [218,219]. The major part of the metal sulfides present the covalent M-S bond. It is weaker than M-O bond, exhibiting a conversion reaction more favorable during charge/discharge process [76]. The mechanism of the charge/discharge processes includes three types of reaction, namely insertion/extraction as intercalation compounds, conversion reaction, and alloy-dealloying reaction, according to the Eq. 1.22, Eq. 1.23, and Eq. 1.24, respectively.

$$MS_x + yNa^+ \rightarrow Na_yMS_x$$

Eq. 1.22

$$Na_yMS_x + (2x - y)Na^+ \rightarrow M + xNa_2S$$

Eq. 1.23

$$M + zNa^+ \rightarrow Na_zM$$

Eq. 1.24

Usually, the sodium ions are inserted into MS_x through the intercalation reaction. The intercalation process is followed by either conversion reaction or conversion and alloy/dealloying concomitant mechanisms [76,220,221]. The combination of intercalation and conversion produces Na_2S and M, providing extra Na ions storage and an additional capacity. The combination of the three mechanisms gives new types of products, Na_2S and Na_zM, and the delivery of a higher value of capacity too, thanks to the higher storage of sodium ions. However, in this case, the MS_x structure also undergoes to a critical volume change which provokes a capacity fading [76]. The performance and the chosen reaction mechanism depends on the metal present in the structure, hereafter summarized [76]):

- Nb (group V B) undergoes to only intercalation/deintercalation mechanism maintaining the crystal structure during cycling and showing a lower specific capacity;
- Sn, Sb, and Bi (groups IV A, V A) demonstrate a multistep reaction mechanism storing more Na ions, hence higher values of specific capacity. However, also a huge volume change occurs, with leads to the structural collapse and a fast capacity fading;
- Ti, V, Mo, and W (groups IV B, V B, VI B) show layered structure. The near layers present weak Van der Waals forces, which make the insertion of foreign ions easier;
- Fe, Co and Ni (group VIII) form different sulphides which do not demonstrate storage activity.

Although few excellent properties, the MS_x materials present different drawbacks too. Firstly, during the discharge step the sulphur dissolution into the electrolyte might occur. This provokes not only the loss of sulphur component which brings to a capacity fading, but also side reactions with the electrolyte. Secondly, a high number of Na ions are included into storage mechanism and a severe volume change, which degrades the electrochemical performance of the anode. Thirdly, the conversion or alloy/dealloying reaction might inhibit the complete recovery of the crystal structure displaying a poor reversibility. Finally, the MS_x are featured by a low electronic and ionic conductivity which negatively affects the rate performance. To face these downsides there are few strategies such as nanostructure particles, electrolyte optimization, voltage range design and carbon modification. This last one is particularly useful to improve the electronic and ionic conductivity as reported in this work in Subsection 19 of 0 and in Section 5 of Chapter 3.

The metal sulphides are manly synthesized by three approaches: hydrothermal method, spraying-related procedure, and sulfidation one. The hydrothermal synthesis is well-known because it is environmental friendly, cheap, and permits a good control on the sample morphology. Hence, it is suitable to synthesize nanostructured powders or surface-modified particles. The spraying-related procedures include spray pyrolysis, spray drying and spray deposition. They guarantee to control and prepare different sample morphologies such as porous, sponge-like or dense. Last but not least, the sulfidation method consists in using metal oxides or metals as precursors and a sulphur containing source to make the solid-state sulfidation reaction happening. Further information is reported in ref. [76].

In this work we synthesize and test the zinc sulfide used as SIBs anode.

Subsection 9 Zinc sulfide (ZnS)

The zinc sulfide ZnS is a wide energy gap semiconductor, low-cost and not toxic. ZnS is present in three different polymorphic forms: wurtzite, sphalerite or zinc blende, and rock-salt. A scheme of the structures is shown in Figure 1.19. Wurtzite (Figure 1.19a) is the high temperature polymorph, it is rare and challenging to be obtained, especially at low temperature. It presents hexagonal structure with $P6_3mc$ space group. Sphalerite (Figure 1.19b) is the low-temperature polymorph and has a cubic structure with $F\bar{4}3m$ space group. Both wurtzite and sphalerite structures display a cubic compact packing and a tetrahedral coordination of Zn and S atoms. Finally, the rock-salt polymorph (Figure 1.19c) is obtained at high pressure and shows a NaCl-structure with an octahedral coordination of Zn and S atoms [222,223].

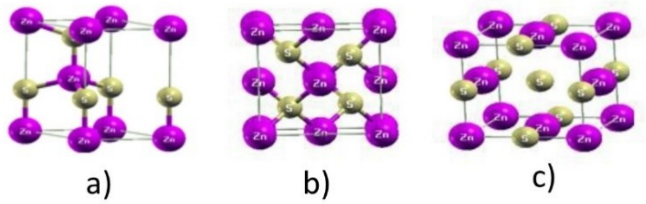

Figure 1.19: The ZnS polymorph: a) wurtzite, b) sphalerite and c) rock-salt (taken from [222])

ZnS finds application in electronic apps such as diodes, sensors, and electrodes [224]. Among them the employment as anode for LIBs and SIBs stands out. The insertion/disinsertion of alkali ions such as Na and Li follows the conversion-alloy/dealloying mechanism and the red-oxs in discharging processes read

$$ZnS + xNa^+ + ze^- \rightarrow Na_xS + Zn,$$

Eq. 1.25

$$Na_xS + (2-x)Na^+ + (2-x)e^- \rightarrow Na_2S \text{ [197].}$$

Eq. 1.26

In the charging step the reverse reaction of Eq. 1.25 occurs. The principal reduction peaks are found at 0.23 V for SEI formation and 0.6 V for $Zn^{2+/}$Zn red-ox couple. While, the oxidation peak is detected at 0.9 V.

In the case of LIBs, the ZnS presents severe volume changes due to the insertion/ disinsertion of alkali ions provoking unstable charge/ discharge cycles. In the case of SIBs, ZnS shows a slow kinetic, and also similar volume problems due to the higher ionic radius of Na ions. To address these issues, the scientific research investigates different synthesis procedures including the use of a carbonaceous and graphitic matrix, which provide good electronic conductivity, storage sites for Na ions, and buffering on the volume change during the cycling [74,90,193,194,224,225]. However, ZnS has proven to be a good choice as anode for SIBs, and this work illustrates the preparation and the analysis on the carbon matrix for ZnS with self-standing anode, see Section 5 in Chapter 3.

In literature, sol-gel [197] and hydrothermal [91,198] procedures stand out as synthesis of ZnS with a carbonaceous matrix. There is a good trade-off among low-cost, simplicity, speed, and the possibility to control the morphology with a carbon component. In the sol-gel synthesis it is possible to prepare ZnS particles in a carbon matrix similar to the graphene oxide (rGO), making the contact between ZnS and rGO higher [197]. While, with the hydrothermal procedure, the GO not only covers the ZnS particles with a carbon layer improving electronic conductivity and buffering volume change, but also control the ZnS particles size to about 10nm, avoiding agglomeration of nanoparticles. The nanodimension implies high surface area, which provide a better contact with the electrolyte [198].

Section 6. Electrochemical notions

In the following section, we introduce the required physical quantities and theories that describe the behavior of electrochemical cells. We provide a brief dissertation on the thermodynamical models about reduction and oxidation reactions, which explain the charge and discharge processes at equilibrium or out-of-equilibrium states.

Subsection 10 The concept of red-ox

In an electrochemical process, chemical energy is converted to electricity or vice versa. To better understand this phenomenon in an electrochemical accumulator, we first introduce the thermodynamic reversibility of chemical reactions. Precisely, a *reversible transformation* describes a system which undergoes a sequence of equilibrium states. As a consequence, it is feasible to return the system to its initial condition by reversing the processes. The term *equilibrium state* denotes that, at a given temperature, the product of a reaction occurs simultaneously with the reactants without their parameters changing over time. Hence, in a secondary battery the electrochemical reaction must be reversible, so that the recovery of the original chemical composition of the electrolyte and active materials is possible upon electric energy exchange.

The chemical process powering an electrochemical accumulator is the reduction-oxidation reaction. It consists in an exchange of ions and electrons e^- simultaneously occurring on the anode and cathode. The transfer direction is determined by whether the RB is charging or discharging. Let us first consider the charge mechanism: Lithium-ions (Li^+) /Sodium-ions (Na^+) are *de-intercalated* on the cathode, then they migrate throughout the electrolyte, and are finally *intercalated* in the anode. The reactions then read:

$$Li^+ + e^- \rightleftharpoons Li,$$

Eq. 1.27

$$Na^+ + e^- \rightleftharpoons Na.$$

Eq. 1.28

During charge process, the cathode goes through the semi-reaction known as oxidation by missing *n electrons* e^-. Meanwhile, at the anode the reduction semi-reaction occurs by intaking the same number of electrons. After producing e^-, they are extracted from electrode active material and drained outwards the accumulator by means of the current collector. Such a process is driven by an external circuit which pipes the electron gain or loss.

In the most general case, the oxidation semi-reaction is:

$$A \rightleftharpoons A^{n+} + ne^-,$$

Eq. 1.29

while the reduction semi-reaction reads:

$$B^{n+} + ne^- \rightleftharpoons B.$$

Eq. 1.30

Both A^{n+}/A *or* B^{n+}/B are generally written as Ox/Red and known as red-ox couples. The total red-ox of complete cell reads as:

$$A + B^{n+} \rightleftharpoons A^{n+} + B.$$

Eq. 1.31

In the discharge process, the reduction at cathode and the oxidation at anode occurs. On the contrary, the reverse reactions take place during charge.

Subsection 11 The Chemical potential

Let us consider a system composed of multiple interacting chemical species and denote the global system energy *U* as the sum of all energies, namely kinetic, vibrational, and rotational energy for all particles, as well as the interaction energy between them. When we add one more particle to the mix, the energy *U* increases because of the energy brought by the particle itself and all particles now interact therewith. So, if we keep constant the number of particles n_j of all other species, the entropy *S*, and the volume *V*, we are able to define the chemical potential μ_i of one specie *i* as the variation of *U*, linked to the addition of new particles of that specie:

$$\mu_i = \left(\frac{\delta U}{\delta n_i}\right)_{V,S,n_{j=i}}$$

Eq. 1.32

Subsection 12 The Gibbs energy of reaction

What happens if the species are charged? The particles interact each other and with any external electric field *E* applied to the system. The electric field *E* is derived from an *outer potential V*. We then add the electrochemical potential $\tilde{\mu}_i$ for each specie i to the energy *U,* which includes the electric field interaction. We can define the Gibbs energy $\widetilde{\Delta G}$ as the sum of the electrochemical potentials of all species.

In the particular case of a redox, the Gibbs energy $\widetilde{\Delta G}$ is the sum of the electrochemical potentials of oxidation and reduction species, plus/minus that of the electron times the number of electrons *n* exchanged during the reaction. Namely:

$$\widetilde{\Delta G} = \tilde{\mu}_{red} - (n\widetilde{\mu_{e^-}} + \widetilde{\mu_{ox}})$$

Eq. 1.33

When current flows through the cell, the electrons are exchanged between the two electrodes. One of them is depleted of electrons while the other is enriched thereby. Therefore, the Gibbs energy is directly linked to the potential difference between the two electrodes and describes the forces that move electrons in or out of the cell.

Subsection 13 The open circuit voltage and Nernst's law

Let us consider an electrochemical cell defined by the two red-ox couples A^{n+}/A and B^{n+}/B at equilibrium and standard condition (std.c.), namely temperature of 298.15 K, atmospheric pressure of 1 atm, all solids and liquids are pure, aqueous species have a concentration of 1 $molL^{-1}$, and all gas species have partial pressures of 1 Atm. The necessary work to transfer one electron from an electrode to the other is proportional to the electrical potential between the two electrodes. If such a potential is measured against the standard hydrogen electrode (SHE) $B^{n+}/B = H^+/H_2$, we obtain the standard potential for the redox couple A^{n+}/A. Indeed, the standard potential of a red-ox couple is defined as

$$\left[E^0_{\frac{ox}{red}}\right]_{SHE},$$

Eq. 1.34

where the *ox/red* subscript indicates the given red-ox couple, *SHE* that the reference electrode is the SHE and the *zero* superscript the standard condition. The red-ox couple with the lowest potential undergoes the oxidation mechanism, whereas the highest one the reduction process. Once the standard red-ox potentials have been measured, the total cell potential ΔE^0_{cell} can be estimated as

$$\left[E^0_{cell}\right] = E^0_{cat} - E^0_{an}.$$

Eq. 1.35

The potential E^0_{cell} is known as the open circuit voltage (OCV). It is the voltage difference measured between two electrodes at equilibrium when no current is supplied or drawn [226]. Finally, we stress that the cell potential ΔE^0_{cell} has a vital role in the behavior of the reaction. Indeed, the Gibbs energy of the complete reaction reads

$$\Delta G^0 = -nF\Delta E^0_{cell},$$

Eq. 1.36

and the reaction occurs spontaneously only if ΔG^0 is negative. Moreover, in an accumulator the red-ox reversibility is guaranteed by its spontaneity, which is a necessary condition.

In the case of non-standard conditions, Eq. 1.34 and Eq. 1.35 are no longer relevant. To solve this issue, Walther Hermann Nernst developed a theory at the beginning of *20th* century which predicts the cell open circuit voltage when deviating from the standard conditions. For the single red-ox couple A^{n+}/A

$$A^{n+} + ne^- \rightleftharpoons A,$$

Eq. 1.37

which takes part to the global red-ox reaction, the Nerst equation for the half-cell potential reads

$$E_{\frac{ox}{re}} = \left[E^0_{\frac{ox}{red}}\right]_{SHE} - \frac{RT}{nF} \cdot \frac{\ln [A]}{[A^{n+}]},$$

Eq. 1.38

where *T* is the temperature, *R* the gas constant of value 8.314462Jmol^{-1}, *[Ox]* the oxidized component, *[Red]* the reduced one. Similar equations can be written for the B^{n+}/B red-ox counterpart, and the Nernst equation for the global red-ox reaction can be obtained as

$$\Delta E_{cell} = E_{\frac{A^{n+}}{A}} - E_{\frac{B^{n+}}{B}}$$

Eq. 1.39

For a generic global cell reaction

$$xA + yB \rightleftharpoons zM + pN,$$

Eq. 1.40

the potential for the total cell out of standard conditions reads

$$\Delta E_{cell} = E^{0}_{\frac{ox}{red}} - \frac{RT}{nF} \cdot ln\frac{[M]^z \cdot [N]^p}{[B]^y \cdot [A]^x},$$

Eq. 1.41

with *n* the total number of electrons exchanged by the reaction.

Subsection 14 Out of equilibrium

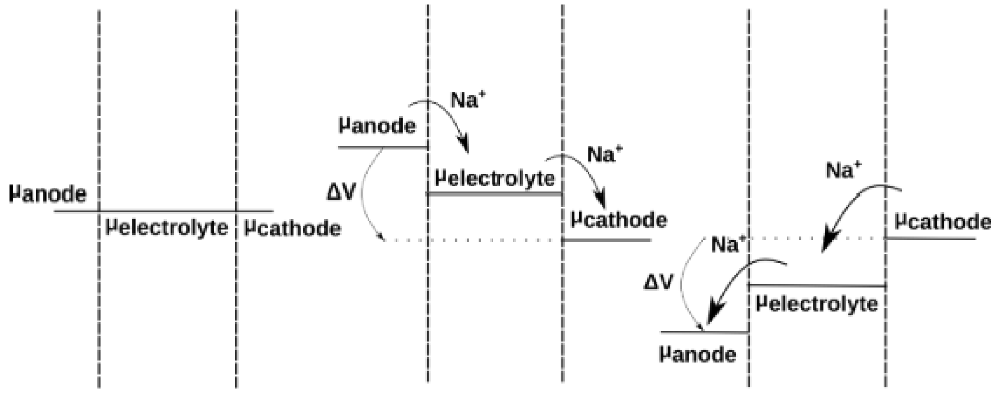

Figure 1.20: Electrode polarization effect on chemical equilibrium and chemical potentials in anode, electrolyte, and cathode [9].

So far, we dealt with electrochemical cells in open circuit setups. This ensures that no current flows through the system and the electrodes remain at equilibrium. Nonetheless, as soon as we connect the cell to source or sink current, we close the circuit. What is then the behavior out of the equilibrium during charge and discharge processes? If the electrodes are not connected to an ohmic contact, the red-ox reactions at the electrodes compensate each other. The equilibrium concentrations establish the potential according to the Nernst equation. It implies that the equilibrium changes only when an external potential is imposed, thus increasing the reactions at electrodes. In the Figure 1.20, three cases are reported: reading from left to right, equilibrium, imposition of a positive external potential, and imposition of a negative external potential. The last two situations are out of the equilibrium. In these two cases, the system must keep up and attempts to restore the chemical equilibrium. The red-ox rate is unbalanced due to the motion of electrons and an ion flow is a consequence. The main difference between charge and discharge is indeed the cause for such an electron unbalance: while discharging the electrons are spontaneously drained from one electrode to the other. On the other hand, while charging the electrons accumulate at one electrode while are depleted at the other, the reduction at one electrode does not find enough electrons to keep the same frequency.

Electrons' path

In the case of the reduction process, the electrons are drained from the positive electrode and after the red-ox reaction electrons are located into the active material, usually an insulator. The electrons are attracted toward the current collector through the electric field of the other electrode. The electric field is created by the presence of a low energy state on the other electrode, and it requires more electrons. At this point it is necessary using the electrons at maximum energy into a circuit to provide maximum power. How is it possible? Since the electrons at maximum energy are already into the active material, it is necessary to create an easy path which brings the electrons firstly into the current collector and secondly into the circuit. As the current collector is a metal, that means it is highly conductive, it provides and easy path with low resistance. The electrons migrate into current collector thanks to the tunnel effect losing part of the energy, as the tunnel effect is part of the internal resistance. Moreover, the electron migration from active material to the current collector is not painless and other energy is lost. It is caused by the fact that the contact between the two parts is complex and composed by a mixture of active material and other components (conducive carbon, binders, additives) or slurry which gives material internal resistance, and it could be detached in time leading to a cell failure. Once the electrons are finally into conductive current collector, they can be used into the circuit. The reverse mechanism occurs for the oxidation process , and ions and electrons are recombined [9].

Ions' path

During the reduction process, while the electrons are drained, the ions of the active material of the positive electrode need to move towards the negative electrode. In other words, they should first diffuse into solid to reach the electrolyte, usually liquid. We recall that the diffusion into a solid is typically more difficult and slower than into other matter states. The ions are attracted by the electric field created by the negative electrode, and this electric field drives the direction of ion path. Ions exit the active material, migrate through the electrolyte, and finally diffuse into the negative solid electrode. It is important that the ions are in the right place when a new red-ox should take place. If it does not happen, the cell must increase the electric field using its internal energy and so the ions are faster moved. The Gibbs energy and available potential become lower. The potential loss is another component of internal cell resistance [9].

Subsection 15 Relevant quantities of an accumulator

We list hereafter a selected collection of notions concerning electrochemical accumulators, along with a brief description of them.

- **Capacity** has the same dimension of charge and is defined as follows

$$Q = \int_0^t I(t)dt.$$

Eq. 1.42

  Where I is the current in Ampere and t is the time in hours. Q is typically measured in ampere per hour Ah.

- **Capacity density** is the capacity per unit mass (Ahg^{-1}), also known as gravimetric capacity, or per unit volume (AhL^{-1}), i.e. the volumetric capacity. In literature, the specific capacity per unit mass of active material is used to compare different active materials in different cell setups.

- **Charge efficiency** or Coulombic efficiency (CE), is the ratio between discharge capacity and charge capacity, displayed as a percentage. High CE means that the battery has an excellent reversible charge/discharge process and almost all the energy provided during charge can be recovered during discharge. Efficiency is important to compare different storage technologies.

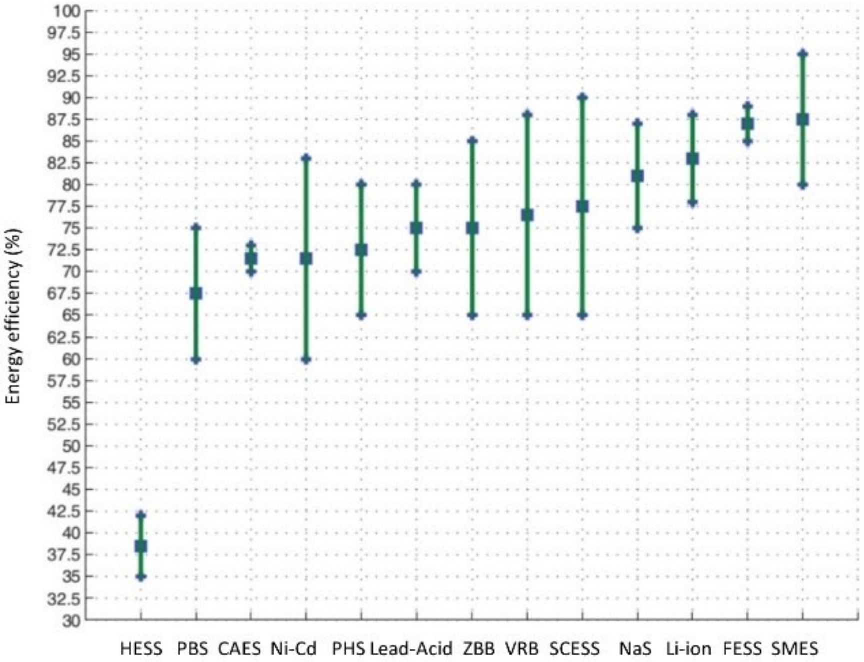

Figure 1.21: Comparison of efficiency of different storage systems (taken from [10]).

In the figure 1.21 the Coulombic efficiency of various storage systems are compared. Li-ion and, generically, ions batteries offer the best efficiency.

- **Cycle life** for a secondary battery is the number of charge/discharge cycles performed before the capacity reaches a fixed capacity (usually the 80% of the starting value).

- **Energy** in a battery is typically expressed in watt per hour, Wh. The energy is related to the capacity of a cell as follows:

$$E = Q \cdot \bar{V}$$

Eq. 1.43

where $\bar{V}$ is the average discharge voltage.

- **Energy density** is the energy normalized on the active material mass (Whg^{-1}) or on its volume (WhL^{-1}).

- **Current Rating (C-Rate)** expresses either charge or discharge currents in respect of the cell nominal capacity, and gives the rate at which the cell is charged or discharged relative to its capacity. When the current flows across the battery, we can write it as the nominal capacity multiplied by the C-rate as a constant with the unit of one over time, typically h^{-1}. In other words, the C-rate is how many times you can charge or discharge the cell in one hour, and it is expressed as the inverse of the time it takes to discharge/charge a battery at the defined current level. As an example, ½C defines the current which completely discharges the battery in 2 hours.

- **Open Circuit Voltage (OCV):** it is defined as the voltage value between positive and negative electrode when no current is drawn or supplied, and it is equal to the ideal generator voltage V. It depends on the previous battery cycle history.

- **Closed Circuit Voltage (CCV):** it depends on the battery history and it is defined as the voltage between two electrodes when the load is connected. It is measurable with a certain precision when the battery is operating. Other parameters should be evaluated from CCV variation with time.

- **Nominal capacity or rated capacity** is the capacity measured under standard conditions of constant current discharge and room temperature.

- **The theoretical specific capacity of an active material** is the maximum quantity of charge that can be extracted per unit mass of active material. It can be estimated as:

$$Q_t = zFM$$

Eq. 1.44

where F = 96500 Cmol^{-1} = 26800 mAhmol^{-1} is the Faraday constant, z is the number of electrons exchanged during the redox reaction, and M is the amount of substance of the active material.

- **State of Charge (SOC):** is the difference between the battery capacity Q and the charges removed from the battery at a defined time t divided by Q, as depicted in

$$SOC(t) = \frac{Q - \int_0^t I(t)dt}{Q}.$$

Eq. 1.45

The battery state, the voltage and the resistance are function of SOC and battery history, in particular the worse performance are obtained when the SOC is too low or too high.

- **Voltage profile (V(SOB)):** the voltage is not a monotonic function of SOC in a short period and so is not constant during the discharge. V(SOB) is a hysteric function of SOC. In particular, the discharge plateau is slightly smaller than the charge one and so it is not perfectly efficient. The cell voltage varies during cycling and is influenced by the temperature and previous cell history.

- **Depth of Discharge (DOD):** is defined as complementary of the minimum SOC at a given time, reached by battery during its cycling.

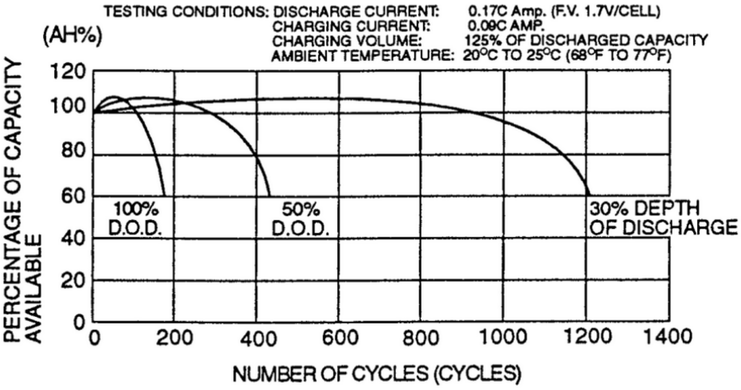

Figure 1.22: Lifespan of lead-acid battery with different DOD (taken from [227])

$$DOD = 100\% - \min(SOC)$$

Eq. 1.46

When the battery is not completely discharged the DOD is lower than 100. Full discharging a battery may lead to a degradation of performance. In
Figure 1.22, we report different lifespans of lead-acid batteries with different DOD.

- **Internal Resistance:** R models the voltage drop proportional to the current flowing in the battery. Based on the R value, we assess if the battery is suited for high C-rate applications. Indeed, the greater the internal resistance the greater the voltage drop.

Subsection 16 Solid-solution interface

In the previous subsections, we have described the behavior of red-ox reactions and their relationships with the concentrations of the chemical species and with the electrical potential. Although this subsection will not be precisely recalled in the Chapter 3, it is reported because it depicts the basic rules of the electrode-electrolyte interface and interaction in a standard electrochemical cell. It is important to understand how an electrochemical cell works.
In this case, we are interested in red-ox that occurs between a conducting solid electrode and an electrolytic solution. Such a system is called *half-cell*.

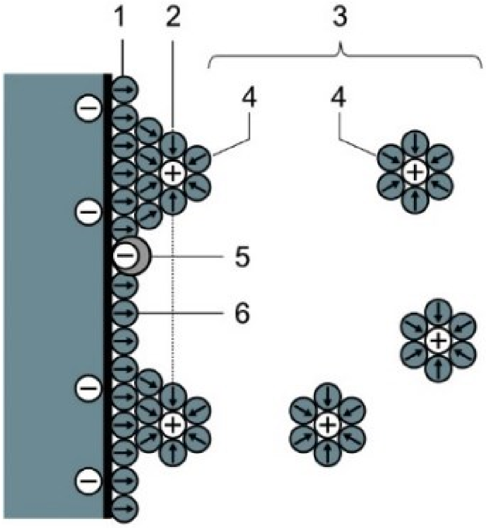

Figure 1.23: A schematic view of the interface between the solid electrode and the electrolyte. The number `1' indicates the Inner Helmotz plane, `2' the Outer Helmotz plane, `3' the diffusive layer, `4' the solvated ions, `5' the adsorbed ions and `6' the solvent’s molecules (taken from [228]).

In addition, we define the *interface* as the region where the two distinct phases are in contact. There, the properties of substances are different from those in the bulk.
We now assume that the electrode is in contact with the electrolyte, forming the interface, and that the electrode is reduced and the red-ox couple of the electrolytic solution is oxidized. Hence, the metal accumulates a surplus of negative charge, which is balanced by a number of ions in the electrolyte solution with an equal and opposite charge. Interim, the ions are assumed as solvated, namely they are directly neither in contact with solid nor interacting with it. The solvated ions are shown in Figure 1.23 by number 4 and the molecules of solvent are marked by number 6. Now, we trace a line throughout the centre of solvated ions, which describes a plane called Outer Helmotz plane (OHP); the system can be seen as an electrical capacitor. Namely, the surface of the electrode and the OHP represent the plates of the capacitor, also known as double electric layer. The two plates are depicted in Figure 1.23 by the thick black line and number `2', respectively. In this way, the capacity is independent from the concentrations of species that form the capacitor [229].
As a matter of fact, the above model does not fully describe all phenomena related to a real interface. Indeed, in a real system the charge excess on the electrode is not balanced only by ions on OHP and,

so, we have to consider the bulk solution. To explain this issue, it is necessary to consider that ions are subjected to two forces: electric force driven by electrode and thermal convection. The former attracts ions to OHP while the latter spreads the ions into the bulk of the electrolyte [230,231].

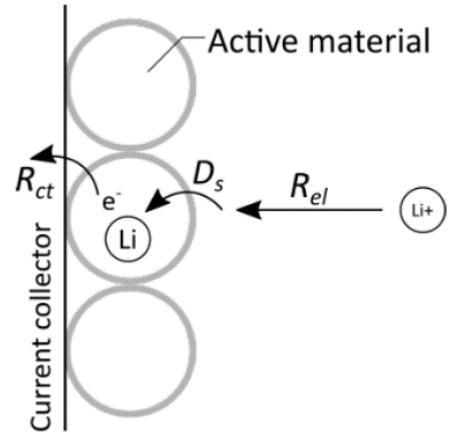

Figure 1.24: Schematic view of the electrolyte resistance R_{el}, solid diffusion constant D_s and charge transfer resistance R_{ct}.

Hence, in addition to the charge at OHP, there is also a double diffusive layer next to the capacitor, also known as bulk of solution. This part is depicted in Figure 1.23 with number 3. The diffusive region guarantees a total charge equilibrium of the double layer [232]. We could then depict the interface as two capacitors in series: the first where capacity is not dependent on concentrations (electrode-OHP) and the second where the dependency on excess charge is non-negligible (electrode-diffusive layer).

From this description it is noticeable that to form the interface between electrode and electrolyte, cations and anions must move through the electrolyte to reach the active material. Specifically, to the ionic transport contribute both ions diffusion and electric migration. The former is caused by the positive charge (e.g. due to Na^+ or Li^+) concentration gradient between the bulk electrolyte and the electrolyte-active material interface, while the latter is due to the electrode potential on charged species.

To complete the half-cell description, we have to consider the absorption of ions on electrode surface[233]. Namely, the ions are absorbed on solid surface and are represented in Figure 1.23 with the number 5. Specific adsorption means that the ion loses its solvation sphere approaching the electrode and forms a rather strong bond with it. This event occurs at the Inner Helmotz plane (IHP), depicted with number 1 in Figure 1.23. This step is peculiar of RB, where ions, such as Na^+ or Li^+, are adsorbed on electrode surface, and the interaction with electrode enables the red-ox to occur. Ion is reduced upon insertion between planes of the intercalation compounds. In this case, the intercalated ions diffuse inside the active material. Once the red-ox occurs, the electrons are produced inside the active material, extracted from electrode and drained towards the current collector to generate current.

The above discussion applies for both the cathode and anode, and their combination guarantees an effective and complete model of an accumulator.

The theoretical part of the interface model was developed between 1879 and 1960 with the contribution of the scientists Helmholtz [229], Gouy [230], Chapman[231], Stern [232] and Grahame [233].

Finally, considering the ions transport through the electrolyte, ions diffusion inside the active material and electric charge transfer, we specify that the ions' rate depends on the following parameters: electrolyte resistance R_{el}, solid diffusion constant D_s and charge transfer resistance R_{ct} (Figure 1.24). These factors influence the rate which the current is produced with, when the cell is in charge. Hence, if the electrodes are characterized by high resistances (R_{el}, R_{ct}) and low solid diffusion, they exhibit poor performances in terms of C-rate. The C-rate denotes a conventional way of representing the current used to charge or discharge a battery. A C-rate of 1C discharges completely the battery in 1h, 2C and C/2 discharge in 1/2h and 2h, respectively (see Subsection 16 for details).

Subsection 17 Theory of diffusion

In this subsection we introduce the theory of diffusion. We explain the rules through which the species such as ions and electron can diffuse into a system (electrochemical cell). Finally, we deduce the *Cottrell equation* which will be recalled in cyclic voltammetry at different scan rate in the Chapter 3 to estimate the diffusion coefficient of Na and Li ions. It is important to understand how an electrochemical cell works and permits to comprehend the beneficial role of a new porous matrix to build electrode.

In an electrochemical cell, the reactant and product particles are transported by the electrolyte to the electrodes, to generate electrons in the external circuit. In the following, we describe in detail the mechanism and laws that govern the transport of molecular and ionic solutes in liquids. We usually refer to this phenomenon as *mass* transport to distinguish it from other kinds of transport, such as heat transport or momentum transport.

There are three types of transport: migration, diffusion, and convection. Each one is governed by a gradient, namely electrical potential, activity or concentration, and pressure, respectively. Particles move so as to decrease the gradient [234].

Migration is provided by an electric field which attracts the charged particles. For example, in the cell the electrolyte ions migrate to the respective electrode whilst the solution remains neutral. This type of transport applies only to ionic species. The generated energy is dissipated as heat.

Diffusion is the consequence of a concentration gradient. Particles move from regions of higher concentration to those featuring a lower one, thereby increasing the overall entropy. Typically, diffusion arises from the Brownian motion of solutes in a static solution, and all kinds of solutes can undergo diffusion.

Finally, the convection is driven by a hydrostatic force, for instance, it occurs when the solute moves into a moving solution because it accelerates the transport of species. Convection includes all types of solutes, and in electrochemistry it is usually an unwelcome complication. In particular, both forced convection and natural one exist. The former is deliberately caused by stirring, sonicating or pumping and it is desired. The latter is an unwanted motion due to the density or vibration gradients. The transport does not start alone, but it always needs a gradient. So, the motion is always late because the particle acceleration depends on its mass. The motion delay could sometimes represent a problem for the migration which can be ignored in electrochemistry [234].

In this work we focus on diffusion, which is particularly interesting in electrochemistry due to its role as limiting factor in certain regimes [234]. Indeed, we assume that the contribution of migration and convection transports can be negligible because their contribution is too little. Hence, we illustrate below the diffusion in solution and in solid, namely electrolyte and electrode for the cell.

Diffusion in a solution

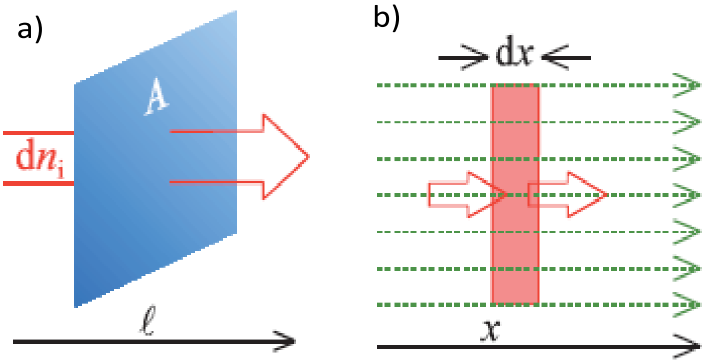

Figure 1.25: a) Representation of flux density definition; b) Representation of planar transport (taken from [234]).

To understand the diffusion phenomenon, we must make a premise. Let us consider a distance *l*, an area *A* perpendicular to the motion direction and moles n_i of a specie *i*, we can then define the *flux density* of specie *i* in a time *t* as:

$$j_i = \frac{1}{A} \cdot \frac{dn_i}{dt} \left[\frac{1}{m^{-2}s^{-1}}\right].$$

Eq. 1.47

The *flux density* is defined as the variation of moles n_i in time *t* on position *l* across an area *A* (Figure 1.25a). It is a vector quantity and is always evaluated in the transport direction. So, j_i could be also described as dependent on *t* and *l*, varying with the variation of *specie I* concentrations c_i and its motion average rate $v_i = l/t$:

$$j_i(l,t) = \overline{v_i} c_i.$$

Eq. 1.48

Clearly, if the flux density involves *charged particles,* we obtain a *current density I*. The j_i is correlated to *I* through the following relationship:

$$I = F \sum z_i j_i,$$

Eq. 1.49

Where z_i is the charge number of the specie *i* of flux j_i [234].

Now, we consider a parallel flux along the x direction for the transport of specie i. Let the amount of specie i lay in a thin wafer at x of depth dx with initial volume V_c(x,t), are shown in Figure 1.25. If we follow the particle flux the final wafer volume after dt time reads

$$V_c(x, t + dt) = V_c(x, t) + Aj_i(x, t)dt - Aj_i(x + dx, t)dt.$$

Eq. 1.50

We obtain *the conservation law for the planar transport from* Eq. 1.50 *V=Adx,* namely:

$$\frac{c_i(x, t + dt) - c_i(x, t)}{dt} = \frac{j_i(x, t) - j(x + dx, t)}{dx},$$

Eq. 1.51

or partial differential notation:

$$\frac{\partial c_i}{\partial t} = -\frac{\partial j_i}{\partial x}.$$

Eq. 1.52

Such a transport is dubbed planar as the equiconcentration surfaces, i.e. the set of all connected points featuring the same concentration, are planes.

We now postulate the diffusive transport flux j being proportional to the concentration gradient. This is also known as the *Fick's first law*:

$$j_i^{diff} = -D_i \frac{\partial c_i}{\partial x},$$

Eq. 1.53

where D_i is the diffusion coefficient or diffusivity of the specie. When the flux lines are parallel and transport is planar, combining the Eq. 1.52 and Eq. 1.53 we obtain the *Fick's second law*

$$\frac{\partial c_i}{\partial t} = D\frac{\partial^2 c_i}{\partial x^2}.$$
Eq. 1.54

Once solved, it models the concentration c_i of diffusive specie *i* for each point along the *x* spatial coordinate and positive time *t*.

To solve this differential equation, three boundary conditions are necessary. Firstly, $\frac{\partial c_i}{\partial t} = D\frac{\partial^2 c_i}{\partial x^2}$. Assuming that the solution being initially composed by uncharged and oxidable specie *R* at a homogeneous concentration c_R^b, the $c_R(x,t)$ denotes the *R* concentration for each point *x* in the solution and at any time *t*. So, the first boundary condition reads

$$c_R(x > 0{,}0) = c_R^b.$$
Eq. 1.55

At time t=0, we close the switch, and the *working electrode (WE)* is unexpectedly brought to and maintained at a positive potential sufficient to take away *R* by the electrode surface. This second condition is written as

$$c_R(0, t > 0) = 0.$$
Eq. 1.56

The diffusion transport is the only one acting for the uncharged specie R in a quiescent solution, so the Fick laws model the transport [234].

Finally, far from the electrode in the electrolyte bulk, the concentration of R remains unchanged. Hence, the third condition reads:

$$c_R(x \to \infty, t) = c_R^b.$$
Eq. 1.57

After these three boundary conditions, the Fick's second law becomes

$$\frac{\partial}{\partial t}c_R(x,t) = D_R\frac{\partial^2}{\partial x^2}c_R(x,t)$$
Eq. 1.58

and, using the Laplace transformation, is solved by

$$c_R(x,t) = c_R^b erf\left\{\frac{x}{\sqrt{4D_{Rt}}}\right\}$$
Eq. 1.59

where Erf is the error function. In Figure 1.26 the concentration profiles of the solution at different times is plotted. Thanks to the first Fick's law, the flux density is obtained:

$$j_R(x,t) = -D_R\frac{\partial}{\partial x}c_R(x,t) = -c_R^b\sqrt{\frac{D_R}{\pi t}}exp\left\{-\frac{x^2}{4D_R t}\right\}.$$
Eq. 1.60

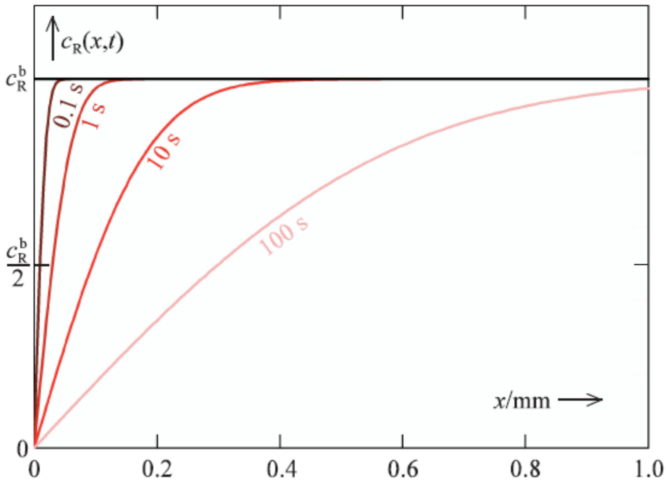

Figure 1.26: The profiles of concentration from the potential-leap experiment (taken from [234]).

However, the electrochemistry is principally focused on the current which is generated by the stoichiometry of the electrode reaction linked to the reactant flux density [234]. If the electrode reaction reads

$$\nu_R R(soln) \rightarrow ne^- + \nu_O O(soln),$$

Eq. 1.61

where ν is the stoichiometric coefficient, then the creation rate of electrons is correlated to the R and O flux densities at the surface of the electrode. The rate of electron creation is nothing more than current density

$$\frac{j_O(0,t)}{\nu_R} = -\frac{j_R(0,t)}{\nu_O} = -\frac{j_e(0,t)}{n} = \frac{i(t)}{nF} = \frac{I(t)}{nAF}.$$

Eq. 1.62

By fixing *x=0*, we obtain the *Cottrell equation* which reads

$$I(t) = \frac{n}{\nu_R} AFc_R^b \sqrt{\frac{D_R}{\pi t}},$$

Eq. 1.63

Eq. 1.63 explains the resulting current when the planar diffusive transport is applied, and the current decreases following the $t^{-1/2}$ power law [234].

Diffusion in solid

The description of diffusion processes in solid state matter is not as straightforward as for liquid solutions. Indeed, the diffusion coefficient shows strong concentration dependence. In a thermodynamically and kinetically ideal intercalation compound, the diffusion coefficient is directly proportional to ion vacancy concentration, decreasing as the ion concentration of the host increases. However, in real electrodes the material is made of intercalation compounds that undergo several dramatic phase transitions during charge/discharge cycles. Furthermore, unique crystallographic characteristics give rise to complex migration mechanisms [235–237].

Section 7. Why choosing self-standing electrode?

In this section we present the difference between traditional slurry electrodes and the self-standing ones. More precisely, we review the advantages and disadvantages of self-standing electrodes over the conventional slurry ones.

Energy is stored in electrochemical cells in the form of chemical energy, namely in the chemical bonds of the active material. Reductions and oxidations are the processes that drain or reserve energy from within the electrodes. Since the red-ox occurs at the interface between electrode and electrolyte, as it is a surface phenomenon, the device power performance is related to the total surface area. On the other hand, the amount of stored energy is proportional to the number of ions present in the crystals, and the number increases with the crystal volume. The ratio between surface and volume is then linked to the energy to power ratio (E/P). Namely, in bulky active materials the ions at the electrode-electrolyte interface immediately release energy when requested, while the inner material must attend that the ions penetrate by diffusion and react. Hence, the larger is the volume and the particle number, the higher the energy. Nonetheless, as a downside the bulk ion reactions are sluggish, and the power performance remains low.

We now focus on the time required to deliver the stored energy or to load a flat battery. In order to increase the power performance by reducing the E/P ratio without losing the energy content, some solutions have been proposed. Namely, crystal with fractal morphology, nanostructured compounds [238], or nanostructured carbon matrix to support the active materials [49,239,240] are some of them. Moreover, slurry electrodes are made of active material nanoparticles on nanostructured carbon matrix to reduce the area and volume ratio.

The use of a 3D carbon framework or support as Carbon nanofiber sheets is a good choice to reach this goal, and it is the method proposed in this work to improve the cathode for SIBs [9].

CNF sheets are a valuable option because they are easily obtained, cheap, made with a tunable production process, simple to implement in laboratory and they can be used with a wide range of active materials in order to enhance their electrochemical features. Finally, the flexibility of CNFs can reduce and help to "buffer" the volumetric variation of the active material during the insertion and extraction of ions [49,239,240]. In Figure 1.27 we give a pictorial representation of the three different interfaces between electrode and electrolyte. Namely, 2D interface of a slurry electrode, the nanostructured active material and 2D interface in slurry electrode, and the porous matrix with 3D interface and embedded active material.

The nanostructured surface of case b increases the contact surface area between electrode and electrolyte thanks to the nanoparticles. Notwithstanding, the last case allows for the best penetration of electrolyte in the electrode bulk by soaking the active material particles. This is the case of CNF sheets. Considering this brief premise, let us compare the customary slurry electrode with a self-standing one and see the advantages of CNFs for electrode assembly.

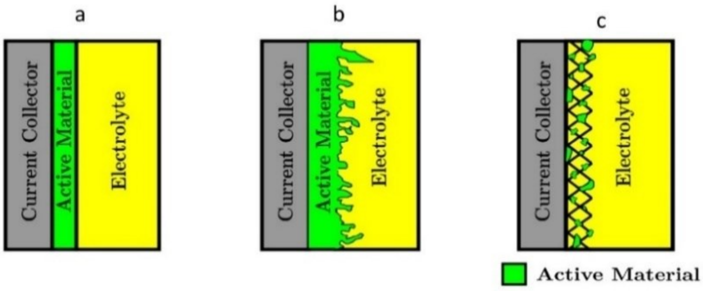

Figure 1.27: a) Slurry and 2D interface; b) Nanostructured active material in slurry with 2D interface; c) 3D interface and porous matrix support (taken from [9]).

Subsection 18 Slurry electrode

In many commercial Li-ion batteries, electrodes are produced via the slurry process. As described in Section 2 of 0, it consists of mixing the active material, carbon and binder together and depositing the slurry on the metallic current collector. The layer is evenly spread at a specified thickness using a doctor blade or similar apparatus, and finally the slurry is pressed on the current collector through a hot-pressing process. Both anode and cathode are prepared in the same way [241].

The cell is then assembled introducing the separator, a thin insulating material permeable to the electrolyte (see Chapter 2 for preparation details). This fabrication method is suitable for mass production, and depositing the slurry on metal foils permits to choose both shape and size of the cell at the end of the process. Moreover, this approach is also flexible as it is adaptable for different active materials and liquid electrolytes.

To further improve the accumulator capabilities, we seek higher energy and power densities, faster charge processes, longer lifespans, higher safety requirements, and lower production costs. Meeting these goals would enable to a greater extent the employment of rechargeable batteries into electric transport, LVD or power grid applications [242–247]. Indeed, the energy density is an essential property for portable devices, while for other applications the power density and fast charge rates are key points. To overcome the issues related to slurry limitations, we work on the electrode design by improving the electrode porosity and introducing active materials that feature higher working potentials [242–244,248,249].

Especially, decreasing the chemically inactive components or studying new high voltage cathodes and anodes help to raise the specific capacity and energy density. On the one hand, the reduction of binder and current collector mass or introducing free-binder electrodes allow for higher active material percentage. On the other hand, high voltage electrodes increase the specific capacity and the amount of energy stored in an accumulator. To improve the power density and charge rate, one option is to work on electrode porosity. Indeed, by increasing the wettability and permeation of electrolyte, we boast the ion diffusion in the electrode bulk, thus obtaining better performance at high C-rates [250–255]. This is due to the higher diffusion coefficient of liquid electrolytes over solid electrode bulks.

During cell manufacturing, the slurry undergoes a pressing stage that negatively affect the porosity of the slurry. In fact, it results in a uniform and dense layer where the active material, the carbon and the binder are stretched out on a metal foil, and the electrode is difficult to wet. As a consequence, the electrolyte does not reach every single active material particle; so, the ion diffusion decreases and the electrochemical active sites are lower and not equal to the total active material loaded into the slurry [244,250,256,257]. Clearly, the problem becomes more critical when thicker and dense slurries are fabricated. Thickening the electrode layer permits to increase the total energy content of the cell, but the specific capacity decreases at higher C-rates.

Subsection 19 CNFs and self-standing electrode

Porosity and thickness of electrodes play a crucial and critical role in the optimization of the electrochemical performance of cells [152,244,258–260].

Particularly, a porous electrode accommodates or constrains the volume change of active material during cycling thanks to the flexibility of its framework. Hence, the irreversible phase transformation could be controlled or even suppressed by the porosity, thus stabilizing active materials.

Thanks to the porous framework, the use of current collectors and binders is avoided. In so doing, we fabricate a self-standing electrode and decrease the global weight of electrode and final cell. The 3D support might also incorporate a secondary conductive phase which helps to increase the electronic conductivity [244,261]. These properties of porous electrodes enable their employment in some storage systems like batteries or super capacitors.

There are different methods to produce porous electrodes: hard templating, such as nanocasting [262,263], colloidal crystal templating and electroplating [264–266], biotemplates [267], pseudomorphic conversion [268–270], and, finally, non-templating methods like electrodeposition

[271], ultrasonication [272], intercalation [273], hydro- or solvo-thermal synthesis [202,244,261,274]. A typical porous electrode is shown in Figure 1.27c.

In the present work, we investigate another technology to prepare porous electrodes without binder and current collector. Namely, we embed active material nanoparticles into a 3D conducive carbon framework made of carbon nanofibers (CNFs).

Some methods to fabricate CNFs are the electrospinning technique followed by heat treatment to prepare web or mat structures, and the catalytic thermal chemical vapor deposition growth to obtain cup-stacked and platelet CNFs [275]. In this work, CNFs are synthetized with the electrospinning technique because it is an easy and industrially scalable technology, and low cost [276,277]; in addition, the obtained fibers are optimal to employ in ion-batteries [278,279]. Details on the synthesis procedure are reported in Chapter 2.

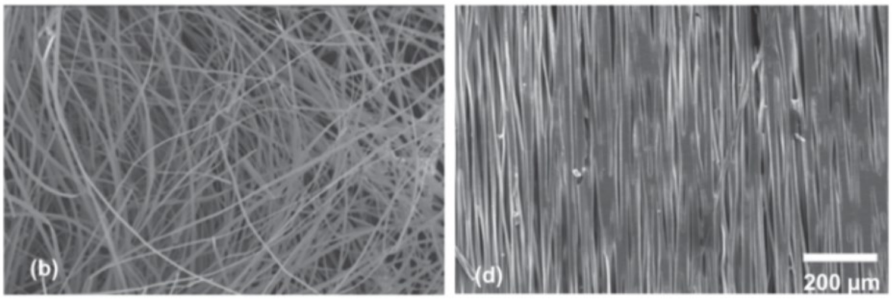

Figure 1.28: Disordered and ordered CNFs by electrospinning technique (taken by [280]).

By electrospinning, the CNFs appears like a non-woven mat of fibers (Figure 1.28), consisting of disordered or ordered distribution of CNFs with small or big pores. This 3D carbon framework is realized by using different type of polymers such as Polyacrylonitrile (PAN), Polyaniline (PANI), Polybenzimidazole (PBI), Polyvinyl alcohol (PVA), Polyvinyl carbazole (PVK), Polyethylene oxide (PEO), Polyamide (PA), Polyimide (PI), Polyvinylidene fluoride (PVdF), Polystyrene (PS), Polyvinyl chloride (PVC), and Polymethyl methacrylate (PMMA) dissolved in the appropriate volatile solvent [281]. The polymeric precursors are chosen based on the final requirements of the CNFs, since the precursor establishes the properties of the non-woven mat. To specifically fabricate CNFs, PVA, PAN, PI, or PVdF are mainly used [282,283]. The polymeric precursors are chosen based on the final requirements of the CNFs, since the precursor establishes the properties of the non-woven mat. Indeed, after the stabilization and carbonization processes, described in depth in Chapter 2, a conducive carbon support excellent for electrochemical energy storage is obtained [284–286]. The electrical conductivity increases with the carbonization level, as the graphitization occurs at a high temperature. Nonetheless, PAN provides a satisfactory electrical conductivity at lower carbonization temperature (750°C-800°C) than other polymers (1000°C-2000°C). In addition, all carbon allotropes present or added to the CNF influence the conductivity of the non-woven mat. For instance, introducing graphite or metal particles improve the conductivity with respect to amorphous and disordered carbon [282,283]. The typical electrical conductivity values are in the range of 10^{-2}-10^{3} or 10^{4} Scm^{-1} [283,287]. The typical diameter of carbon nanofibers is in the range of nanometer to tens of micrometer [275,283,288,289]. The diameter can be controlled by a proper choice of the precursor polymer and it is a critical synthesis parameter, as it affects the mat pores. By varying the fiber diameter and mat pore sizes, we modulate the porosity and the surface contact area of the electrodes with the electrolyte. In doing so, the ion diffusion coefficient and electrical conductivity can be improved by the 3D carbon framework, compared to the slurry deposition. Indeed, the CNF structure allows a lower electrical resistance and an intimate contact between active material and electrolyte, as shown in the Figure 1.27c.

Finally, the stabilization heat treatment offer a great degree of control on the mechanical properties of CNFs, among which the flexibility [290], allowing the employment of the ion batteries into, for example, heated clothing. The flexibility of the active material support and CNF sheets limits the irreversible phase transformation and the volume changes during the cycling, thus avoiding the cell death. Carbon nanofibers are electrochemically active as anodes for both Li- and Na-ion batteries. In the case of LIBs the CNFs anode shows an initial capacity of about 800 mAh/g, at 0.1C, followed by a capacity loss to 340 mAh/g and to 260 mAh/g, maintained for over 50 cycles, with a lifespan of 550 cycles [291], (see also the results of our work in Subsection 4 of Chapter 3). While for SIBs the CNFs anode delivers an initial specific capacity value of 399 mAh/g at 0.1C followed by a capacity loss to 217 mAh/g for 50 cycles at 0.1C, and a capacity of 173 mAh/g at 1C for 200 cycles, with an initial coulombic efficiency of 41.8% increased to 99% after the first 10 cycles [292] (see also the results of our work in Subsection 4 of Chapter 3). The same does not apply if CNFs are employed as positive electrodes. Indeed, we show that carbon nanofiber sheets are inert at working potentials between 3 V and 4.5 V. Therefore, we must enrich the carbonaceous support with cathodic active material so that carbon nanofibers act as conductive porous matrix and improve the electrochemical performance of the cathode. On the other hand, loading active material into CNFs in the anode is optional. We prove that great synergy arises if CNFs are loaded with a suitable anodic active material.

Electrospinning process

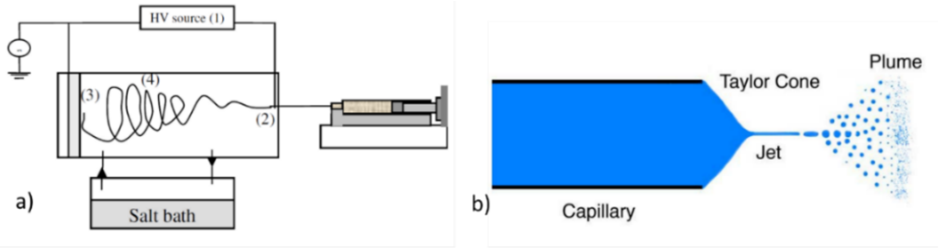

Figure 1.29: a) Schematic setup of electrospinning deposition (taken from [293]); b) Taylor Cone representation (taken from [294]).

Thanks to the simple syntheses and to their interesting properties, the CNFs are employed in a lot of different industrial fields. Their first application is in 1981 as dust filter in cars and trucks [9]. In the nineties their popularity increased, especially for biomedical and electronic applications such as tissue engineering, drug delivery, gas sensors and fuel cells [279,281,283,295–297].

Polymeric fibers can be produced from a solution by the electrospinning process, where the polymer flows from the source to the collection area and there the solvent evaporates leaving solid and dry fibers [280].

The apparatus of electrospinning deposition for laboratory scale is schematically displayed in Figure 1.29a. The setup is composed of three important components: the high voltage generator capable of suppling up to 40 kV, a syringe pump emitting the polymeric fibers and a conductive collector made of an Aluminum foil. The collector could be either a fixed plane foil or a rotating collector, depending on the desired fiber order of the outcome mat. Indeed, the former collector allows for the deposition of random fibers, whereas the latter let them lay well aligned. The type of collection is dependent on the end-use of the product. For instance, aligned fibers are used in the textile sector, while a random mat is suitable for electrodes, to better disperse active material. In large-scale systems, the setup is upgraded by installing multiple needles. They must be properly spaced, so to avoid the interaction between electrical fields. Otherwise, compressed air is employed to create bubbles on the surface and obtain multiple jets [49,280].

An electric field is applied between the syringe needle and the current collector. The syringe pump ejects the polymeric solution creating a droplet at whose tip the charges are accumulated. The droplet shape is modified by the loss of surface tension. By increasing the voltage, the electric field on the droplet increases forming a cone known as Taylor cone (Figure 1.29b). When the repulsion forces become stronger than the surface tensions, a solution jet is released which takes a complex path and finally is collected on the metal foil. The solvent evaporation is favored by the motion and stretching of the jet [280].

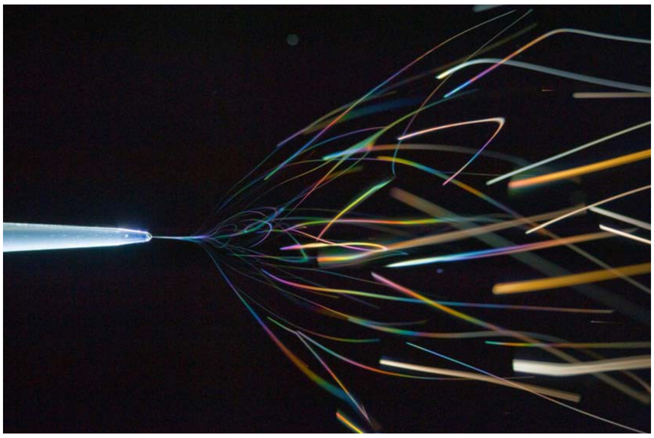

Figure 1.30: Generation of jet from tip of the needle (taken by [280]).

To optimize the morphology and features of the deposited CNFs, the experimental setup properties, the solution characteristics, and the external environment conditions are controlled. At the setup the flow rate, the distance between needle and collector, and the applied voltage are tuned. The main challenge is to keep the polymer drop at a fixed and constant size and to maintain the Taylor cone shape, so to ensure a stable jet, see Figure 1.30. The flow rate must be accurately chosen to avoid any excess or lack of polymer solution. An unstable jet may lead to an inhomogeneous morphology of the deposition production of artifacts such as the "bead-on-a-string", as reported in refs. [280,298]. The flow rate must be adjusted together with the applied voltage. Indeed, if the rate is too slow and the applied electric field is high, the polymerization could occur before leaving the needle. While, if the rate is fast but the applied voltage is too low, the jet becomes unstable, and the solution drops from the needle tip without being spun. The applied electric field can be tuned by varying the applied voltage or adjusting the distance between the tip and the collector. The applied electric field must be strong enough to exceed the surface tension but not too high to make the jet unstable. For tabletop installations the potential is in the 8-20kV range. The higher the voltage, the thinner are the nanofibers, as the ejected fluid speed increases while the flow rate remains constant [280,298]. Finally, increasing the applied voltage may cause the stretching of the solution thread and a fast solvent evaporation.

The resulting product characteristics are strongly affected by the solution features as well. In particular, we focus on the viscosity, concentration, and molecular weight (MW) of the polymer. The solution viscosity is critical because fibers cannot be electrospun if the solution is too viscous. On the contrary, if the solution is too fluid the fibers ejection is discontinuous. The viscosity influences the fiber size and morphology as well. Usually, when the viscosity is in the 1-20 poise range, the deposited nanofibers are uniform. The viscosity is influenced by the solution concentration and the polymer MW. Indeed, higher concentration and MW lead to higher viscosity, and the fibers have consequently larger diameter [298,299]. The concentration of the polymeric solution is strictly correlated to the viscosity of the solution. In refs. [280,298,300], different ranges of polymer concentrations have been tested. Notably, it is highlighted that if the concentration is lower than 5 wt%, the produced nanofibers are inconsistent and coiled. When the concentration is in the 6 - 9 wt% range, conventional fibers with the diameter in the range of 250nm-2µm are obtained, because the viscosity resistance becomes higher. Finally, for concentrations higher than 9 wt%, flat fibers are prepared, due to the inability to maintain the flow solution at the needle tip (Figure 1.31). The molecular weight of the electrospun solution influences the viscosity too. Indeed, it follows the relationship of Mark-Houwink:

$$[\eta] = KMW^{\alpha}$$

Eq. 1.64

where η is the viscosity, k and α are empirical constants. By increasing the MW and viscosity, the concentration increases too. The MW reflects the number of polymer chains' entanglements, and even when the polymer concentration is low, if we increase the MW it leads to a sufficient viscosity level of solution to create a continuous electrospinning jet. A high MW also produces high viscosity and polymer chain interactions which lead to higher nanofiber diameters, while if the MW is low the electrospun solution forms beads. The MW influences also the surface tension: when the MW is high, the proper viscosity level is found and the concentration is low, the surface tension effect are restrained and influence the morphology of fibers. Particularly, when the surface tension is low the beading effect is reduced in the CNFs, but if it is high, it inhibits the deposition making the jets unstable. In the last case, the jet is divided into droplets, and it is not continuous, so consistent fibers are not obtained. The relationship between viscosity and surface tension is depicted by the following equation:

$$\nu = \frac{\sigma}{6r\eta},$$

Eq. 1.65

where ν is the growth rate of the jet instability, σ is the surface tension, η the viscosity and r the initial radius of the jet [280,298].

Finally, the environment conditions, such as temperature and moisture, have a significant impact on the electrospinning process [293]. Particularly, if the air temperature is high, the intrinsic solution viscosity decreases, which implies the aforementioned consequences. On the other hand, the ambient humidity influences negatively the deposition as few polymers could polymerize in contact with water vapor, because the higher the humidity is, the higher is the solvent vaporization which makes the loss of charge easier [280,298].

After the nanofiber's deposition, we proceed with a heat treatment in order to obtain carbonized CNFs. This is extremely important for rechargeable batteries, where the carbonized CNFs support must exhibit an high electronic conductivity. In the present work, the PAN nanofiber sheets undergo a two-step heat treatment: stabilization and carbonization [239,280,284,301–307]. The stabilization consists of dehydrogenation, cyclization, and oxidation of the polymer, as schematized in Figure 1.32. The stabilization process is made in air with different temperature ranges. At lower temperatures, the dehydrogenation occurs and the double bonds C=C are introduced. Dehydrogenation needs air because it implicates two steps, firstly the oxidation, and secondly the elimination of water.

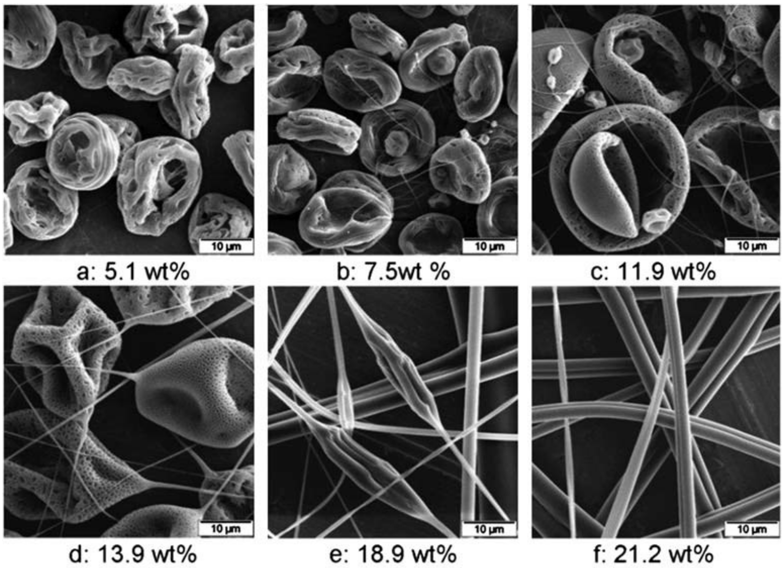

a: 5.1 wt% b: 7.5wt % c: 11.9 wt%

d: 13.9 wt% e: 18.9 wt% f: 21.2 wt%

Figure 1.31: Polystyrene electrospun samples with MW=393400, solution at different concentrations (taken from [280]).

The cyclization is the step when the rings are formed, and it occurs in the 180°–250°C temperature range. The nitrile group cyclizes converting themselves from triple into double bonds C=N, and it is necessary to hold together molecules in fibers; in this step gas products are released. Finally, the last oxidation step lets the fibers reach the final structure containing imine and nitrile groups among the PAN molecules. The step of stabilization is extremely important to guarantee a satisfactory carbonization of the fibers. Indeed, during the stabilization process the bonds change thus making the graphitization more favorable [305].

During the carbonization step, an aromatic growth and polymerization occur. This step requires an inert atmosphere and a thermal treatment in the 700–3000°C temperature range. It is chosen depending on the desired graphitization degree. Typically, the nitrogen atmosphere lowers the graphitization temperature in respect of the argon one. This step is divided into two parts: the pyrolysis and the graphitization, namely the transformation of carbon chains into graphite [305].

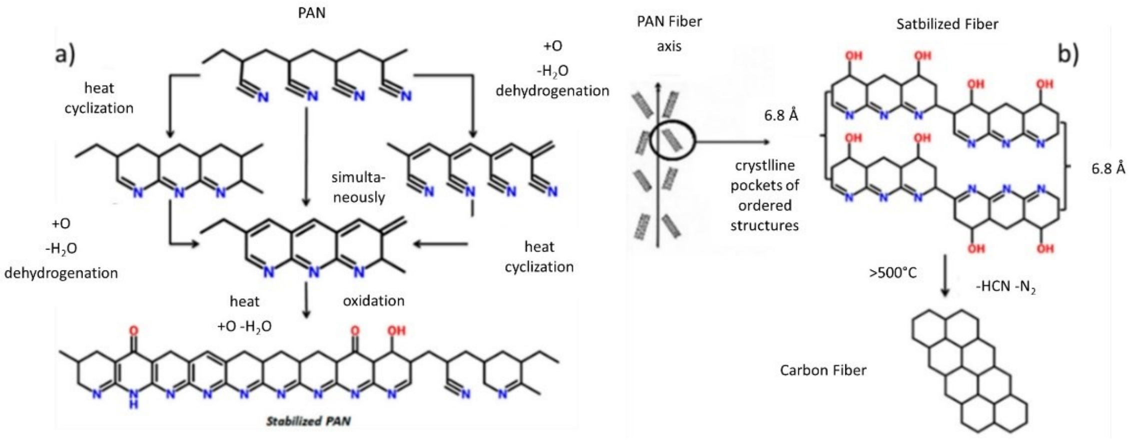

Figure 1.32: a) Stabilization and b) carbonization processes of PAN (taken from [307]).

Section 8. Thesis's aim

The work developed during this Ph.D. thesis aims at fabricating new types of active material/CNFs self-standing electrodes for Na-ion batteries, with improved electronic conductivity and ion diffusion, avoiding binders, current collectors and electrochemically inactive materials, typically used to prepare conventional slurry electrodes. CNFs are not only the active material's support, but also the porous 3D framework suitable to guarantee fast electronic conductivity and fast ions diffusion into the cathode, thanks to the easy permeation of the electrolyte. All these features create the right conditions to achieve enhanced specific capacities at high C-rates and improved cell lifespan, compared to traditional tape-casted electrodes.

In this work we synthesized and investigated some electrochemically active materials/CNFs composites as self-standing electrodes for SIBs. We chose as active materials two *NaSICON*-structured compounds as cathodes, and *ZnS* as anode. The electrodes were prepared by both slurry and self-standing approach, and their electrochemical performances in terms of specific capacity at different C-rates, coloumbic efficiency, capacity retention and cycling capability were compared.

Firstly, we focused on investigating the electrospinning technique as synthetic approach to fabricate carbon nanofiber sheets: we evaluated the suitable instrumental parameters to successfully prepare the conducive, porous, and homogeneous CNF. The CNFs are used to fabricate a 3D carbon network suitable to host the active material and develop self-standing electrodes. CNFs are not only the active material's support, but also the porous 3D framework suitable to guarantee fast electronic conductivity and fast ions diffusion into the cathode, thanks to the easy permeation of the electrolyte. All these features create the right conditions to achieve enhanced specific capacities at high C-rates and improved cell lifespan, compared to traditional tape-casted electrodes. We studied the CNFs morphology, structure, and electrochemical properties in the voltage range of the active materials for ion-batteries. The CNF sheets alone were also investigated as possible anodes for Li-ion and Na-ion batteries.

Then, we investigated the synthesis conditions to fabricate self-standing electrodes based on active-materials/CNFs composites by electrospinning. A preliminary study was carried out on a well-known and commercially available active material for Lithium-ion batteries, $LiFePO_4$; it was combined in different amounts (10 and 30 wt%) to CNFs to develop a self-standing electrode. This new electrode was characterized by several techniques (X-ray powder diffraction, scanning electron microscopy, electron dispersion spectroscopy, transmission electron microscopy, thermogravimetric analysis, Raman spectroscopy) and was electrochemically tested. The structure, physic-chemical properties, and electrochemical performances of the self-standing electrode were compared to those obtained for a conventional tape-casted $LiFePO_4$ cathode (slurry method), appositely prepared. Differences, drawbacks, and advantages/disadvantages of both type of electrodes were analyzed and discussed. The preliminary investigation on the well-known cathode revealed to be very useful to establish the optimal experimental conditions to fabricate CNFs-based self-standing electrodes and paved the way for the development of other free-standing cathodes and anodes for SIBs.

The compounds selected as cathode materials for fabricating the self-standing electrodes for SIBs are the *NaSICON*-structured $Na_3MnZr(PO_4)_3$ and $Na_3MnTi(PO_4)_3$: their structural, chemical, electrochemical and physical features have been reported in Section 4 of 0. Both active materials were synthesized via sol-gel with different amount of citric acid to obtain a particulate with an optimal carbon coating. The raw materials were properly characterized. Then the synthesized active material was dispersed in a polymer solution, and the solution was electrospun to develop the self-standing electrodes. In the case of $Na_3MnZr(PO_4)_3$ compound, different deposition settings (vertical or horizontal apparatus for electrospinning) and diverse reaction conditions (dip/drop-coating of the active material precursors on pre-synthesized CNFs, followed by thermal treatment to synthesize $Na_3MnZr(PO_4)_3$) were investigated. All the synthesized cathodes were characterized and electrochemically tested, and the results were compared to those obtained for slurry electrodes, appositely prepared.

Finally, we prepared and characterized a ZnS-GO/CNFs self-standing electrode, as suitable anode for SIBs. This preliminary study paves the way to develop a full cell for SIBs, based on only free-standing electrodes.

Chapter 2. Experimental

In this chapter we illustrate the synthesis method to prepare the *NaSICON*-structured $Na_3MnZr(PO_4)_3$ and $Na_3MnTi(PO_4)_3$ compounds, and ZnS-GO composites. We also report the synthetic procedure used to prepare CNFs and active materials/CNFs self-standing electrodes. Finally, we report the characterization and electrochemical techniques and the experimental conditions used to investigate the samples.

Section 1. Active materials synthesis

Subsection 1 Synthesis of the *NaSICON*-structured compounds

The $Na_3MnZr(PO_4)_3$ and $Na_3MnTi(PO_4)_3$ carbon-coated powders were synthesized by sol-gel route. In the sol-gel synthesis a solution containing the product's precursors is properly treated to form a gel that, once calcined at suitable temperatures, forms the final product. The precursors are usually inorganic/organic salts and are typically mixed in an aqueous solution with a polymeric/carbonaceous component, which acts as chelating agent for the formation of the intermediate gel. The use of a polymeric component guarantees a homogeneous dispersion of the precursors, avoiding possible by-products or starting materials precipitation. The calcination process can be performed in an inert atmosphere or in air; inert gases are used in the case we need to preserve the carbonaceous network as conducive carbon coated on the product's particles. The calcination process converts the intermediate gel into the final sol. The advantage of the sol-gel synthesis is the low cost and the reduced particles' size.

In this work we used citric acid as carbon source to obtain carbon-coated $Na_3MnZr(PO_4)_3$ and $Na_3MnTi(PO_4)_3$ powders. Different amount of citric acid were employed, in order to investigate the best coating conditions for optimized electrochemical performances.

$Na_3MnZr(PO_4)_3$

$Na_3MnZr(PO_4)_3$ was synthesized following the procedure reported by Gao et al. [56]. An aqueous solution containing CH_3COONa (Aldrich, 99%), $(CH_3COO)_2Mn \cdot 4H_2O$ (Aldrich, 99%), $NH_4H_2PO_4$ (Aldrich, 99%) and $Zr(C_5H_7O_2)_4$ (Merck, 97%) in stoichiometric amount, and citric acid (Aldrich, 99%) is prepared. The solution is heated at 80°C to obtain the gel, which is then dried at 100°C in an oven. The powder is ground in an agate mortar and heat-treated at 750°C for 10 h under nitrogen flux, to form the final product. Three different solutions are prepared by changing the citric acid/compound mole ratio: 8.8, 3 and 2. The three samples are labelled 8.8-MnZr, 3-MnZr and 2-MnZr (Table 2.3 in Section 6). The samples are also ball-milled at 100rpm for 40 minutes in order to reduce the particles size for the electrochemical tests.

$Na_3MnTi(PO_4)_3$

$Na_3MnTi(PO_4)_3$, was synthesized following the procedure reported by Zhou et al. [55]. An aqueous solution of NaC_2H_3O (Aldrich, 99%), $(CH3COO)_2Mn \cdot 4H_2O$ (Aldrich, 99%), $NH_4H_2PO_4$ (Aldrich, 99%) and citric acid (Aldrich, 99%) is prepared (solution A). Another solution is obtained by dissolving $C_{12}H_{28}O_4Ti$ (Aldrich 99%) in absolute ethanol (solution B). All the precursors are in stoichiometric amount. The solution B is added to solution A dropwise, stirred and heated at 80°C until the gel forms. The gel is dried at 100°C and ground in an agate mortar. The obtained powder is heat-treated at 650°C for 12 h in nitrogen flux to obtain the final product. We prepare three different A solutions by changing the citric acid/compound mole ratio: 8.8, 3 and 2. The samples are labelled 8.8-MnTi, 3-MnTi and 2-MnTi (Table 2.4 in Section 6). The samples are also ball-milled at 100rpm for 40 minutes in order to reduce the particles size for the electrochemical tests.

Subsection 2 Synthesis of ZnS-GO

The hydrothermal route is used to synthesize the ZnS-GO composite. In this procedure the active material (ZnS) is properly coated with GO, to enhance its poor electronic conductivity. In the hydrothermal process the combined action of temperature/pressure is used to obtain high purity and crystalline products. The ZnS-GO composite is prepared following the procedures reported in [74,198,308]; the final sample is used to prepare slurry and self-standing anodes.

0.1 g of GO (5-20 sheets, 4-10% edge-oxidized, Sigma-Aldrich) are dispersed into 60 mL of distilled water. The solution is sonicated until a homogeneous dispersion is obtained, them 0.88g of zinc acetate dihydrate ($Zn(CH_3COO)_2 \cdot 2H_2O$; 99%, Sigma Aldrich) are added and the solution is sonicated for 1h. An ammonium hydroxide solution (NH_4OH; ≥25%NH_3 basis, Sigma Aldrich) is added dropwise until the pH=9 is reached. A second solution is prepared by dissolving 1.92g of $Na_2S \cdot 9H_2O$ (≥98%, Sigma Aldrich) in 10mL of distilled water, and added to the previous one, stirred for 1 h, and finally transferred into a stainless-steal autoclave for the thermal treatment at 140°C for 10 h. The idrogel product is washed in water and ethanol, and finally centrifuged at 6000 rpm for 10 min, recovered and dried.

Section 2. Synthesis of CNFs and Self-standing electrodes by electrospinning

In a conventional electrospinning process the polymer solution is pumped from the spinneret and collected on an Aluminum current collector in the form of fibers [278]. The theory of the process is explained in the introduction in Subsection 19. In this section we present the experimental setting and the thermal treatments applied in this work to deposit CNFs and active materials/CNFs sheets, to prepare the self-standing electrodes.

Subsection 3 Preparation of the solutions

CNFs

The solution containing 8 wt% of PAN in 50mL of DMAc is prepared to synthesize the pure CNFs. They are fabricated to be compared to the self-standing electrodes, in which the active material is dispersed in this matrix, and to investigate possible electrochemical activity of the CNFs sheets without the presence of active materials.

Active materials/CNFs

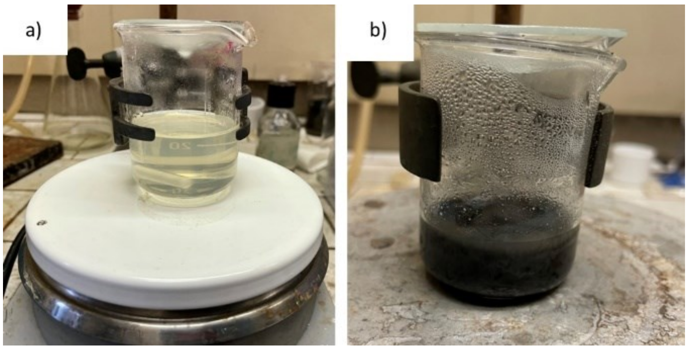

Figure 2.1: a) Solution of PAN for pure CNFs deposition; b) Solution of PAN and active materials powder for self-standing electrodes deposition.

The solution to fabricate the active material/CNFs electrodes by electrospinning is prepared by dispersing 10 wt% and 30 wt% of active materials into a 8%wt of PAN in DMAc [74,142]. The active material powder (0.376g and 1.128g of commercial $LiFePO_4$ (Aldrich 759546), $Na_3MnZr(PO_4)_3$, $Na_3MnTi(PO4)_3$, or ZnS-GO for 10 wt% and 30 wt% samples, respectively) is added to 50 mL of DMAc and the suspension is sonicated for 1 h, in order to avoid the agglomeration of the active material particles. Thereafter, 3.760g PAN is combined and the suspension is stirred overnight at 60°C, see Figure 2.1.

Electrospinning deposition

The abovementioned solutions were electrospun by using a EF050—Starter Kit Electrospinning of SKE Research Equipment (C/O Leonardino S.r.l, Bollate, MI, Italy) horizontal set-up. In the case of the $Na_3MnZr(PO_4)_3$/CNFs cathode, the 30 wt% solution is deposited also with a vertical set-up. For this deposition a NANON01A apparatus equipped with dehumidifier 501 (MEEC instruments, MP, Pioltello, Italy) is employed, in collaboration with the Department of Drug Sciences, University of Pavia (Italy).

The horizontal deposition setting conditions are: 10.5 mL of dispersion loaded in the syringe, 3.5 mL/h flow rate, 16 Gauge needle, applied voltage 16 kV, needle–collector distance 18 cm, and deposition time 3 h. The abovementioned values were chosen after checking different conditions, as they give the best quality depositions. Finally, a homemade humidity sensor included box is built for humidity control <20% (see Figure 2.2).

The selected conditions for the vertical set-up are: 10 mL of dispersion loaded in the syringe, 0.5 mL/h flow-rate, 16 Gauge needle, applied voltage 28 kV, needle-collector distance 15 cm, deposition time 3 h, and temperature and relative humidity values of 23 ± 2 °C and 20 ± 3% respectively.

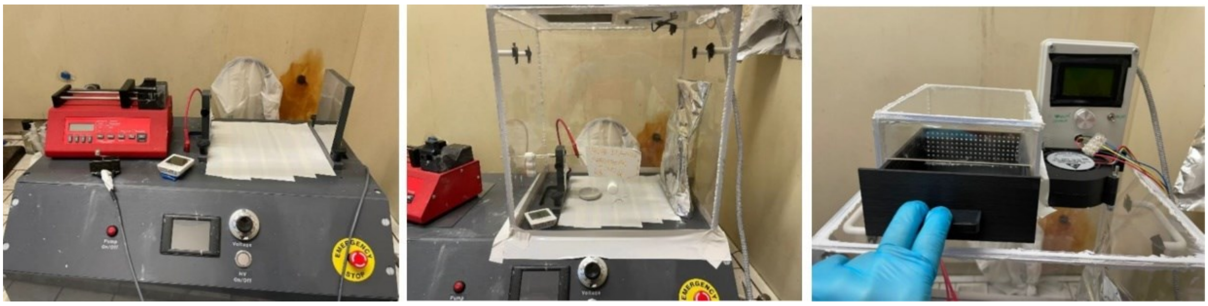

Figure 2.2: Electrospinning instrument and homemade box with humidity sensor.

Subsection 4 Thermal treatment

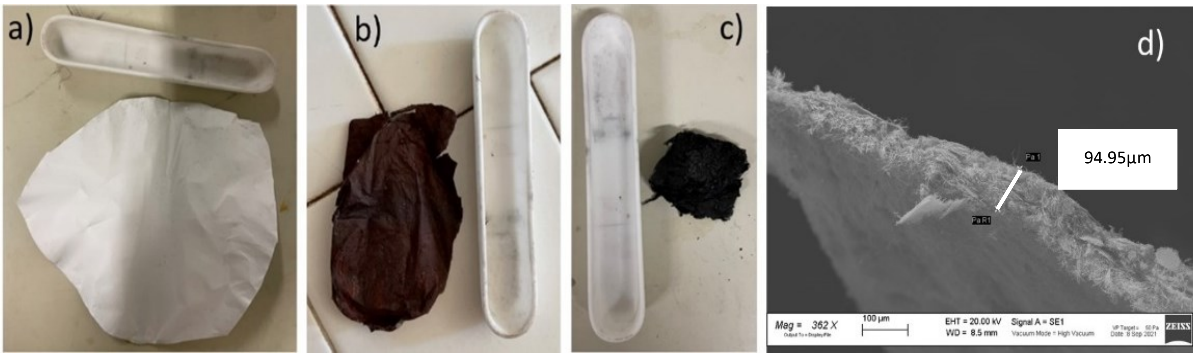

Figure 2.3: CNF a) only electrospun, b) after stabilization and c) after carbonization; d) the view of a CNF sheet after thermal treatment by SEM analysis.

The electrospun sheets are removed from the support (aluminium foil) and stabilized in air for 30 minutes at 100°C, 30 minutes at 200°C, and finally 2 hours at 260°C (heating ramp: 5 °C min^{-1}). They are further heat-treated in a tubular furnace (Carbolite) at 750°C for 2 hours (heating ramp: 10°C min^{-1}) in nitrogen atmosphere for the carbonization process. The same thermal treatment is used for pure CNFs sample which are carbonized at different temperatures and in diverse atmosphere (for details see results in Section 1 of Chapter 3). The obtained sheets as electrospun and after the stabilization and carbonization process are shown in Figure 2.3. The sheet thickness is evaluated by scanning electron microscopy analysis (see Figure 2.3d), reported in Subsection 7 of Chapter 2.

Subsection 5 Different approaches to deposit active materials/CNFs electrodes: the case of dip-drop coating

This is a different strategy we adopted to prepare the self-standing electrodes, applied only to the $Na_3MnZr(PO_4)_3$ and $Na_3MnTi(PO_4)_3$ cathodes. The pure CNFs sheets were firstly prepared as reported in Subsection 3, and thermally treated for stabilization and carbonization at 900°C. Then, an aqueous solution of the active materials' precursors is prepared by using the reagents' amount of the sol-gel synthesis and a citric acid/compound mole ratio of 2. The carbonized CNFs sheet is deeply drenched into the precursor's solution, and the same solution is also dropped on the CNFs sheet surface. The drenched CNFs are dried in a vacuum oven at 120°C for one night, and thermal-treated in N_2 atmosphere 10 h at 750°C to synthesize the $Na_3MnZr(PO_4)_3$ self-standing cathode, and 12 h at 650°C for the $Na_3MnTi(PO_4)_3$ one. The advantage of this procedure is a higher amount of active material loaded into CNFs, but the downsides are a nonuniform distribution or active material particles into CNFs and the double thermal treatment to which the CNFs undergo. This causes a decrease of CNFs sheet thickness and area, which makes difficult to obtain a proper size for the sample's tests. The Figure 2.4 schematizes the dip-drop method.

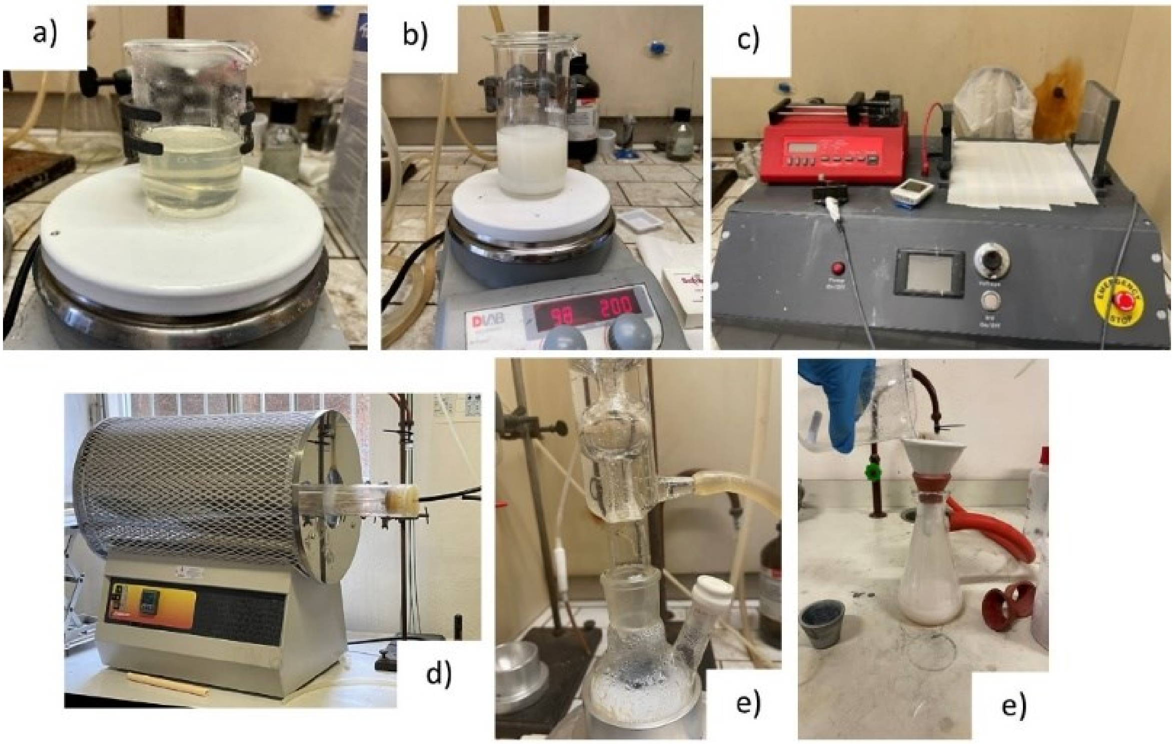

Figure 2.4: Dip-drop synthesis; a) 8 wt% PAN solution in DMAc; b) Aqueous solution of active material's precursors; c) Electrospinning process of the pure CNFs; d) stabilization and carbonization of CNFs; e) drenching of the CNFs sheet into the precursors' solution; e) precursors' solution dropped onto CNFs sheet. The drenched sheets were further thermal-treated to synthesize the active materials into CNFs.

Section 3. Preparation of the Tape-casted electrodes

As aforementioned, conventional slurry electrodes were prepared and investigated, and their electrochemical performance was evaluated, to discuss advantages/disadvantages compared to the self-standing electrodes. We report the procedure applied to prepare the tape-casted electrodes.

$LiFePO_4$

The slurry is prepared by mixing the commercial (Sigma Aldrich) $LiFePO_4$ powder (80 wt%), acetylene black (10 wt%) and Polyvinylidene fluoride (Kynar, 10 wt%) in N-methyl-2-pirrolidone (NMP). The solution is stirred for 2 h, then it is tape-casted (Doctor Blake method) on an Aluminum foil and dried at 100°C for 3 h. The composition of the slurry used for $LiFePO_4$ is taken from the patent [309].

$Na_3MnZr(PO_4)_3$

The active material is synthesized as reported in Subsection 1 of Chapter 2, and ball-milled at 100 rpm for two cycles (20 min each). The slurry is prepared by mixing the active material (70 wt%), acetylene carbon (20 wt%) and PVdF binder (Solvay 5130, 10 wt%) in NMP. The slurry is stirred 2 h, tape-casted (Doctor Blade coating technique) on Aluminum foils and dried at 70°C for 3 hours.

$Na_3MnTi(PO_4)_3$

The active material is synthesized as reported in Subsection 1 of Chapter 2, and ball-milled at 100 rpm for two cycles (20 min each). The slurry is prepared by mixing the active material (70 wt%), Super P carbon (20 wt%), PVdF binder (Kynar, 10 wt%) and NMP. The slurry is stirred 2 h, tape-casted (Doctor Blade coating technique) on Aluminum foils and dried at 70°C for 3 hours.

ZnS-GO

The active material is synthesized as reported in Subsection 2 of Chapter 2, and ball-milled at 100 rpm for two cycles (20 min each). The ZnS-GO slurry is prepared with 70 wt% of active material, 20 wt% Super P carbon, and 10 wt% CMC binder in distilled water, and stirred for 2 h. The slurry was tape-casted on copper foils and dried at 70 °C for 3 hours.

Section 4. Characterization techniques

Subsection 6 X-Ray powder diffraction (XRPD)

X-ray power diffraction is a crystallographic investigation technique applied to evaluate the crystal structure of solids with long-range periodic order. The phenomenon of diffraction consists of the constructive interference between diffracted waves from the reticular planes of a crystal. The Bragg's law relate the incident radiation wavelength and the order of reflection (n) to the interplanar distances (d) and to the diffraction angle (θ).

All samples' data are collected by using a Bruker D5005 diffractometer equipped with a Copper K_α radiation, a curve graphite monochromator and a scintillation detector.

The following conditions were used for the XRPD data collection:

- pure CNFs sample. 16° - 80° 2θ range; step size: 0.03°(2θ); counting time: 22 s/step.
- $LiFePO_4$ powder and self-standing electrodes. 16° - 80° range; step size: 0.03°(2θ); counting time: 22 s/step.
- $Na_3MnZr(PO_4)_3$ powder and self-standing electrodes. 16° - 80° 2θ range; step size: 0.03°(2θ); counting time: 22 s/step.
- $Na_3MnTi(PO_4)_3$ powder and self-standing electrodes. 18° - 80° 2θ range; step size: 0.03°(2θ); counting time: 22 s/step.
- ZnS-GO and 10%ZnS-GO/CNF samples. 17° - 80° 2θ range; step size: 0.03°(2θ); counting time: 16 s/step.

The TOPAS 3.0 software (Bruker AXS, Karlsruhe, Germany) [310] is used to apply the Rietveld structural and profile refinement to the diffraction data.

In the case of the commercial $LiFePO_4$ and pristine $Na_3MnZr(PO_4)_3$, $Na_3MnTi(PO_4)_3$ and ZnS active materials, the following parameters were refined: (i) global parameters: polynomial background (third degree polynomial function), sample displacement; ii) active material phase: scale factor, lattice parameters, isotropic thermal factors. The profile was refined by applying the Fundamental Parameters Approach [311–313], and the crystallite size is evaluated by the Scherrer equation.

In the case of the active materials/CNFs samples, a broad band centered at about 25°(2θ), attributed to the CNFs amorphous phase, dominates the diffraction pattern, and the peaks of the crystalline active material are weak, due to its low amount (10-30 wt%) (see XRPD results in Chapter 3). The refinement procedure was modified as follows: (i) global parameters: polynomial background (third degree polynomial function) and sample displacement; ii) active material phase: scale factor and lattice parameters. The profile was refined by applying the Fundamental Parameters Approach, and the crystallite size is evaluated by the Scherrer equation. (iii) amorphous broad band: peak's position, intensity and profile (Pearson-VII function and Full width at Half Maximum). We believe we cannot obtain reliable values by adding other structural parameters of the active material phase, due to its low amount and the relevant broad amorphous band. Finally, the degree of crystallinity can be calculated by the total area of crystalline peaks (active material) over the total area of all peaks (active material plus amorphous phase). The degree of crystallinity does not represent the crystalline phase amount, but we used it to suggest the similarity of the 10%MnTi/CNF and 30%MnTi/CNF samples, as confirmed by other characterization techniques (see Subsection 13 of Chapter 3).

Subsection 7 Scanning Electron Microscopy (SEM) and Energy Dispersive X-ray spectroscopy (EDS)

The scanning electron microscopy (SEM) technique gives relevant information about the topography and morphology of solids. In this technique a primary electron beam is suitably collimated and accelerated by a series of electromagnetic lenses to scan the surface of the sample. The interaction between the beam and the sample generates secondary electrons, which are revealed and converted into electrical impulses. The outcoming signal is processed to give a high-resolution image of the investigated surface. The sample is required to be conductive for the analysis.

SEM micrographs of all the investigated samples are collected with a Zeiss EVO MAH10 (Carl Zeiss, Oberkochen, Germany) scanning electron microscope on Au sputtered samples (20 kV, secondary electron images, working distance 8.5 mm). The microscope is equipped with an energy dispersive detector (X-max 50 mm 2, Oxford Instruments, Oxford, UK) for the EDS analysis. SEM analysis is applied to investigate the morphology of active materials' powders, CNFs, and active-materials/CNFs composites.

Energy dispersive X-ray spectroscopy provides qualitative and quantitative information on the chemical elements present in the sample and their distribution, namely the distribution maps of the elements. This technique detects the X-Ray emitted by the elements present in the sample when it interacts with a high energy electron beam. The analysis is performed by using the same instrumentation employed for SEM thecnique (Subsection 7), but, in this case, the samples' conductivity is not required. The EDS is mainly used to verify the homogeneous dispersion of the $LiFePO_4$, $Na_3MnZr(PO_4)_3$, $Na_3MnTi(PO_4)_3$, and ZnS-GO active materials on the surface and along the thickness of the CNFs sheets. The preparation of CNFs sheets is detailly reported in Section 2 of Chapter 2.

Subsection 8 Transmission Electron Microscopy (TEM)

The transmission electron microscope gives information about the morphology, topography, and crystal structure of a material. An electron beam is generated in vacuum, and focalized on the sample. The sample must be extremely thin (thickness of 5-500nm), to be crossed by the electron beam. Thereafter the beam is modulated using electrical and magnetic field and hits a fluorescent surface projecting and magnifying the sample image.

The TEM images of the investigated samples are collected with a JEOL JEM-1200EXIII equipped with TEM CCD camera Mega View III transmission electron microscope to highlight the distribution of the carbon coating around the $Na_3MnZr(PO_4)_3$ and $Na_3MnTi(PO_4)_3$ particles, and the presence of $LiFePO_4$, $Na_3MnZr(PO_4)_3$, $Na_3MnTi(PO_4)_3$, ZnS-GO powders into the carbon nanofiber sheets. Both active materials powders and self-standing electrodes are dispersed in water, and a drop of 0.7µL is deposited on the formvar/carbon coated Ni grid and dried. The measurement were performed at the “Centro Grandi Strumenti” of the University of Pavia.

Subsection 9 Thermogravimetric Analysis (TGA)

The thermogravimetric technique investigates the mass changes when a substance is submitted to a controlled temperature program (heating, cooling, or isotherm). The weight loss can be attributed to different phenomena, such as release of water, carbon combustion/pyrolisis, the oxidation/reduction or decomposition.

The TGA data collection is performed with a TA Q5000 instrument in air, in the 20 °C-725 °C temperature range (heating rate: 10 $Kmin^{-1}$). The technique is used to determine the amount of carbon coating in the $Na_3MnZr(PO_4)_3$ and $Na_3MnTi(PO_4)_3$, and ZnS-GO powders, and the effective amount of $LiFePO_4$, $Na_3MnZr(PO_4)_3$, $Na_3MnTi(PO_4)_3$, and ZnS-GO active materials loaded into CNFs for the self-standing electrodes.

Subsection 10 Micro-Raman spectroscopy (micro-RAMAN)

The Raman spectroscopy is used to investigate the vibrational modes in molecules or solids, to determine their structural features, as vibrational modes depend on the chemical bonds and symmetry. The mechanism is based on the inelastic scattering of photons, and the laser light is used as monochromatic source. The Raman effect consists in the interaction between the electron cloud of the substance and the external electric field of the source: a temporary dipole moment is induced.

In the case of micro-Raman analysis, the Raman apparatus is equipped of a microscope, to focalize the laser beam on a sample region with micrometric size.

The Raman measurements are performed with a micro-Raman spectrometer, XploRA Plus HORIBA Scientific, equipped with an Olympus microscope BX43.

For all $LiFePO_4$, $Na_3MnTi(PO_4)_3$, and ZnS-GO powder and correspondent self-standing electrodes, the laser red light at 638 nm (90 mW) is used as excitation source, and the incident laser power is tuned by a set of neutral filters with different optical densities. While, for the $Na_3MnZr(PO_4)_3$ powder and $Na_3MnZr(PO_4)_3$/ CNF samples, the green laser light at 532 nm is used as excitation, tuning the 100 mW output power by a set of neutral filters with different optical density. The samples are placed on a motorized xy stage. Spectral resolution is about 2 cm^{-1} for $LiFePO_4$, $Na_3MnTi(PO_4)_3$ and ZnS based materials, while it is 3 cm^{-1} for the $Na_3MnZr(PO_4)_3$ based ones. An Open Electrode CCD camera, with a multistage Peltier air-cooling system, is used as detector. The measurements have been performed using a 50x objective with a long working distance, that leads to a spatial resolution of the order of 4 µm.

The Raman spectra are acquired on 10 accumulations, and with mean integration time of about 20 s, 10 s, 10 s and 20 s for the $LiFePO_4$, $Na_3MnZr(PO_4)_3$, $Na_3MnTi(PO_4)_3$, and ZnS-GO samples, respectively. All the reported data are obtained as the average spectrum, sampling the materials in several different regions.

The micro-Raman analysis is applied to determine the presence of ordered carbon, by evaluating the I_G/I_D ratio in the active materials’ powders, in pure CNFs carbonized at different temperatures, and in the active materials/CNFs composites. In the latter samples, the signals from the active material structure can be partially or totally overwhelmed by the intense carbon-related Raman features, with two broadened bands peaked at about 1350 cm^{-1} (D-mode) and 1590 cm^{-1} (G-mode), attributed to the sp^3 type amorphous carbonaceous material and to the sp^2 graphite-like one, respectively. This is explained by the different Raman cross-sections, and by the fact that the carbon coating prevents the excitation of inner active material structure. So, the active material’s Raman signals will be partially or not detected, depending on the active material amount and distribution within the CNFs matrix (see Raman results in Chapter 3).

Section 5. Electrochemical characterization: cell preparation and electrochemical techniques

In this section we report the experimental procedures applied to assemble the cells and the electrochemical techniques used to characterize both self-standing and slurry (tape-casted) electrodes.

Subsection 11 Cell-assembly

All the cells are assembled in an Argon-filled dry box (M. Braun H_2O<0.1 ppm O_2<0.1 ppm), using a home-made Swagelok type T cell with polypropylene body. Two disks are cut (1 cm diameter) for each cell: one of slurry or self-standing electrode as working electrode (WE), and one of metallic Lithium or Sodium (depending on the investigated active material) as both counter (CE) and reference electrode (RE). For $LiFePO_4$ electrodes a commercial electrolyte $LiPF_6$ 1M in ethylene carbonate: diethyl carbonate (EC: DEC) 1:1 (Aldrich) is used. $NaClO_4$ 1M in Propylene carbonate (PC) with 5% of 4-Fluoro-1,3-diocolan-2-one (FEC) is used as electrolyte for both *NaSICON*-structured $Na_3MnZr(PO_4)_3$ and $Na_3MnTi(PO_4)_3$. The FEC is added as it provides improved electrolyte stability in the high working voltage of the two cathodes. Finally, for ZnS-GO anode, the $NaClO_4$ 1M in EC:DEC (1:1) and 5 wt% FEC electrolyte is used.

Subsection 12 Contact angle

The contact angle analysis is typically used to evaluate hydrophobic/apolar or hydrophilic/polar nature of a solid surface. It could be small or large based on the physical properties of the investigated materials. When the contact angle is large, the spreading of the droplet is poor, as shown in the Figure 2.5b (left droplet). When the contact angle is small, the droplet is spread on the surface and there is the wetting phenomenon illustrated in Figure 2.5c (right droplet). The surface wettability of the solid is determined by the intermolecular interactions between the surface and the liquid droplet. The contact angle θ is measured between the liquid and solid surface [314].

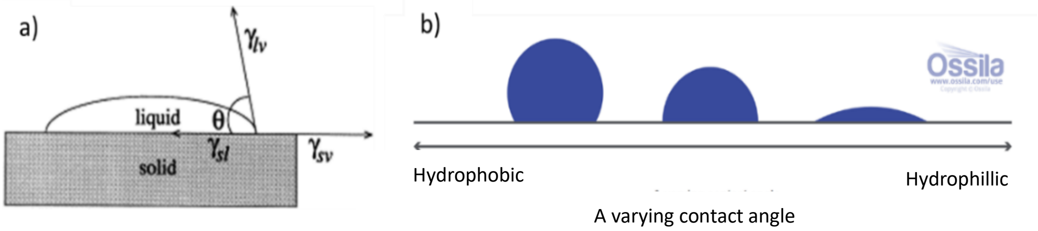

Figure 2.5: Schematic representation of the wetting contact angle (taken from [315]) and b) its dependence on the hydrophilic or hydrophobic solid surface (taken from [314]).

In this work, this analysis is used to qualitatively evaluate the wettability of the carbonized self-standing electrode when its surface is wetted with water and the electrolyte drop. The measurements are performed using the goniometer Cam200 contact angle and surface tension meter (KSV instrument).

Subsection 13 Cyclic voltammetry (CV)

Cyclic voltammetry is a potentiodynamic electrochemical method developed on the application of a triangular wave form potential. A stationary electrode is immersed in a solution and the potential of the working electrode has varied linearly over time with a scanning speed measured in volt per second (V/s). The potential is measured between the reference electrode (Li or Na), and the working electrode (cathode material), whereas the current is measured between the working electrode and the counter electrode (Na). The current I is reported against the applied potential E, to give the cyclic voltammogram. For each analyte that is reduced (or oxidized), an electron exchange with the working electrode occurs; the measured current changes, and a peak is recorded in the voltammogram. If the process is reversible, by scanning the voltage range in the opposite direction, a peak due to the oxidation (or reduction) process is detected at the same voltage value, but with opposite sign.

The electrochemical properties of the slurry and self-standing electrodes are investigated at ambient temperature by cyclic voltammetry (CV) and galvanostatic charge/discharge cycles using a Swagelok cell. The CV is performed with an Autolab PGSTAT30 potentiostat. The cells are cycled for three cycles at 0.1mV in the 2.5-3.9V, 2.5-4.5V, 1.5-4.5 V, and 0.01-3V potential range, for the $LiFePO_4$, $Na_3MnZr(PO_4)_3$, $Na_3MnTi(PO_4)_3$ and ZnS-GO electrodes, respectively. Finally, we also investigated the diffusion process of the electrodes by cycling the half-cells at different scan rates (0.1mV/s, 0.2mV/s, 0.5mV/s and 1mV/s) in the above-mentioned potential ranges. The data are analyzed to unravel the faradaic/diffusive and non-faradaic/pseudo-capacitance phenomena which dominate the electrochemical activity of the investigated active materials.

Subsection 14 Galvanostatic charge/discharge cycles

The working principle of a potentiostat/galvanostat depends on the type of application, and so the instrument is connected to the electrochemical cell in different set-up. We use the galvanostatic mode and the two-electrode setup. In the former we control the current flow between the WE and the CE. The potential difference between the RE and WE and the current flowing between the CE and WE are continuously monitored. In the latter, the CE and RE are shortcut at one electrode, whereas the WE and sense (S) are shortcut on the opposite electrode. A schematic view is reported in Figure 2.6. In this case, we measure the potential across the complete cell. The two- electrode configuration is used when precise control of the interfacial potential through the working electrode-electrolyte interface is not critical, and the behavior of the entire half-cell is investigated.

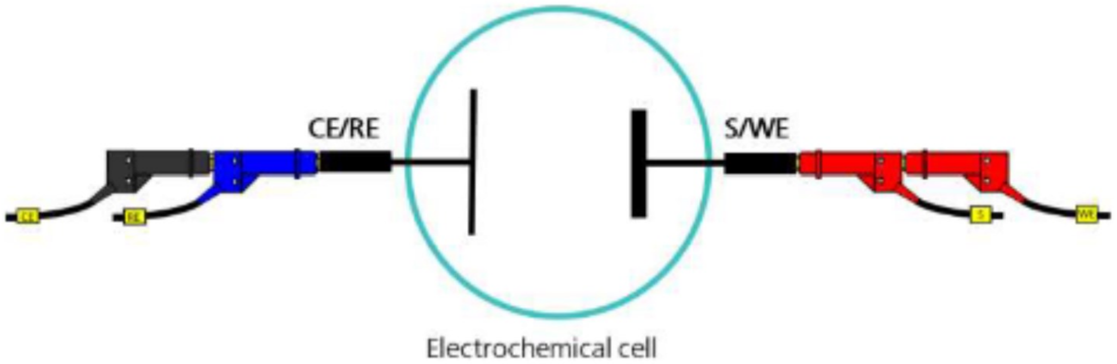

Figure 2.6: Schematic representation of the two-electrode setup in the tested cell.

Galvanostatic charge/discharge cycles are obtained with a Neware-4000BTS apparatus at different current rates (0.05C, 0.1C, 0.2C, 0.5C, 1C, 2C, 5C, 10C and 20C) in the abovementioned potential ranges (Subsection 13) for all $LiFePO_4$, $Na_3MnZr(PO_4)_3$, $Na_3MnTi(PO_4)_3$, and ZnS-GO tape-casted and self-standing electrodes. We also test the lifespan of the most promising cathodes by cycling for about 300 cycles the tape-casted electrodes, and 1300 cycles the self-standing ones. While, The ZnS-GO anode was cycled 5 cycles t 0.05C and 200 cycles at 0.5C, as a preliminary investigation of its possible employment as anode of SIBs.

The analytical method used for cycling analysis is the constant current and constant potential (CCCV) one: a scheme is shown in Figure 2.7 [316–319]. In the first part we impose constant current (CC) at proper C-rate to charge/discharge the cell, and the current makes the cell voltage increase. Once reached the respective voltage limit, the cell is maintained at this constant voltage (CV) to permit a full-charge/discharge of the cell, storing the maximum possible capacity, and preventing from overcharged potential. While the potential is constant, the current exponentially decreases, until below the 5% of the rated-current which is not relevant for the storage of capacity [317]. So, we define the cut-off current, under which the cell in charging begins the discharge step, and vice versa. The cut-off current defines the capacity utilization together with the constant voltage imposed. The CC step permits the reversible migration of alkali metal ions from the cathode-electrolyte to the anode-electrolyte interfaces, increasing the alkali metal concentration at solid/liquid interface, and making the charged capacity percentage higher. Instead, at CV step, the alkali metal ions diffusion occurs from the anode-electrolyte interface to the anode bulk and from the cathode bulk to its interface with electrolyte [317]. The CV step also helps in studying the degradation of LIBs, because, when the aging mechanism increases, the cut-off current is reached earlier. This analysis is employed in the current commercial fast charger and makes cell lifespan longer [319,320].

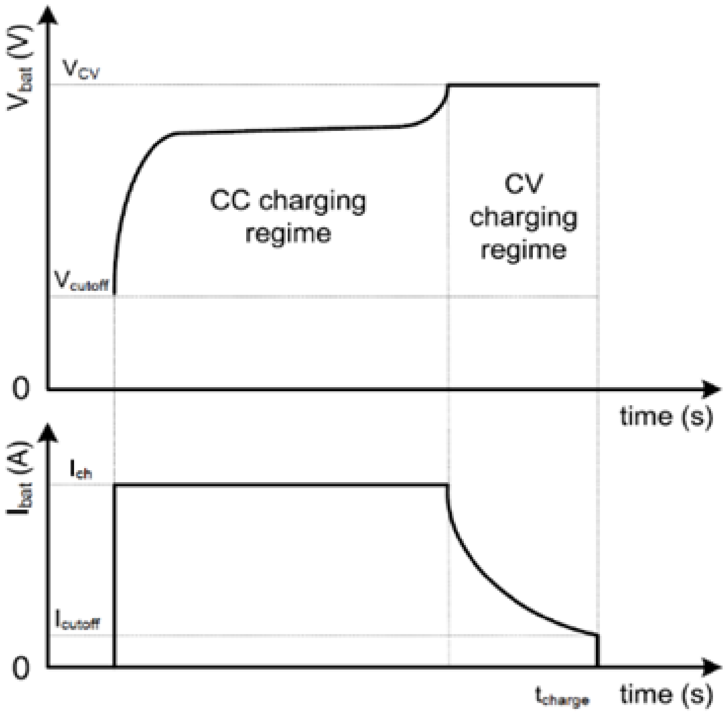

Figure 2.7: Representation of CCCV analysis (taken by [316]).

Section 6. Scheme of samples and codes

In this section we summarize in Table 2.1Table 2.5 the investigated samples and specify the code used in this work to identify them.

Table 2.1: List and preparative details of CNFs samples.

Label	***Description***
Spin	CNFs are only electrospun
Stab	CNFs undergo to stabilization process
Carb	CNFs undergo to carbonization process
600-CNF	CNFs are carbonized at 600°C
700-CNF	CNFs are carbonized at 700°C
750-CNF	CNFs are carbonized at 750°C
800-CNF	CNFs are carbonized at 800°C
900-CNF	CNFs are carbonized at 900°C

Table 2.2: List and preparative details of $LiFePO_4$ samples.

Label	***Description***
$LiFePO_4$	$LiFePO_4$ (commercial powder) for slurry
10%$LiFePO_4$/CNF	self-standing electrode: 10 wt% $LiFePO_4$ (commercial powder) loaded into carbonized CNF
30%$LiFePO_4$/CNF	self-standing electrode: 30 wt% $LiFePO_4$ (commercial powder) loaded into carbonized CNF

Table 2.3: List and preparative details of $Na_3MnZr(PO_4)_3$ samples.

Label	***Description***
8.8-MnZr	citric acid / compound mole ratio = 8.8
3-MnZr	citric acid / compound mole ratio = 3
2-MnZr	citric acid / compound mole ratio = 2
2-MnZr	Slurry electrode: $Na_3MnZr(PO_4)_3$ powder; citric acid/compound mole ratio = 2
h-10%$Na_3MnZr(PO_4)_3$/CNF	self-standing electrode: horizontal setting 10 wt% $Na_3MnZr(PO_4)_3$ powder loaded into carbonized CNF
h-30% $Na_3MnZr(PO_4)_3$/CNF	self-standing electrode: horizontal setting 30 wt% $Na_3MnZr(PO_4)_3$ powder loaded into carbonized CNF
v-30% $Na_3MnZr(PO_4)_3$/CNF	self-standing electrode: vertical setting 30 wt% $Na_3MnZr(PO_4)_3$ powder loaded into carbonized CNF
dd-MnZr\CNF	self-standing electrode: horizontal setting $Na_3MnZr(PO_4)_3$ deposited by dip-drop coating on carbonized CNF

Table 2.4: List and preparative details of $Na_3MnTi(PO_4)_3$ samples.

Label	***Description***
8.8-MnTi	compound /citric acid mole ratio = 8.8
3-MnTi	compound /citric acid mole ratio = 3
2-MnTi	compound /citric acid mole ratio = 2
2-MnTi	Slurry electrode: $Na_3MnTi(PO_4)_3$ powder; citric acid/compound mole ratio = 2
10% $Na_3MnTi(PO_4)_3$/CNF	self-standing electrode: horizontal setting 10 wt% $Na_3MnTi(PO_4)_3$ powder loaded into carbonized CNF
30% $Na_3MnTi(PO_4)_3$/CNF	self-standing electrode: horizontal setting 30 wt% $Na_3MnTi(PO_4)_3$ powder loaded into carbonized CNF
dd-MnTi/CNF	self-standing electrode: horizontal setting $Na_3MnTi(PO_4)_3$ deposited by dip-drop coating on carbonized CNF

Table 2.5: List and preparative details of ZnS-GO samples.

Label	***Description***
ZnS-GO	Powder of ZnS prepared with hydrothermal synthesis, adding graphene oxide (GO)
10%ZnS-CNF/GO	self-standing electrode: horizontal setting 10 wt% ZnS-GO powder loaded into carbonized CNF
30%ZnS-CNF/GO	self-standing electrode: horizontal setting 30 wt% ZnS-GO powder loaded into carbonized CNF

Chapter 3. Results and discussion

In this chapter we report and discuss the results obtained by the the characterization techniques and the electrochemical tests. Firstly, we present the results on pure CNFs samples. Secondly, we investigate the $LiFePO_4$/CNFs self-standing cathode for LIBs: the use of the commercial active material allows us to evaluate the suitable experimental conditions to deposit CNFs sheets displaying homogeneous dispersion of $LiFePO_4$. Then, self-standing $Na_3MnZr(PO_4)_3$/CNFs and $Na_3MnTi(PO_4)_3$/CNFs electrodes for SIBs are investigated. In the case of the $Na_3MnZr(PO_4)_3$/CNFs cathodes, the results obtained by electrospinning deposition with different approaches are discussed. Finally, we present the preliminary results of the ZnS-GO/CNFs anode for SIBs. The electrochemical performance of all the self-standing electrodes were compared to those obtained for tape-casted ones, appositely prepared, to evidence the advantages/disadvantages of the devices.

Section 1. CNFs investigation

The CNFs sheets are synthesized as reported in Figure 3.1. We firstly investigate the influence of the inert gas atmosphere (Ar_2 and N_2) and the thermal treatment temperature of the carbonization process on the morphology and electronic conductivity of CNFs.

Subsection 1 XRPD

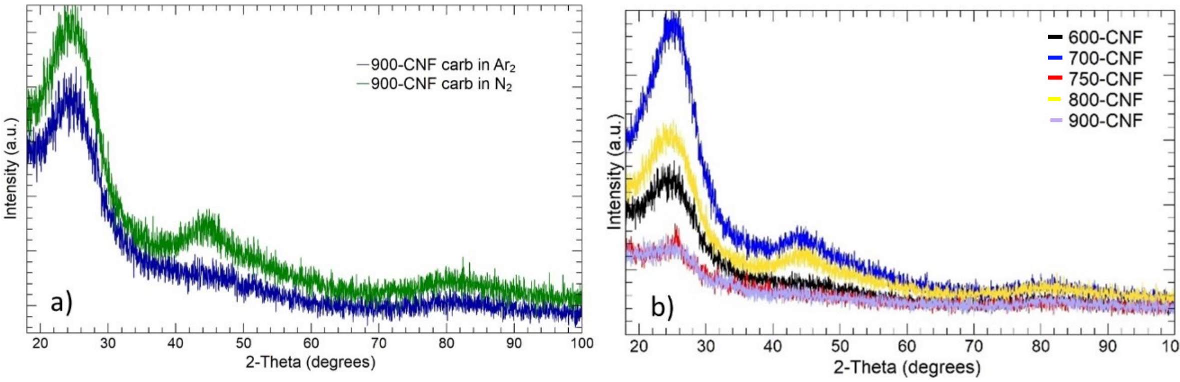

Figure 3.1: X-Ray diffraction patterns of the CNFs sheets carbonized a) at different atmospheres, b) at different carbonization temperature.

The X-Ray powder diffraction analysis is applied to detect the band of not graphitic and graphitic carbons. The Figure 3.1a shows the patterns of CNFs samples carbonized at the same temperature (900°C) under two different atmospheres: N_2 (green) and Ar_2 (blue). Two bands are visible at 25° and 45°, which correspond to the (002) and (101) planes of the turbostratic carbon structure [81,291,321]. The two bands indicate that the main component of carbonized carbon display graphitic structure with well-defined crystallinity [321]. No differences are detected by using the two atmospheres, so we chose Nitrogen to carbonize the sample, as it is cheaper than Argon. The next step is to carbonize CNF sheets at different temperatures: 600°C, 700°C, 750°C, 800°C, and 900°C. The diffraction patterns are shown in Figure 3.1b: the patterns are comparable, and the bands of the graphitic carbon are detected.

Subsection 2 Morphological analysis

The Figure 3.2 displays the SEM images of CNF sheets (9kX and 25kX) treated at the different carbonization temperatures: 600°C, 700°C, 750°C, 800°C, and 900°C. The nanofibers diameters are rather variable and there is not a clear trend with temperature, but it seems to decrease with temperature. At 600°C the diameter size is about 300 nm and achieves values of about 700 nm at 700°C. Then, for higher temperatures, the CNFs diameter decreases: 129.3-242.8 nm, 227.8 nm, and 103.7-309.4 nm at 750°, 800°C and 900°C, respectively. So, increasing the temperatures the nanofibers diameters decrease, as also reported in the literature [322], where the diameter at 800°C is about 274 nm. Finally, at 600°C the nanofibers appear less continuous and more broken compared to other temperatures.

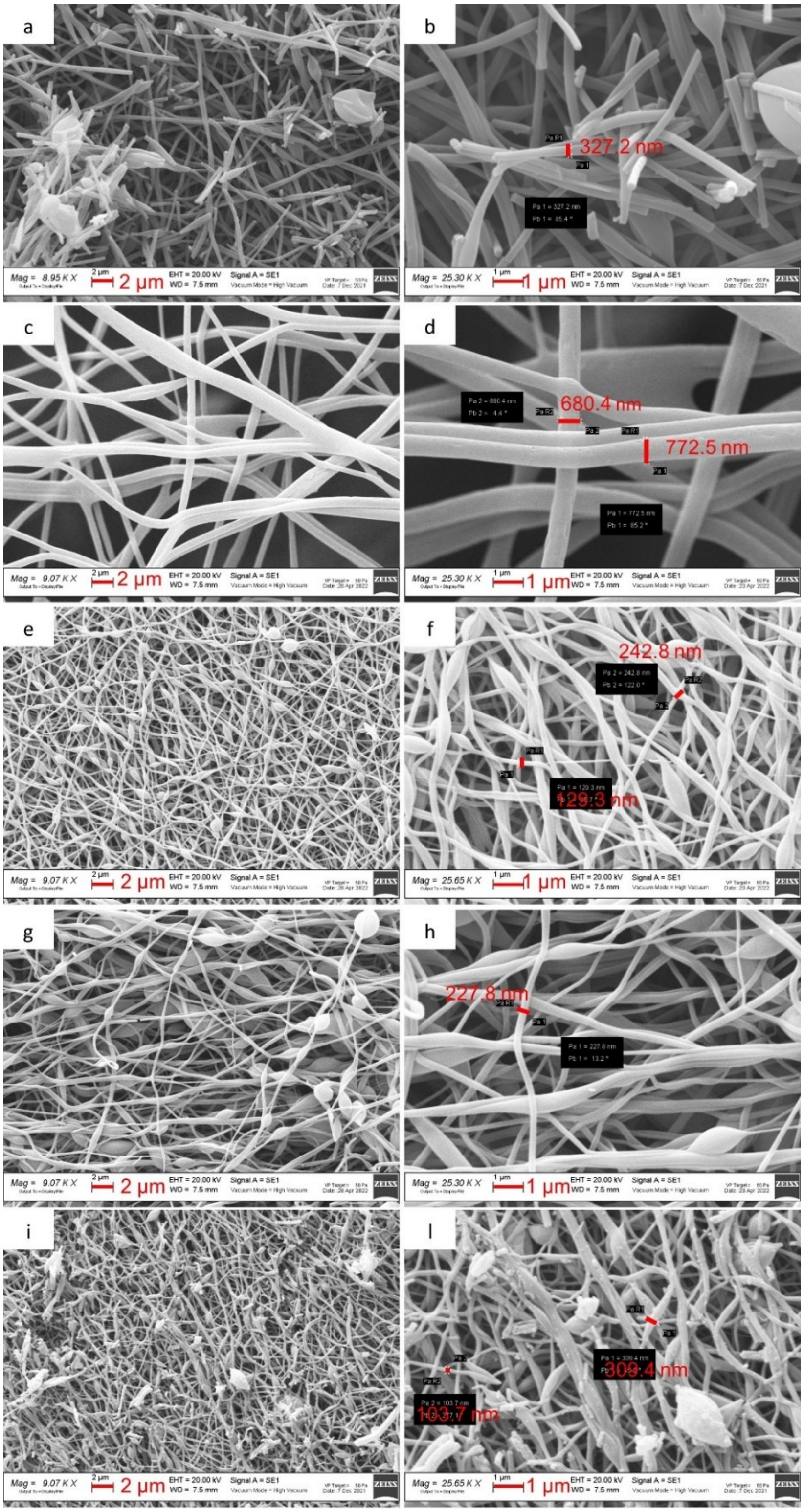

Figure 3.2: SEM images of CNFs carbonized at different temperatures: a,b) 600-CNF; c,d) 700-CNF; e,f) 750-CNF; g,h) 800-CNF; i,l) 900-CNF.

Subsection 3 RAMAN spectroscopy

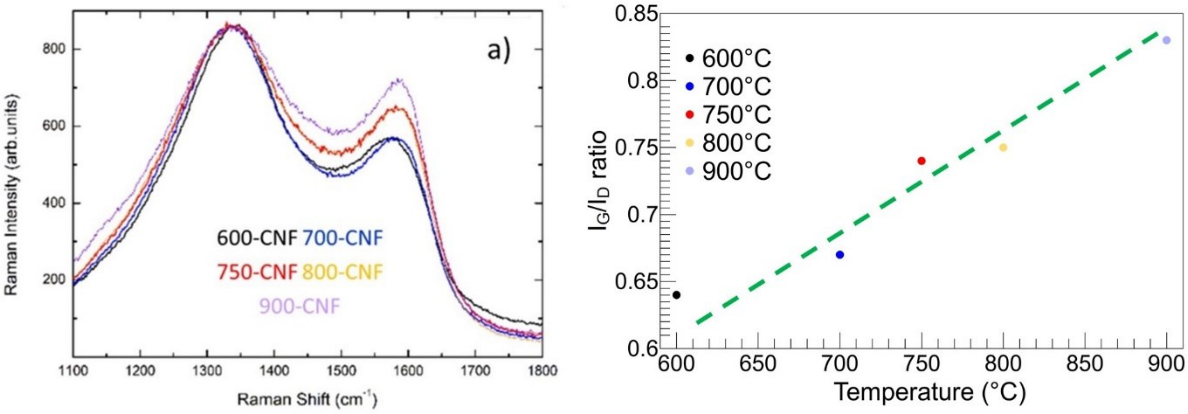

Figure 3.3: Raman analysis of CNFs sheets carbonized at different temperatures: a) Raman spectra (800-CNF yellow line is overwhelmed by the black line 600-CNF) the; b) representation of I_G/I_D of all samples.

The Figure 3.3 reports the RAMAN spectra of CNFs sheets carbonized at different temperatures; we investigate possible changes in the graphitization degree with carbonization temperature [284,291,323]. The highest is the amount of the graphitic carbon, the highest is the electronic conductivity, and this is beneficial for the electrochemical performances. To obtain the graphitization degree, we investigate the I_G/I_D ratio with RAMAN analysis. The RAMAN spectra (Figure 3.3a) display the band at about 1350 cm^{-1} (D band), attributed to the presence of disordered carbon and defects of sp^3 carbon, and the band at about 1600 cm^{-1} (G band), typical of ordered sp^2 graphitic carbon, as reported by ref. [321]. It is well-known that the value of the I_G/I_D ratio evaluated through the integrated areas of the G and D bands gives an indication of the degree of graphitic carbon present in the sample: the higher the I_G/I_D ratio, the higher is the amount of ordered carbon [321]. In Figure 3.3b, the I_G/I_D ratio of each sample is shown: the values of 0.64, 0.67, 0.74, 0.75, and 0.83 at 600°C, 700°C, 750°C, 800°C, and 900°C, respectively, are obtained. The results confirm that the higher carbonization temperature increases the graphitic carbon amount. This trend is already confirmed by Liu et al. reporting a I_G/I_D value of 0.85 and 1.11 at 700°C and 1000°C, respectively [323]. So, we should obtain the best electronic conductivity for 900°C.

Subsection 4 Electrochemical results

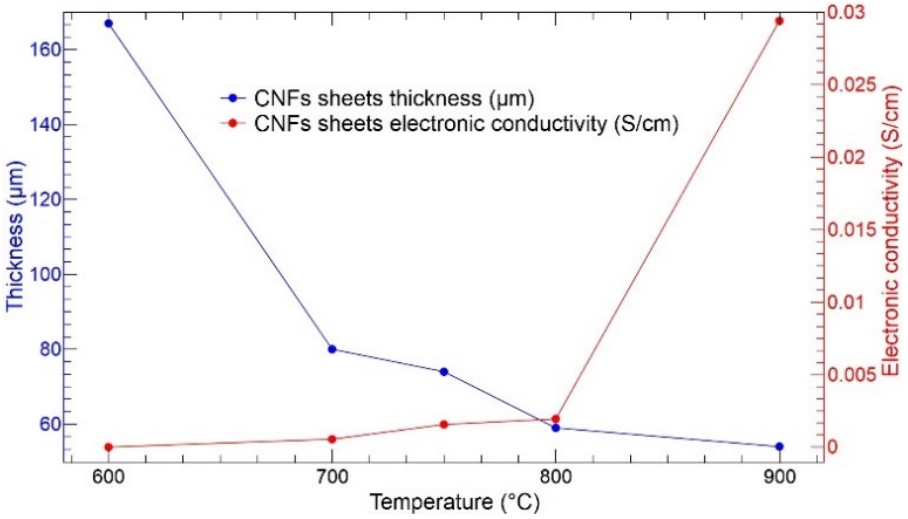

Figure 3.4: Variation of CNFs sheets thickness (blue) and electronic conductivity (red).

The Figure 3.4 shows the electronic conductivity and the nanofiber sheet thickness (evaluated by SEM) trend with the carbonization temperature. The electronic conductivity increases as the carbonization temperature increase. The values of electronic conductivity are 1.76x10^{-6}, 5.45x10^{-4}, 1.56x10^{-3}, 1.94x10^{-3}, and 2.94x10^{-2} S/cm at 600°C, 700°C, 750°C, 800°C, and 900°C, respectively. The results confirm that at higher graphitization/carbonization temperature, higher electronic conductivity is achieved. This trend is also confirmed in the literature for other temperature values [320], where Munajat et al. report electronic conductivity values of 0.13 S/cm, 63.82 S/cm and 73.17 S/cm at 800°C, 1000°C and 1200°C, respectively [284]. So, in our case, the best temperature choice should be 900°C, to prepare the self-standing electrodes benefiting from highly conducive carbon. However, it is necessary to strike a trade-off between a good electronic conductivity and the synthesis temperature/degradation of the active material. Indeed, for too high carbonization temperatures, structural transition/degradation of the active material may occur. Moreover, the higher is the carbonization temperature, the lower the thickness of nanofiber sheets is, and this may give problems during the cells assembling. The trade-off to prepare CNFs with active material powder is found at 750°C, as reported in the following Section 2Subsection 5 of Chapter 2.

Here we report the electrochemical behavior of only CNFs at 900 °C, because we are interested in studying the electrochemical activity of the pure CNFs at their best synthesis conditions and without the presence of active materials.

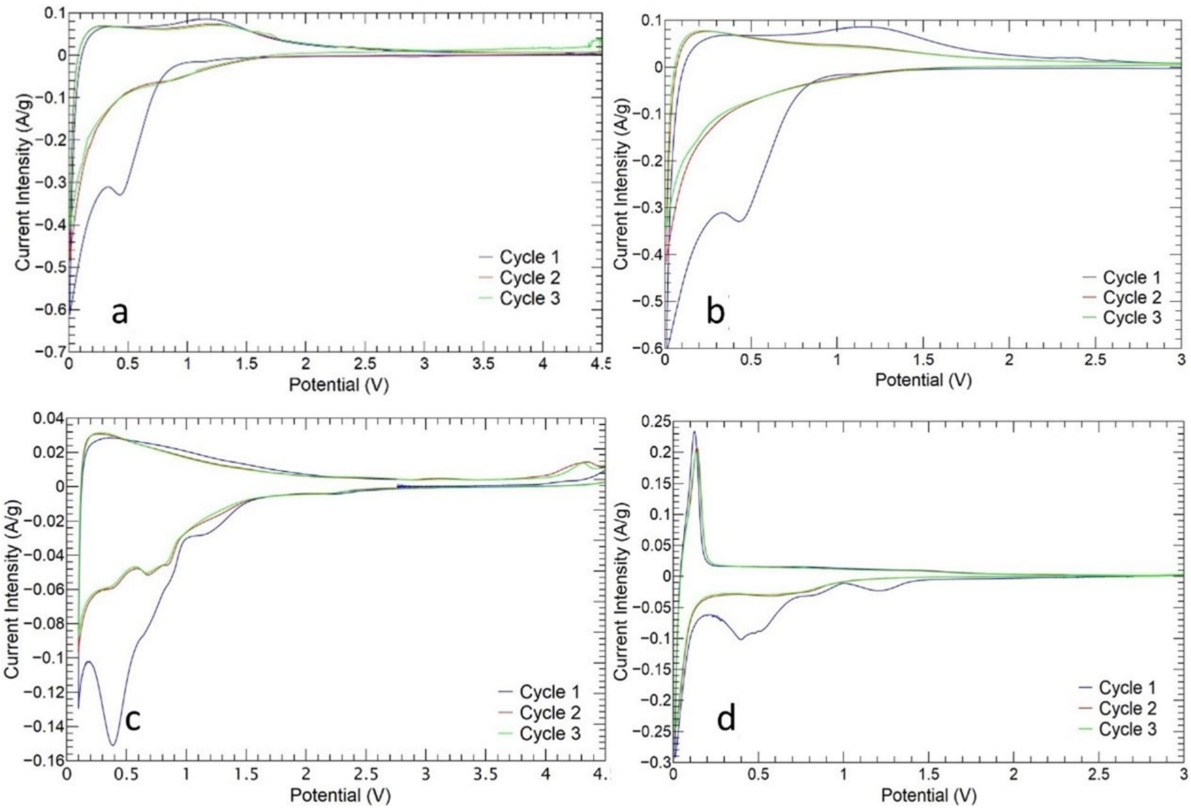

Figure 3.5: Cyclic voltammetry curves of CNF sheets used as electrode: global view of red-ox peaks for a) LIBs and c) SIBs in the voltage range of 0.01V-4.5V, red-ox peaks of CNF anode for b) LIBs and d) SIBs in the voltage range of 0.01V-3V.

Cyclic Voltammetry is applied to pure CNFs, to investigate their electrochemical activity. The CV curves of the pure 900-CNFs in the 0.01-4.5V range for Lithium and Sodium are shown in Figure 3.5a,b and Figure 3.5c,d, respectively. Red-ox peaks are detected only below 3 V, this suggests that 900-CNFs could be used as self-standing anode for both LIBs and SIBs. The anodic CNFs behavior at 750°C, i.e. the temperature chosen to synthesize the self-standing electrodes, is instead elucidated in Section 5 of Chapter 3, together with the study of the ZnS anode.

The LIBs CNF anode shows red-ox anodic and cathodic peaks at 1.16 V and 0.84 V, respectively (Figure 3.5a,b), and the CV matches the results found in literature by Kumar et al [324]. A peak at 0.43 V is detected only in the first cycle, possibly caused by the formation of SEI. As reported in literature [324], the formation of SEI includes the polycarbonate, polyethylene oxide and inorganic products which imply more lithium consumption during the first cathodic cycle [324]. The anodic current intensity achieves 0.1 A/g, while the cathodic one is about -0.33 A/g.

For SIBs' anode (Figure 3.5c,d), the red-ox anodic peak is at 0.13 V with a current intensity of 0.23 A/g and the cathodic one at 0.07 V with a current intensity of -0.15 A/g. In the case of anodic peak, the current intensity of SIBs is higher than the LIBs one, while it is opposite for the cathodic peak. Finally, the first CV cycle of SIBs presents two additional cathodic peaks at 1.20 V and 0.40 V, attributed to the SEI formation as reported by Jin et al. [81]. The potential of SEI formation is different between LIBs and SIBs due to the difference of standard electrode potential [81]. In the case of SIBs, an anomalous variation of anodic red-ox peak can be noted by changing the voltage range of analysis from 0-4.5V to 0-3V (Figure 3.5c,d). The phenomenon is under investigation, and we checked the data reproducibility by further analyses. The behavior is also confirmed by literature results [81], which report similar CV shape in the potential range of 0-2.5V.

The Figure 3.6a and b displays the charge/discharge cycles at different C-rate for LIBs and SIBs, respectively, in the 0.01-3V potential range. In the case of LIBs (Figure 3.6a), the initial discharge capacity is 1308.0 mAh/g for the SEI formation, and after the first cycle there is a capacity loss to 566.5 mAh/g. The capacity is retained in the following cycles. The average discharge capacities are 663.2, 363.4, 289.9, 140.4, 111.5, 67.0, and 57.0 mAh/g at 0.05C, 0.1C, 0.2C, 0.5C, 1C, 2C, and 5C, respectively. The coulombic efficiency is ≥99.8%, and the capacity retention at the end of the measurement is 57.7%. We obtained improved performance compared to the literature, where the initial specific capacity is about 800 mAh/g, with a specific capacity decrease to 260 mAh/g at 0.1C [291]. The irreversible capacity loss is almost half of the initial capacity; this is also verified for literature data. Kumar et al. [324] explain that this phenomenon is due to the following reasons: (i) the lithium consumption during the formation of SEI and (ii) the lithium adsorption on the graphitic layers of CNFs surface (pseudocapacitive storage).

In the case of SIBs (Figure 3.6b), the initial discharge capacity is 300.3 mAh/g for the SEI formation, and after the first cycle there is a capacity loss to 167.6 mAh/g. The following cycles maintain a stable capacity. The average discharge capacities are 188.9, 146.8, 133.9,115.9, 114.9, 61.51, and 35.7 mAh/g at 0.05C, 0.1C, 0.2C, 0.5C, 1C, 2C, and 5C, respectively. The coulombic efficiency is ≥96.8%, and the capacity retention at the end of the measurement is 74.1%. In this case, the results are similar to the literature ones, which report an initial specific capacity of 399 mAh/g, followed by a specific capacity loss to 217 mAh/g at 0.1C, and a coulombic efficiency ≥97% [292].

Both samples could be employed as self-standing anodes.

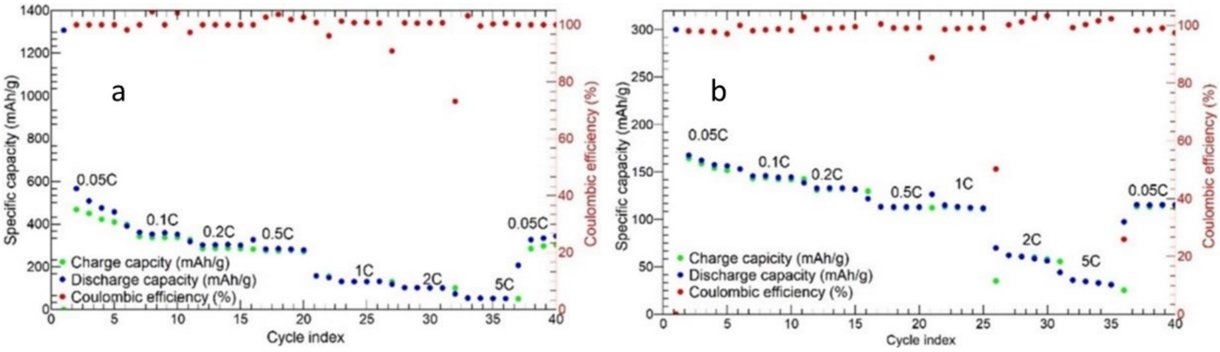

Figure 3.6: Charge\Discharge cycles at different C-rate of CNFs sheets used as a) Lithium-ion anode and b) Sodium-ion anode.

Section 2. Testing CNFs with $LiFePO_4$ cathode

In this section we present the characterization and electrochemical performance of the $LiFePO_4$/CNFs self-standing cathode for LIBs, prepared as reported in Section 2 of Chapter 2. We loaded the commercial $LiFePO_4$ powder into CNFs, by simply adding it to the solution to be electrospun. Proper comparison to the tape-casted counterpart is presented. As reported in Section 8 of Chapter 1, this study is a preliminary investigation of the synthesis conditions to fabricate self-standing electrodes based on active-materials/CNFs composites by electrospinning. So, we pointed at using known and characterized commercial $LiFePO_4$ to make our study independent of the active material's synthesis approach. The commercial $LiFePO_4$ is not carbon-coated.

The following results and discussion are published in a paper of our research group [325].

A scheme of the synthetic approaches is shown in Figure 3.7.

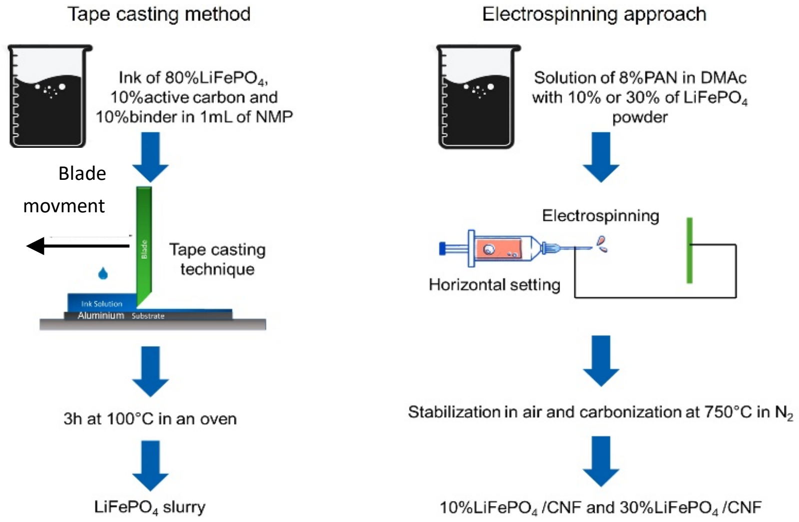

Figure 3.7: Scheme of the synthetic approaches used for the electrodes' preparation.

Subsection 5 XRPD

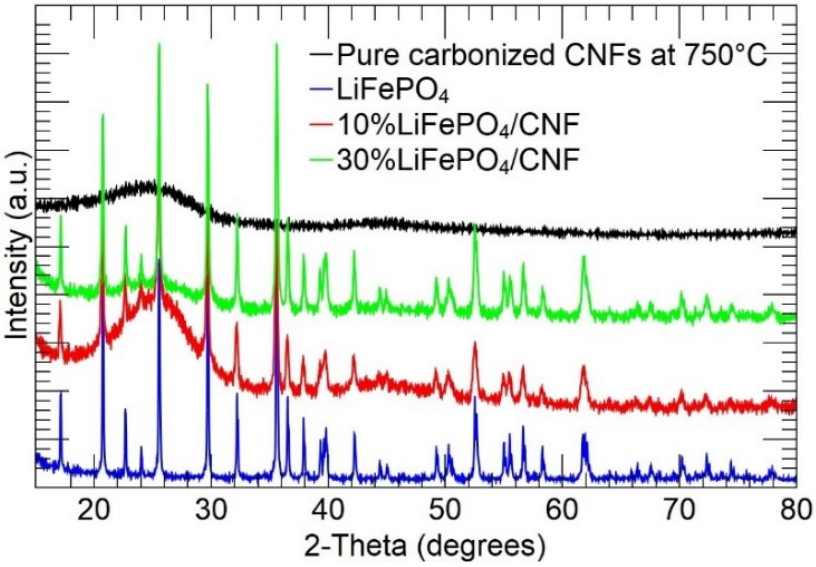

Figure 3.8: X-Ray analysis of $LiFePO_4$ (blue), 10%$LiFePO_4$/CNF (red), 30%$LiFePO_4$/CNF (green), and pure carbonized CNF at 750°C (black) samples.

In the Figure 3.8, the pure CNFs, $LiFePO_4$, 10%$LiFePO_4$/CNF, and 30%$LiFePO_4$/CNF X-ray diffraction patterns are shown. The peaks of the $LiFePO_4$ powder well fit the two-theta positions reported in the JCPDS database (PDF# 40-1499) and the orthorhombic olivine-type crystal structure with *Pnma* space group (a = 10.3268(1) Å, b = 5.9975 Å, c = 4.6945 Å) [326]. The pure CNF sample shows the broad band at about 25° typical of the amorphous phases. The diffraction patterns of $LiFePO_4$/CNF samples display both the amorphous component and the crystalline olivine-type structure, confirming that the $LiFePO_4$

is loaded into CNFs. For the $LiFePO_4$ and $LiFePO_4$/CNF samples, the Rietveld refinement of the diffraction data is carried out, based on the structural model reported in [326]. The refined lattice parameters, cell volume and discrepancy factors are reported in Table S. 1, and the experimental and calculated patterns are compared in Figure S. 1. The refined model fits the experimental diffraction data. The $LiFePO_4$ lattice parameters and cell volume of the $LiFePO_4$/CNF samples well compare to the pure $LiFePO_4$ one. The carbonization process in nitrogen at 750°C does not affect the olivine-type crystal structure. In the Figure S. 2, the X-Ray diffraction patterns of the 10%$LiFePO_4$/CNF and the 30%$LiFePO_4$/CNF samples after electrospinning, stabilization, and carbonization processes are shown. The olivine structure is retained after the thermal treatments applied to synthesize of self-standing electrodes. For this reason, in the following analysis, we show only the results for carbonized $LiFePO_4$/CNF and commercial powder samples, as the carbonized sample is that used for the electrochemical investigation.

Subsection 6 Morphological analysis

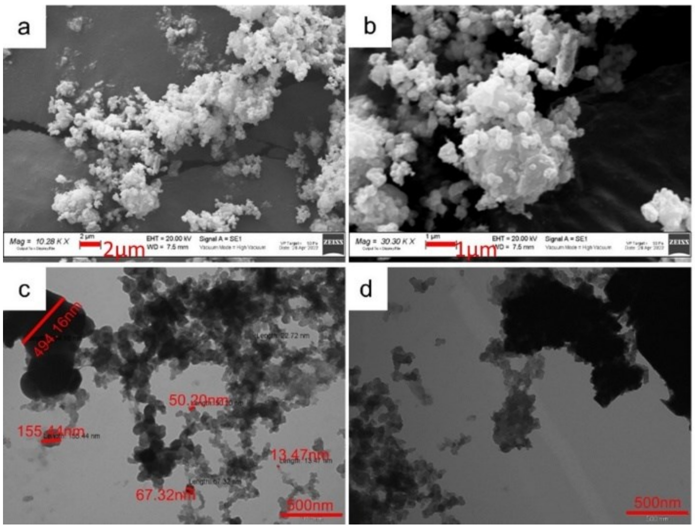

Figure 3.9: a,b) SEM and c,d) TEM image of $LiFePO_4$ sample.

Figure 3.9 shows the SEM and TEM images of the carbon uncoated $LiFePO_4$ powder. The SEM images (Figure 3.9a,b) display aggregates of micrometric size composed by nanometric particles. The agglomerates' surface is defined but irregular and the sub-particles show homogeneous morphology. The TEM micrographs (Figure 3.9c,d) confirm the presence of aggregates of nanoparticles with diameter in the 13-155 nm range.

The Figure 3.10 reports the surface and cross-section SEM images of the self-standing electrodes. The 10%$LiFePO_4$/CNF sample (Figure 3.10a-c) is composed by $LiFePO_4$ micrometric agglomerates spread between and into the CNFs. The agglomerates are constituted by particles comparable in size to the pristine and commercial $LiFePO_4$ powder, shown in Figure 3.9a,b. The CNFs sheet have diameters of about 250 nm and the thickness of the sheet is about 200 µm. The Figure 3.10d-f displays the SEM images of the surface and cross-section of the 30%$LiFePO_4$/CNF sample. Similar to the 10%$LiFePO_4$/CNF self-standing cathode, $LiFePO_4$ agglomerates are greater than 1µm and are distributed into CNF fibers with diameter of about 80 nm. In the 30%$LiFePO_4$/CNF sample the agglomerates of $LiFePO_4$ active material are embedded into CNF diameter and are more evident. The sheet thickness is about 180 µm. The Figure 3.11 reports TEM images of the self-standing electrodes. The TEM analysis confirms the SEM results: the $LiFePO_4$ agglomerates are spread between and within the nanofibers for both the 10%$LiFePO_4$/CNF (Figure 3.11a,b) and 30%$LiFePO_4$/CNF (Figure 3.11c,d) cathodes. In the case of 10%$LiFePO_4$/CNF electrode the agglomerates are composed by sub-particles with nanometric size ranging between 45 and 72 nm, and similar to that detected for the pristine commercial $LiFePO_4$ powder (see Figure 3.9c,d). The CNFs show variable diameter in the 90 - 250 nm range. In the case of the 30%LiFePO$_4$/CNF sample, the agglomerates connect nanofibers and are larger. The CNFs diameter is in the range of 200-330 nm.

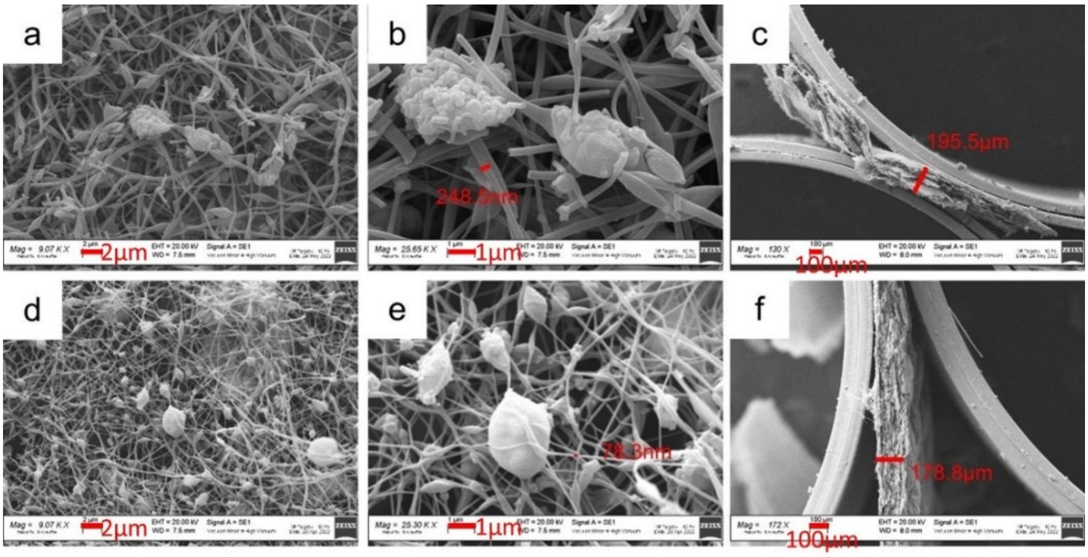

Figure 3.10: SEM images of a,b) surface and c) cross-section of the 10%LiFePO4/CNF sample. SEM images of d, e) surface and f) cross-section of the 30%LiFePO4/CNF sample.

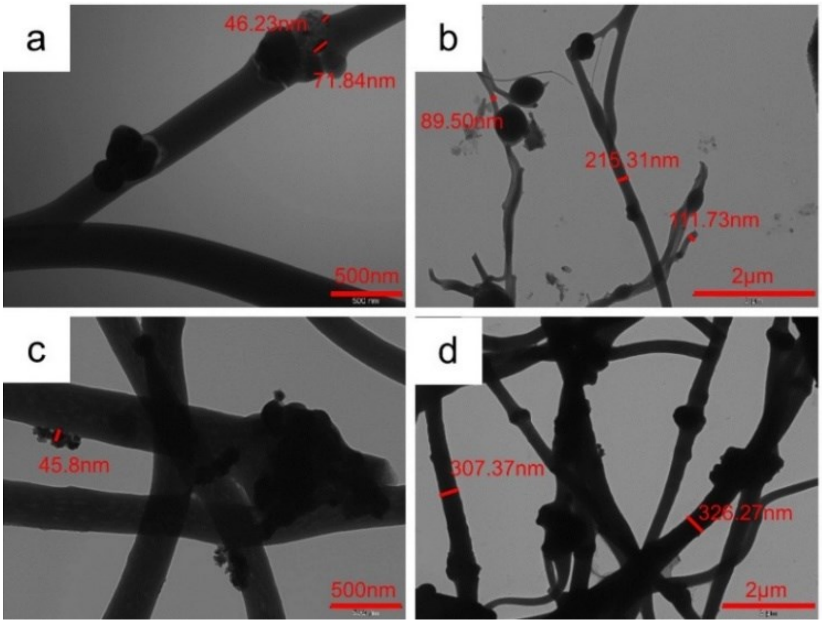

Figure 3.11: TEM images of the a,b) 10%LiFePO$_4$/CNF and c,d) 30%LiFePO$_4$/CNF samples.

The EDS analysis gives insights into the LiFePO$_4$ powder distribution on the surface (Figure 3.12) and within the cross-section (Figure 3.13) of the self-standing cathodes. In both LiFePO$_4$/CNF samples, the P and Fe distribution maps confirm that the agglomerates detected within and between the CNFs are LiFePO$_4$, and the particles are homogeneously distributed along the sheet thickness. This is beneficial to reach good electrochemical performance and it is difficult to be obtained with other routes used to prepare self-standing electrode as, for example, dip-drop coating.

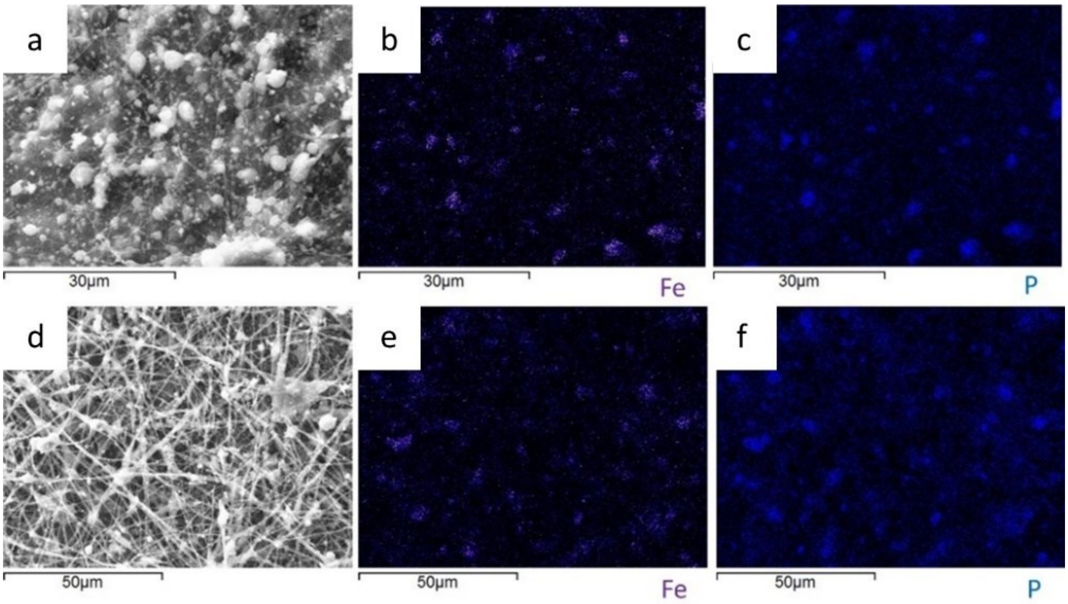

Figure 3.12: EDS analysis. 10%$LiFePO_4$/CNF sample: investigated a) surface and b) Fe and c) P distribution maps; 30%$LiFePO_4$/CNF sample: d) investigated surface and e) Fe and f) P distribution maps.

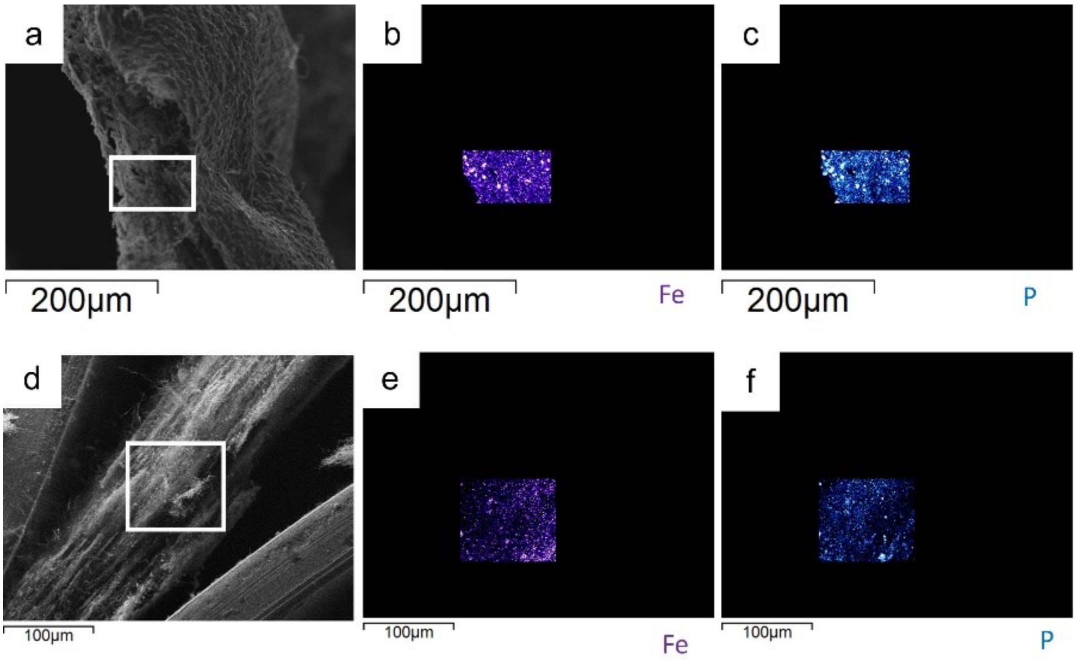

Figure 3.13: EDS analysis. 10%$LiFePO_4$/CNF sample: investigated a) cross-section and b) Fe and c) P distribution maps; 30%$LiFePO_4$/CNF sample: d) investigated cross-section and e) Fe and f) P distribution maps.

Subsection 7 Thermogravimetric and RAMAN analysis

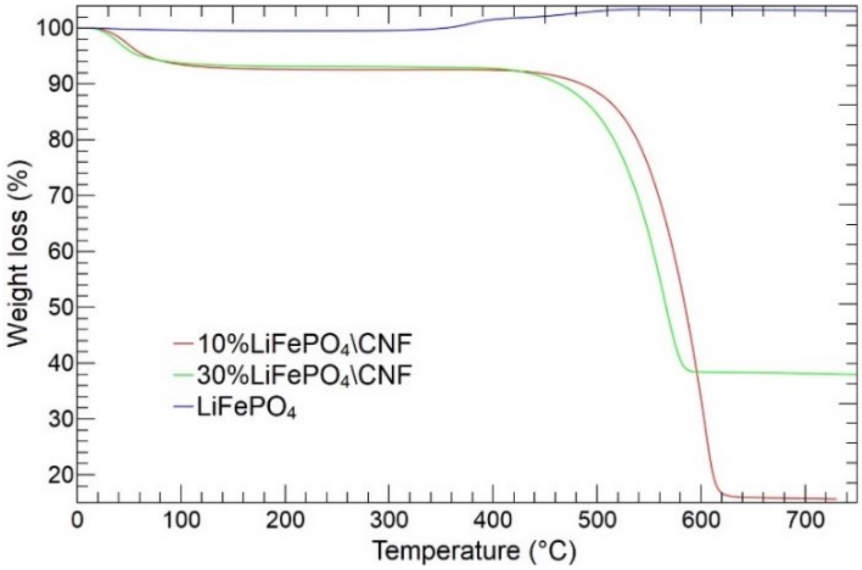

Figure 3.14: TGA curves of 10%LiFePO4/CNF (red), 30%LiFePO4/CNF (green) and c-LiFePO4 (Blue).

The thermogravimetric analysis is applied to evaluate the weight percentage of $LiFePO_4$ loaded into the carbon nanofiber sheets, to be compared to that used in the self-standing electrode synthesis (10 and 30 wt%).

The thermogravimetric curves of the $LiFePO_4$, 10%$LiFePO_4$/CNF, and 30%$LiFePO_4$/CNF samples are shown in Figure 3.14. The TG curve of the $LiFePO_4$ sample well compares to the literature data [327–329]. A small mass loss is detected below 200°C, due to the release of adsorbed water, then a mass gain occurs in the 350-600°C temperature range, reaching the final mass value of 103.4 wt%. The mass increase is attributed to the $LiFePO_4$ oxidation in air to form $Li_3Fe_2(PO_4)_3$ and Fe_2O_3 [327–329]. In the case of the $LiFePO_4$/CNF samples, a little mass loss occurs below 200°C for adsorbed water release, then in the 400-650°C temperature range a relevant mass loss is detected. This mass changes are due to the simultaneous occurrence of the thermal phenomena: (i) the oxidation of the carbon component and CO_2 release (mass loss) and (ii) $LiFePO_4$ oxidation (mass uptake) [329]. The carbon amount in the self-standing electrodes is calculated as the difference between the final masses of the $LiFePO_4$ powder (103.4 wt%) and the $LiFePO_4$/CNF samples (15.65 and 37.93 wt% for the 10%$LiFePO_4$/CNF and 30%$LiFePO_4$/CNF samples, respectively). Hence, the active material amount into the CNFs sheets can be evaluated. The $LiFePO_4$ content is 12.25 and 34.53 wt% in the 10%$LiFePO_4$/CNF and 30%$LiFePO_4$/CNF samples, respectively, and the values well compare to those loaded in the synthesis.

Raman spectroscopy aims to evaluate the carbon coating and to further assess the crystalline quality of the different samples. In Figure 3.15 the Raman spectra of the 10%$LiFePO_4$/CNF and 30%$LiFePO_4$/CNF samples are shown in the 200-1800 cm^{-1} range: the CNF sample is also shown for comparison. In the inset the Raman spectrum of commercial $LiFePO_4$ powder is reported as well.

For $LiFePO_4$ sample we obtain a Raman spectrum perfectly matching the expected Raman yield of the olivine structure. The main Raman band at 950 cm^{-1} is attributed to the ν_1 intramolecular stretching mode of PO_4^{3-} unit. Close to this mode, at slightly higher energies, the ν_2 *and* ν_3 modes caused by symmetric and asymmetric P–O bonds vibrations are visible [330,331].

Below 400 cm^{-1} the Raman signals are attributed to the external modes of the olivine structure, composed principally of whole body translatory and vibrational motions of the PO_4^{3-} ions and translatory motion of the Fe^{2+} ions. Between 400 and 700 cm^{-1} other Raman features are detectable, and they are caused by bending vibrations of PO_4^{3-} and the mixing of other modes. All these characteristics clearly indicate a well-ordered olivine structure. When the Raman is collected from carbon coated samples the behavior changes. The signal from $LiFePO_4$ is totally overwhelmed by the intense carbon-related Raman features, with two broadened bands peaked at about 1350 and 1590 cm^{-1}, and attributed to the sp^3 type amorphous carbonaceous material (D-mode) and to the sp^2 graphite-like (G band). The absence of olivine Raman signal is not surprising because of the different

Raman cross-sections, and the fact that the carbon coating prevents the excitation of inner olivine structure.

It is interesting to compare the ordered and disordered carbon qualities of different samples evaluating the intensities of G and D modes. Indeed, it is well-known that the integrated intensity ratio of G and D bands is a choice parameter to verify the quality of carbon materials [332]. In this case the I_G/I_D ratio for 10%$LiFePO_4$/CNF and 30%$LiFePO_4$/CNF is 0.71 and 0.68, respectively. The values are very similar to that obtained from CNF sample (I_G/I_D =0.67).

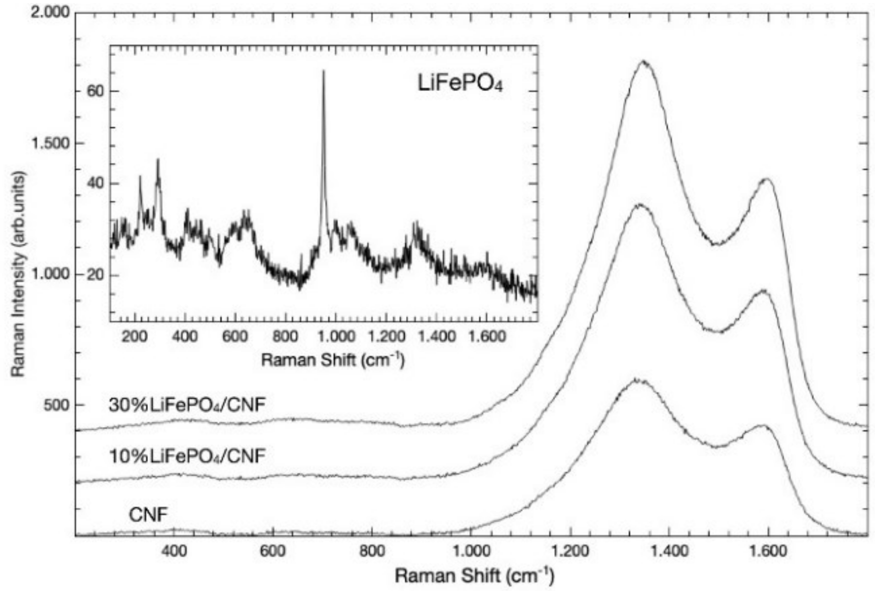

Figure 3.15: Raman spectra of $LiFePO_4$, 10%$LiFePO_4$/CNF, 30%$LiFePO_4$/CNF, and pure CNF carbonized at 750°C.

Subsection 8 Electrochemical results

The $LiFePO_4$ presents one well-known red-ox peak caused by the reduction and oxidation of Fe(II)/Fe(III) pair. The red-ox reactions are [333]:

$$Oxidation:\ xLiFePO_4 \rightarrow xFePO_4 + xLi^+ + xe^-$$

Eq. 3.1

$$Reduction:\ FePO_4 + xLi^+ + xe^- \rightarrow xLiFePO_4 + (1-x)FePO_4$$

Eq. 3.2

The mechanism of Li insertion has been extensively investigated [334]. Briefly, the iron is the transition metal ion donating or accepting electrons. When the Fe(II) is oxidized to Fe(III) the lithium ions are extracted, while the reduction of Fe(III) to Fe(II) leads to the insertion of metal alkali ions.

Cyclic voltammetry

The Figure 3.16 reports the CV curves and charge/discharge profiles of the first three cycles at 0.05C for the $LiFePO_4$, 10%$LiFePO_4$/CNF, and 30%$LiFePO_4$/CNF samples. The anodic/cathodic peaks of the Fe(II)/Fe(III) red-ox pair are detected at 3.56/3.29 V, 3.50/3.37 V and 3.50/3.35 V, respectively, and these peaks match the respective voltage plateaus in their charge/discharge profiles. The protocol exploited for charge/discharge profiles is described in Subsection 14 of Chapter 2. In the case of $LiFePO_4$ slurry electrode, the CV cycles and the charge/discharge curves are quite overlapped, confirming a good electrochemical reversibility. The current intensity of anodic/cathodic peak is 0.35/-0.27 A/g, and the ΔV is 270 mV, suggesting a significant polarization phenomenon. For the 10%$LiFePO_4$/CNF and 30%$LiFePO_4$/CNF self-standing samples, the peaks' current intensity increases as cycles increase, indicating a progressive activation of active particles due to the Li ions insertion/deinsertion, as reported in literature [335]. It is confirmed by the charge/discharge curves, too. The current intensities for the two samples are 0.045/-0.030 A/g and 0.24/-0.20 A/g, respectively: the values are lower than for the slurry electrode, consistent with the lower active material amount (12.25 and 34.53 wt%) present in the self-standing electrodes. For both free-binder samples the ΔV is in the 130-150 mV range, lower than the slurry one, underling a smaller overpotential and polarization in the case of self-standing cathodes. Finally, the Figure 3.16d presents an anomalous behavior of charge/discharge profiles for 10%$LiFePO_4$/CNF with respect to other samples studied with the same protocol. The reason for this is unclear, and need further investigations. The phenomenon seems to be reflected by the values of specific capacity in Figure 3.18b.

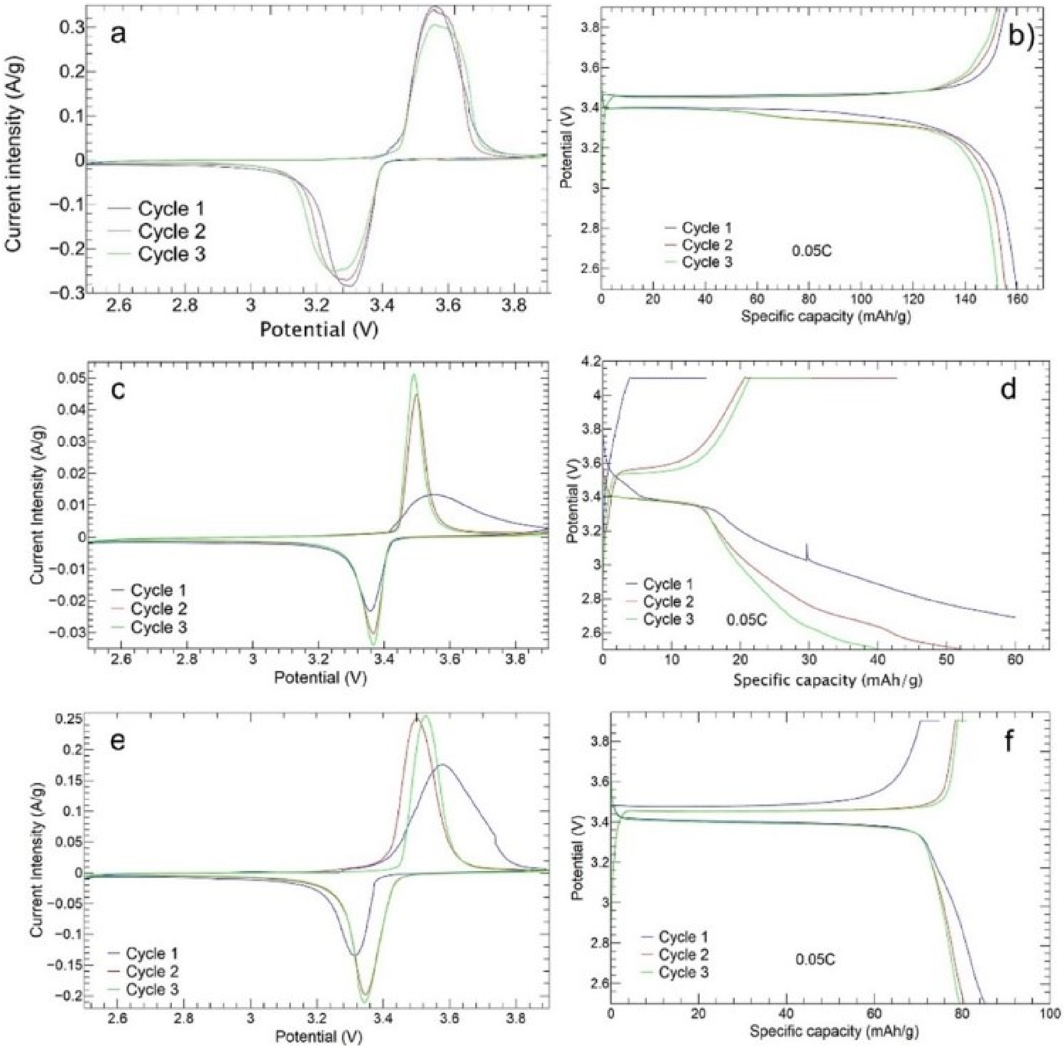

Figure 3.16: Cyclic voltammetry and charge/discharge curve of a,b) $LiFePO_4$; c,d) 10%$LiFePO_4$/CNF; e,f) 30%$LiFePO_4$/CNF.

The Figure 3.17a,c,e report the cyclic voltammetry of both slurry and self-standing electrodes at different scan rates: 0.1 mV/s, 0.2 mV/s, 0.5 mV/s and 1 mV/s. The Figure 3.17b,d,f display the capacitive and diffusive contributions at each scan rate for the three samples. The data are analyzed to calculate the lithium-ion diffusion coefficient and the alkali metal-ion faradaic contribution (diffusion control) and non-faradaic one (pseudo-capacitance control) due to the creation of the double layer on the material surface. The relation between redox current i_p (A) and scan rate ν (mV/s) is:

$$\mathrm{i_p} = \mathrm{k_1}\nu + k_2\sqrt{\nu}$$

Eq. 3.3

here v is the scan rate, i_p is the peak current, k_1 and k_2 are adjustable parameters [336]. The diffusion contribution is controlled by the square root term thanks to the evaluation of the i_p by Randles-Sevick equation:

$$i_p = 2.69 \times 10^5 n^{\frac{3}{2}} AC\sqrt{D\nu}$$

Eq. 3.4

with n number of transferred electrons, A area, C Li^+ concentration and D diffusion coefficient. The quantities are given in the CGS unit system and at standard conditions. Using Eq. 3.3 and Eq. 3.4, the diffusion coefficient D is calculated by evaluating the k_2 term for the three samples.

The slurry $LiFePO_4$ electrode (A = 0.78 cm^2) shows diffusion coefficients for anodic and cathodic peak of 4.66×10^{-12} cm^2/s and 3.34×10^{-12} cm^2/s, respectively, which is consistent with the literature ones of the order of 10^{-13} and 10^{-14} cm^2/s [336,337]. The same analysis can be carried out for the 10%$LiFePO_4$/CNF and 30%$LiFePO_4$/CNF self-standing cathodes as well. The free-standing electrodes should benefit of the 3D structure, suitable to increase the active material surface. Indeed, the effective areas A cannot be easily evaluated, and we estimate an equivalent cathodic and anodic diffusion coefficient by using the area of the electrode section, as already made in literature with other self-standing electrodes [338]. For the 10%$LiFePO_4$/CNF the anodic diffusion coefficient is 5.08×10^{-14} cm^2/s, while the cathodic one is 1.82×10^{-14} cm^2/s. The result is consistent with the lower amount of the active material, as the Fe(II)/Fe(III) red-ox pair gives lower current intensity than the slurry counterpart (see Figure 3.17a and c). However, the anodic and cathodic diffusion coefficients of the 30%$LiFePO_4$/CNF cathode are 1.98×10^{-11} cm^2/s and 1.36×10^{-11} cm^2/s, respectively, comparable to the literature's values in the range of 10^{-11}-10^{-14} cm^2/s, depending on how much carbon additive is present in the sample [339,340]. D values are enhanced of about one order of magnitude compared to the slurry electrode. The result is also aligned with the comparable values of the current intensity (Figure 3.17a,e). The advantage of a higher active surface which is reached with the 30% of active material powder into the CNFs self-standing structure, compared to the 80% of the slurry electrode, is envisaged.

Figure 3.17b,d,f compares the diffusion- and reaction- (capacitive contribution) control at different CV scan rates of the slurry and free-standing cathodes. The 10%$LiFePO_4$/CNF and 30%$LiFePO_4$/CNF samples show higher diffusion contribution at high scan rate values compared to the slurry one, as expected in the presence of the very porous CNF sheets. The non-woven nanofibers permit an easy electrolyte diffusion which promotes the contact with active material particles [244]. The easy permeation of the electrolyte in the CNFs is also qualitatively confirmed by the contact angle analysis shown in Figure S. 3: a drop of 5 µL electrolyte completely permeates the support within 50 ms, contrary to the slurry electrode which displays a contact angle in the range of 32°-45°, as reported in literature by Wang and coworkers [341]. Moreover, the 30%$LiFePO_4$/CNF shows a diffusion control gain of about 18% at the highest scan rate (1m V/s) with respect to the tape-casted, confirming the results of coefficient diffusion. Notably, for all electrodes the anodic and cathodic peaks clearly move toward right and left, respectively, as the scan rate increases, but this trend is lowered for self-standing cathodes (Figure 3.17a,c,e). The Fe(II)/Fe(III) red-ox peak overpotentials of $LiFePO_4$ sample are 303 mV, 486 mV, 774 mV and 1237 mV as scan rate increases, *vs.* 124 mV, 143 mV, 189 mV and 236 mV for the 10%$LiFePO_4$/CNF, and 185 mV, 239 mV, 335 mV and 422 mV for the 30%$LiFePO_4$/CNF. This indicates more reversible redox processes in the free-standing cathodes than in the tape-casted one.

The electrochemical impedance spectroscopy (EIS) analysis is performed on the cycled cathodes, and the Nyquist plot and the equivalent circuit are shown in Figure S. 4. The improved electrochemical performance of the 30%$LiFePO_4$/CNF cathode is confirmed by the smaller charge-transfer resistance (147.15 Ω vs. 232.70 Ω and 239.94 Ω for the 12.3 wt% self-standing and the tape-casted electrodes) and faster charge-transfer at the electrode-electrolyte interface. The obtained charge-transfer resistances fairly compared to the literature ones [342]. The larger slope of Warburg impedance for 30%$LiFePO_4$/CNF cathode suggests a more favorable Li ion-transport in this self-standing electrode.

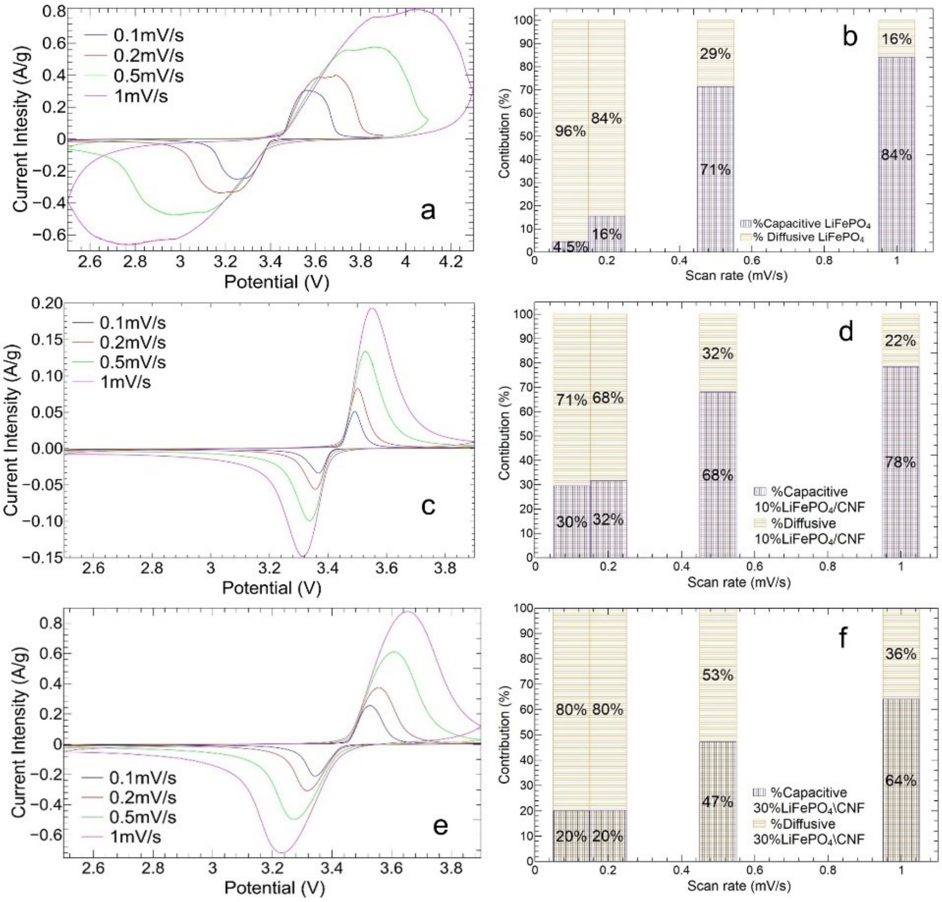

Figure 3.17: CV at different C-rate and capacitive/diffusive contributions of a,b) $LiFePO_4$; c,d) 10%$LiFePO_4$/CNF; e,f) 30%$LiFePO_4$/CNF.

Charge and discharge cycles

The charge/discharge data for $LiFePO_4$, 10%$LiFePO_4$/CNF and 30%$LiFePO_4$/CNF samples are shown in Figure 3.18. The protocol exploited for charge/discharge cycles is described in Subsection 14 of Chapter 2. The slurry cathode (Figure 3.18a) gives initial charge and discharge capacities of 155.48 and 159.84 mAh/g, respectively. The average discharge capacities are 153.07, 136.62, 123.40, 102.05, 80.10, 68.04, 52.95, 38.56 and 8.21 mAh/g at 0.05C, 0.1C, 0.2C, 0.5C, 1C, 2C, 5C, 10C and 20C, respectively. A capacity retention of 80% and coulombic efficiency ≥99% are obtained at the end of the measurement.

The 10%$LiFePO_4$/CNF (Figure 3.18b) exhibits an initial charge and discharge capacity of 48.20 and 77.99 mAh/g, respectively. The average discharge capacities of 48.17, 27.34, 25.27, 22.88, 20.36, 17.87, 13.97, 11.20, and 7.96 mAh/g at 0.05C, 0.1C, 0.2C, 0.5C, 1C, 2C, 5C, 10C and 20C, respectively are obtained. The initial capacity is completely recovered with a coulombic efficiency ≥99% at the end of the measurements. Differently from the $LiFePO_4$ cathode, the self-standing 10%$LiFePO_4$/CNF one shows increased capacity in the first five cycles at 0.05C, confirming the availability of progressively activated particles for lithiation/delithiation, as suggested by CV analysis (Figure 9c,d), and reported by Bachtin et al. [335] presenting an initial peak current of 0.01mA and finishing with a current peak of 0.04mA at 100th cycles.

The 30%$LiFePO_4$/CNF shows an initial charge capacity of 74.90 mAh/g and a discharge capacity of 81.80mAh/g at 0.05C (Figure 3.18c). The average discharge capacities at 0.05C, 0.1C, 0.2C, 0.5C, 1C, 2C, 5C, 10C, and 20C are 85.15, 77.81, 74.52, 68.14, 61.68, 54.44, 43.11, 34.94, and 25.58 mAh/g, respectively. The capacity retention is 96.99% and the coulombic efficiency is ≥99.5%. As for the 10%$LiFePO_4$/CNF sample, the 30%$LiFePO_4$/CNF cathode shows an increasing value of capacity in the first five cycles at 0.05C (see also Figure 3.16e,f).

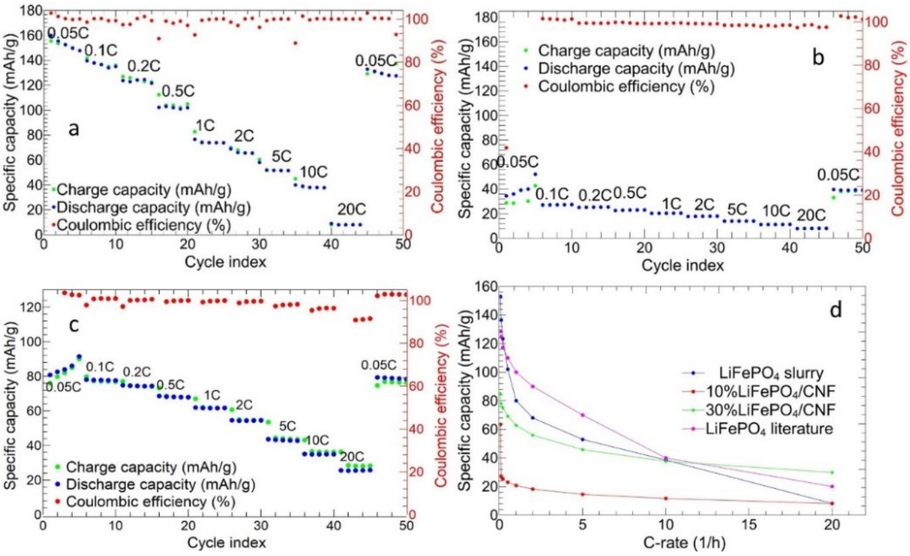

Figure 3.18: Charge/discharge cycles at different C-rate of a) $LiFePO_4$; b) 10%$LiFePO_4$/CNF; c) 30%$LiFePO_4$/CNF, and d) comparison of electrochemical performance.

The Figure 3.18d reports plots of the average discharge capacities vs. C-rate for the three investigated cathodes. The $LiFePO_4$ slurry electrode exhibits higher capacity values below 5C. The capacity is similar at 20C for the 10%$LiFePO_4$/CNF and at 10C for the 30%$LiFePO_4$/CNF cathode. While the literature slurry data taken from [343] are even higher than other samples but not at 20C, where the 30%$LiFePO_4$/CNF free-standing cathode shows the best performances. Moreover, the 30%$LiFePO_4$/CNF displays a slower capacity loss than other samples by changing the C-rate. These improved performances are also confirmed by the higher diffusion coefficient evaluated by the CV analysis at different scan rates. To conclude, the 30%$LiFePO_4$/CNF exhibits (i) a slower capacity fading increasing the C-rate, (ii) good reversibility and stability of Lithium storage and (iii) promising performances also at C-rates higher than 5C. The 30%$LiFePO_4$/CNF good cycling at high C-rate is due to the CNFs 3D porous network which guarantees an easier diffusion of Li-ions. The consequence is a high-power density, as reported in literature [244], too. Compared to self-standing $LiFePO_4$ cathode at 40% of active material reported in the literature [335] with a specific capacity of about 10mAh/g at 1C, we show at the same C-rate a greater average value of 20.36 mAh/g for 10%$LiFePO_4$/CNF and 61.68mAh/g for 30%$LiFePO_4$/CNF. Moreover, considering the study of Bachtin and coworkers [344], we can compare similar self-standing electrodes with $LiFePO_4$ commercial powder. Their capacity values at 1C fairly compares to ours, for not chemically activated electrodes [344]. In the case of the 10%$LiFePO_4$/CNF sample, the poorer electrochemical performances than the 30%$LiFePO_4$/CNF may be due to the very low amount of active material powder. Based on this, we carried out the long-term cycling only on the 30%$LiFePO_4$/CNF and the $LiFePO_4$ tape-casted cathodes.

$LiFePO_4$ is a well-known cathode for lithium-ion batteries in both forms of slurry and self-standing electrodes, and we have specifically chosen it to investigate the CNFs role in free-binder cathodes. Hence, in the literature we find different procedures to prepare and test the $LiFePO_4$ cathode, and in the following we compare the electrochemical performances, to demonstrate that our results are in the range of the literature ones. Bacthin et al. [342] present $LiFePO_4$–CNF–MWCNT composites where $LiFePO_4$ is prepared in situ; the composites display very promising electrochemical performance with a specific capacity of 123 mAh/g at 2C, vs. 54 mAh/g of our 30%$LiFePO_4$/CNF at the same C-rate. In another study [328] the electrode shows 85 mAh/g at 0.5C, or a specific capacity of 100.9 mAh/g at 5C [345]. However there are some cases where the binder-free cathodes display specific capacity of 37 mAh/g at 2C [346], , lower than the value of 54 mAh/g at 2C of our 30%$LiFePO_4$/CNF sample. To conclude, the electrochemical performance is deeply affected by the preparation method of the self-standing electrode, by the active material/carbon ratio in the sample, and by the temperature of the carbonization process [328], which influence the graphitization degree and so the electronic conductivity. In many studies [328,342,345] the $LiFePO_4$ active material is synthesized in situ, preparing a mixture of $LiFePO_4$ precursors and polymer. This approach gives binder-free cathodes with higher amount of $LiFePO_4$ active material, and nanometric particles with poor agglomeration, and this is beneficial for the electrochemical performance. In addition, the carbonization temperature is fixed at 800°C leading to a higher value of electronic conductivity. In the study of Bacthin at al. [342] the electrochemical performances are further improved by adding MWCNT to $LiFePO_4$-CNFs. To conclude, our study demonstrate that satisfactory electrochemical performance, which results in the range of the $LiFePO_4$ literature scenario, can be obtained by (i) a simple and feasible procedure based on dispersing $LiFePO_4$ powder in the polymeric solution to be electrospun, (ii) loading into CNFs only the 37 wt% of active material, lower than the literature ones, and (iii) using a lower carbonization temperature as for the ref. [346].

In Figure 3.19a long cycling of $LiFePO_4$ tape-casted electrode is reported. It is cycled for five cycles at 0.05C, two-hundred cycles at 0.2C and finally fifty cycles at 1C. The average coulombic efficiency is ≥97%, and the initial discharge/charge capacities are equal to 145.4/147.6 mAh/g. The specific capacity progressively decreases increasing the cycle index and achieves negligible values at the 230th cycle at 1C. The long charge/discharge cycling for the 30%$LiFePO_4$/CNF is shown in Figure 3.19b. The cathode is tested at 0.05C, 0.2C, 1C, 5C, 10C and 20C for 5, 50, 1000, 100, 100, and 50 cycles, respectively. The initial charge and discharge capacities are 71.3 and 77.3 mAh/g, and the average coulombic efficiency is ≥99%. Even though the initial capacity is lower than the tape-casted electrode, the self-standing cathode exhibits a slower capacity loss and demonstrates electrochemical activity at C-rate higher than 0.2C, too. The average value of discharge capacities at 1C, 5C, 10C, and 20C are 35.2 mAh/g, 22.0 mAh/g, 16.9 mAh/g, and 14.9 mAh/g, and the value of 57.4 mAh/g is obtained for further cycling (10 cycles) at 0.05C. The capacity retention at the end of the measurement is 74.3%, while it is 35.4% at the end of the 1000 cycles at 1C. This is a good long cycling result if compared to the $LiFePO_4$ self-standing cathodes reported in the literature [328,335,342,345], where capacity values of 30-40 mAh/g are obtained over 200 cycle at 0.5C: the cell is tested for 750 cycles at 0.05C, 0.1C, 0.2C and 0.5C. In our work, similar capacity values are obtained at 1C over 1000 cycles, and the electrode can be further cycled at higher C-rate up to 20C. So, we can conclude that the self-standing electrode with only 34.53 wt% of active material shows a longer lifespan than the slurry one. It is due to the CNFs support which limits the volume and structural changes of the active material and guarantees a good permeation of the electrolyte and a higher electronic conductivity.

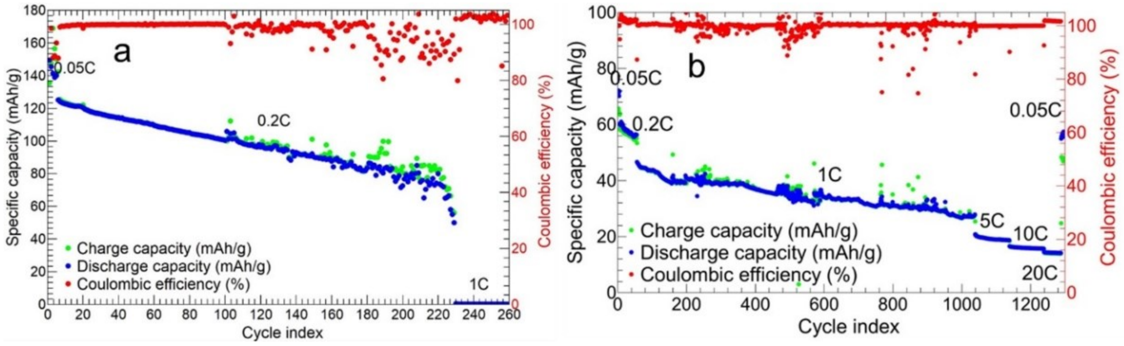

Figure 3.19: Long charge/discharge cycles of a) $LiFePO_4$ tape-casted, and b) 30%$LiFePO_4$/CNF self-standing cathodes.

Section 3. $Na_3MnZr(PO_4)_3$ self-standing cathode

In this section we report the results of our investigation of $Na_3MnZr(PO_4)_3$ powders synthesized via sol-gel with different amount of citric acid, to evaluate the proper quantity which gives a homogeneous carbon coating of the $Na_3MnZr(PO_4)_3$ particles. Then, we report the characterization and electrochemical investigation of the self-standing cathodes. The electrochemical performances are compared to those obtained for the tape-casted electrode, to put into light the benefits and drawbacks of each approach.

Subsection 9 Optimization of the $Na_3MnZr(PO_4)_3$ carbon coating

We synthesized $Na_3MnZr(PO_4)_3$ powders with different amounts of citric agent as chelating agent in the sol-gel synthesis, as reported in Subsection 1 of Chapter 2. The tested samples are 8.8-MnZr, 3-MnZr and 2-MnZr (see Table 2.3 of Chapter 2).

X-Ray powder diffraction analysis

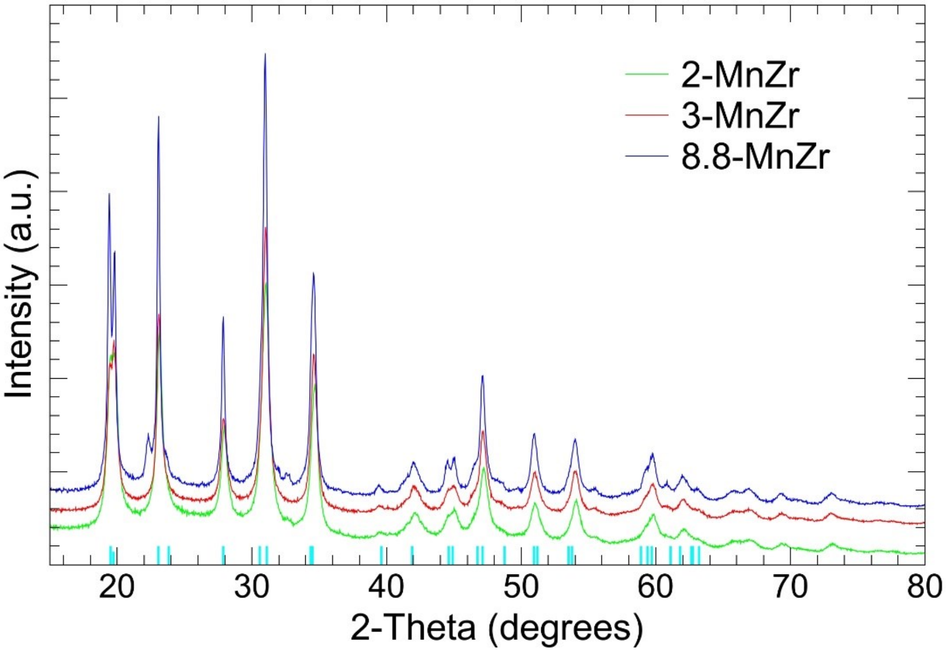

Figure 3.20: Diffraction patterns of $Na_3MnZr(PO_4)_3$ powder with different amount of citric acid in the sol-gel synthesis. The peaks positions of the $Na_3MnZr(PO_4)_3$ compound (JCPSD Database: PDF# 041-0504) are also shown (light blue bars)

Table 3.1: Lattice parameters and discrepancy factors of 2-MnZr sample, obtained by Rietveld refinement.

Lattice parameters	***2-MnZr***
a (Å)	8.970(1)
c (Å)	22.585(5)
V(Å^3)	175.45
Crystallite size (nm)	30(1)
R_{wp}	5.51
gof	1.41

In the Figure 3.20, the patterns of the $Na_3MnZr(PO_4)_3$ samples with different citric acid amount are shown. All patterns display the typical *NaSICON* Rhombohedral structure with $R\overline{3}c$ space group (a= 8.9689Å, c= 22.585Å), and the different quantity of citric acid does not influence the crystalline phase, as expected. The peaks positions match those reported in the JCPDS database (PDF# 041-0504) for the $Na_3MnZr(PO_4)_3$ compound. For the 8.8-MnZr sample, an additional peak is detected at about 23.5° and attributed to the carbon source [347], present in huge amount in this sample [91,197,198]. The Rietveld analysis is carried out on the 2-MnZr sample. The graphical comparison on the experimental and refined pattern is shown in Figure S. 5. It confirms the successful synthesis of the compound. The values of the lattice parameters, and the discrepancy factors obtained by the Rietveld refinement are shown in Table 3.1. The obtained results are consistent with those reported by [56]. There are not extra peaks caused by Mn and Zr long-range ordering, and the transition metal ions are randomly distributed on the octahedral site of the *NaSICON* framework [348,349].

Morphological analysis

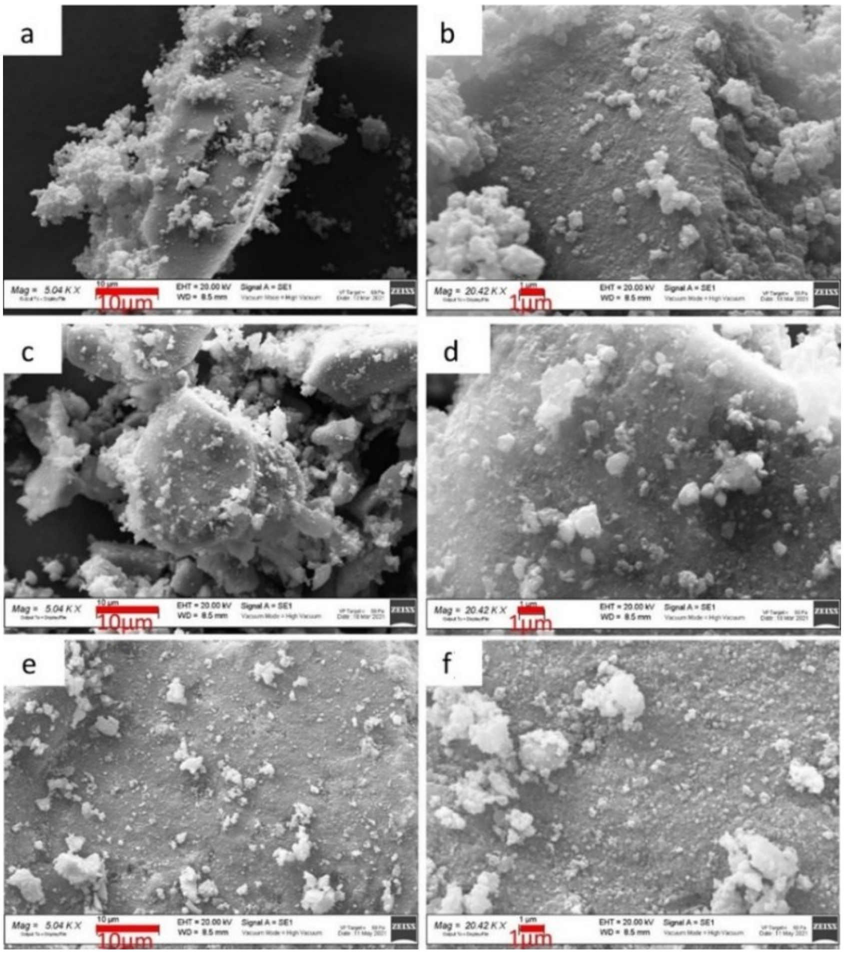

Figure 3.21: SEM images of $Na_3MnZr(PO_4)_3$: a,b) 8.8-MnZr; c,d) 3-MnZr; e,f) 2-MnZr.

The Figure 3.21 and Figure 3.22 show the SEM and TEM images, respectively, of the $Na_3MnZr(PO_4)_3$ sample with different amount of citric acid. In 8.8-MnZr SEM images (Figure 3.21a,b), we observe aggregates greater than 10µm, which are composed by particles of about 1µm or smaller. The grain's surfaces are irregular but defined and the powder's morphology is rather homogeneous. The TEM photographs (Figure 3.22a,b) confirm the presence of great aggregate of particles surrounded by carbon coating. The amount of carbon coating is well evident, spread in the powder and not always bounded to $Na_3MnZr(PO_4)_3$ particles. In the case of the 3-MnZr sample, the SEM images (Figure 3.21c,d) show aggregates with size and morphology comparable to the 8.8-MnZr one. The TEM photographs (Figure 3.22c,d) confirm the presence of great aggregates of particle surrounded by carbon coating. The carbon layer on the active material's particles seems thinner than for the 8.8-MnZr sample, and nanocubes-shaped particles aggregate around the $Na_3MnZr(PO_4)_3$ are observed. This indicates that carbon is spread in the sample and not always bounded to the active material. Also, in the case of the 2-MnZr sample, the SEM images (Figure 3.21e,f) particles morphology and aggregate size are comparable to the 8.8-MnZr and 3-MnZr powders; instead, the particles composing the aggregates are smaller. The TEM photographs (Figure 3.22e,f) confirm the presence of great aggregate of particle surrounded by carbon coating. Compared to the other samples, synthesized with higher amount of citric acid, the 2-MnZr one displays a thinner and more homogeneous carbon coating of the active material's particles.

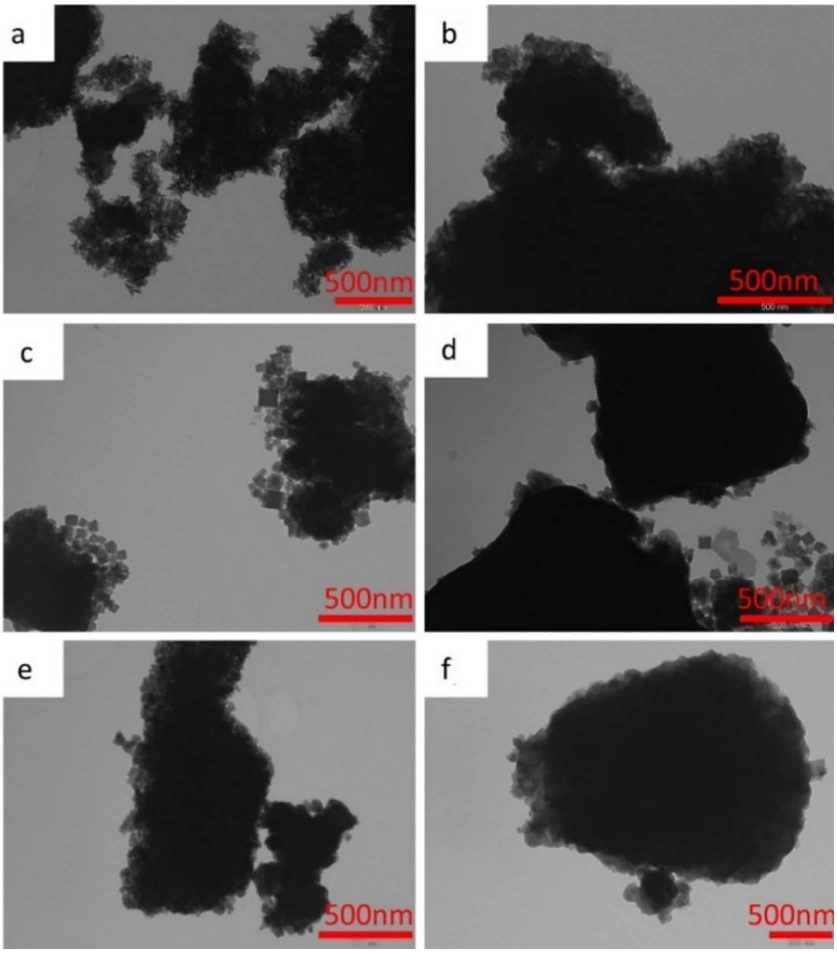

Figure 3.22: TEM images of $Na_3MnZr(PO_4)_3$: a,b) 8.8-MnZr; c,d) 3-MnZr; e,f) 2-MnZr.

Thermogravimetric and RAMAN analysis

In Figure 3.23 the TGA analyses for the $Na_3MnZr(PO_4)_3$ samples are reported. The TGA analysis is employed to evaluate the amount of carbon coating of the 8.8-MnZr, 3-MnZr and 2-MnZr samples. The amount of carbon coating depends on the quantity of chelating agent (citric acid) used in the sol-gel synthesis.

All the $Na_3MnZr(PO_4)_3$ samples display an initial weight loss due to the presence of absorbed water, and a second more pronounced weight loss in the temperature range 400°C-500°C, attributed to the carbon combustion in air. Namely, the greater is the quantity of carbon source in the synthesis, the greater is the weight loss: 29.77%w/w for 8.8-MnZr, 17.70%w/w for 3-MnZr and 5.13%w/w for 2-MnZr. This trend confirms the results of SEM and TEM analyses, which put into evidence an homogeneous and thinner carbon coating in the 2-MnZr sample.

The room temperature Raman spectra of the $Na_3MnZr(PO_4)_3$ samples with different carbon coating amount are shown in Figure 3.24a,b.

The Figure 3.24b shows the value of the I_G/I_D ratio for each sample. Usually, the I_D and I_G values correspond to the intensities of the modes, however to better account for the broadening of the peak, we have used the integrated intensity of the two Gaussian functions used to fit the experimental data. The higher is the I_G/I_D value, the higher is the presence of the ordered carbon. In this case, the I_G/I_D ratio is comparable for 8.8-MnZr and 3-MnZr samples, 0.819 and 0.815, respectively. While, for the 2-MnZr one, the value is slightly higher: 0.845. It is consistent with the fact that the stoichiometric amount of citric acid in the 2-MnZr undergoes to a better graphitization process forming a homogeneous carbon coating. It can help in improving the electronic conduction into the cathode.

In the 200-1000 cm^{-1} spectral range, all the samples (8.8-MnZr. 3-MnZr and 2-MnZr) show weak signals ascribed to the *NaSICON* structure, better described in the Subsection 10 on $Na_3MnZr(PO_4)_3$ self-standing electrode.

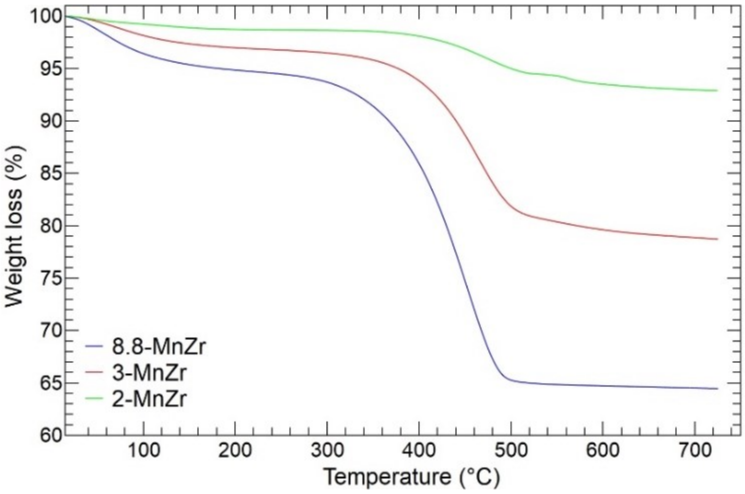

Figure 3.23: Weight percentage loss for different amount of citric acid: 8.8-MnZr, 3-MnZr, and 2-MnZr samples.

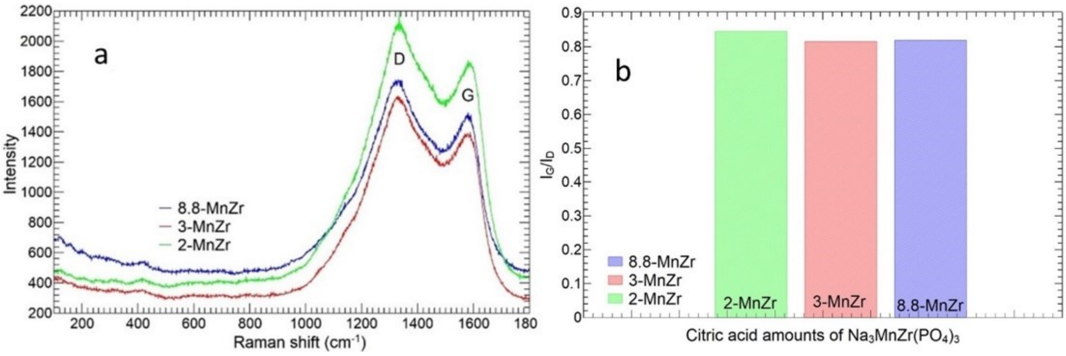

Figure 3.24: a) Raman spectra and b) I_D/I_G ratio of the $Na_3MnZr(PO_4)_3$ samples synthesized with different amount of citric acid.

Electrochemical results

The cyclic voltammetry and the first three charge/discharge profiles at 0.05C of the 8.8-MnZr, 3-MnZr and 2-MnZr samples are shown in Figure 3.25a,c,e, and Figure 3.25b,d,f, respectively. The results suggest the electrochemical performances depend on the citric acid amount used in the synthesis. All samples are electrochemically active and show the red-ox peak of Mn^{2+}/Mn^{3+} at 3.6V and Mn^{3+}/Mn^{4+} at 4.2V, but the 8.8-MnZr sample show weaker peaks than the 3-MnZr and 2-MnZr ones. Moreover, it displays a relevant intensity loss after the first cycle: from 0.01A/g to 0.007A/g for the red-ox peak at 3.6V, and from 0.006A/g to 0.003A/g for that at and 4.2V (Figure 3.25a), and the red-ox plateau in Figure 3.25b become less evident after the first cycle.

For the 3-MnZr (Figure 3.25c,d) and 2-MnZr (Figure 3.25e,f) samples, the peaks intensities display comparable values of about 0.06 A/g for the Mn^{2+}/Mn^{3+}red-ox peak, while for the Mn^{3+}/Mn^{4+}one, the peak's intensities are 0.04 A/g and 0.048 A/g for the 3-MnZr and 2-MnZr cathodes, respectively. Hence, in the second red-ox peak at 4.2V, the sample with the thinner and homogeneous carbon coating gives the highest peak current intensity, implying a better capacity storage.

For all three cyclic voltammetry, but especially for the 8.8-MnZr sample, an initial degradation of electrolyte is visible at 4.5V. We already use the $NaClO_4$ in PC with 5% of FEC as electrolyte, which is one of the high voltage working solution, among the electrolytes used today for this type of cathode. The phenomenon is under investigation and further analysis is ongoing.

The charge/ discharge cycles at different C-rates for the 8.8-MnZr, 3-MnZr and 2-MnZr samples are shown in the Figure 3.26.

The 8.8-MnZr sample shows an initial specific charge/discharge capacity of 77.68/49.98 mAh/g, and average capacity values of 47.78, 39.95, 31.46, 26.82, 22.63, and 12.89 mAh/g at 0.05C, 0.1C, 0.2C, 0.5C, 1C, and 2C, respectively. The coulombic efficiency is 97%, and the initial capacity is completely recovered at the end of the measurement.

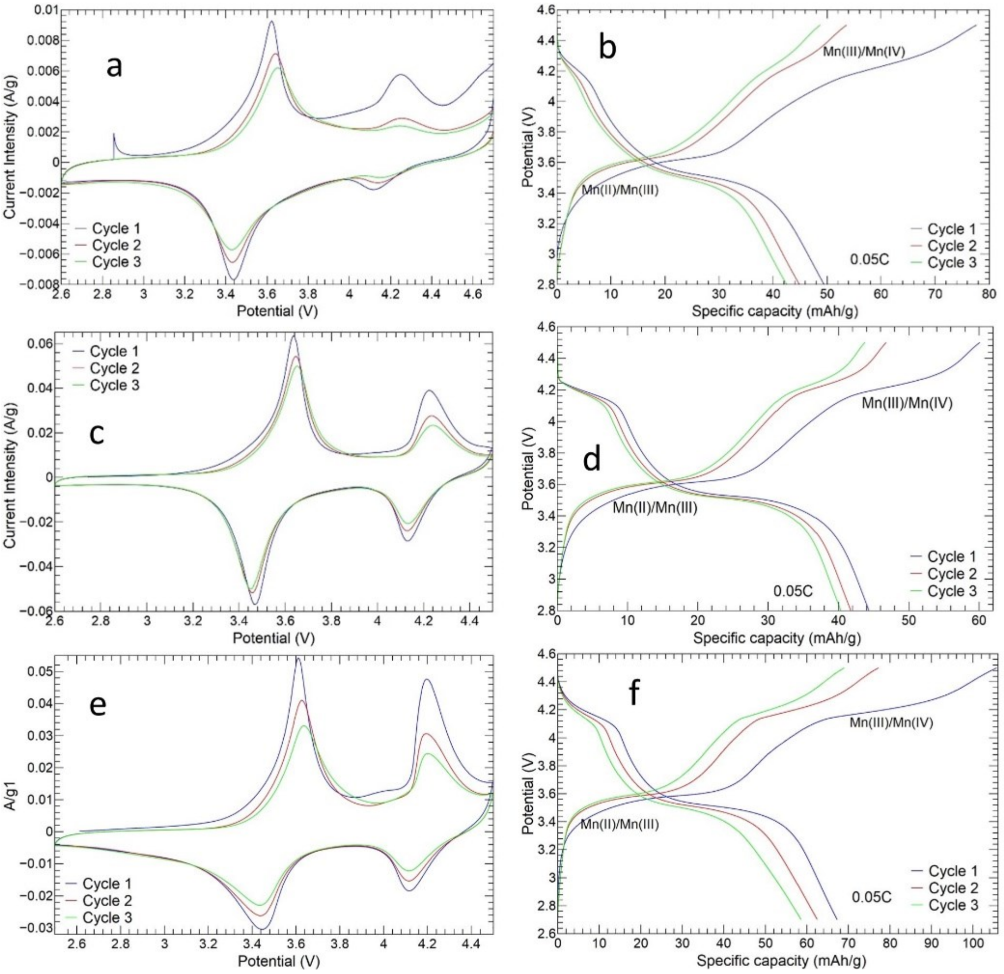

Figure 3.25: Cyclic voltammetry and charge/discharge cycles at 0.05C of a,b) 8.8-MnZr, c,d) 3-MnZr, and e,f) 2-MnZr samples.

The 3-MnZr sample gives an initial specific charge/discharge capacity of 60.10/45.01 mAh/g, with a coulombic efficiency of 98%, and a complete capacity recovery at the end of the measurement, too. The average values of the specific capacity are 42.61, 33.75, 28.02, 23.15, 18.05, and 10.88 mAh/g at 0.05C, 0.1C, 0.2C, 0.5C, 1C, and 2C, respectively. The 3-MnZr presents lower values of specific capacity at each C-rates, compared to the 8.8-MnZr.

Finally, the 2-MnZr sample shows an initial specific charge capacity of 105.7 mAh/g, approaching the theoretical one (107.9 mAh/g), and specific discharge capacity of 67.21 mAh/g. The average capacity values of 57.92, 27.87, 17.51, 11.37, 7.59, 4.56, and 4.01 mAh/g at 0.05C, 0.1C, 0.2C, 0.5C, 1C, 2C, and 5C, respectively. The coulombic efficiency is 97%. Compared to the 8.8-MnZr and 3-MnZr electrodes, the 2-MnZr one shows a higher initial specific capacity, followed by a capacity loss during the first cycles. The average capacity values are lower than those of the other cathodes, but it is the only cell which can be cycled also at 5C.

Comparing to other *NaSICON* cathodes, the $Na_3MnZr(PO_4)_3$ works at higher voltage range than $Na_3V_2(PO_4)_3$ [172,350,351] and $Na_3Fe_2(PO_4)_3$ [58,58,117], and similar to that of $Na_3Cr_2(PO_4)_3$ [117,118,352]. It is a key parameter, as it means our cathode material has the theoretical possibility to store more energy than other well-known *NaSICON* ones. The theoretical capacity is similar to the $Na_3Cr_2(PO_4)_3$ (117 mAh/g) [352] and $Na_3V_2(PO_4)_3$ (117.6 mAh/g) [351]. Although our active material display little worse values of the specific capacity at different C-rate than the other NaSICON cathodes reported in literature, the $Na_3MnZr(PO_4)_3$ is considered a promising alternative as active material for SIBs, thanks to its environmental friendly elements.

The obtained results of our study demonstrate that the different amount of carbon coating undoubtedly influences the electrochemical performance, confirmed by the fact that the peak current intensity of cyclic voltammetry increases when the amount of carbon coating decreases. So, for the $Na_3MnZr(PO_4)_3$ cathode we have to choose between the 8.8-MnZr sample and the 2-MnZr one. The former gives a lower initial capacity and does not work at C-rate higher than 2C, but, at the same time, it provides the complete capacity recovery and a lower capacity loss after the first cycle and at the C-rate change. While, the 2-MnZr cathode gives a higher value of initial capacity, and it works also at 5C. In this work, we are interested in obtaining cathodes with high power and energy density, so high values of both initial capacity and C-rates are preferred. Hence, to prepare the self-standing electrodes, we decided to use the 2-MnZr powder, which approaches the theoretical capacity in the initial cycles, and exhibits a more homogeneous carbon coating, which enhances the electronic conductivity.

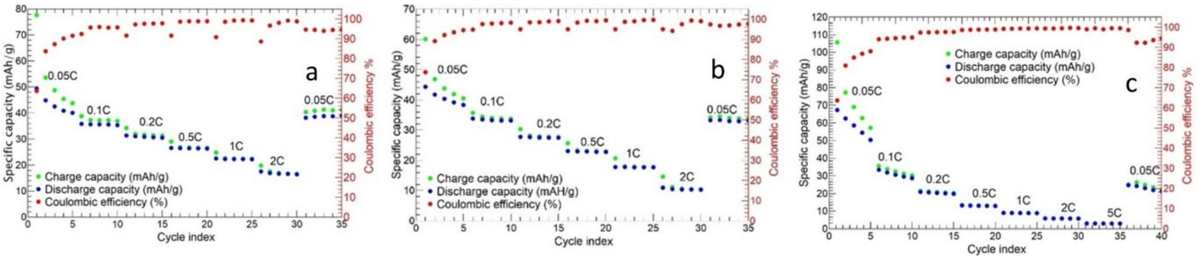

Figure 3.26: Charge/discharge cycles at different C-rate of a) 8.8-MnZr, b) 3-MnZr, and c) 2-MnZr tape-casted cathodes.

Subsection 10 Self-standing cathode characterization

Now we report the results on the self-standing electrodes synthesized as reported in Section 2 of Chapter 2. Firstly, we verify the presence of $Na_3MnZr(PO_4)_3$ *NaSICON* structure into CNFs, then we investigate the electrochemical properties of self-standing electrodes compared to the abovementioned 2-MnZr tape-casted cathode. For this active material we report the results obtained on self-standing electrodes prepared by different electrospinning approaches: deposition with the horizontal set-up, the vertical set-up and dip-drop coating, as schematized in Figure 3.27. The results and discussion is taken from the paper published by our research group [145].

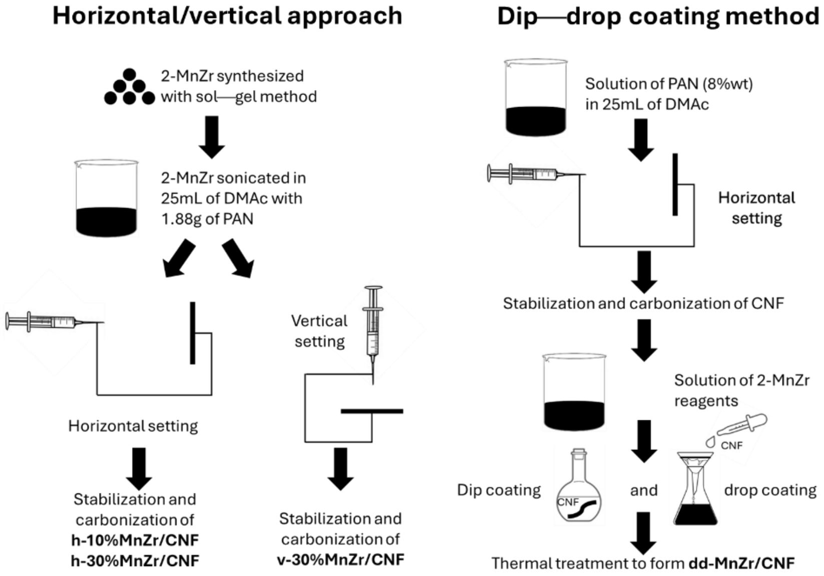

Figure 3.27: A scheme of the samples' synthesis.

X-Ray powder diffraction analysis

Pristine $Na_3MnZr(PO_4)_3$ powder was synthesized via sol-gel [56], and used as active material source in preparing both tape casted electrode and some of the free-standing cathodes. Two different approaches are applied to prepare the self-standing electrodes, differing on the method employed to load the active material onto CNFs: i) dip-drop coating of $Na_3MnZr(PO_4)_3$ precursors onto electrospun CNFs sheets, followed by thermal treatments to synthesize the active material ii) electrospinning the dispersion of pristine $Na_3MnZr(PO_4)_3$ powder synthesized via sol-gel into PAN in N,N-dimethylacetamide solution. In the latter case, two different $Na_3MnZr(PO_4)_3$ amounts (10 and 30 wt%) and two electrospinning settings (horizontal and vertical) were investigated. Also, pure CNFs were prepared for comparison. A scheme of the samples' synthesis is shown in Figure 3.27 and details are reported in Section 2 of Chapter 2. The prepared samples and their alphanumeric codes are listed in Table 2.3 of Chapter 2.

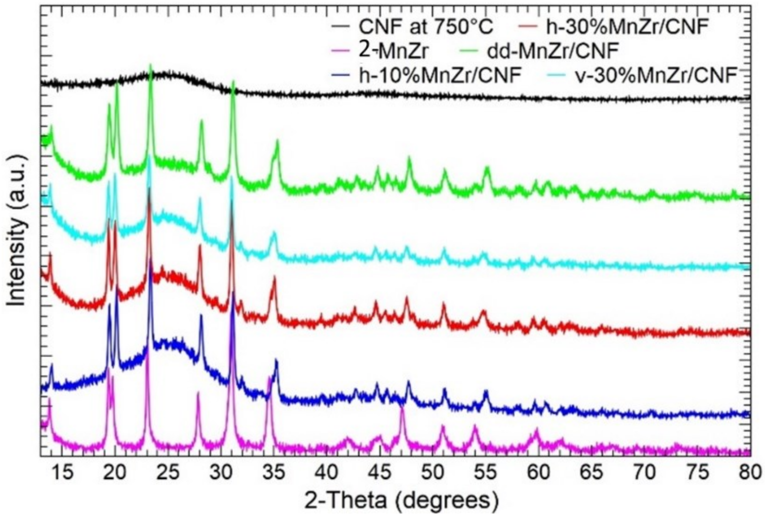

Figure 3.28: X-Ray diffraction patterns of electrospun and carbonized samples h-10%MnZr/CNF (blue), h-30%MnZr/CNF(red), v-30%MnZr/CNF (light blue), and dd-MnZr/CNF (green). The pattern of the 2-MnZr powder (purple) and pure CNF carbonized at 750°C (black) are also shown.

In Figure 3.28, the XRPD patterns of CNF, 2-MnZr, dd-MnZr/CNF, h-10%MnZr/CNF, h-30%MnZr/CNF and v-30%MnZr/CNF samples are shown. For the CNF sample, a broad band centred at 2-theta value of about 25° is detected, as expected for amorphous components. The 2-MnZr sample displays the peaks pertinent to the NASICON-type $Na_3MnZr(PO_4)_3$ compound ($R\overline{3}c$ space group) and deposited in the JCPDS database (PDF# 041-0504). The diffraction data are well explained by the literature structure given by Gao and co-workers [56], as demonstrated by the Rietveld refinement results reported in Table S. 2 and the graphical comparison shown in Figure S. 5. No extra peaks due to Mn and Zr long-range ordering are detected, and the random distribution of the transition metal ions on the octahedral site of the *NaSICON* framework is confirmed [348,349]. For the MnZr/CNFs samples, both the broad band, typical of the amorphous component, and the reflections of the $Na_3MnZr(PO_4)_3$ *NaSICON* structure are observed, independently of the deposition method. Moreover, the self-standing cathode obtained by dip-drop approach display a very weak peak at about 29° due to small amount of an unidentified impurity phase, while those prepared by dispersing the active material into the PAN solution display a weak peak at 2-theta of about 32°: this signal is explained by small amount of $Na_3MnZr_4(PO_4)_6$ phase (PDF# 045-0016), possibly formed during the further thermal treatment at 750°C for the carbonization process. The Rietveld refinement results for the MnZr/CNFs samples are reported in Table S. 2, and the graphical comparisons are shown in Figure S. 6. The crystalline component of the diffraction patterns fairly matches the $Na_3MnZr(PO_4)_3$ phase. The difference curve evidences some mismatch on some peaks intensities, due to the choice to limit the structural refinement to the lattice parameters (see for details Subsection 6 of Chapter 2). Notably, the *c* lattice parameter increases and *a* decreases compared to the pristine $Na_3MnZr(PO_4)_3$ powder. This leads to a slight cell volume decrease and a c/a ratio increase (See Table S. 2). The crystallite size is slightly increased in the self-standing cathodes obtained by the dispersion approach, and it is consistent with the prolonged thermal treatment at 750°C for the additional carbonization process, not required in the pristine and dip-drop synthesis route.

For the sake of completeness, in the Figure S. 7 we report the diffraction pattern of the electrospun, stabilized and carbonized samples of all the MnZr/CNF materials. For the horizontal and vertical samples, the thermal treatments do not influence the *NaSICON* structure, pre-sythesized by sol-gel method and loaded onto the CNFs sheets. While, for the dd-MnZr/CNF material, the *NaSICON* compound is formed in situ only after the carbonization step. For these reasons we focuses our investigations on all the MnZr/CNF carbonized samples.

Morphological analysis

Figure 3.29 shows the SEM images of self-standing cathodes. For each sample both the surface and the cross-section are investigated. All the self-standing samples are characterized by a matrix of non-owen carbon nanofibers which hosts the $Na_3MnZr(PO_4)_3$ aggregates of micrometric size. Also, the carbon nanofibers display variable diameters, of about 250 nm for the samples prepared dispersing the active material in the PAN solution before electrospinning, and larger in the dip-drop sample (about 700 nm). The cross-section images put into evidence that higher thickness (about 150 mm) is obtained for the 30 wt% samples, independently of the deposition setting. The sheets seem more compact and structured for the h-10%MnZr/CNF, h-30%MnZr/CNF and v-30%MnZr/CNF samples, and fluffier in the case of the dip-drop one.

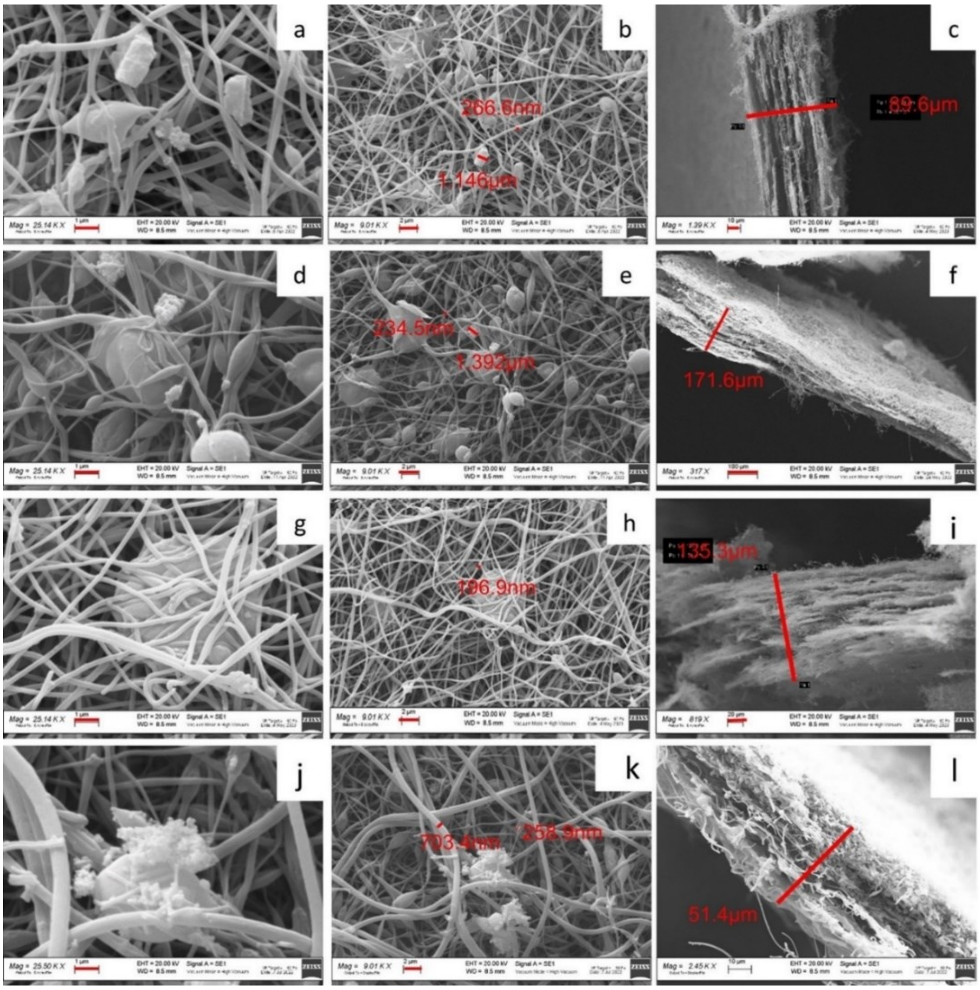

Figure 3.29: SEM images of: h-10%MnZr/CNF surface a,b) and cross-section c); h-30%MnZr/CNF surface d,f) and cross-section f); v-30%MnZr/CNF surface g,h) and cross-section i); dd-MnZr/CNF surface j-k) and cross-section l).

Figure 3.30 shows the TEM images of the self-standing samples, which confirm the presence of active material agglomerates into CNFs, as evidenced by SEM analysis. The aggregates are formed by sub-particles of about 20-40 nm, whose size compares to that evaluated by XRPD analysis (Table S. 2). Interestingly, in the samples prepared by dispersion of pristine $Na_3MnZr(PO_4)_3$ into the polymeric solution to be electrospun, the active material covers parts of the CNFs surface, but is also embedded into nanofibers; the latter feature is particularly evident in the v-30%MnZr/CNF sample. Differently, the agglomerates reside mainly on the CNFs surface and between them in the case of the dip-drop approach. This is consistent with the latter synthetic route, in which the active material is formed in-situ on carbonized electrospun nanofibers.

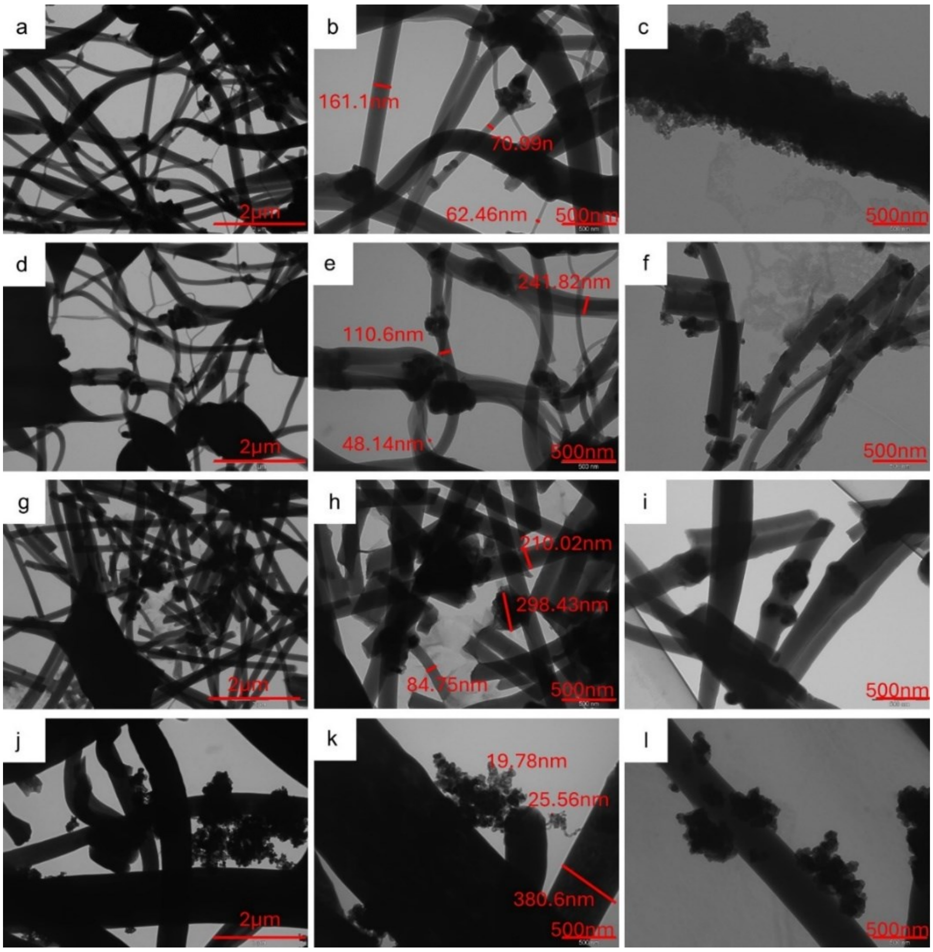

Figure 3.30: TEM images at different magnifications (20kX e 50kX) of a-c) h-10%MnZr/CNF, d-f) h-30%MnZr/CNF g-i) v-30%MnZr/CNF, and j-l) dd-MnZr/CNF samples.

The EDS analysis is applied to evaluate the $Na_3MnZr(PO_4)_3$ distribution on the surface and within the cross-section of the MnZr/CNF self-standing electrodes. For each sample a surface and a cross-section portion are selected and the distribution maps of the Na, Mn, Zr and P elements is evaluated. The results are shown in Figure 3.31-Figure 3.34 for the h-10%MnZr/CNF, h-30%MnZr/CNF, v-30%MnZr/CNF and dd-MnZr/CNF self-standing cathodes. In the case of the active material loading by dispersion into the polymeric solution, the EDS analysis demonstrates that the agglomerates spread into and within the CNFs correspond to the $Na_3MnZr(PO_4)_3$ composition. They are homogeneously distributed on the sample surface, and along the sheet thickness, too (Figure 3.31-Figure 3.33). For the dd-MnZr/CNF sample (Figure 3.34), again the $Na_3MnZr(PO_4)_3$ agglomerates are detected on the surface and in the cross-section, but their distribution along the sheet thickness is non-homogeneous, and the active material preferentially resides on the external edges. This justifies the clearly visible Raman fingerprint of $Na_3MnZr(PO_4)_3$ in the dd-MnZr/CNF composite compared to the other self-standing cathodes (see Figure 3.36), and is consistent with the dip-drop synthetic approach used to load the active material:

the permeation of the precursors' solution into the inner part of the pre-synthesized CNF sheets is less effective. The different concentration of the active material along the sheet may influence the electrochemical performance of the self-standing electrode. Independently of the self-standing MnZr/CNF cathodes, the Na:Mn:P molar ratio is close to 3:1:3, as expected for the compound stoichiometry.

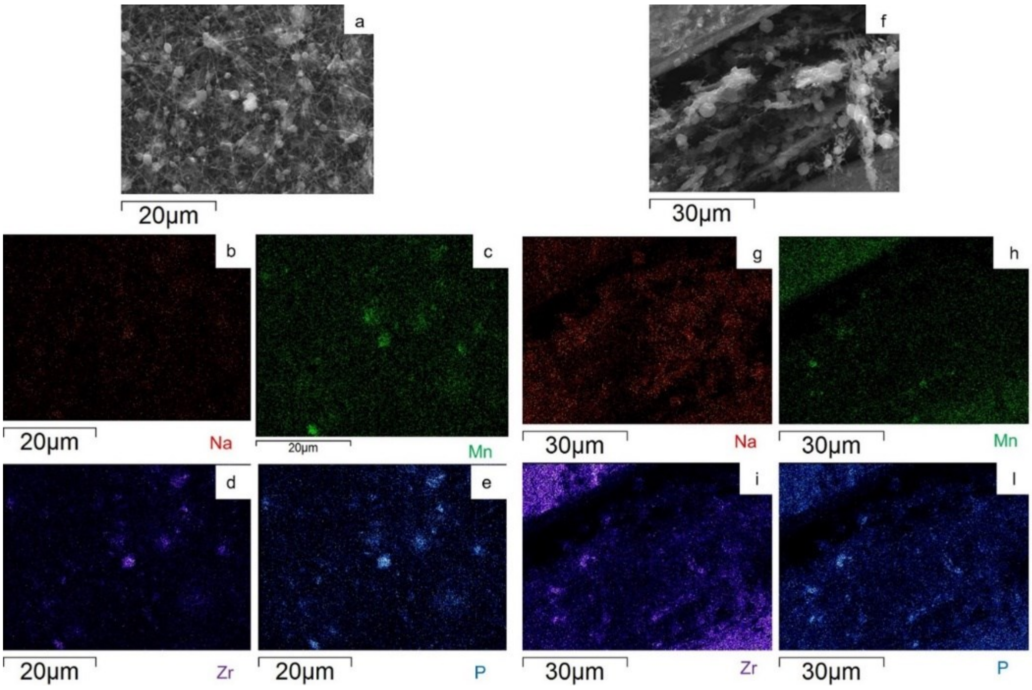

Figure 3.31: SEM image and EDS maps of the different elements for h-10%MnZr/CNF a-e) surface and f-l) its cross-section.

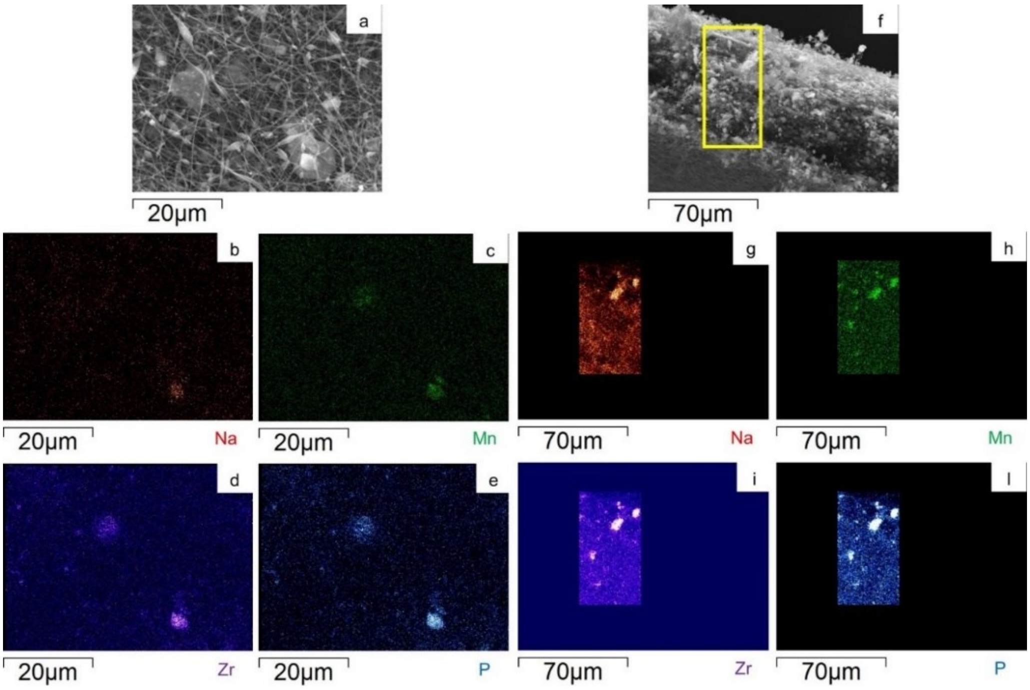

Figure 3.32: SEM image and EDS maps of the different elements for h-30%MnZr/CNF a-e) surface and f-l) its cross-section.

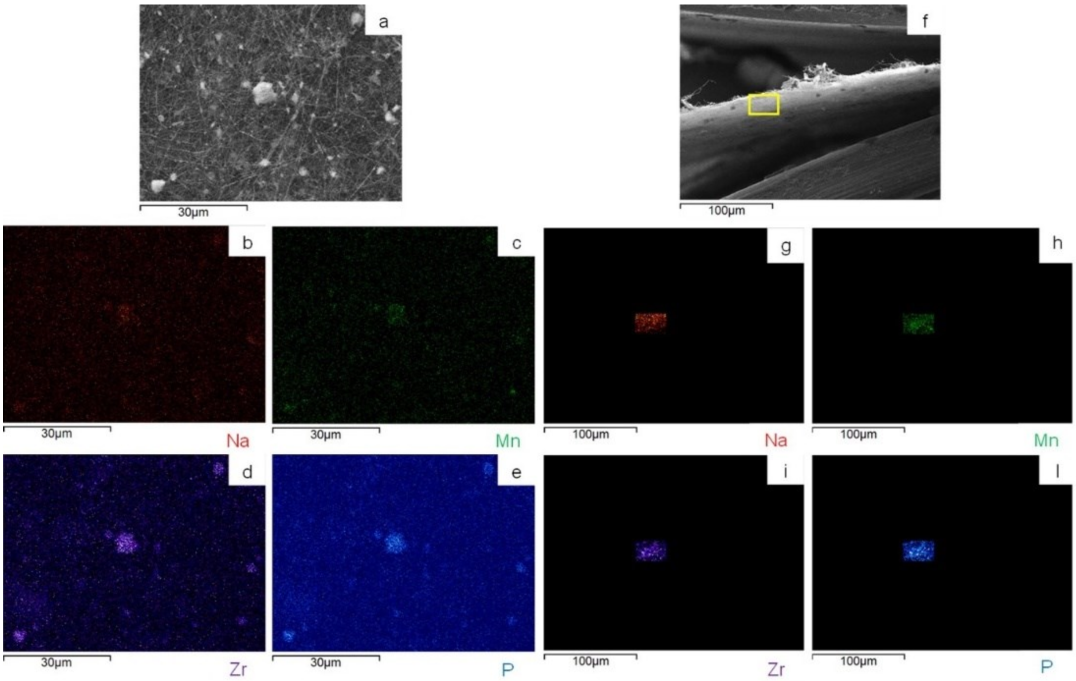

Figure 3.33: SEM image and EDS maps of the different elements for v-30%MnZr/CNF a-e) surface and f-l) its cross-section.

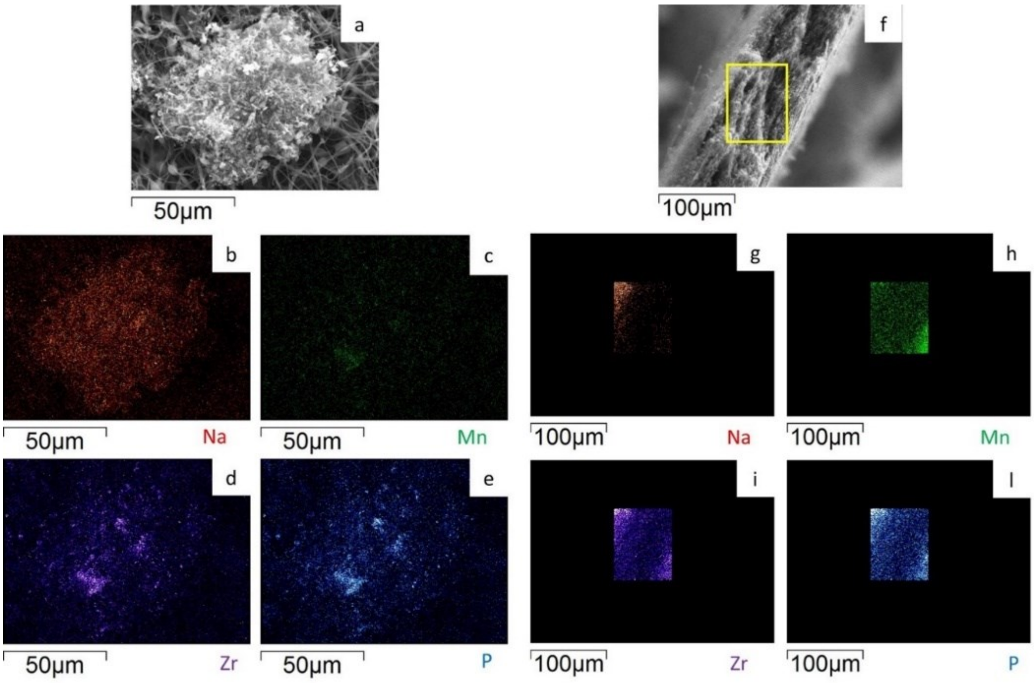

Figure 3.34: SEM image and EDS maps of the different elements for dd-MnZr/CNF a-e) surface and f-l) its cross-section.

Thermogravimetric and RAMAN analysis

The thermogravimetric data were used to evaluate the effective amount of the $Na_3MnZr(PO_4)_3$ active material present in the self-standing cathodes. The thermal behavior of the pristine $Na_3MnZr(PO_4)_3$ powder was also investigated, for comparison.

The thermogravimetric curves of 2-MnZr, h-10%MnZr/CNF, h-30%MnZr/CNF, v-30%MnZr/CNF and dd-MnZr/CNF samples are shown in Figure 3.35. For the 2-MnZr sample (black line) a small mass loss due to the release of adsorbed water is detected below 100°C, while the second mass loss of 5.13% occurring in the temperature range 400°C-650°C is attributed to the combustion of the carbon coating (source: citric acid used in the sol-gel synthesis).

The h-10%MnZr/CNF (blue line), h-30%MnZr/CNF (red line) v-30%MnZr/CNF (green line) and dd-MnZr/CNF (purple line) TGA curves display similar thermal behavior. As for 2-MnZr sample, the first mass loss below

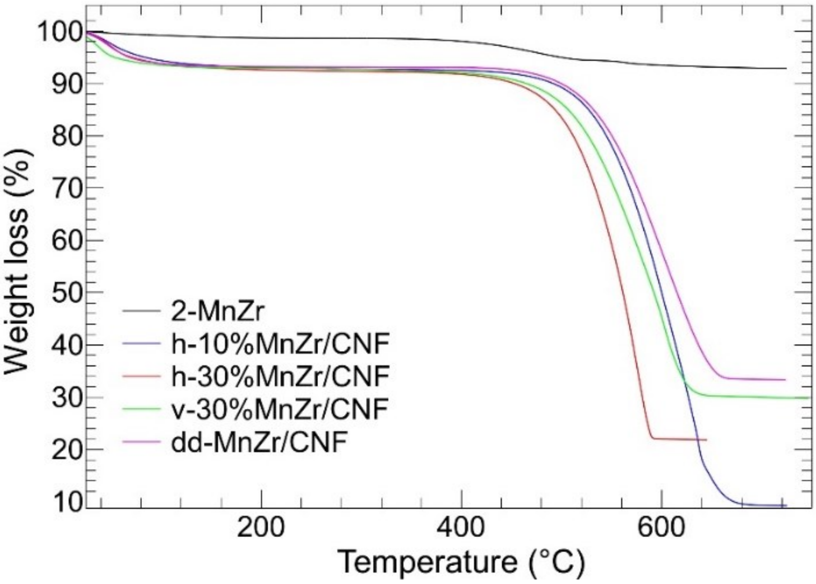

Figure 3.35: TGA analysis of 2-MnZr (black), h-10%MnZr/CNF (blue), and h-30%MnZr/CNF (red) and v-30%MnZr/CNF (green), and dd-MnZr/CNF (purple) samples.

100 °C is attributed to the adsorbed water release. The second mass loss in the 400°C–650°C temperature range is again due to the combustion of the carbonaceous component present as both carbon coating and carbon nanofibers. So, it is expected this mass loss is higher for MnZr/CNFs than for the 2-MnZr sample. The residual mass values reached by each self-standing cathode are reported in Table 3.2. In the case of the h-10%MnZr/CNF self-standing electrode, the obtained value well matches the synthesis one. On the contrary, for h-30%MnZr/CNF the value is lower. This may depend on the horizontal experimental setting used for the deposition: we noted the partial settling of particle agglomerates in the syringe. To achieve the 30 wt% loading, the vertical experimental setting was used. Indeed, for v-30%MnZr/CNF sample the mass loading matches the synthesis value. The highest active material loading is obtained for the dd-MnZr/CNF sample by electrospinning the polymeric solution containing the $Na_3MnZr(PO_4)_3$ precursors. The values of electrode residual masses of about 1.9 mg/cm^2, especially for v-30%MnZr/CNF and dd-MnZr/CNF samples, are consistent with the literature values of self-standing electrodes [142,353].

Table 3.2: Residual mass values of the self-standing cathodes evaluated by TGA analysis.

SAMPLE	***RESIDUAL MASS (wt%)***
h-10%MnZr/CNF	9.3
h-30%MnZr/CNF	21.8
v-30%MnZr/CNF	29.8
dd-MnZr/CNF	33.3

In order to analyze the phase formation and composition of the composite samples, we also employed micro-Raman spectroscopy. The Raman spectra of the pristine $Na_3MnZr(PO_4)_3$ and of the MnZr/CNFs samples are shown in Figure 3.36. In case of highly diffusive powders, it is important to note that micro-Raman sampling is strongly effective in surface layers.

In all cases we can distinguish two different spectral regions; the first (200 -1100 cm^{-1}) presents the Raman features ascribed to the active material [354], the second (1100-1800 cm^{-1}) presents the typical fingerprints of carbon-based structures, with the well-known D and G bands [332].

In the first spectral region the typical spectrum of $Na_3MnZr(PO_4)_3$ is observed for the pristine sample. The strong signal at around 1000 cm^{-1} is due to the overlapping of the Raman activity associated with PO_4 symmetric (ν_1) and asymmetric (ν_3) stretching vibrations. At lower energies different Raman activities can be present. The strong signal at around 430 cm^{-1} should be due to symmetric (ν_2) bending vibrations of the PO_4 unit, with the corresponding asymmetric (ν_4) bending mode responsible for the lower intensity signals around 540 cm^{-1}. Bands observed in the 350−330 cm^{-1} range should be instead associated to metal-oxygen vibrations, while bands below 250 cm^{-1} are usually attributed to lattice vibrations. Even for the pristine sample the typical carbon-related Raman features are observed, due to the carbon coating.

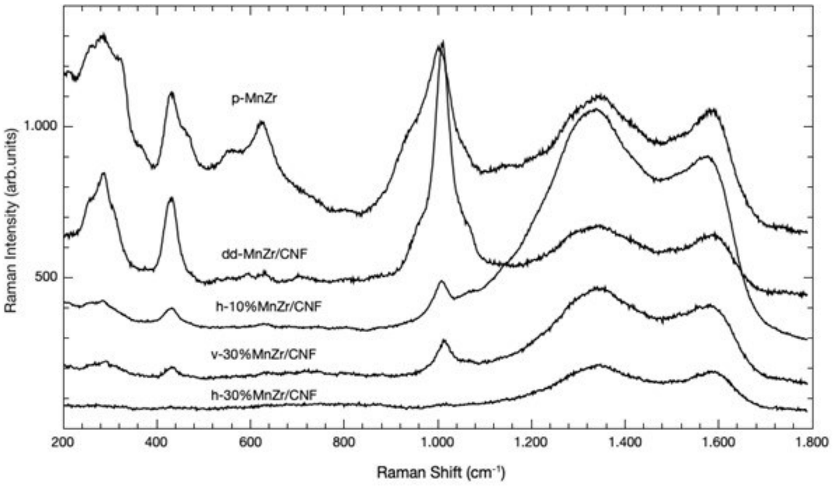

Figure 3.36: Raman spectra of 2-MnZr, h-10%MnZr/CNF, h-30%MnZr/CNF, v-30%MnZr/CNF, and dd-MnZr/CNF

For what concerns the other samples we can observe that the active material Raman fingerprint is clearly visible for dd-MnZr/CNF sample, while it is attenuated for the other samples. This is firstly due to the different Raman cross-sections, and secondly to the different methods applied to load the active material; this leads to different active material distribution within CNFs matrix, as confirmed by the EDS analysis reported above. Indeed, differently from h-10%MnZr/CNF, h-30%MnZr/CNF, and v-30%MnZr/CNF cathodes, in the dd-MnZr/CNF sample the active material powder mainly distributes on the surface of the CNFs matrix. This favors the exposure of *NaSICON* structure to the micro-Raman sampling, which is strongly effective in the surface layers. Based on these considerations, we expect to weakly or not detect the Raman signals of $LiFePO_4$, $Na_3MnTi(PO_4)_3$ and ZnS in the self-standing electrodes(see Subsection 7, Section 4, and Subsection 17, respectively), as we prepared electrodes only by horizontal deposition of pre-synthesized active material; this synthetic approach favors a deep powder dispersion into CNFs matrix, and makes more difficult to detect the olivine, *NaSICON* and sphalerite Raman signals into the spectra.

Concerning the carbon-related features i.e. the bands at 1333 and 1586 cm^{-1}, the former related to the disordered carbon, the latter to the G band, we observe an almost constant ratio between their intensities except for h-10%MnZr/CNF sample where the disorder, i.e. a greater I_D/I_G ratio, is more pronounced.

The morphological and structural results put into evidence the analogies/differences of the self-standing cathodes prepared by different synthetic approaches and settings. In all cases, the active material is successfully loaded into carbon nanofibers. The direct dispersion of pre-synthesized $Na_3MnZr(PO_4)_3$ powder into the polymeric solution before electrospinning seems a promising and feasible route for loading the active material. It is homogeneously dispersed both into and within CNFs. The effective loading is quantitative by using the vertical setting, which prevents possible settling of the powder before the needle is reached. The dip-drop coating of the active material precursors solution onto electrospun carbon nanofibers allows the load of the highest $Na_3MnZr(PO_4)_3$ amount, but the product mainly resides on the CNFs sheet surface and does not distribute homogeneously along the sheet thickness.

Now we show the electrochemical comparison between the slurry cathode and the self-standing electrodes obtained by different deposition approaches, to establish which gives the better electrochemical performance.

Subsection 11 Tape-casted and Self-standing cathodes electrochemical comparison

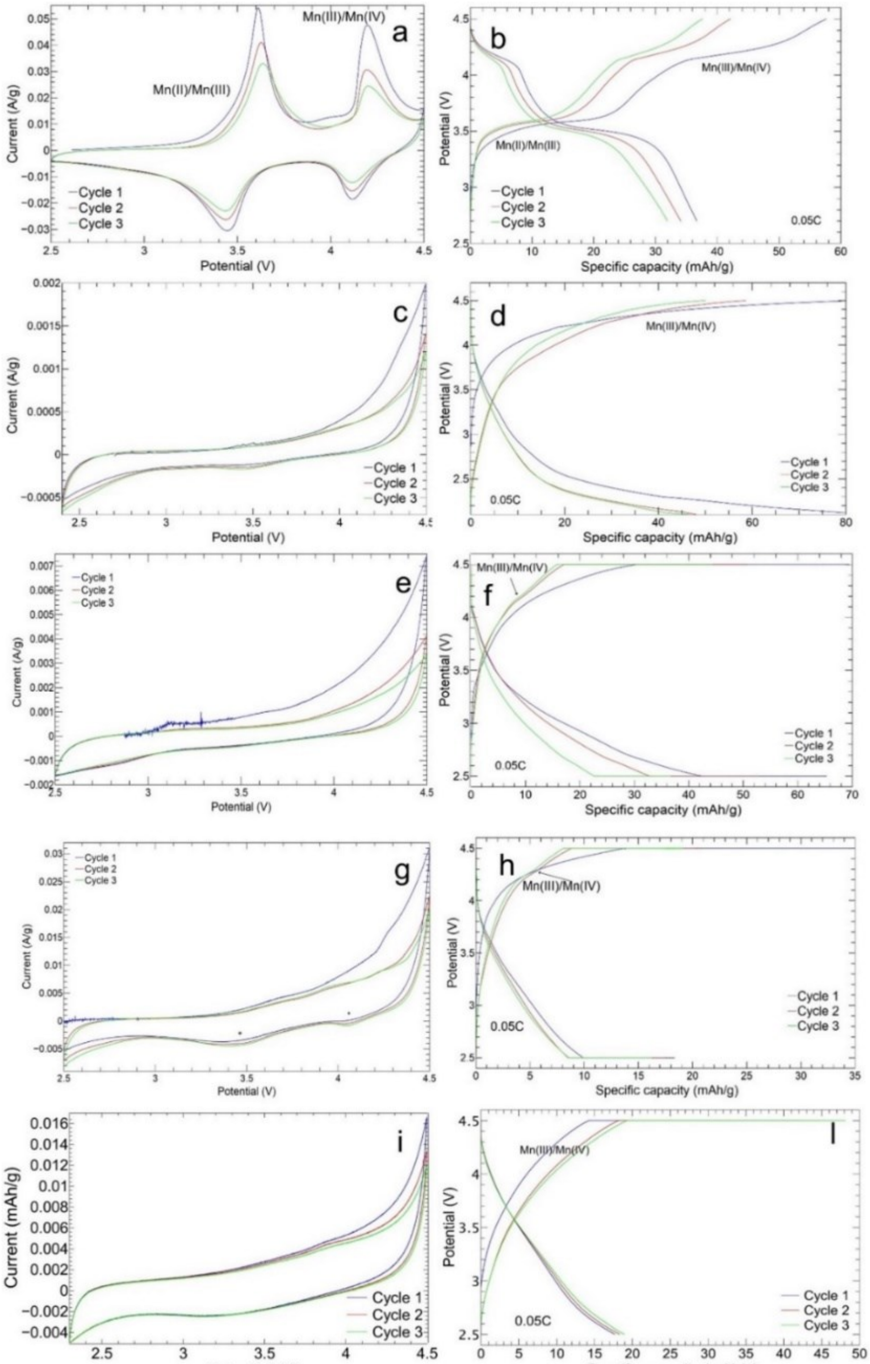

Figure 3.37: CV and charge/discharge curves of a,b) slurry 2-MnZr, c,d) h-10%MnZr/CNF, e,f) h-30%MnZr/CNF, g,h) v-30%MnZr/CNF, and i,l) dd-MnZr/CNF cathodes.

Figure 3.37 reports the cyclic voltammetry and charge/discharge curves for the 2-MnZr slurry and MnZr/CNF self-standing electrodes. The 2-MnZr slurry electrode curves (Figure 3.37 a,b) well compare to the literature ones [56]: the two redox peaks of Mn^{2+}/Mn^{3+} and Mn^{3+}/Mn^{4+} are detected at 3.61/3.45 V and 4.19/4.12 V, respectively. The small ΔV values between the cathodic and anodic peaks (16 mV for Mn^{2+}/Mn^{3+} and 7 mV for Mn^{3+}/Mn^{4+}) indicate a very small polarization phenomenon. The current intensity is higher than 0.05 A/g and lower than -0.03 A/g for anodic and cathodic peaks, respectively. The two redox phenomena are also confirmed by the two plateaus detected at 4.2 V and 3.5 V in the charge/discharge curves.

In the case of the self-standing cathodes, it is difficult to individuate the Manganese redox peaks, as they are very faint. This may depend on the active material amount, which is lower than that used in the tape-casted cathode. It is also confirmed by the CV analyses performed on samples with different amount of carbon coating, discussed in the Subsection 9 of Chapter 3. In fact, it is observed that the intensity of red-ox peak is negatively affected by the amount of carbon present in the sample: the peaks intensity increases when the carbon coating amount decreases, passing from 8.8-MnZr to 2-MnZr sample. In this case the amount of carbon is quite higher than in the Subsection 9, because we have both carbon-coated and carbonized CNFs matrix as carbon source. In particular, in the case of h-10%MnZr/CNF and h-30%MnZr/CNF samples we have only the 9.35 and 21.8 wt% of 2-MnZr. Anyway, further investigation is ongoing, to unravel the anomalous behavior of the Manganese redox peaks. Only in the v-30%MnZr/CNF and dd-MnZr/CNF samples weak peak curves are visible. Especially for the v-30%MnZr/CNF, weak cathodic peaks at 3.44 V and 4.05 V are clearly detected and confirmed by the presence of the small plateau of Mn^{3+}/Mn^{4+} at about 4.1 V in the charge/discharge curves (Figure 3.37 g,h). We recall that, among the cathodes prepared by dispersion of pre-synthesized $Na_3MnZr(PO_4)_3$, the v-30%MnZr/CNF sample has the highest active material loading (29.8 wt%). For the dd-MnZr/CNF cathode, a comparable $Na_3MnZr(PO_4)_3$ amount (33.0 wt%) is detected, but the active material is not embedded into CNFs and non-homogeneously dispersed along the CNFs thickness, as demonstrated by TEM and EDS analyses: this may affect the electrochemical performance. For this cathode it is not possible to evaluate the Na-ion diffusion coefficient due to the difficulty to identify the peak current. However, we estimate the percentage of diffusion current during the cyclic voltammetry at different scan rate: as shown in Figure S. 8, the MnZr/CNF samples exhibit a higher amount of diffusion current. It confirms that the CNF porous matrix help in making the Na-ion diffusion easier into the electrode. Finally, the fast electrolyte permeation is also demonstrated by the contact angle measurements reported in Figure S. 9 (v-30%MnZr/CNF sample). After only 50 ms a complete diffusion and permeation of electrolyte in the self-standing electrode occurs. The same behavior is observed for the other MnZr/CNF samples.

Figure 3.38 shows the charge/discharge values at different C-rates for the slurry and MnZr/CNF self-standing cathodes. The tape-casted electrode 2-MnZr shows an initial charge and discharge capacity of 105.88 and 67.21 mAh/g, respectively (Figure 3.38a). The initial capacity loss is typical of the NASICON-structured cathodes containing Zr^{4+} or Ti^{4+} or Al^{3+}, which present a voltage hysteresis $Al^{3+}<Ti^{4+}<Zr^{4+}$[355]. Average discharge capacities of 58.62, 34.61, 21.19, 13.27, 9.01, 5.87 and 3.01 Ah/g at 0.05C, 0.1C, 0.2C, 0.5C, 1C, 2C and 5C are obtained, respectively. The cell does not completely recover the capacity at the end of the measurement (a capacity of 24.18 mAh/g is reached at 0.05C) and the coulombic efficiency is ≥93%.

The h-10%MnZr/CNF cathode exhibits an initial charge and discharge capacity of 40.1 and 70.7mAh/g, respectively (Figure 3.38b), with a discharge capacity that reaches the value of 46.9 mAh/g in the second cycle. We obtain average discharge capacities of 48.6, 19.0, 17.0, 13.1, 11.0, 8.8, 5.9, 3.9 and 2.7 mAh/g at 0.05C, 0.1C, 0.2C, 0.5C, 1C, 2C, 5C, 10C and 20C, respectively, and a coulombic efficiency ≥95%. Contrary to the slurry electrode, the self-standing h-10%MnZr/CNF cathode exhibits firstly a lower loss capacity as the C-rate increases, and secondly works at C-rates higher than 5C and completely recovers the initial capacity at the end of the measurement. Indeed, the 10% self-standing cathode displays capacity values at 10C comparable to those obtained for the 2-MnZr slurry at 5C, and a better coulombic efficiency, which confirms a better reversibility of the charge and discharge process. Improved electrochemical performance is obtained for the h-30%MnZr/CNF sample (Figure 3.38c), which displays an initial charge and discharge capacity of 83.9 mAh/g and 83.4 mAh/g, respectively. In this case, the initial capacity loss after the first cycle is not detected and a coulombic efficiency ≥97% is reached, but the capacity is not completely recovered at the end of the measurement (capacity of 45.2 mAh/g). The average discharge capacities of 53.6, 27.6, 22.5, 11.4, 8.5, 5.8, 3.6, 2.7 and 2.1 mAh/g are obtained at 0.05C, 0.1C, 0.2C, 0.5C, 1C, 2C, 5C, 10C and 20C, respectively. The discharge capacity values are higher than the one reported for h-10%MnZr/CNF sample at 0.05C, 0.1C, and 0.2C. This is probably due to the higher amount of 2-MnZr powder loaded into CNF sheets (21.8 wt%).

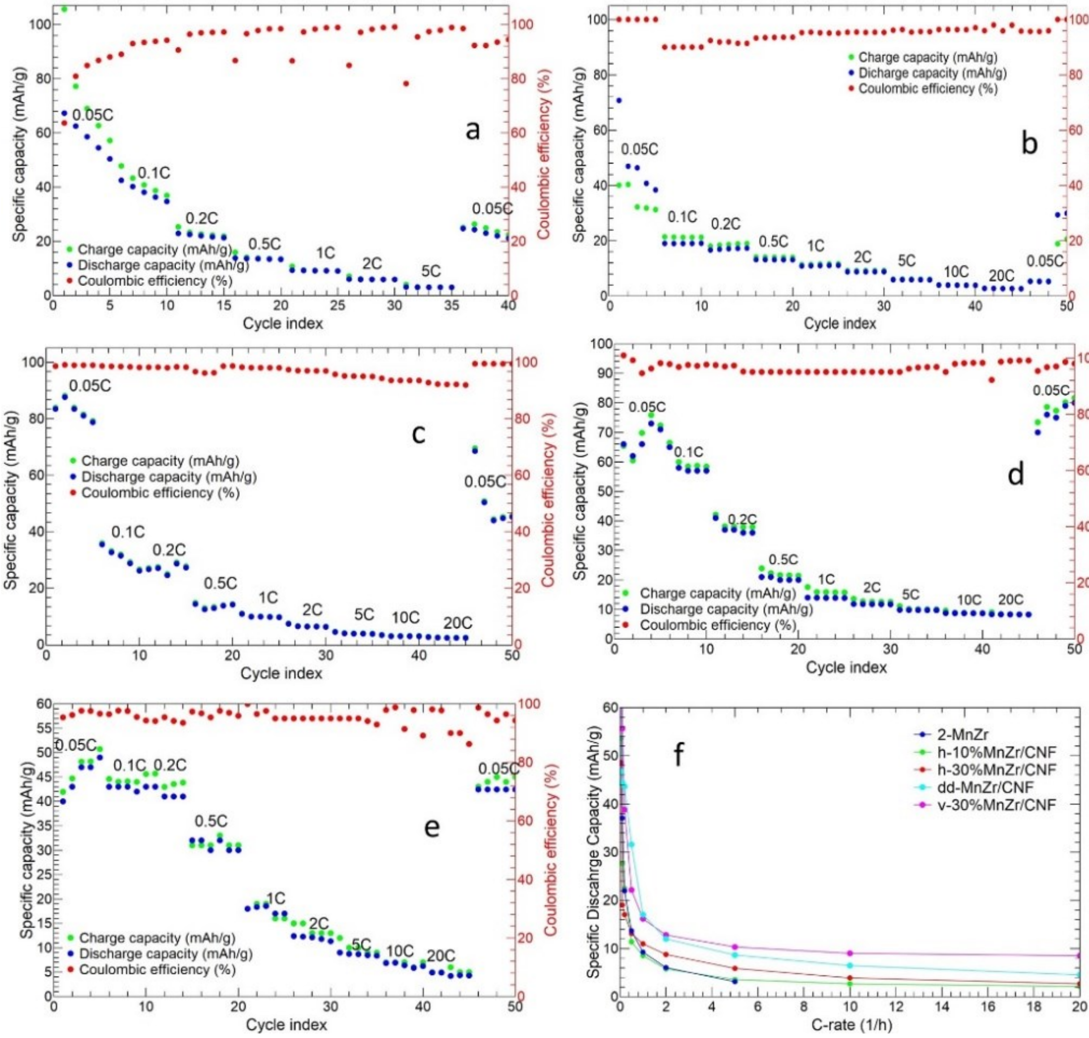

Figure 3.38: Charge/discharge cycles at different C-rate of a)2-MnZr, b) h-10%MnZr/CNF, c) h-30%MnZr/CNF, d) v-30%MnZr/CNF, and e) dd-MnZr/CNF. f) Comparison of average discharge capacity values for all samples at different C-rates.

Figure 3.38d shows the charge and discharge cycles at different C-rate for the v-30%MnZr/CNF sample. It exhibits an initial charge and discharge capacity of 65.4 mAh/g and 100.9 mAh/g, respectively, and the discharge value approaches the theoretical one (107 mAh/g) [56]. As for the h-30%MnZr/CNF, no initial discharge capacity loss is detected, and the sample completely recovers the initial capacity at the end of the measurement with a coulombic efficiency ≥96%. The average values of discharge capacity at 0.05C, 0.1C, 0.2C, 0.5C, 1C, 2C, 5C, 10C, and 20C, are 78.2, 55.7, 38.8, 22.2, 16.2, 12.8, 10.3, 9.0, and 8.5 mAh/g, respectively. These values are higher at each C-rate than the h-10%MnZr/CNF and h-30%MnZr/CNF samples, thanks to the higher amount of the 2-MnZr powder loaded into CNF sheets.

Finally, the charge/discharge cycles at different C-rates of the dd-MnZr/CNF sample are shown in Figure 3.38e. The initial charge and discharge capacities are 41.9, and 40.0mAh/g, respectively, similar to the value of h-10%MnZr/CNF cathode. In this case, the capacity is rather stable at low C-rates, and the capacity loss becomes remarkable only at C-rates higher than 0.2C. Indeed, the average capacity values are 46.7, 44.5, 43.6 mAh/g at 0.05C, 0.1C, and 0.2C, 31.6 and 17.0 mAh/g at 0.5C and 1C, 12.0, 8.7, 6.5

and 4.5 mAh/g at 2C, 5C, 10C and 20C, respectively. The capacity is completely recovered at the end of the measurement and a coulombic efficiency ≥94% is reached. Hence, the dd-MnZr/CNF self-standing cathode displays better electrochemical performances than the h-MnZr/CNF electrodes, but worse than the v-30%MnZr/CNF one. The results can be explained by the higher amount of active material (33 wt%) present in the CNFs compared to that of the horizontal samples (9.3 and 21.8 wt%). However, the active materials aggregates are non-homogeneously distributed along the CNFs sheets thickness and are preferentially located on their surface, and this undoubtedly affects the electrochemical performances. Notably, the v-30%MnZr/CNF cathode exhibits both high loading (29.8 wt%) and homogeneous distribution of the active material, and improved electrochemical performances are expected.

Figure 3.38f compares the average discharge capacities of all the investigated cathodes at the different C-rates. All the MnZr/CNF self-standing electrodes exhibit improved electrochemical performance compared to the 2-MnZr slurry cathode. Indeed, independently of the $Na_3MnZr(PO_4)_3$ amount in the CNF sheets, the self-standing electrodes are performant at C-rate higher than 5C, and the higher is the active material amount, the higher is the capacity value at each C-rate. This results confirm the beneficial role of CNFs especially at high C-rates, where the required fast ions diffusion is invalidated in packed materials, such as in tape casted cathodes [244,356]. However, among the three approaches applied to synthesize the self-standing electrodes, the dip-drop method lies between the horizontal and vertical settings, in terms of capacity value and electrochemical performance at high C-rate. The best electrochemical results are provided by the v-30%MnZr/CNF cathode, which exhibits not only the highest initial capacity values but also the best performance at high C-rate. The reported results confirm that the vertical set-up provides the best self-standing electrode. Based on this, we complete our investigation by testing the long cycling capability and lifespan of the v-30%MnZr/CNF sample, compared to the slurry one. We want to confirm that the right synthesis of self-standing electrode gives a cathode with longer cycling and better performance at high C-rates than slurry one, thanks to the CNFs properties.

The long charge/discharge cycling of the two cathodes is shown in Figure 3.39.

The tape-casted cathode (Figure 3.39a) is tested at 0.05C, 0.2C, and 1C for 5, 200, and 100 cycles. After the initial charge and discharge specific capacity of 104.3 mAh/g and 94.2 mAh/g, respectively, the cell undergoes a specific capacity loss: the value of 16.5 mAh/g is reached at the 82nd cycle at 0.2C. This specific capacity value is quite constant up to the 200th cycle at 0.2C with a capacity retention of 15.8% and an average coulombic efficiency ≥98%. When the cell is tested at 1C the specific capacity decreases down to 2.6 mAh/g, and cannot be further cycled at 0.05C.

The v-30%MnZr/CNF self-standing cathode is tested at 0.05C, 0.2C, 1C, 5C, 10C and 20C for 5, 50, 1000, 100, 50, and 30 cycles, respectively (Figure 3.39b). The initial charge and discharge capacity at 0.05C are 87.2 mAh/g and 85.4 mAh/g, respectively. Then, a discharge capacity loss is detected (45.2 mAh/g at 0.2C for 50 cycles), and an average value of discharge capacity of 19.3mAh/g at 1C, 4.2mAh/g at 5C, 3.7mAh/g at 10C, and 2.5mAh/g at 20C. The average coulombic efficiency is ≥91%, and the capacity is completely recovered at the end of the measurement in the last cycles at 0.05C. The capacity retention at 0.2C for 50 cycles and at 1C for 1000 cycles is 52.9% and 22.6%, respectively. We can conclude that, contrary to the 2-MnZr slurry cathode, the v-30%MnZr/CNF self-standing electrode presents a better capacity value at each C-rate, and it works at a high C-rate after 1000 cycles at 1C, too. Moreover, it also shows better capacity retention at both 0.2C and 1C.

Compared to the literature on other NASICON-type cathodes for SIBs [160], the v-30%MnZr/CNF sample gives lower values of specific capacity at different C-rate, in fact $Na_3V_2(PO_4)_3$ displays 107 mAh/g at 0.2C vs. 55.7 mAh/g for our cathode at the same C-rate. However, v-30%MnZr/CNF shows improved long-cycle life (1000 cycles at 1C), compared to 120 cycles at 0.2C for $Na_3V_2(PO_4)_3$ [160]. Compared to the work by Liu et al. in which $NaFePO_4$ nanodots (about 1.6 nm) are synthesized in-situ into N-doped CNFs [167], our v-30%MnZr/CNF shows lower values of specific capacity at different C-rate ($NaFePO_4$@C 129 mAh/g at 1C *vs.* v-30%MnZr/CNF 19.3 mAh/g at 1C) with shorter cycle life. This is attributed to the minimized size of the active material synthesized in situ into the CNFs matrix. This approach surely minimizes the active material's particles agglomeration, which increases the electrical resistance during cycling and inhibits the ion diffusion. Our synthetic gives different advantages: firstly, the active material particles can be modified, coated, functionalized or embedded increasing their electrochemical performance, secondly other upgrades can be reached simply adding the composite to the carbon precursor solution employed for electrospinning.

The electrochemical impedance spectroscopy (EIS) analysis is performed on the v-30%MnZr/CNF and 2-MnZr cathodes, to further investigate the effect of CNFs on the kinetic process of the self-standing electrodes. The Nyquist plot and the equivalent circuit are shown in Figure S. 10. The EIS spectra are consistent with those reported in the literature for the $Na_3MnZr(PO_4)_3$ active material [113]. The smaller diameter of the semicircle in the high-frequency region for the v-30%MnZr/CNF electrode suggests smaller charge-transfer resistance (807 Ω *vs.* 1092 Ω of the tape-casted cathode) and faster charge-transfer at the electrode-electrolyte interface. Moreover, the decrease of electrolyte resistance in self-standing electrode (10.7 Ω vs. 24.2 Ω for the tape-casted counterpart) suggests the better electrolyte permeation into MnZr/CNF electrodes, thanks to the presence of CNFs porous matrix. Finally, the larger slope of Warburg impedance for v-30%MnZr/CNF than for 2-MnZr cathode, indicates more favorable Na ion-transport is in the self-standing electrode.

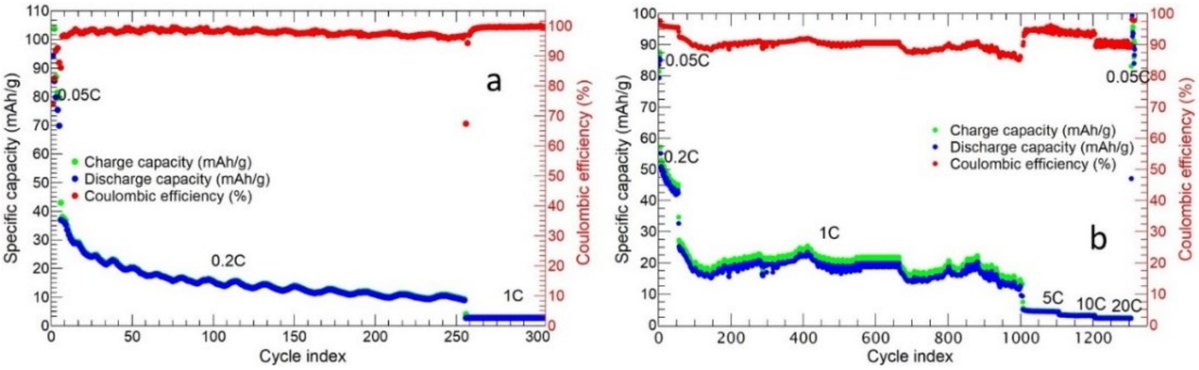

Figure 3.39: Comparison of long cycling of a) 2-MnZr slurry electrode and b) v-30%MnZr/CNF self-standing cathode.

The reported results put into evidence the advantages of using CNFs to assemble cathodes for SIBs. Improved electrochemical performance is obtained, as they enhance the electronic conductivity and guarantee a good electrolyte-active material contact, thanks to the easy permeation of the electrolyte into the CNFs porous matrix. Notably, they demonstrate to be a suitable support to realize free-standing electrodes, avoiding the use of Al foils as current collectors. Among the synthetic approaches to prepare electrospun active material/carbon nanofibers cathodes (see Figure 3.27), better electrochemical performance in terms of capacity values and lifespan are obtained for higher $Na_3MnZr(PO_4)_3$ amount, achieved by using a vertical setting in the electrospinning process: in this case, the active material particles, pre-synthesized via sol-gel, are quantitatively deposited in the CNFs sheets, compared to the horizontal setting. When comparable active material amount is loaded into CNFs (v-30%MnZr/CNF and dd-MnZr/CNF samples), the best performances are obtained by dispersing the pre-synthesized $Na_3MnZr(PO_4)_3$ powder into the polymeric solution to be electrospun, as this approach gives a homogeneous dispersion of the active material along the CNFs sheets and the agglomerates are present both within and embedded into the CNFs. On the contrary, in the dip-drop approach the active material is preferentially distributed on the sheets surface and the external surface of the carbon nanotubes.

Section 4. $Na_3MnTi(PO_4)_3$ self-standing cathode

As for the $Na_3MnZr(PO_4)_3$ cathode for SIBs, in this section we investigate the $Na_3MnTi(PO_4)_3$ powders synthesized via sol-gel with different amount of citric acid. Then, we characterize and investigate the electrochemical performances of self-standing $Na_3MnTi(PO_4)_3$/CNFs and tape-casted electrodes, to put into light the benefits and drawbacks of each approach. We recall that the $Na_3MnTi(PO_4)_3$ material has higher theoretical capacity than $Na_3MnZr(PO_4)_3$ for SIBs, and can be applied as both cathode and anode. In this work we focus our attention on the cathodic electrochemical activity for SIBs.

Subsection 12 Optimization of the $Na_3MnTi(PO_4)_3$ carbon coating

X-Ray powder diffraction analysis

In the Figure 3.40, the patterns of $Na_3MnTi(PO_4)_3$ samples synthesized with different citric acid amount are shown. All samples display pure and crystalline *NaSICON*-type crystal structure, consistent with the literature data [55]. We applied the Rietveld refinement to the diffraction data of the 2-MnTi sample. The structural model reported by Zhou and co-workers is used ($R\overline{3}c$ S.G. and lattice parameters a = 8.73352 Å, c= 21.84703 Å) and the Rietveld refinement results are reported in Table 3.3. The Figure S. 11 displays the experimental data are well fitted by the and refined structure.

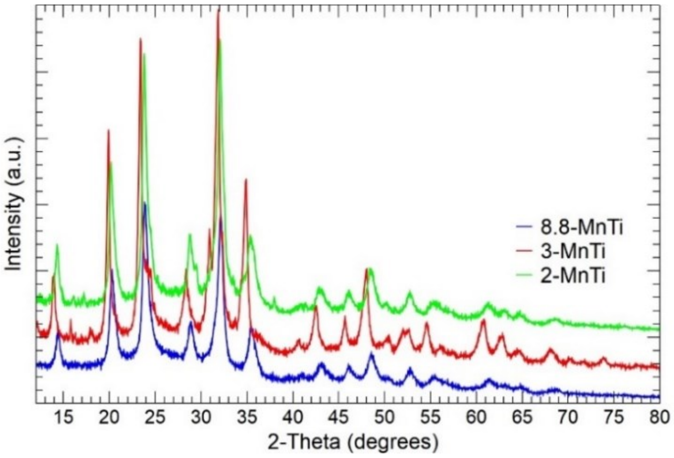

Figure 3.40: X-Ray diffraction patterns of $Na_3MnTi(PO_4)_3$ powder with different amount of citric acid in the sol-gel synthesis.

Table 3.3: Lattice parameters of 2-MnTi sample obtained by Rietveld refinement.

Lattice parameters	***2-MnTi***
a (Å)	8.696(2)
c (Å)	21.851(5)
V(Å^3)	1431.00
Crystallite size (nm)	18.7(3)
R_{wp}	6.26
Gof	1.34

Morphological analysis

The Figure 3.41 and Figure 3.42 shows SEM and TEM images, respectively, of the $Na_3MnTi(PO_4)_3$ samples with different amount of citric acid. The 8.8-MnTi SEM images (Figure 3.41a,b) display aggregates greater than 10µm which are composed by particles of about 1µm or maller, and the particles' morphology is rather homogeneous. The grain's surfaces are irregular but defined. The TEM photographs (Figure 3.42a,b) of the 8.8-MnTi sample confirm the presence of large carbon-coated aggregates of particles, but also carbonaceous agglomerates are detected. In the case of the 3-MnTi sample, SEM images (Figure 3.41c,d) show aggregates and particles morphology comparable to the 8.8-MnTi powder. The glassy effect on the particles' surface is present. The TEM photographs (Figure 3.42c,d) of the 3-MnTi powder confirm the presence of carbon-coated active material's aggregates, and carbonaceous agglomerates. The carbon layer is thinner and homogeneous, compared to the 8.8-MnTi powder. Again, the 2-MnTi sample SEM images (Figure 3.41e,f) display aggregates and morphology comparable to the other samples. The TEM photographs (Figure 3.42e,f) confirm the carbon coating, in lower amount compared to the 8.8-MnTi and 3-MnTi samples. Moreover, the carbon coating seems more homogeneously spread.

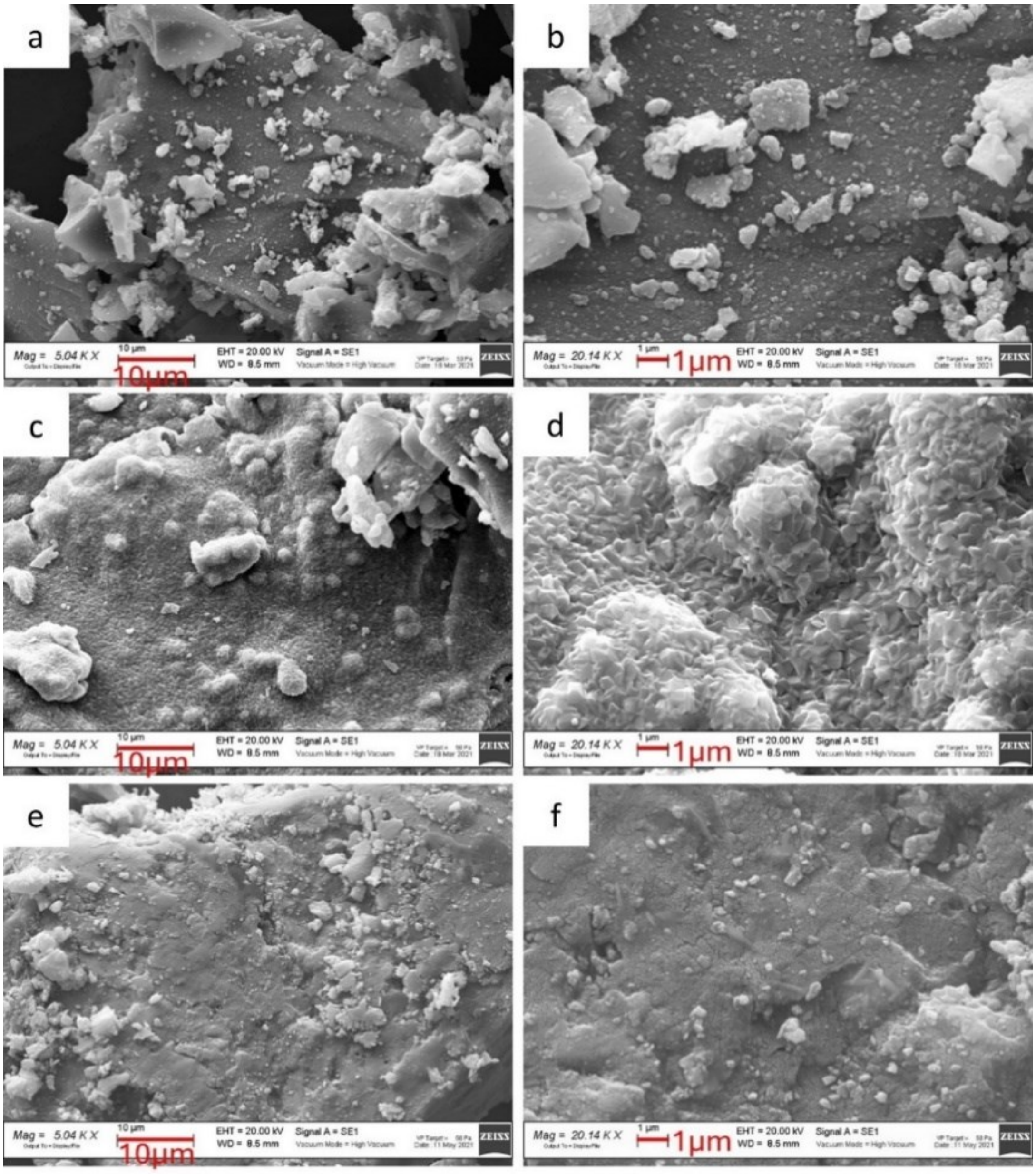

Figure 3.41: SEM images of $Na_3MnTi(PO_4)_3$: a,b) 8.8-MnTi; c,d) 3-MnTi; e,f) 2-MnTi.

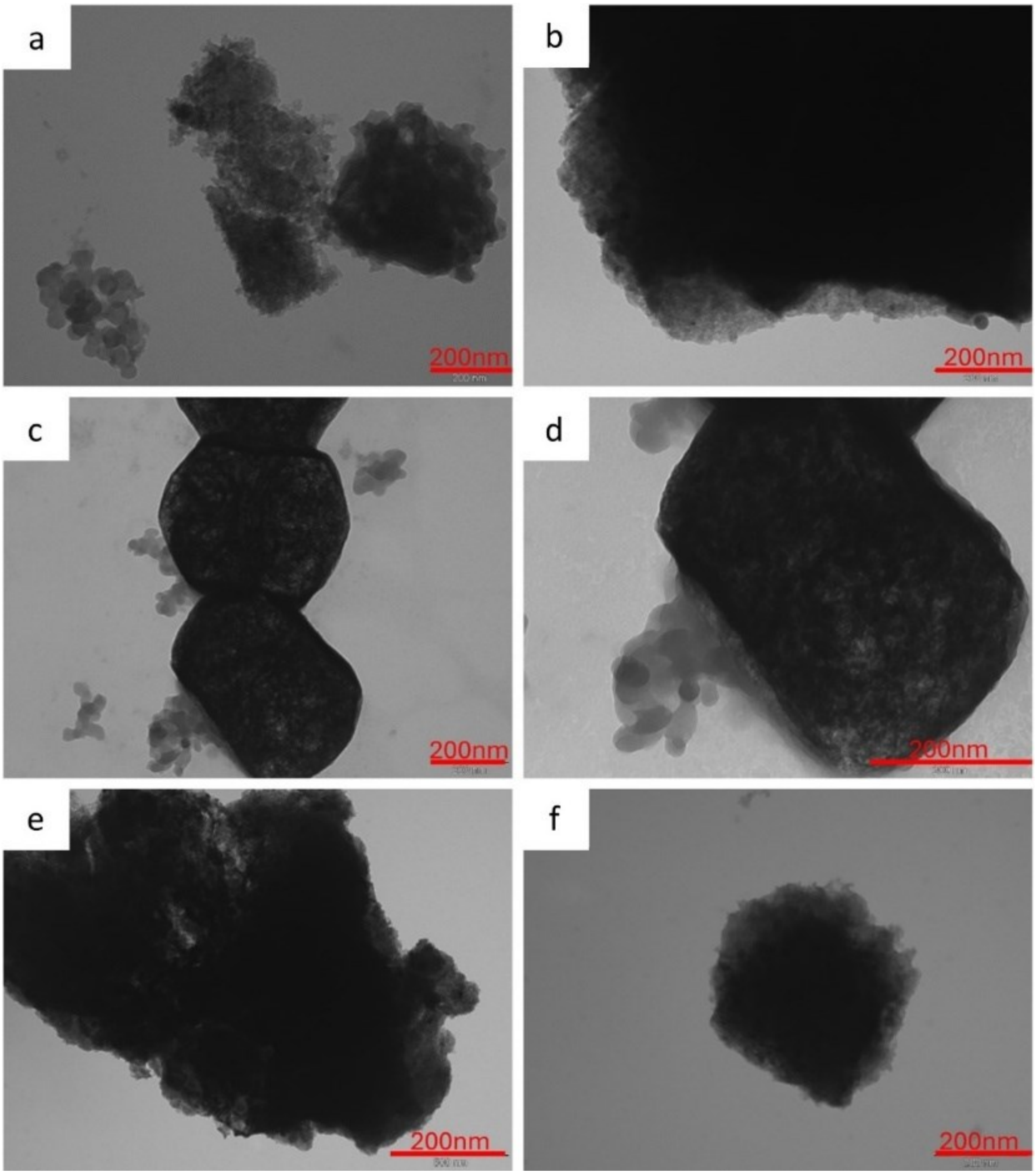

Figure 3.42: TEM images of $Na_3MnTi(PO_4)_3$: a,b) abundant citric acid, 8.8-MnTi; c,d) intermediate citric acid, 3-MnTi; e,f) stoichiometric citric acid, 2-MnTi.

Thermogravimetric and RAMAN analysis

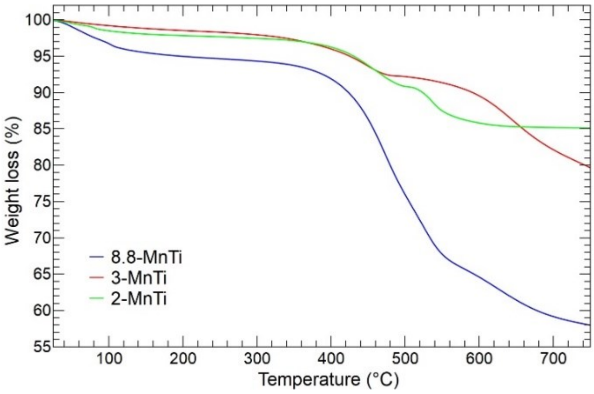

Figure 3.43: TG curves of 8.8-MnTi, 3-MnTi, and 2-MnTi samples.

The thermogravimetric analysis is used to determine the carbon amount present in the 8.8-MnTi, 3-MnTi, and 2-MnTi samples. The TGA curves are shown in Figure 3.43.

The 8.8-MnTi, 3-MnTi and 2-MnTi samples TG curves display three weight carbon losses. The first, at about 100°C, is due to the release of adsorbed water, while the second at 400-500°C and the third at 600°C are due to the combustion of the carbon coated on the powders agglomerates. For the 8.8-MnTi sample, the second and the third weight loss are 29.6 wt% and 5.01 wt%, respectively, with a total weight loss of 36.6 wt%. In the case of the 3-MnTi powder, the two weight losses at 400-500°C and 600°C are of 7.8 wt%, and 10.0 wt%, respectively, with a total loss of 17.8 wt%. The 2-MnTi sample displays two weight losses of 13.88 wt% at 400-500°C and 0.89 wt% at 600°C, with a final percentage of 14.77 wt %. Finally, the 2MnTi sample shows a very weak weight increase at 500°C, explained by the oxidation of the low-valence-state of metal species induced by carbon combustion, as reported by Zhou and co-workers [55].

The room temperature Raman analysis of all $Na_3MnTi(PO_4)_3$ samples with different amounts of citric acid are shown in Figure 3.44a,b. The presence of D and G bands into the samples' spectra confirms the morphological analysis on the presence of a carbon coating on the particles of each powder. The D mode seems to be broader than the G one in all the samples, suggesting the presence of disordered carbon.

The Figure 3.44b shows the value of I_G/I_D ratio for each sample. Usually, the I_D and I_G values correspond to the intensities of the modes, however, to better account for the broadening of the peak, we have used the integrated intensity of the two Gaussian functions used to best-fit the signal. The higher is the I_G/I_D value, the higher is the amount of graphitic carbon. We obtain comparable values for 8.8-MnTi and 3-MnTi samples, 0.87 and 0.815, respectively. While, for 2-MnTi powder, the value is slightly increased to 0.90. It suggest a better graphitization process in the 2-MnTi, that can improve the electronic conduction.

In the 200-680 cm^{-1} spectral range, all the samples (8.8-MnTi, 3-MnTi and 2-MnTi) display weak signals, attributable to the *NaSICON* structure, and better detectable in the Figure 3.54 of the $Na_3MnTi(PO_4)_3$ self-standing electrode.

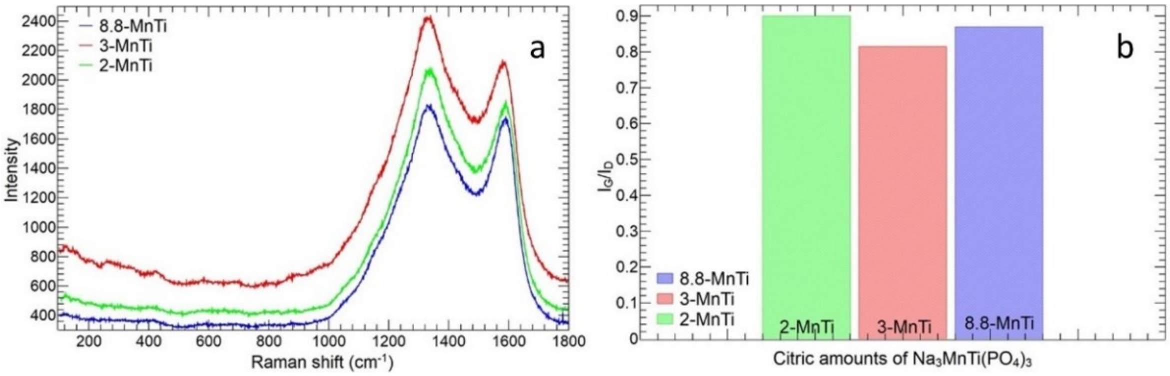

Figure 3.44: a) Raman spectra and b) I_G/I_D ratio for the $Na_3MnTi(PO_4)_3$ samples with different citric amount.

Electrochemical results

The cyclic voltammetry, and charge/discharge curves of the 8.8-MnTi, 3-MnTi, and 2-MnTi are shown in the Figure 3.45a,b, Figure 3.45c,d, and Figure 3.45e,f, respectively. The 8.8-MnTi sample shows only the red-ox peak of the Ti^{3+}/Ti^{4+} couple at 2V, with anodic/cathodic current of 0.01/-0.03 A/g (Figure 3.45a,b), and the manganese peaks Mn^{2+}/Mn^{3+} at 3.6V and Mn^{3+}/Mn^{4+} at 4.2V are faint. Instead, they are detected by decreasing the amount of citric acid in the synthesis (3-MnTi and 2-MnTi samples). Hence, the electrochemical performances depend on the amount of the citric acid used in the synthesis.

The 3-MnTi CV curves (Figure 3.45c,d) show anodic/cathodic peak current values of 0.02/-0.01 A/g at 3.7 V (Mn^{2+}/Mn^{3+}red-ox), 0.02/-0.009 A/g at 4.1 V (Mn^{3+}/Mn^{4+}red-ox peak), and 0.03/-0.03 A/g at 2.1 V (Ti^{3+}/Ti^{4+} red-ox peak). In the charge/discharge curves the plateaus at each red-ox reaction voltage are observed.

While the 2-MnTi presents higher value of anodic/cathodic current peaks with respect to 8.8-MnTi and 3-MnTi samples, implying an higher capacity storage (Figure 3.45e,f). Indeed, 2-MnTi shows anodic/cathodic peak values of 0.03/-0.02 A/g at 3.6 V, 0.02/-0.02 A/g at 4.0 V, and 0.05/-0.07 A/g at 2.1 V. The charge/discharge plateaus are clearly observed, flatter and more extended than other samples.

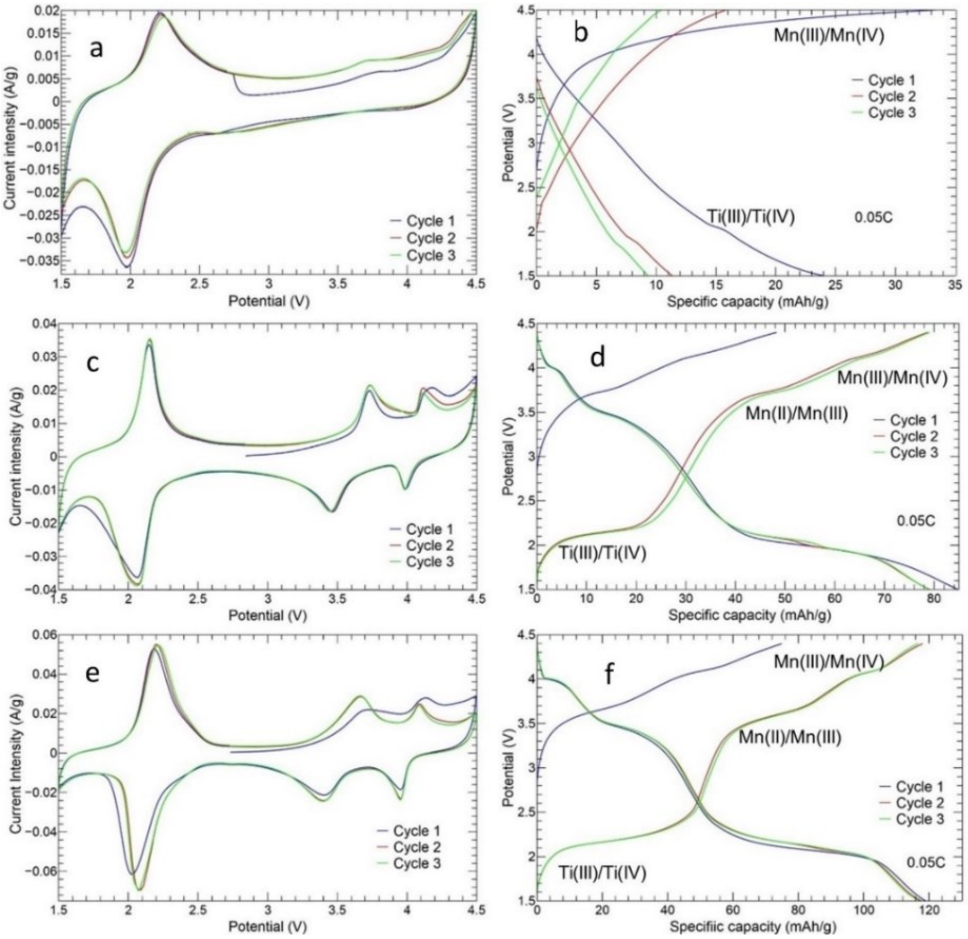

Figure 3.45: Cyclic voltammetry and charge/discharge cycles at 0.05C of a,b) 8.8-MnTi, c,d) 3-MnTi, and e,f) 2-MnTi samples.

The Figure 3.46a,b displays the charge and discharge cycles at different C-rate for the 3-MnZr and 2-MnZr cathodes, respectively, as the 8.8-MnTi does not show the manganese peaks in the CV.

The 3-MnTi powder displays an initial specific charge/discharge capacity of 49.12/84.8 mAh/g, with a coulombic efficiency ≥99%, and a complete capacity recovery at the end of the measurement, too. The initial charge capacity is lower than the following cycles because the OCV (between 2.5-2.8 V) is higher than the Ti^{3+}/Ti^{4+} redox potential. The average value of specific capacity are 79.9, 78.4, 69.2, 55.5, 44.2, 35.1 and 22.6 mAh/g at 0.05C, 0.1C, 0.2C, 0.5C, 1C, 2C and 5C, respectively.

Finally, the 2-MnTi sample shows an initial specific charge discharge capacity of 77.22 mAh/g and discharge capacity of 119.1 mAh/g close to the theoretical one (107.9mAh/g). The average capacity values of 117.8, 108.9, 102.2, 93.2, 85.3, 72.1, and 40.7 mAh/g at 0.05C, 0.1C, 0.2C, 0.5C, 1C, 2C, and 5C, respectively. The coulombic efficiency is ≥99%. Compared to the 3-MnTi electrode, the 2-MnTi shows higher specific capacities at all C-rates.

Compared to other *NaSICON* cathodes, the $Na_3MnTi(PO_4)_3$ working voltage range is higher than $Na_3V_2(PO_4)_3$ [172,350,351] and $Na_3Fe_2(PO_4)_3$ [58,58,117], and similar to the $Na_3Cr_2(PO_4)_3$ [117,118,352], and this suggests our cathode can theoretically store more energy than other well-known *NaSICON* materials. $Na_3MnTi(PO_4)_3$ display a theoretical capacity higher than the $Na_3Cr_2(PO_4)_3$ (117 mAh/g) [352] and $Na_3V_2(PO_4)_3$ (117.6 mAh/g) [351] and it can be applied both as anode and cathode for SIBs, making possible and easier the building of a symmetric cell. Thanks to the $Na_3MnTi(PO_4)_3$ environmental friendly elements and its better value of specific capacity at different C-rate than the other NaSICON structures, the $Na_3MnTi(PO_4)_3$ is a promising choice as cathode for SIBs.

To conclude, as for $Na_3MnZr(PO_4)_3$ samples, the amount of carbon coating affects the electrochemical performance. Indeed, in the case of $Na_3MnTi(PO_4)_3$, the influence is more pronounced, as for the 8.8-MnTi sample the Mn red-ox peaks are absent, while decreasing the amount of carbon coating (3-MnTi and 2-MnTi samples) the Mn-peaks are detected. In this work, the best electrochemical performances are obtained for the 2-MnTi sample, in terms of high energy density. We use this sample to prepare the self-standing electrodes.

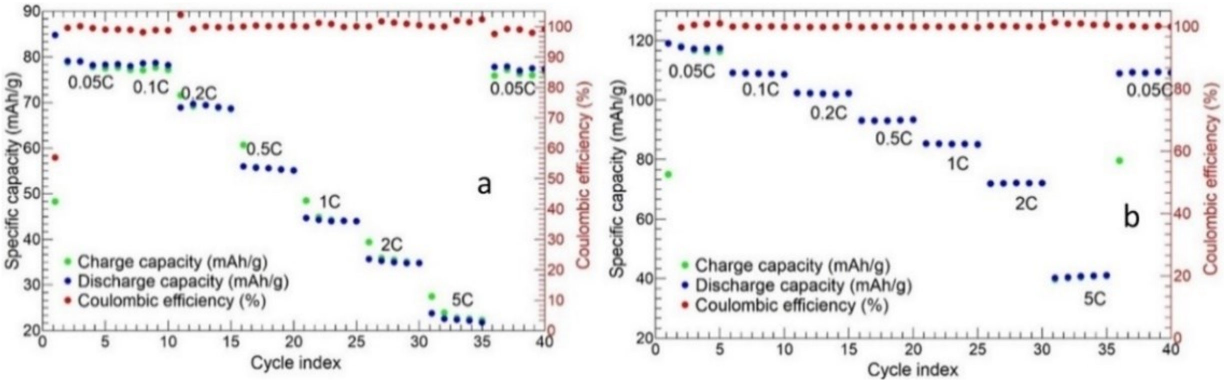

Figure 3.46: Charge/discharge cycles at different C-rate of a) 3-MnTi, and b) 2-MnTi samples.

Subsection 13 Self-standing cathode characterization

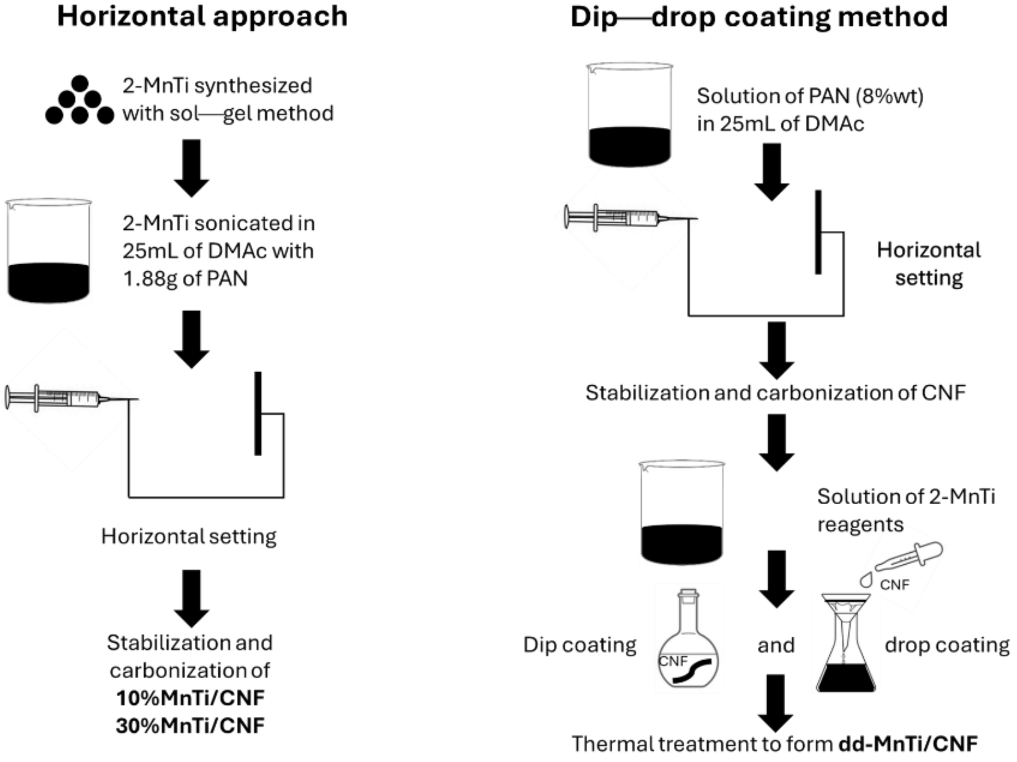

Figure 3.47: A scheme of the samples' synthesis.

We report the results for the self-standing electrodes prepared with the two synthesis approaches given in Section 2 of Chapter 2. Once verified that the $Na_3MnTi(PO_4)_3$ with *NaSICON* structure is successfully loaded into CNFs sheets without structural changes, we investigate the electrochemical properties of the self-standing electrodes compared to the abovementioned 2-MnTi tape-casted cathode. For this sample we report the results obtained by using the horizontal electrospinning apparatus and the dip-drop coating method, as schematized in Figure 3.47. The reported results obtained by the horizontal set-up are published by our research group in ref. [146].

X-Ray powder diffraction analysis

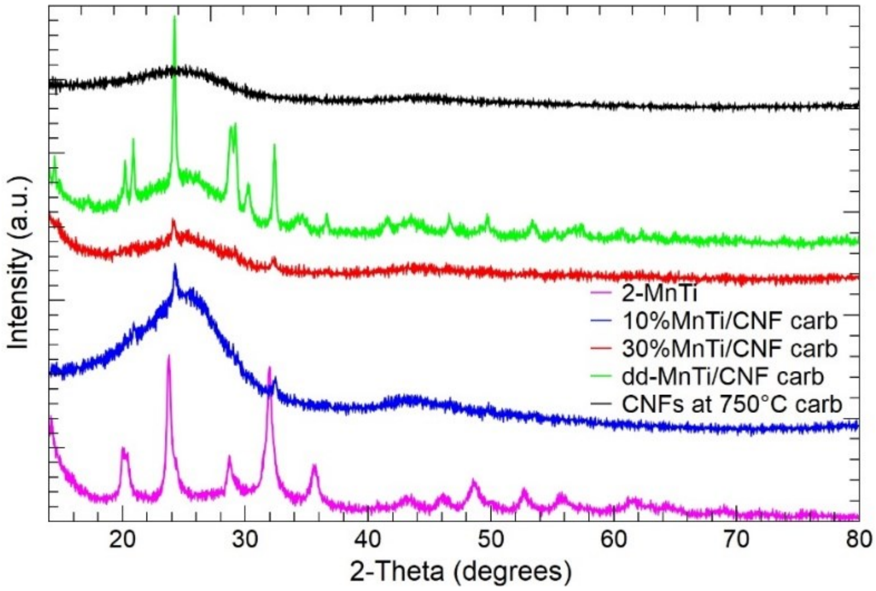

Figure 3.48: X-Ray diffraction patterns of the 2-MnTi, MnTi/CNF and pure CNF samples.

In the Figure 3.48 the diffraction patterns of all samples are shown. The 2-MnTi sample displays the diffraction peaks of the *NaSICON*-type crystal structure and well compares to the literature data [55]; no impurity phases are detected. The pure CNF sample displays the broad band at about 25°/2θ typical of amorphous components. In the MnTi/CNF samples, the peaks of the *NaSICON* structure and the amorphous CNF phase are detected. The Rietveld refinement is applied to the 10%MnTi/CNF and 30%MnTi/CNF diffraction patterns. The structural model reported by Zhou and co-workers [55] is used ($R\overline{3}c$ S.G. and lattice parameters a = 8.73352 Å, c= 21.84703 Å). The lattice parameters, crystallite size and degree of crystallinity obtained by the Rietveld refinement are reported in Table S. 3, and Figure S. 12 compare the experimental and calculated patterns. Table S. 3 also reports the refined data of the 2-MnTi sample, for comparison.

The discrepancy factors values (Table S. 3) and the graphical comparison (Table S. 3: Na3MnTi(PO4)$_3$ lattice parameters, crystallite size, crystallinity degree, discrepancy factor and goodness of fit obtained by the Rietveld refinement of the 2-MnTi and MnTi/CNF samples. Cell volumes and c/a ratios are also reported.

Figure S. 12a,b) demonstrate the refined model properly fits the experimental XRPD data. For both 10%MnTi/CNF and 30%MnTi/CNF samples, a decrease of the *a* lattice parameter is observed, causing the cell volume shrinkage and the *c/a* ratio increase (Table S. 3). The cell volume decrease may be attributed to the sintering temperature of 750°C used for the carbonization process, and not to the inclusion into carbon nanofibers. In fact, the same shrinkage was detected on $Na_3MnTi(PO_4)_3$ synthesized at the same temperature by Liu and coworkers [357]. Moreover, the temperature higher than that usually chosen in the sol-gel synthesis (650°C) may increase intrinsic anti-sites defects, responsible for the charge/discharge voltage hysteresis [358]. The cell shrinkage inhibits the Na2 reversible insertion/extraction and impacts the electrochemical performances. However, we choose the carbonization temperature of 750°C, based on the improved conductivity of pure CNFs: 1.56×10^{-3} S/cm and 1.76×10^{-6} S/cm for carbonization at 750°C and 650°C, respectively. The $Na_3MnTi(PO_4)_3$ active material particles in both 2-MnTi and MnTi/CNF samples are nanocrystalline (Table S. 3) and the crystallite size does not depend on the sintering temperature. The degree of crystallinity is about 9 % for both the 10%MnTi/CNF and the 30%MnTi/CNF samples (Table S. 3). This suggests the 10%MnTi/CNF and 30%MnTi/CNF samples are comparable, notwithstanding the different composition of the electrospun dispersions.

Instead, the Rietveld refinement of the dd-MnTi/CNF sample, prepared by dip-drop coating method, clearly demonstrate the presence of the peaks pertinent to the *NaSICON* structure, but also additional peaks of impurity phases (Figure S. 12c). The impurities are probably due to the multiple heat treatments at the temperature of 750°C, necessary to enhance the CNFs conductivity, and by the synthesis in situ of the compound, which could depend by the presence of the CNFs matrix.

In the Figure S. 13, the X-Ray pattern of all samples at each synthesis step are reported.

Morphological analysis

The SEM surface and cross-section images of the 10%MnTi/CNF sheets (Figure 3.49(a-c)) demonstrate that the $Na_3MnTi(PO_4)_3$ is dispersed into nanofibers and forms agglomerates with widely varying size distribution. The 10%MnTi/CNF sheet thickness is 47.93 µm. As in the case of the 10%MnTi/CNF, the SEM surface and cross-section images of the 30%MnTi/CNF sample (Figure 3.49(d-f)) displays agglomerates with uneven size spread into the CNFs matrix. The sheet thickness is 292.5 µm.

The morphology, particle size and distribution of the active material in self-standing electrodes is deeply investigated by TEM analysis. The TEM images of the 10%MnTi/CNF sample (Figure 3.50a-c) display $Na_3MnTi(PO_4)_3$ nanoparticles of about 28 nm, consistent with the crystallite size reported inTable S. 3, which aggregate and segregate between and into nanofibers. The CNFs diameter ranges between 120 and 170 nm. The 30%MnTi/CNF sample displays comparable morphology (Figure 3.50d-f), with $Na_3MnTi(PO_4)_3$ aggregates both between and embedded into nanofibers. The CNFs diameter ranges between 90 and 120 nm. In both MnTi/CNF samples, the agglomerates display widely varying sizes.

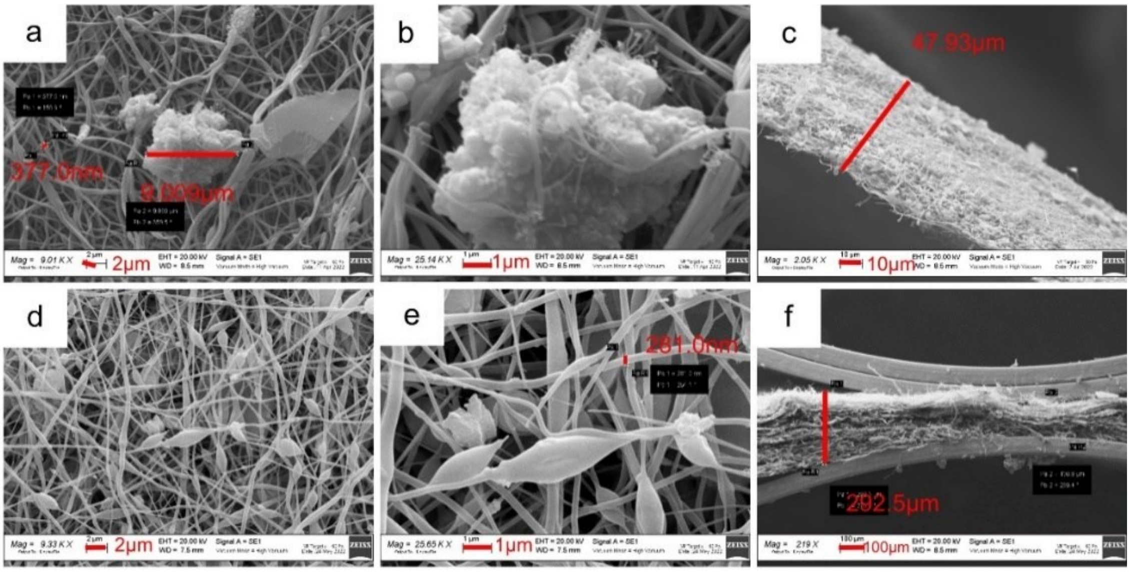

Figure 3.49: SEM images of surface a, b) and cross-section c) of the 10%MnTi/CNF sample. SEM images of surface d, e) and cross-section f) of the 30%MnTi/CNF sample.

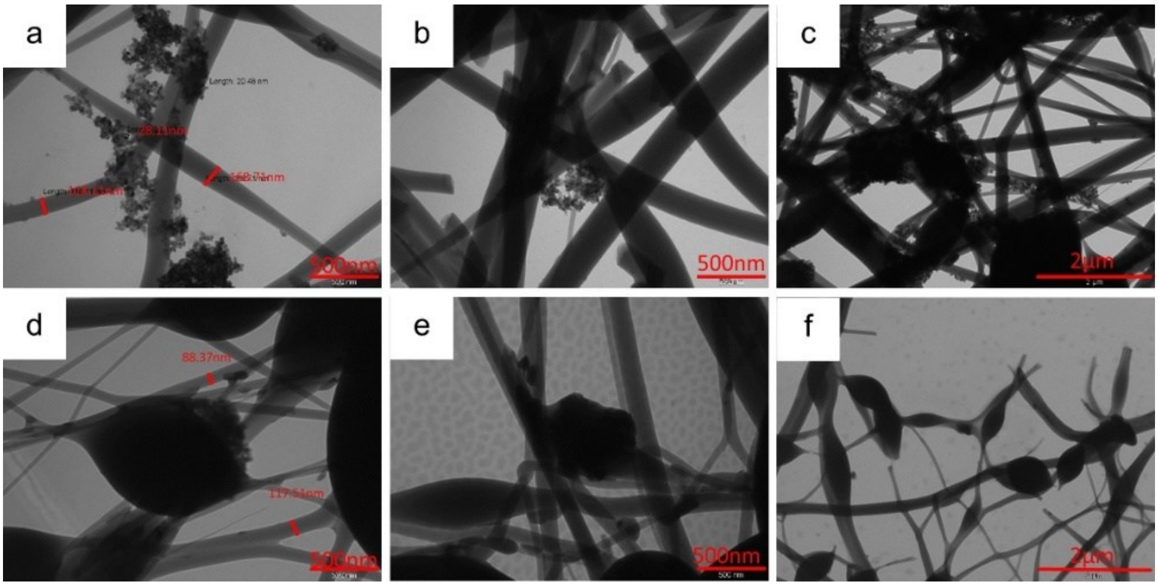

Figure 3.50: TEM images of a, b, c) 10%MnTi/CNF and d, e, f) 30%MnTi/CNF samples taken at different magnification.

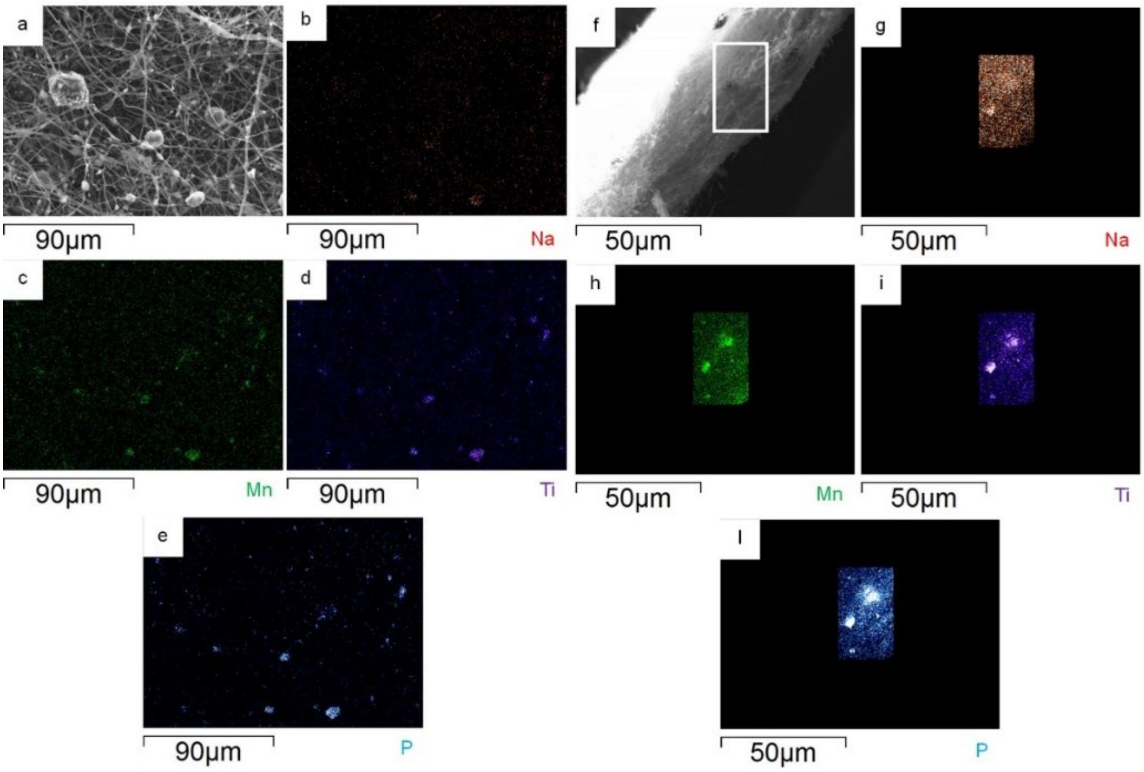

Figure 3.51: On the left: a) surface portion of 10%MnTi/CNF sample and distribution maps of b) Na, c) Mn, d) Ti and e) P. On the right: f) cross-section portion of 10%MnTi/CNF sample and distribution maps of g) Na, h) Mn, i) Ti and l) P.

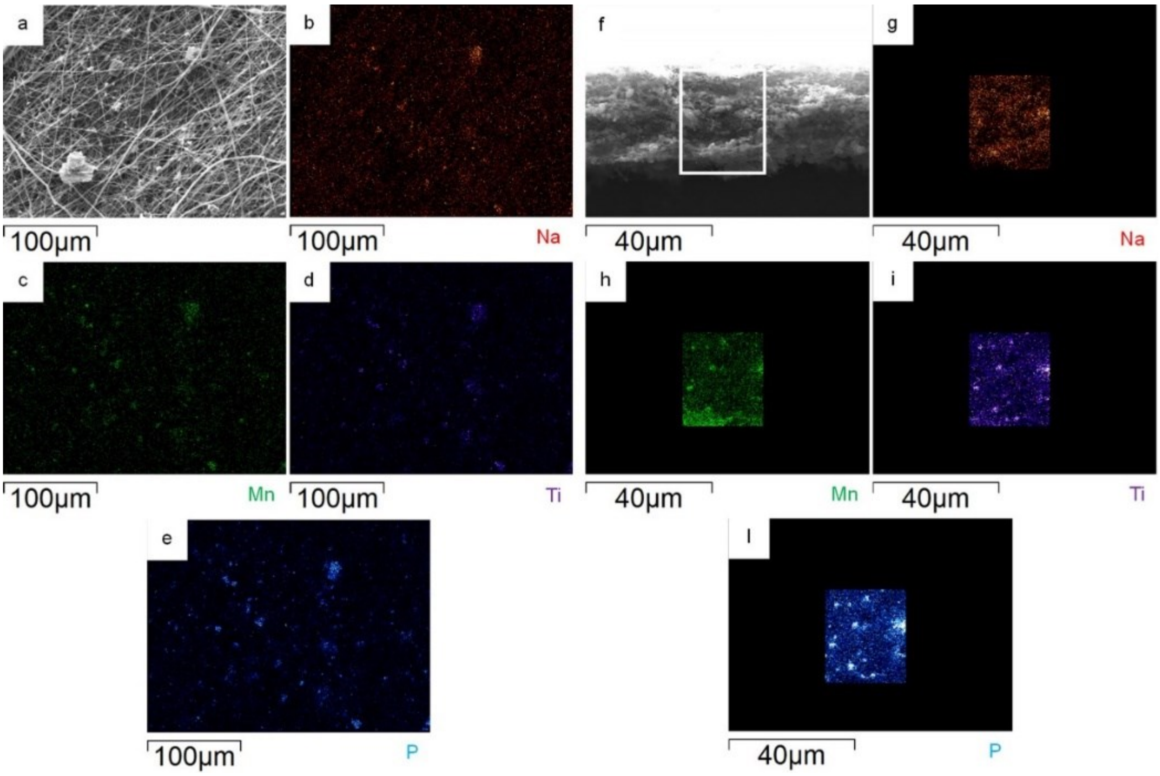

Figure 3.52: On the left: a) surface portion of 30%MnTi/CNF sample and distribution maps of b) Na, c) Mn, d)Ti and e) P. On the right: f) cross-section portion of 30%MnTi/CNF sample and distribution maps of g) Na, h) Mn, i) Ti and l) P.

The surface and bulk distribution of 2-MnTi powder in the MnTi/CNF self-standing electrodes is investigated by EDS. The Na, Mn, Ti, and P distribution maps of the surface portion of the 10%MnTi/CNF sample (Figure 3.51a-e) confirm the active material aggregates within and between CNFs, and is homogeneously spread in CNFs. Noteworthy, the particles of the active material are spread along the sheet thickness, as demonstrated by the cross-section elements distribution maps (Figure 3.51f-l); this is beneficial to obtain enhanced electrochemical performances and it is not easily achieved by dip-and drop-coating approach for loading the active material onto CNFs. Comparable EDS results are obtained for 30%MnTi/CNF, as demonstrated by the elements distribution maps on the sample's surface (Figure 3.52a-e) and cross-section (Figure 3.52f-l).

Thermogravimetric and RAMAN analysis

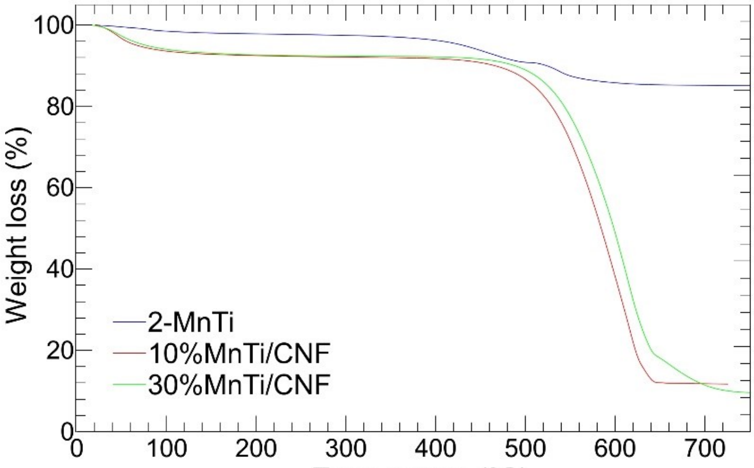

Figure 3.53: TGA curves of 2-MnTi (blue), 10%MnTi/CNF (red) and 30%MnTi/CNF (green) samples.

The $Na_3MnTi(PO_4)_3$ amount loaded into CNFs is evaluated by thermogravimetric analysis. The thermogravimetric curves of 2-MnTi, 10%MnTi/CNF and 30%MnTi/CNF samples are shown in Figure 3.53.

The 2-MnTi TGA curve displays three weight losses: 1.43 wt% at 100°C, 13.88 wt% at 400-500°C and 0.89 wt% at 600°C. The first loss is due to the release of adsorbed water, the second and third account for the carbon coating content in the 2-MnTi sample: 14.77 wt%. Finally, the very weak weight increase at 500°C is explained by the oxidation of the low-valence-state of metal species induced by carbon combustion, as reported by Zhou and co-workers [55].

The TGA curves of the 10%MnTi/CNF and 30%MnTi/CNF samples also show two mass losses (i) below 100 °C, due to the adsorbed water release and (ii) in the 500°C–650°C temperature range, involving the carbonaceous component combustion of both the $Na_3MnTi(PO_4)_3$ carbon coating and the carbon nanofibers. The 10%MnTi/CNF and 30%MnTi/CNF samples give a residual mass of 11.73 wt% at 650 °C and 9.59 wt% at 700°C, respectively. The results are comparable and matches the synthesis value of the 10%MnTi/CNF self-standing electrode. In the case of the 30%MnTi/CNF sample, the $Na_3MnTi(PO_4)_3$ amount is much lower than the synthesis value (30 wt%). We recall that the two samples also give comparable degree of crystallinity (Table S. 3). We repeated the synthesis of the 30%MnTi/CNF sample, and we noticed that active material's sedimentation occurs along the tube connecting the pump and the needle of the horizontal spinneret. We also tried to prepare the self-standing electrode by using a vertical set-up, but again the $Na_3MnTi(PO_4)_3$ amount in the self-standing electrode does not achieve the 30 wt% value. Based on the above-mentioned reasons, we decided to investigate the electrochemical performances of the MnTi (tape-casted) and 10%MnTi/CNF (self-standing) electrodes.

The room temperature Raman spectra of the 10%MnTi/CNF and 30%MnTi/CNF self-standing samples, of the 2-MnTi powder and of CNFs are reported in Figure 3.54a. The 2-MnTi spectrum displays some broad signals in the low frequency region (see inset). According to [189], the most prominent features at about 565 and 680 cm^{-1} could be ascribed to P−O and P−O−Na vibrations together with possible contribution by Ti−O ones; while less intense modes are visible below 300 cm^{-1} and they could arise from the vibrations involving Mn ions. Despite the 2-MnTi sample that shows low energy modes, each spectrum is only dominated by two intense modes that fall at about 1340 and 1585 cm^{-1}. These features are the characteristic signature of carbonaceous materials, through which it is possible to obtain information about the order/disorder as well as the crystalline quality of the structure. As mentioned in the Subsection 10, the synthesis route affects the dispersion of the active material powder into CNFs, and so its exposure to the Raman sampling. In addition, for both 10%MnTi/CNF and 30%MnTi/CNF self-standing samples, we loaded only the 10% of active material, and the NASICON-structure Raman signals are overwhelmed by carbon peaks present in large amount.

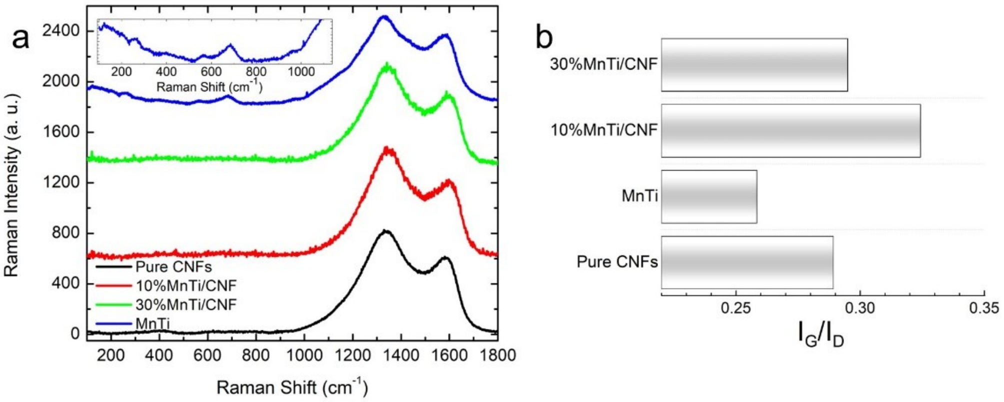

Figure 3.54: a) Room temperature Raman spectra of pure CNFs, 10%MnTi/CNF, 30%MnTi/CNF and 2-MnTi powder (from bottom to top); b) I_G/I_D values reported for each investigated sample.

The presence of the D and G band also in the 2-MnTi spectrum confirm the morphological analysis on the presence of a carbon coating on the 2-MnTi particles. The D mode seems to be broader than in the other samples, pointing out a more disordered structure.

In Figure 3.54b the value of the I_G/I_D ratio is reported for each sample. The smallest I_G/I_D value (0.26) is obtained for the 2-MnTi sample as it is reasonable to be expected: CNFs are the main source of ordered carbon, beneficial for the electronic conductivity enhancing the performance of electrodes. Noteworthy, the higher I_G/I_D value is detected in the 10%MnTi/CNF sample, which will be electrochemically evaluated.

Subsection 14 Tape-casted and Self-standing cathodes electrochemical comparison

The 2-MnTi CV curve is shown in Figure 3.55a. The slurry electrode displays the three redox peaks of Ti^{3+}/Ti^{4+}, Mn^{2+}/Mn^{3+} and Mn^{3+}/Mn^{4+} at 2.20 V/2.06 V, 3.67 V/3.41 V and 4.08 V/3.95 V, respectively. The ΔV for of Ti^{3+}/Ti^{4+} peak is 139 mV and progressively diminishes for Mn^{2+}/Mn^{3+} (26 mV) and Mn^{3+}/Mn^{4+} (13 mV). It indicates a quite small polarization phenomenon. The current intensity is higher than 0.04 A/g and lower than -0.06A/g for anodic and cathodic peaks, respectively. The three redox couples are also consistent with the three evident plateaus detected in the Galvanostatic charge-discharge profiles shown in Figure 3.55b. In the first charge process, the plateau of the Ti^{3+}/Ti^{4+} redox couple is not observed due to the initial open circuit voltage (2.5 V-2.7 V). The 10%MnTi/CNF CV curves and charge/discharge profiles are reported in Figure 3.55c and Figure 3.55d, respectively. In this case, only the Ti^{3+}/Ti^{4+} redox peaks at 2.12 V/2.06 V are detected while the Mn^{2+}/Mn^{3+} and Mn^{3+}/Mn^{4+} ones become very faint. The sluggish redox activity may be attributed to the cell shrinkage at a sintering temperature of 750°C, and to the intrinsic anti-site defect: Mn occupies the Na2 vacancy and hampers the sodium ion diffusion and the manganese redox processes, as reported also in the literature [358].

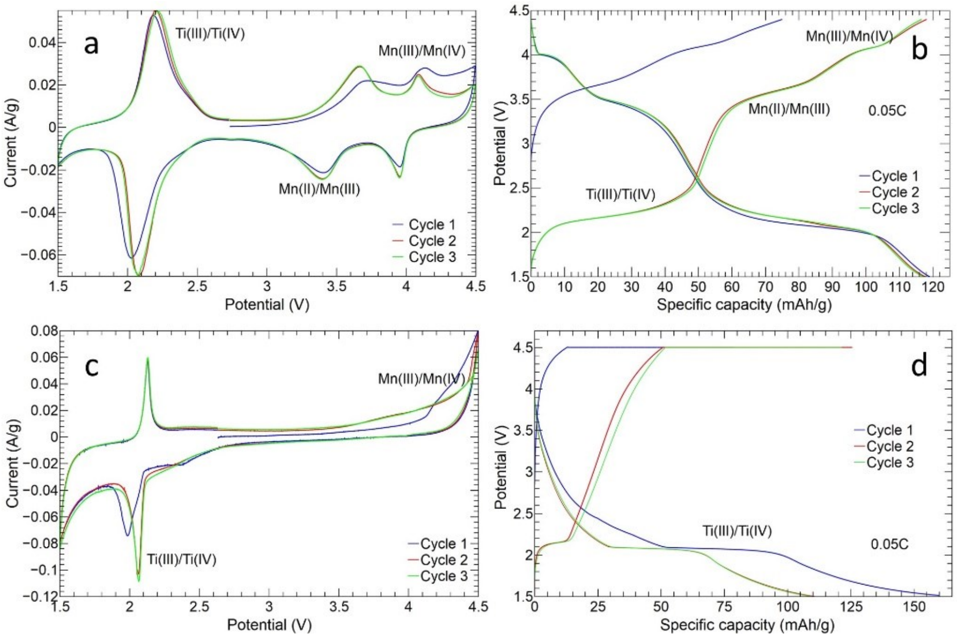

Figure 3.55: Cyclic voltammetry curves and first three charge/discharge profiles of a, b) 2-MnTi tape-casted and c, d) 10%MnTi/CNF electrodes. The analysis is made in the range of 1.5-4.5V at 0.1 mV/s.

However, the temperature of 750°C is necessary to obtain a successful carbonization. Secondly, we underline the 10%MnTi/CNF electrode contains only 10 wt% of active material against the 70 wt% present in the 2-MnTi slurry electrodes, and this can influence the CV. As already mentioned for $Na_3MnZr(PO_4)_3$ structure, a high carbon amount negatively affects the electrochemical performance. Especially in the case of $Na_3MnTi(PO_4)_3$, we observed only the red-ox peak of titanium, while the manganese peaks are absent in the cyclic voltammetry of 8.8-MnTi sample, which exhibits the higher amount of carbon coating (see Subsection 12 of Chapter 3, Figure 3.45: Cyclic voltammetry and charge/discharge cycles at 0.05C of a,b) 8.8-MnTi, c,d) 3-MnTi, and e,f) 2-MnTi samples.).

The 10%MnTi/CNF Ti^{3+}/Ti^{4+} redox reaction is also confirmed by the evident plateau in Figure 3.55d. In the CV (Figure 3.55c) the weak peak at 2.4 V is explained by the disproportion reaction of Mn^{3+} dissolved in the electrolyte [359]. Finally, the cycles are overlapped to demonstrate a good redox reversibility.

Figure 3.56Figure 3.57a,b show the CV curves at different scan rates for MnTi and 10%MnTi/CNF samples, respectively. The data were analyzed to evaluate the sodium ion diffusion coefficient, the alkali metal-ion faradaic contribution (diffusion control), and the non-faradaic one (pseudo-capacitance control) caused by the formation of the double layer at the material surface.

The pseudo-capacitance contributions are shown in Figure 3.56(b-c) and Figure 3.56(e-f) for the 2-MnTi and 10%MnTi/CNF samples, respectively.

The slurry electrode (A = 0.78 cm^2) exhibits diffusion coefficients for anodic peaks $D_{Ti(III)/Ti(IV)}$=1.3x10^{-9}cm^2/s, $D_{Mn(II)/Mn(III)}$=8.4x10^{-9}cm^2/s and $D_{Mn(III)/Mn(IV)}$=1.6x10^{-10} cm^2/s. In the case of the cathodic peak, the D values are $D_{Ti(III)/Ti(IV)}$=2.2x10^{-9} cm^2/s, $D_{Mn(II)/Mn(III)}$=7.6x10^{-9} cm^2/s and $D_{Mn(III)/Mn(IV)}$= 1.4x10^{-9} cm^2/s. The results are consistent with the literature ones [55,357].

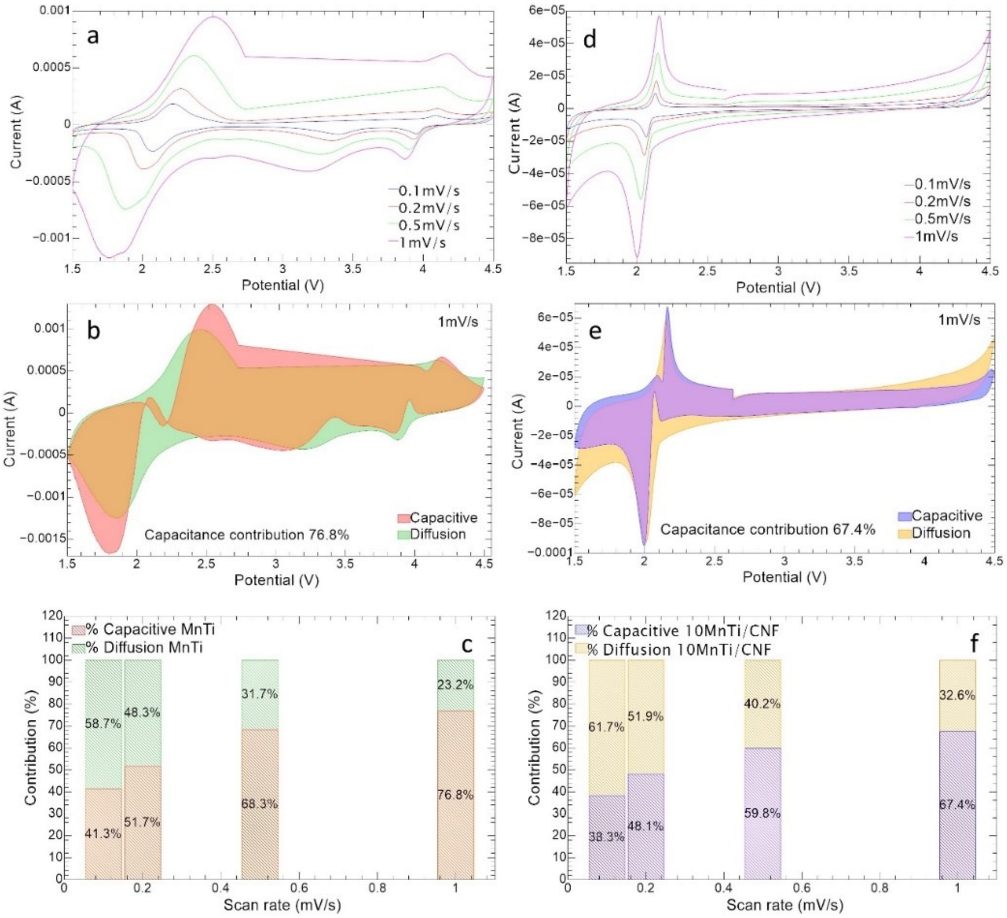

Figure 3.56: Cyclic voltammetry at different scan rate for a) MnTi slurry and d) 10%MnTi/CNF electrodes. Capacitance contribution at 1mV/s for b) MnTi slurry and e) 10%MnTi/CNF electrodes. Capacitance and diffusion histogram for c) MnTi slurry and f) 10%MnTi/CNF.

An equivalent analysis can be conducted for the self-standing electrode as well. Contrary to the 2-MnTi slurry, the 10%MnTi/CNF electrode features a three-dimensional structure, whose main advantage is the substantial increase of the active material surface. Indeed, the 10%MnTi/CNF area A cannot be estimated from the electrode section. Therefore, we evaluate an equivalent anodic diffusion coefficient D_{eq} = 2.6x10^{-12} cm^2/s and cathodic D_{eq} = 1.0x10^{-11} cm^2/s for Ti^{3+}/Ti^{4+} redox couple, where we assume the electrode area A be equal to its section. The result is consistent with the fact that the Ti^{3+}/Ti^{4+} self-standing cathode shows lower current intensity than its slurry counterpart (see Figure 3.56a and d), and this depends on the $Na_3MnTi(PO_4)_3$ amount in the 10%MnTi/CNF and 2-MnTi electrodes (10 and 70 wt%, respectively). The low amount of the active material leads to a low electrochemical active area. To compare the performance of slurry and self-standing electrodes, the capacity contribution of diffusion- and reaction- (capacitive contribution) control as a function of CV sweep rates were calculated. As shown in Figure 3.56(e-f), the 10%MnTi/CNF sample exhibits a higher contribution of diffusion control at each scan rate than the slurry counterpart (Figure 3.56b and c), thanks to the presence of the very porous CNF sheets. Indeed, the porosity of non-woven nanofibers guarantees an easier electrolyte diffusion which easily gets in touch with active material particles as reported in the literature [244,250]. This aspect is also confirmed by the analysis of electrolyte permeation shown in Figure S. 14, for the 10%MnTi/CNF sample. The electrolyte permeation is complete and fast in carbonized samples. After 50 ms the electrolyte is completely absorbed by the 3D CNFs network. The impregnation of the self-standing electrode is demonstrated, because the electrode swells. The contact angle cannot be evaluated due to the fast electrolyte adsorption.

Finally, comparing the Figure 3.56a and Figure 3.56d, all slurry anodic and cathodic peaks tend to move to the right and left, respectively, as the scan rate increases, while this behavior is less pronounced for self-standing sample. As example, the Ti^{3+}/Ti^{4+} redox peak overpotentials of the 2-MnTi sample are 139 mV, 280 mV, 503 mV and 768 mV as scan rate increases, against 63 mV, 58 mV, 119 mV and 154 mV for the 10%MnTi/CNF. The results suggest more irreversible redox processes in the slurry electrode than in the self-standing one.

Figure 3.57 shows the charge/discharge analysis for both 2-MnTi and 10%MnTi/CNF samples.

The 2-MnTi displays an initial charge and discharge capacity of 75.02 and 119.08 mAh/g, respectively (Figure 3.57a). The initial charge capacity is lower than the following cycles because the OCV (between 2.5-2.8 V) is higher than the Ti^{3+}/Ti^{4+} redox potential. We obtain average discharge capacities of 117.76, 109.80, 102.69, 93.67, 85.09, 71.83, 42.03, 5.70 and 4.12 mAh/g at 0.05C, 0.1C, 0.2C, 0.5C, 1C, 2C, 5C, 10C and 20C, respectively. The cell exhibits a good capacity recovery at the end of the measurement and a coulombic efficiency ≥98%. In the Figure 3.57b the long charge/discharge cycles are shown. After the first 5 cycles at 0.05C, the cell is tested at 0.2C, 1C and 5C for 240, 50, 20 cycles, respectively. The initial discharge capacity is 106.48 mAh/g and the cell exhibits a coulombic efficiency ≥99%. The specific capacity decreases increasing both cycle index and C-rate value. For the first 190 cycles at 0.2C the average capacity value is 84.24 mAh/g, while it diminishes to 71.63 mAh/g in the following 50 ones at the same C-rate with a capacity retention of 73.97% at the 240th cycle. By increasing the C-rate from 0.2C to 1C the capacity value decreases to 16.18 mAh/g, while at 5C the cell does not work. So, it can be concluded that the 2-MnTi sample does not support C-rate higher than 1C after 290 cycles.

The 10%MnTi/CNF shows an initial charge and discharge capacity of 109.9 and 160.04 mAh/g, respectively (see Figure 3.57c). We obtain average discharge capacities of 124.38, 115.68, 111.04, 100.68, 93.6, 91.42, 89.15, 88.30 and 77.60 mAh/g at 0.05C, 0.1C, 0.2C, 0.5C, 1C, 2C, 5C, 10C and 20C, respectively. At the end of the measurement the cell completely recovers the initial capacity with a coulombic efficiency ≥98%. Contrary to the slurry 2-MnTi electrode, the self-standing 10%MnTi/CNF one exhibits (i) a very moderate capacity loss by increasing the C-rate, (ii) good stability and reversibility of sodium storage and (iii) promising performances also at C-rates higher than 5C. The 10%MnTi/CNF ability to cycle at high C-rate is guaranteed by the presence of CNFs 3D network that gives high porosity and so an easier diffusion of Na-ion. The consequence is an high power density, as reported by Vu and co-workers [244]. The capacity values of the 10%MnTi/CNF electrode shown in Figure 3.57c are comparable to the literature ones [184,359]. Notably, these promising electrochemical performances are obtained on an electrode synthesized by a simple and feasible approach with an active material amount of 10 wt%, against the 70-80 wt% of the conventional tape-casted electrodes. We underline some drawbacks can be envisaged in the sintering temperature of 750°C, necessary for the CNFs graphitization, as it induces the cell shrinkage and the sluggish of the redox process. Anyway, they are overcome thanks to the advantages of the CNFs: they provide conducive carbon, porous matrix beneficial for electrolyte-active material contact, easy sodium ions diffusion, light and self-standing electrode.

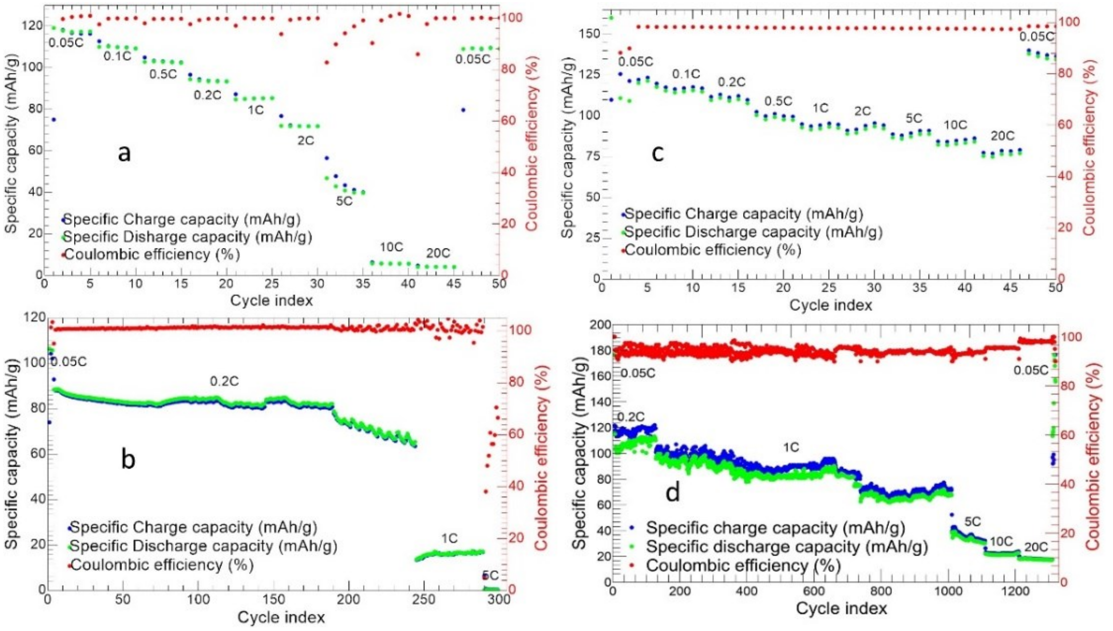

Figure 3.57: Charge/Discharge cycling at different C-rate of a) MnTi tape-casted and c) 10%MnTi/CNF electrodes. Long Charge/Discharge cycles for b) MnTi tape-casted and d) 10%MnTi/CNF electrodes.

The very promising electrochemical performances of the 10%MnTi/CNF sample are also confirmed by the long-term charge/discharge cycling shown in Figure 3.57d, where the lifespan cell is tested at 0,05C, 0.2C, 1C, 5C, 10C and 20C for 5, 50, 1000, 100, 100 and 100 cycles respectively. At 0.05C, the discharge capacity of 173.4 mAh/g in the first cycle approaches the theoretical one, then values of about 120 mAh/g are achieved. The specific capacity decreases increasing the cycle index and at the C-rate change. For the 1000 cycles at 1C the specific capacity is in the 67.3-110.1 mAh/g range. Notably, after 1000 cycles at 1C the cell is again able to run other cycles at high C-rate with a final capacity retention of 59.6%. Contrary to the tape-casted electrode that display a dramatic decrease of capacity at 1C (16.18 mAh/g) after 250 cycles at 0.2C (Figure 3.57b), the self-standing 10%MnTi/CNF electrode shows a longer lifespan, and its capacity is completely recovered in the last ten cycles at 0.05C after 1350 total cycles. The long-term cycling is another advantage brought by CNFs support for the electrode. As reported by Vu group [244], the porosity helps not only to guarantee better ions diffusion in bulk electrode but also to avoid or limit the volume change during the charge and discharge cycle, providing a longer cell lifespan. The coulombic efficiency is ≥93% which implies a lower redox reversibility, especially in the first 50 cycles. Increasing the C-rate the specific capacity is 33.6, 22.6 and 17.3 mAh/g at 5C, 10C and 20C, respectively.

Compared to the study by Li et al. [160], the 10%MnTi/CNF surely presents higher values of specific capacity at different C-rate. Our material shows 111.04 mAh/g at 0.2C against 107 mAh/g at 0.2C of $Na_3V_2(PO_4)_3$. Moreover, the 10%MnTi/CNF electrode displays improved long-cycle life: 1000 cycles at 1C **vs.** 120 cycles at 0.2C for $Na_3V_2(PO_4)_3$ [160]. Finally, as already illustrated for the v-30%MnZr/CNF sample, the 10%MnTi/CNF presents lower values of specific capacity at different C-rate: 93.6 mAh/g at 1C vs 129 mAh/g at the same C-rate for $NaFePO_4$@C [167] with a longer cycle life. The better electrochemical performance of $NaFePO_4$@C is explained by the fact the $NaFePO_4$@C is synthesized in situ into the CNFs matrix. Indeed, this synthesis route takes advantage of nanometric particles size and little agglomeration, which increases conductivity and promotes ions diffusion.

Finally, we performed the Electrochemical Impedance Spectroscopy measurements on the tape-casted and 10%MnTi/CNF self-standing electrode after cycling. The Nyquist plot is shown in Figure S. 15. The impedance spectra are consistent with those reported in the literature for the $Na_3MnTi(PO_4)_3$ active material for samples with different carbon coting with and without graphene oxide [184]. The smaller diameter of the semicircle in the high-frequency region for the 10%MnTi/CNF electrode confirms smaller charge-transfer resistance (585.7 Ω vs. 803.8 Ω of the tape-casted cathode) and faster charge-transfer at the electrode-electrolyte interface. The larger slope of Warburg impedance for

10%MnTi/CNF than for 2-MnTi cathode indicates more favorable Na ion-transport in the self-standing electrode.

Section 5. ZnS-GO as anode for SIBs

In this section, we report a preliminary study of ZnS-GO, used as self-standing anode for SIBs. We pre-synthesize the ZnS-GO powder, and disperse it into the polymeric solution (10% and 30% of active material powder) to be electrospun. This part of the thesis is developed in collaboration with a master student which contributed to the sample's preparation. The reported results are published by our research group [74].

Subsection 15 XRPD

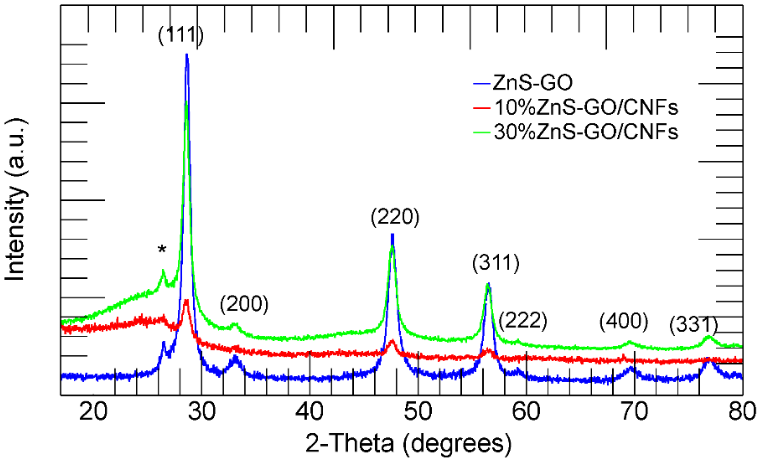

Figure 3.58: XRPD patterns of the ZnS–GO (blue), 10%ZnS–GO/CNF (red) and 30%ZnS–GO/CNF (green) samples. (002) plane of graphitic carbon (*) and Miller indices of the sphalerite phase are also shown.

The XRPD patterns of ZnS–GO, 10%ZnS–GO/CNF and 30%ZnS–GO/CNF samples are reported in Figure 3.58. The ZnS–GO pattern is consistent with those found in the literature [198]. The sample shows the peaks of ZnS sphalerite crystal structure (JCPDS: 05-0566). The peak at about 26.5° (2-Theta) identify the (0 0 2) plane of carbon [91,197,198], and confirms the reduction of GO into graphitized carbon.

The X-Ray patterns of the ZnS–GO and the ZnS–GO/CNF samples are comparable: the ZnS–GO/CNF samples present the sphalerite phase and graphitized carbon peaks. A broad band at about 25° (2–Theta) is attributable to the CNFs' amorphous component. The 30%ZnS–GO/CNF sample shows more intense peaks of the sphalerite phase with respect to the 10%ZnS–GO/CNF. Hence, we conclude that the electrospinning process does not cause structural changes to the active material, and a higher amount of active material is loaded in the 30%ZnS–GO/CNF sample.

For each sample, the lattice parameters and the crystallite size of the ZnS phase are evaluated by Rietveld Refinement. The calculated and experimental patterns are shown in Figure S. 16, and the refined parameters are reported in Table S. 4. The ZnS–GO and ZnS–GO/CNF samples present comparable lattice parameters and a crystallite size of about 12 nm, which compares to the literature values [198].

Subsection 16 Morphological analysis

The SEM images of the ZnS–GO samples are shown in Figure 3.59a,b. Agglomerates dimensions range between a few hundred nanometers and 10 µm. As evidenced in Figure 3.59b, the agglomerates consist of stacked sheets covered by nanometric rounded particles. In fact, the TEM images reported in Figure 3.59c,d confirm the presence of (i) nanoparticles' diameter of 10–20 nm, comparable to that obtained by the Rietveld refinement for the ZnS sphalerite phase (Table S. 4) and (ii) cracked sheets. The results confirm the sample consists of ZnS nanoparticles and graphene sheets. The cracked graphene foils are desirable, because they provide a homogeneous dispersion of the composite in the slurry or in the solution for electrospinning, and an intimate contact with the active material.

Figure 3.60illustrates the SEM images of the ZnS–GO/CNF samples after the carbonization thermal step, ready to be used as self-standing anodes.

Figure 3.60a,b report the surface morphology of 10%ZnS–GO/CNF sample, while the Figure 3.60c displays 10%ZnS–GO/CNF cross-section. The presence of carbon nanofibers are undeniable: they present a variable diameter reaching values of about 650 nm. In the same figure, rounded agglomerates of variable size, both dispersed between the CNFs (Figure 3.60a,b) and embedded into them (Figure 3.60a, on the left), are clearly visible and attributed to the active material loaded in the carbon nanofibers. The 10%ZnS–GO/CNF shows a sheet thickness of about 220 µm (Figure 3.60c).

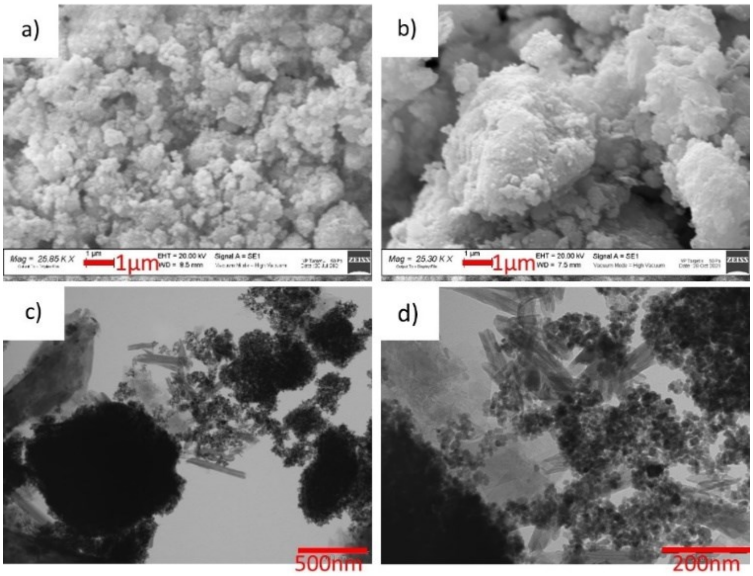

Figure 3.59: ZnS–GO powder: a) and b) SEM images at 25 kX, c) and d) TEM images at 50 kX and 150 kX, respectively.

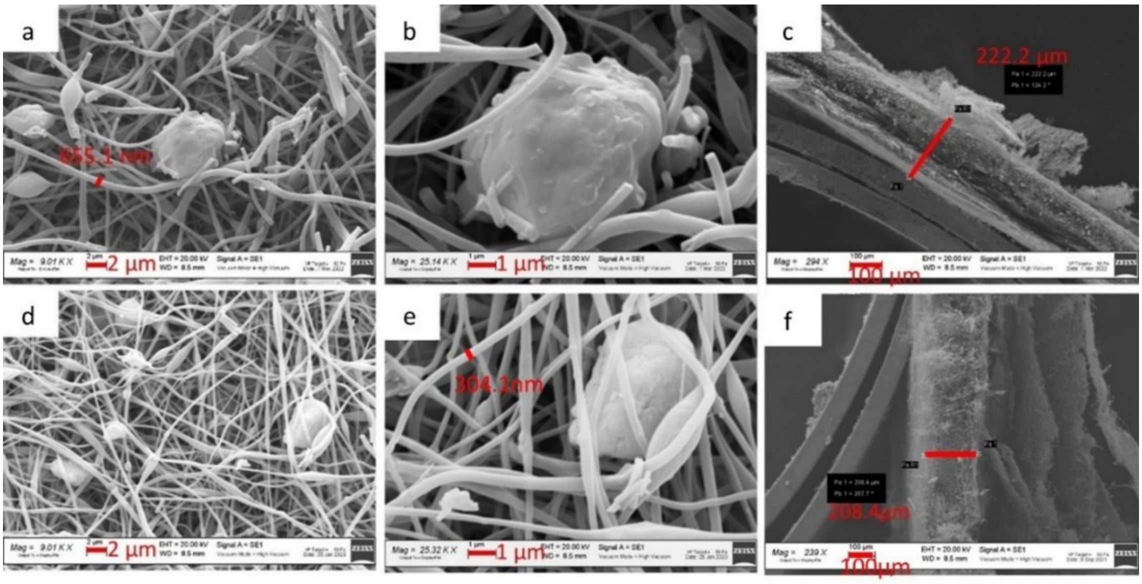

Figure 3.60: SEM images of 10%ZnS–GO/CNF sample: a) and b) at 9 and 25 kX, respectively, and c) cross-section. SEM images of 30%ZnS–GO/CNF sample: d) and e) at 9 and 25 kX, respectively, and f) cross-section.

Figure 3.60d,e illustrate the surface morphology of the 30%ZnS–GO/CNF sample, and Figure 3.60f reports the cross-section. 30%ZnS–GO/CNF displays carbon nanofibers with an average diameter of about 300 nm. Compared to 10%ZnSGO/CNF, the 30%ZnS–GO/CNF sample presents higher amount of agglomerates with variable size, due to the higher quantity of ZnS–GO loaded into CNFs sheet. The sheet thickness is 208 µm, comparable to the value evaluated for the 10%ZnS–GO/CNF sample.

Figure 3.61 illustrates the TEM images of the ZnS–GO/CNF samples after the carbonization process.

In the 10%ZnS–GO/CNF sample (Figure 3.61a,b), the ZnS–GO agglomerates are clearly observed, both between nanofibers and connecting them, and within the nanofibers. Each agglomerate consists of nanometric particles of about 10 nm, while the CNF's diameter is about 200 nm. The 30%ZnS–GO/CNF sample reports similar features. ZnS–GO nanoparticles of 13 nm are present, both between and embedded into nanofibers, and the CNF's diameter is about 150 nm.

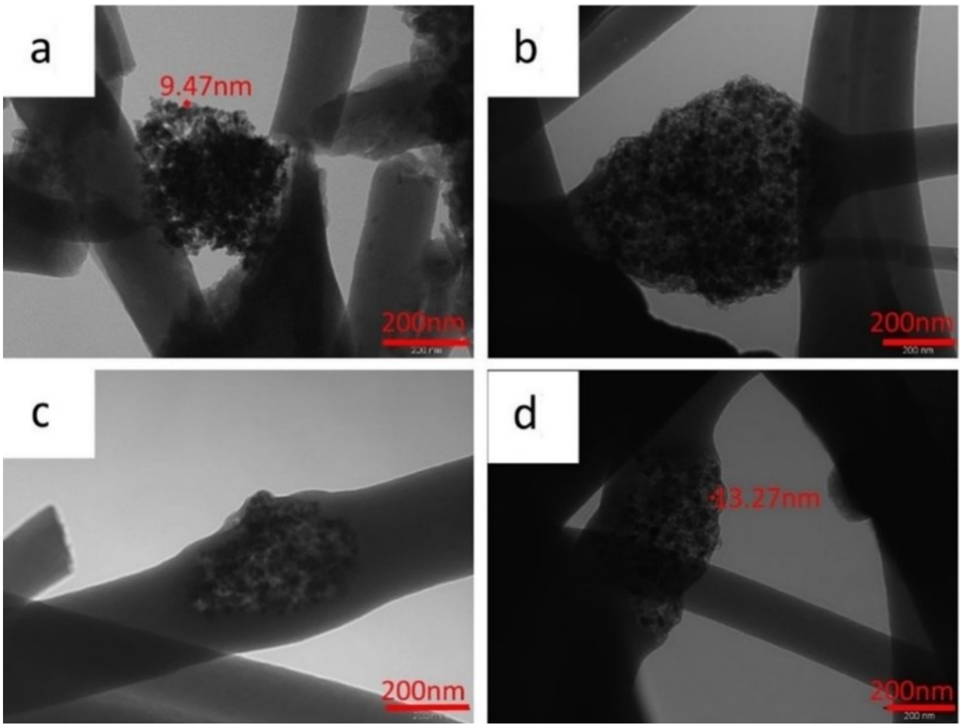

Figure 3.61: TEM images of a) and b) 10%ZnS–GO/CNF sample at 100 kX and c) and d) 30%ZnS– GO/CNF sample at 100 kX.

The EDS analysis is employed to investigate the ZnS agglomerate's distribution on the surface and within the bulk of the ZnS–GO/CNF sheets. The Zn and S distribution maps of the 10%ZnS–GO/CNF sample are shown in Figure 3.62. The images of the sample surface (Figure 3.62a–c) confirm that the aggregates are present between and within the CNFs are ZnS particles. The cross-section images (Figure 3.62d–f) demonstrate that the ZnS–GO active material is homogeneously spread along the sheet thickness, and no concentration gradients are visible. This feature is crucial for good electrochemical performance and is seldom obtained loading active material with different synthetic approaches, such as dip-and drop-coating.

The Zn and S distribution maps of the 30%ZnS–GO/CNF sample are shown in Figure 3.63. As for the 10%ZnS–GO/CNF sample, ZnS–GO aggregates are detected between and within the carbon nanofibers (Figure 3.63a–c) and the cross-section images (Figure 3.63d–f), confirming a homogeneous distribution of the active material along the sheet thickness. As shown in Figure 3.62a and Figure 3.63a, ZnS graphene/CNF composites are very segregated and the particle size distribution is very broad, too. This result is confirmed by the particle size distribution: 3.2(1.2) and 4.3(1.2) µm for the 10%ZnS–GO/CNF and 30%ZnS–GO/CNF samples, respectively. The agglomerate's size is not homogeneous and does not depend on the ZnS–GO amount loaded onto the CNFs.

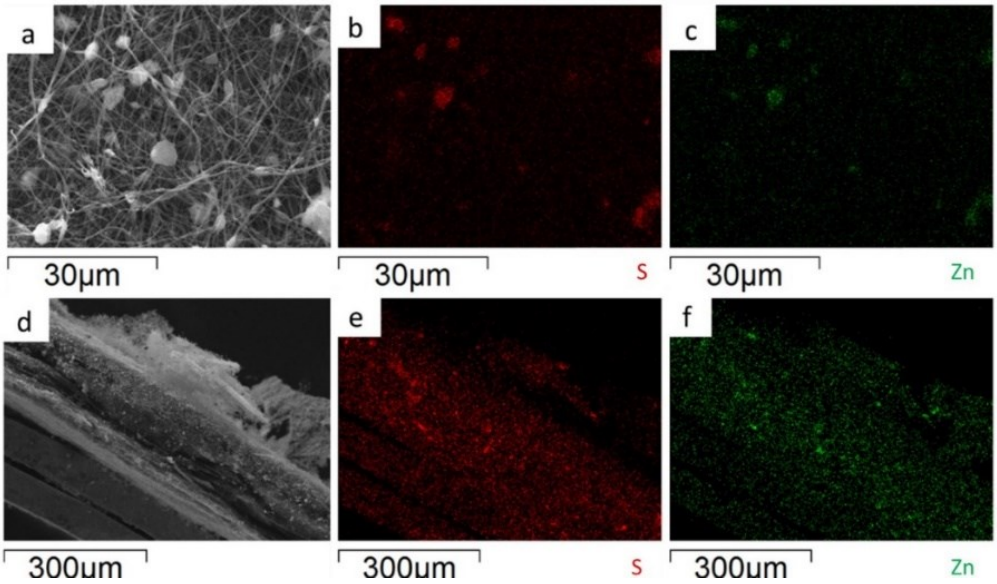

Figure 3.62: 10%ZnS–GO/CNF anode: a) sample surface portion and distribution maps of b) S and c) Zn; d) cross-section portion and distribution maps of e) S and f) Zn.

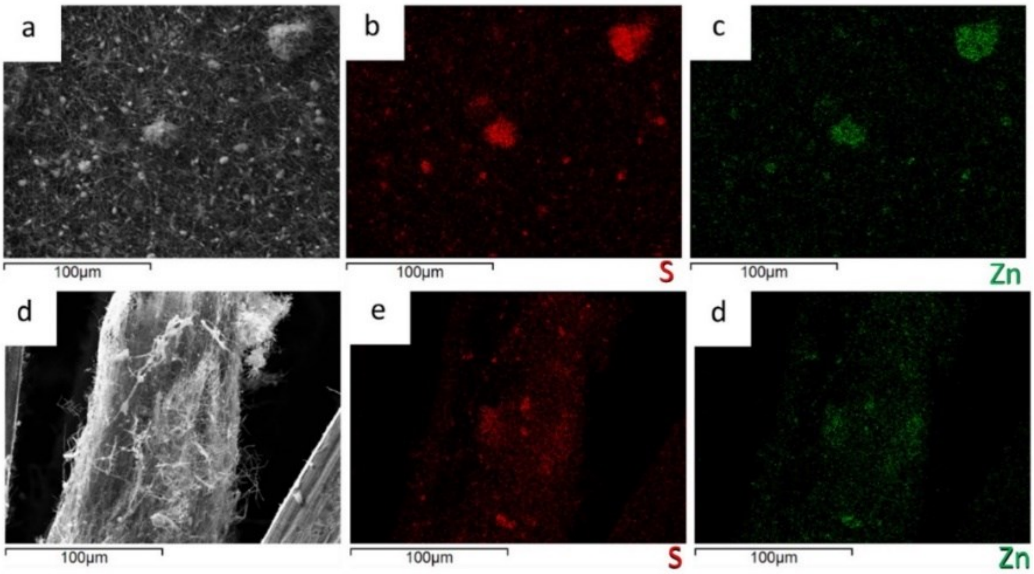

Figure 3.63: 30%ZnS–GO/CNF anode: a) sample surface portion and distribution maps of b) S and c) Zn; d) cross-section portion and distribution maps of e) S and f) Zn.

Subsection 17 Thermogravimetric and RAMAN analysis

The thermogravimetric curves of ZnS–GO, 10%ZnS–GO/CNF and 30%ZnS–GO/CNF samples are reported in Figure 3.64.

The pristine ZnS–GO sample displays two subsequent weight losses of 2.25 wt% and 35.33 wt% at 150 °C and 650 °C, respectively. As reported by Zhang et al. [198], the first loss is caused by the release of adsorbed water molecules. The second one occurs in the 250–650 °C temperature range and is due to the ZnS and C oxidation in air according to Eq. 3.5 and Eq. 3.6:

$$ZnS + \frac{3}{2}O_2 \rightarrow ZnO + SO_2$$

Eq. 3.5

$$C + O_2 \rightarrow CO_2$$

Eq. 3.6

At temperature higher than 650 °C, the sample weight is constant and attributable to the ZnO. From the ZnS–GO TG curve, a residual mass of 62.42 wt% is calculated, and the evaluated content of ZnS in the sample is about 75 wt%.

As for the case of ZnS–GO sample, both 10%ZnS–GO/CNF and 30%ZnS–GO/CNF TG curves display weight losses. Again, the former at about 100 °C is due to the release of the adsorbed water molecules. The latter occurs in the 250 °C–650 °C temperature range, and is due to carbonaceous component combustion (Eq. 3.6) and ZnS oxidation (Eq. 3.5). As expected, the second mass loss in the ZnS–GO/CNFs samples is higher than in the ZnS–GO, as the combustion also involves the carbon nanofibers. The 10%ZnS– GO/CNF sample reports a residual mass of 7.15 wt% at 650 °C, caused by the formation of ZnO. The evaluated ZnS amount is 8.5 wt%, and the ZnS–GO amount is 11.3 wt% (the ZnS–GO powder contains 75% ZnS, as evaluated by TG data). The value fairly compares to that used in the synthesis (10 wt% of ZnS–GO). The 30%ZnS–GO/CNF sample reports a residual mass of 15.6 wt% at 650 °C; the calculated ZnS amount is 18.7 wt%, and the ZnS–GO amount is 24.9 wt%. Also in this case the value fairly matches that of the synthesis (30 wt%).

Raman spectroscopy provided information about these multicomponent materials. In particular, the technique allowed the analysis of the structural changes of their carbonaceous parts at different preparation stages and comparison of the order degree of samples with different amounts of graphitic component [198].

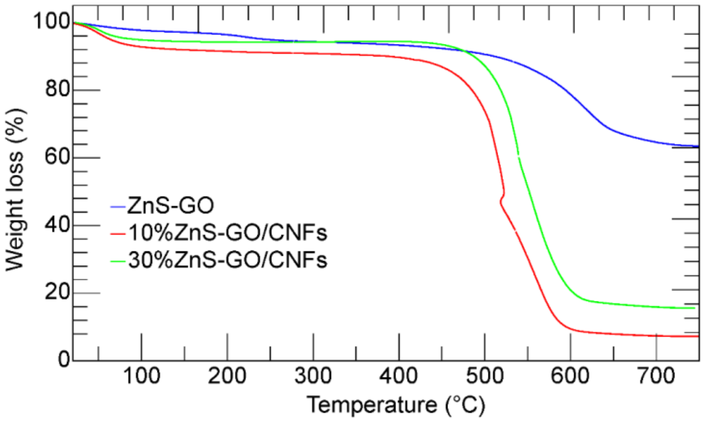

Figure 3.64: Thermogravimetric curves of ZnS–GO powder (blue), 10%ZnSGO/CNF sheet (red) and 30%ZnS–GO/CNF sheet (green).

In Figure S. 17, the room temperature Raman spectra are reported for the 30%ZnS–GO/CNF sample, as prepared after electrospinning, after stabilization and post-carbonization.

At the first two processes, the Raman yield is overwhelmed by a very broad and structureless signal, probably associated with fluorescence. Nevertheless, when the data are processed by subtracting a structureless background, a weak signal appears for the as prepared sample in the region between 300–500 cm^{-1}, where the vibrations of sphalerite ZnS structure should be active [360]. This Raman activity is accompanied for the stabilized sample by the appearance of the well-known Raman structures associated with graphene [332].

The results are shown in Figure 3.65, where the spectra for ZnS–GO, 10%ZnS–GO/CNFs and 30%ZnS–GO/CNFs are reported, together with the Raman spectrum for CNFs. One can appreciate the changes in line shapes and intensity ratios between G and D bands. Less significative are the very small changes in the peak energies. In the inset, the intensity ratio parameter (I_G/I_D) is reported for the four considered samples. The values for this parameter have been derived by best-fitting procedures in the range 1000–1800 cm^{-1} using a sum of Lorentzian curves as fitting functions, as shown in Figure S. 18 for the ZnS–GO sample and according to [361,362].

For all samples, the absence of sphalerite Raman signals is not surprising, based on the different Raman cross-sections, and on the fact that the rGO carbon coating and CNFs matrix prevent the excitation of inner sphalerite structure.

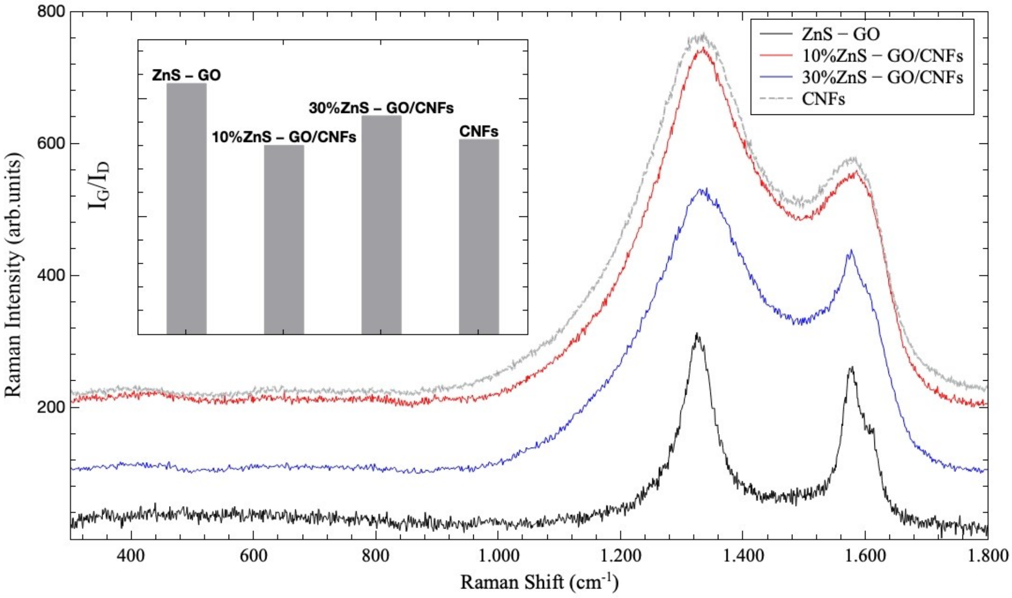

Figure 3.65: Room temperature Raman spectra for ZnS–GO (black line), 10%ZnS–GO/CNFs (red line) and 30%ZnS–GO/CNFs (blue line), together with the Raman spectrum for starting CNFs (gray line). In the inset, the intensity ratio (I_G/I_D) is reported for the same samples.

The higher value (0.85) is obtained for ZnS/GO composite, indicating a good crystalline order of the matrix. This is consistent with the presence of the graphene sheets embedding the ZnS nanoparticles and obtained by the graphene oxide reduction. When this matrix is added to CNFs, the I_G/I_D value decreases and a net broadening of the line shape is observed. The lowest I_G/I_D value (0.64) is obtained for 10%ZnS–GO/CNFs according to the lowest amount of the ordered carbon matrix; in this case, the value is practically equal to that obtained for pure CNFs. Increasing the amount of the ZnS–GO part leads to an increase of I_G/I_D value (0.74), in any case lower than that for ZnS–GO.
These results evidence that the ordered carbon component present in the ZnS–GO/CNF samples is mainly related to the graphene embedding the ZnS nanoparticles. Indeed, the fitted peak position of the (0 0 2) reflection of carbon (see Figure S. 16) is very comparable for the three samples, and a d_{002} interplanar distance of 3.36 Å is calculated, independent of the presence of the CNF component and its amount.

Subsection 18 Electrochemical results

The cyclic voltammetry and charge/discharge curves (GDG) of the ZnS–GO, 10%ZnS–GO/CNF and 30%ZnS– GO/CNF samples are reported in Figure 3.66.
The reduction and oxidation peaks are detected at 0.5 V–0.7 V and at about 1.0 V, respectively. During the cathodic cycle, the insertion of Na^+ and the conversion of ZnS to metallic Zn occurs [198], while in the anodic process the conversion of Zn to ZnS and the extraction of Na^+ takes place [198] (see Section 5 for further information on ZnS red-ox). The first cycle presents, in the cathodic region, the broad peak between 0.1 V–0.5 V attributed to the SEI formation, caused by the intercalation of Na^+ and the structure settling [198].
In the case of the ZnS–GO sample (Figure 3.66a,b), the anodic and cathodic peaks show a current intensity higher than 0.5 A g^{-1}, and a quite high ΔV values of about 0.3 V, which underline the polarization phenomena. While the anodic peaks are visible at 1 V, the cathodic peak at 0.9 V moves

to 0.5 V–0.7 V after the first cycle and the SEI formation. Finally, the peaks are not perfectly overlapped, confirming that the redox reversibility is not strong.

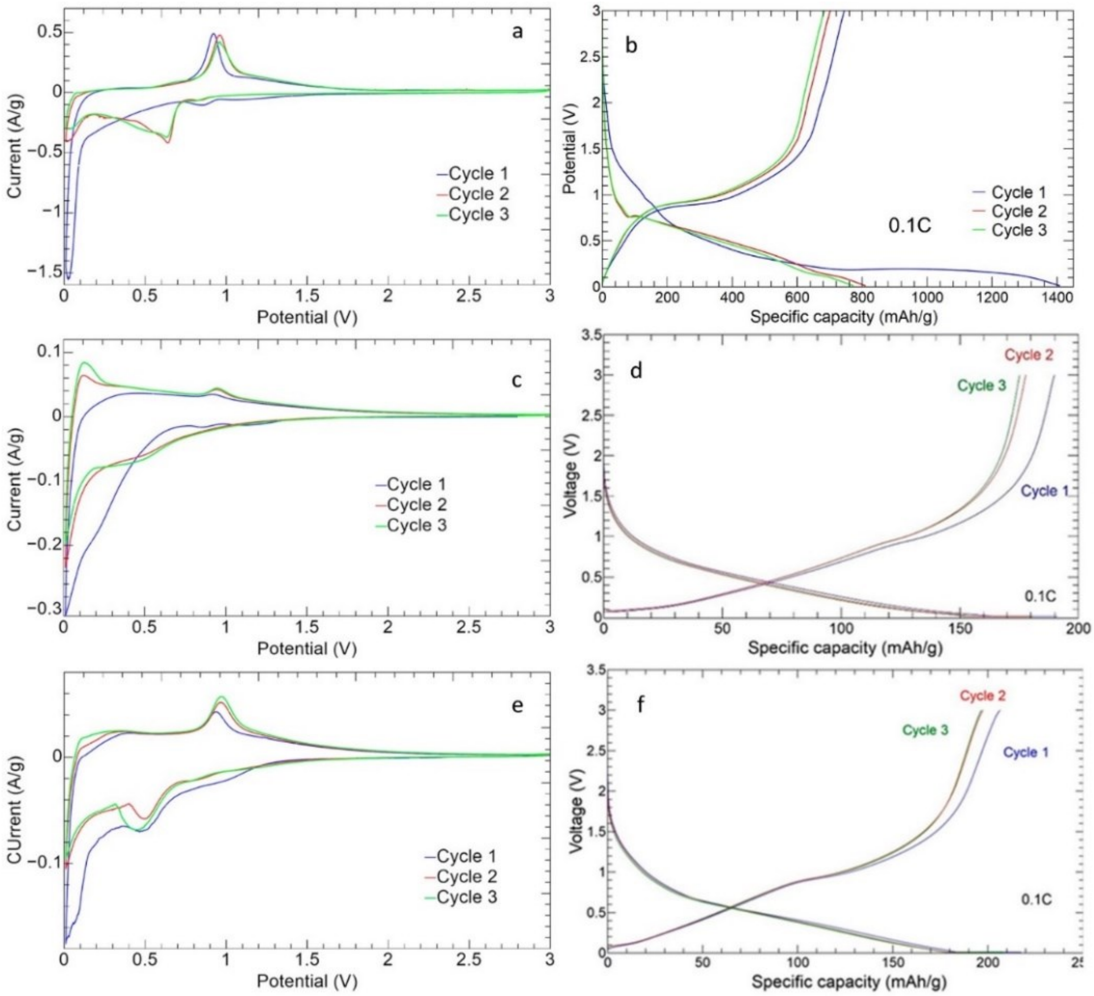

Figure 3.66: Cyclic voltammetry and charge/discharge curves of a,b) ZnS–GO, c,d)10%ZnS–GO/CNF and e,f) 30%ZnS–GO/CNF samples.

In the 10%ZnS/CNF CV (Figure 3.66c,d), the redox peaks are broader and show lower current intensities than the ZnS–GO (Figure 3.66a). It can be underlined that, in the free-standing anode, the active material amount is only 11.3 wt% vs. 70% in the slurry ZnS–GO electrode. Noteworthy, for the 10%ZnS–GO/CNF sample the redox peaks are overlapped, suggesting a good reversibility of the red-ox process. In the anodic region, a red-ox peak is also visible at about 0.1 V. This can be ascribed to the CNF component as reported by refs. [82,363], because the sample contains about 90 wt% of carbon nanofibers, (see Section 1 in Chapter 3 for further information of electrochemical activity of CNFs as anode for LIBs and SIBs).

In the CV curve of the 30%ZnS–GO/CNF (Figure 3.66e,f), the redox peaks show currents of 0.05 A/g in charge and −0.08 A/g in discharge. These values are lower than the slurry electrode but higher than the 10%ZnS–GO/CNF. This is explained by the ZnS–GO powder amount in the 30%ZnS–GO/CNF: lower than the 70% of slurry, but higher than the 11.3% in the other self-standing electrode. In this case, it is possible to see the formation of SEI in the first cycle, too.

The variation of CV curve between 10%ZnS–GO/CNF and 30%ZnS–GO/CNF is due to the different amount of active material powder, which cause variation in intensity current of the peak.

The GCD profiles at 0.05 C (Figure 3.66b,d,f) agree with the CV results. The high overlap of the second and third cycle curves of the 30%ZnS–GO/CNF sample confirms a satisfactory reversibility of charge and discharge processes. The curve's shape is well-comparable to ZnS anodes reported in the literature

[193,196]. The voltage plateau at about 1 V is more evident in the 30%ZnS–GO/CNF sample, containing a higher amount of active material (24.9 vs. 11.3 wt%).

The charge/discharge cycling at different C-rates of ZnS–GO, 10%ZnS–GO/CNF and 30%ZnS–GO–CNF samples are reported in Figure 3.67.

The ZnS–GO (Figure 3.67a) presents an initial charge/discharge capacity of 770.82/1409 mAh g^{-1} and initial coulombic efficiency (ICE) of 58.89%. CE% increases to 91.93% in the second cycle. The initial capacity loss is attributable to both the SEI formation and Na^+ trapping. Averaged capacities of 671.93, 423.14, 279.27, 155.42, 94.97, 51.72 and 36.76 mAh g^{-1} are reached at 0.05 C, 0.1 C, 0.2 C, 0.5 C, 1C, 2C and 5C, respectively. After the first cycle, a progressive capacity loss is visible for each C-rate, until the cell reaches good stability and a high overlapping of charge and discharge capacity, suggesting a reversibility of the red-ox process. The good electrochemical performance is confirmed by the value of the coulombic efficiency ≥98%, too. At the end of the analysis, the capacity at 0.05 C is 43.89% of the initial one after SEI formation.

In the first cycle of the 10%ZnS–GO/CNF sample (Figure 3.67b), the charge/discharge capacity is 200.02/385.3 mAh g^{-1}. The ICE is 52.10%, and increases to 99.16% in the second cycle. Averaged specific capacities of 233.79, 181.06, 162.01, 140.57, 97.42, 80.55, and 57.68 mAh g^{-1} are obtained at 0.05 C, 0.1 C, 0.2 C, 0.5 C, 1 C, 2 C and 5 C, respectively. By switching again to 0.05 C, a good capacity recovery is obtained, corresponding to 94.41% of initial capacity after SEI formation.

In Figure 3.67c, the 30%ZnS–GO/CNF self-standing electrode shows an initial charge/discharge capacity of 205.03/428.7 mAh g^{-1}. The ICE value of 57.95% increases to 88.34% in the second cycle. Averaged specific capacities of 271.89, 215.6, 196.38, 156.25, 132.28, 113.83 and 80.80 mAh g^{-1} are obtained at 0.05 C, 0.1 C, 0.2 C, 0.5 C, 1 C, 2 C and 5 C, respectively. At the end of the measurement, at 0.05 C the capacity is totally recovered. Both self-standing anodes show an increased stability with respect to the slurry electrode, as a lower capacity loss is detected by increasing the C-rate. Noteworthy, the electrospun electrodes report an improved capacity recovery compared to the tape-casted ZnS–GO anode.

Figure 3.67d, the specific capacity of the three electrodes as a function of C-rate is reported and compared to the electrochemical activity of the pristine CNF anode. The capacity value is the average specific capacity at each C-rate. For all anodes, increasing the C-rate the specific capacity gradually decreases, but for the free-standing electrodes the capacity decay is not so steep as for the slurry anode. In addition, both the 10%ZnS–GO/CNF and 30%ZnS–GO/CNF samples show fair capacity values at high C-rates: 69.93 and 92.59 mAh g^{-1} at 5 C, respectively, vs. 50 mAh g^{-1} for the ZnS–GO slurry anode. The electrochemical activity of the pristine CNFs self-standing electrode stands between the slurry and self-standing anodes. At low C-rate, the pristine CNF anode shows lower capacity than slurry, 10%ZnS–GO/CNF and 30%ZnS–GO/CNF electrodes, while at C-rate higher than 1 C. the pristine CNFs displays capacity values higher than slurry but lower than both 10%ZnS–GO/CNF and 30%ZnS–GO/CNF anodes. At 1 C, the pristine CNFs, 10%ZnS–GO/CNF and slurry electrodes show comparable electrochemical performance.

The obtained charge/discharge results suggest that the self-standing anodes display a lower value of specific capacity at low C-rates, due to the lower amount of active material in the electrode but seem really promising at high C-rates thanks to the presence of porous CNFs matrix which permits a faste ion-diffusion.

Figure 3.68 shows the cycling performance for the ZnS–GO, 10%ZnS–GO/CNF and 30%ZnS–GO/CNF samples. The cells are tested at 0.5 C for 200 cycles, and the ZnS– GO/CNF electrodes are cycled at 5 C for 50 cycles, too.

For ZnS–GO (Figure 3.68a), the initial capacity at 0.05 C is 1847 mAh g^{-1}. In the following cycles at 0.5 C, a gradual capacity loss is detected, and the capacity achieves stable values (in the range 185–223 mAh g^{-1}) only after the 100th cycle. The charge and discharge capacity values are overlapped and a coulombic efficiency ≥98% is obtained. The cell is also tested at 5 C after 200 cycles at 0.5 C, but this does not work. The capacity retention after 200 cycle is 21.20%.

In the 10%ZnS–GO/CNF sample (Figure 3.68b), the initial capacity is 389.6 mAh g^{-1} at 0.05 C. In the following cycles, the capacity decays, but the cell quickly reaches a stable capacity value (about 150 mAh g^{-1}) at the 13th cycle. The charge/discharge capacities are overlapped and coulombic efficiencies

≥99% are obtained at 0.5 C. The cell is tested at 5 C for 50 cycles, after 200 cycles at 0.5 C. Compared to the slurry ZnS–GO electrode, the 10% self-standing anode reaches stable capacity values quicker and withstands cycling at high C-rate after 200 cycles at 0.5 C. The capacity retention after 200 cycle is 66.51%.

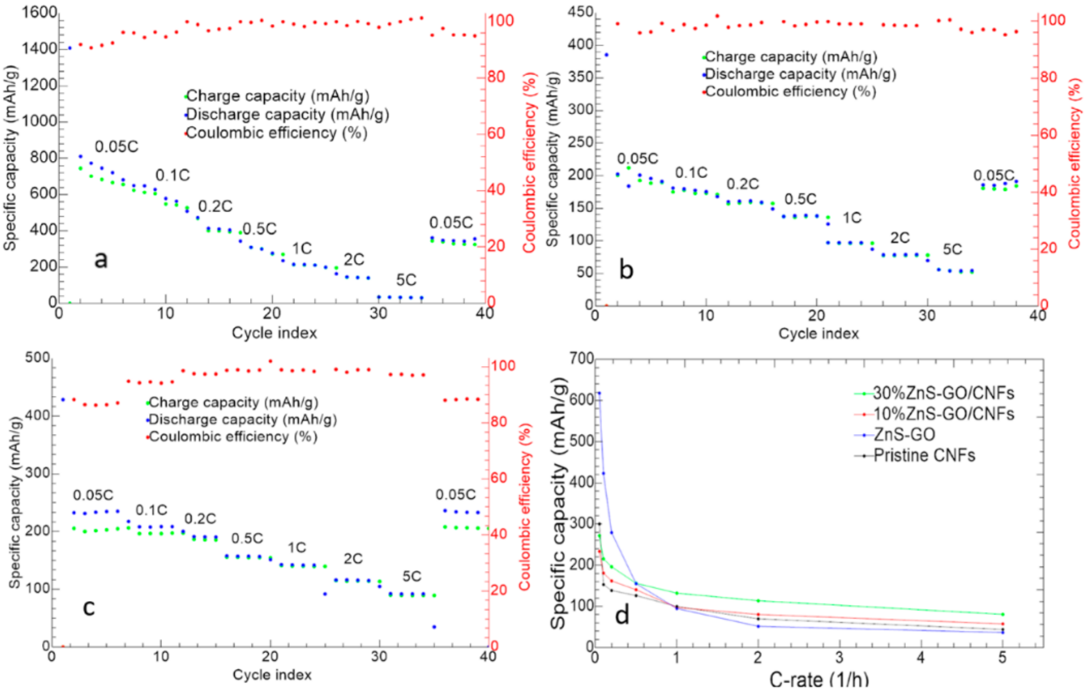

Figure 3.67: Charge/discharge cycles at different C-rates of a) ZnS–GO, b) 10%ZnS–GO/CNF and c) 30%ZnS–GO/CNF samples. d) Samples' capacity vs. C-rates. Charge (green), discharge (blue) and coulombic efficiency (red).

Finally, the 30%ZnS–GO/CNF sample (Figure 3.68c) displays an initial capacity of 789 mAh g^{-1} at 0.05 C. In the following 200 cycles at 0.5 C, the cell shows better cyclability than the slurry, but worse than the 10% self-standing anode. Interestingly, the 30% self-standing electrode reports capacity values in the 255–400 mAh g^{-1} range for 200 cycles at 0.5 C. The charge and discharge capacities are overlapped and coulombic efficiencies ≥99% are reached. The electrode also shows good cycling performances at 5 C for other 50 cycles, demonstrating a capacity of 80–90 mAh g^{-1}, and the cell still works at the end of the cycling test. The capacity retention after 200 cycles is 69.57%.

We can compare the electrochemical results obtained at 0.5 C for the 30%ZnS–GO/CNF sample (ZnS: 24.9 wt%) to recent literature results for metal sulfide/CNF anodes synthesized by electrospinning and used for SIBs. Bell string-like hollow ZnS–CNF (ZnS: 50 wt%) displays a reversible capacity of 361.7 mAh g^{-1} at 0.2 A g^{-1} and 433.5 mAh g^{-1} after 50 cycles at 0.1 A g^{-1} [196]. Capacity values of about 510 mAh g^{-1} at 0.2 A g^{-1} and 499.9 mAh g^{-1} after 100 cycles at 0.1 A g^{-1} were reached by low crystallinity SnS encapsulated in CNT decorated and S-doped CNF anodes (SnS: 48.3 wt%) [205]. Finally, rGO-encapsulated MoS$_2$/CNF electrodes (Sulphur: 20.9 wt%) display a capacity of 345.8 mAh g^{-1} at the 90th cycle at 0.1 A g^{-1} [209] and 3D-hierarchical MoS$_2$-CNF nanostructures (MoS$_2$: 63 wt%) retain a capacity of 438 mAh g^{-1} after 100 cycles at 0.1 A g^{-1} [364]. The long-term cycle life is comparable to other electrospinned anodes such as SnS$_2$ [365] which presents 200 cycles at 0.1C with a specific capacity of 400-600mAh/g. It presents quite stable value of capacity during the long cycling, ad s for our ZnS-GO/CNFs materials. Our results with the 30%ZnS–GO/CNF sample seems appealing, if we take into consideration the lower amount of active material loaded onto CNFs (ZnS: 24.9 wt%).

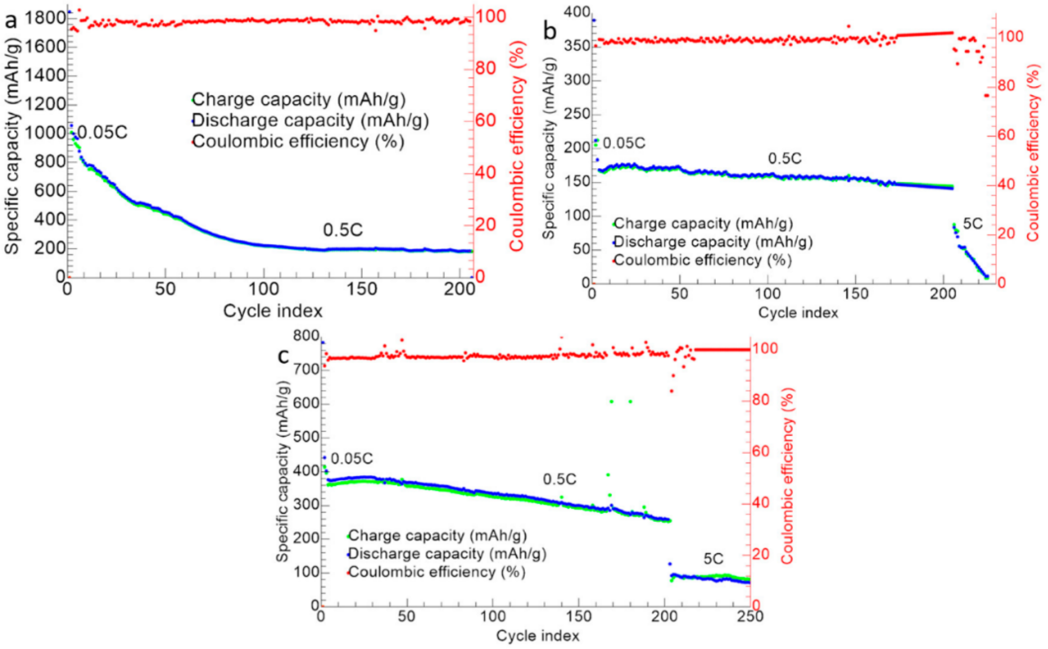

Figure 3.68: Cycling performance of a) ZnS–GO, b) 10%ZnS–GO/CNF and c) 30%ZnS–GO/CNF samples. Charge (green), discharge (blue) and coulombic efficiency (red).

The 30%ZnS–GO/CNF anode electrochemical performances suggest that the self-standing electrode investigated in this study is very promising in terms of improving the specific capacity at high C-rate and the lifespan of the cell. The goal is reached thanks to the role played by both the graphene sheets embedding the ZnS nanoparticles and the carbon nanofibers. The ordered carbon component, suitable for increasing the poor electronic conductivity of ZnS, principally resides in the graphene sheets coating the active material, as depicted by the Raman spectroscopy results. However, the CNFs buffer the huge volumetric changes of crystal structure during the sodiation/desodiation processes: this results in the improved cycling performances at high C-rate with respect to the conventional tape-casted anode. The improvement is given by using a lower amount of active material (24.9 wt% vs. 70 wt% of the tape-casted anode), and neither metal support nor binder is necessary. To conclude, a feasible and simple two-step synthesis is used. In this study, we prepared ZnS–GO composites and simply added them to the carbon precursor solution to be electrospun, stabilized and carbonized, and we prepare the ZnS–graphene embedded in carbon nanofibers. This synthetic approach may be extended to other active materials: in the first step, they can be modified, coated or embedded to increase their electrochemical performance, then a further upgrade can be matched simply by adding the composite to the carbon precursor solution employed for electrospinning.

Chapter 4. Conclusions

In this work, we synthesized and characterized active materials/carbon nanofibers composites as free-standing cathodes and anodes for SIBs. The flexible CNFs matrix is a suitable support for our electrodes. Moreover, CNFs display good electronic conductivity and high porosity, beneficial for electron migration and electrolyte/active material contact. We loaded $LiFePO_4$, $Na_3MnZr(PO_4)_3$, $Na_3MnTi(PO_4)_3$, and ZnS-GO active materials into CNFs.

Firstly, we investigated the matrix, namely the pure CNFs deposited by electrospinning. We evaluated the optimal carbonization temperature to obtain highly conducive carbon: a good graphitization is achieved for thermal treatments in N2 flux at temperatures higher than 700°C. The CNFs carbonized at 900°C give the highest value of electronic conductivity, and their electrochemical activity is investigated. The carbon nanofibers do not exhibit red-ox peaks in the cathode range, whilst they are electrochemically active as anodes. This point has been taken into account in the study of the ZnS-GO/CNF self-standing anode, as the electrochemical performance depends on both ZnS and CNFs.

Then, we synthetized the active material/CNFs self-standing electrodes. We chose the carbonization temperature of 750°C as a good compromise, to guarantee a good electronic conductivity and avoid possible structural changes of the active material.

Before starting the systematic synthesis and characterization of self-standing cathodes and anodes for SIBs, we carried out a preliminary investigation on the $LiFePO_4$/CNFs cathode for LIBs. This study aims at evaluating the best experimental conditions to prepare the composites by electrospinning, and at investigating the role of CNFs on a well-known active material. Indeed, lithium-iron-phosphate is widely studied in literature and commercially employed in industry for LIBs. The $LiFePO_4$ powder (Sigma Aldrich) is simply dispersed (10 and 30 wt%) into the polymeric solution, which is electrospun and further thermal-treated for the carbonization process. We achieved an active material loading of 12.25 and 34.53 wt% in the two self-standing cathodes. The olivine-type crystal structure of $LiFePO_4$ is retained, and the active material is homogeneusly dispersed into and within CNFs. A conventional tape-casted $LiFePO_4$ cathode (80 wt%) is appositely prepared, for comparison. The low active material amount of self-standing electrodes leads to lower anodic and cathodic peak current intensities compared to the tape-casted one, as well as lower charge and discharge capacities at low C-rates. However, the 30% $LiFePO_4$/CNF sample gives better cycling performance and charge/discharge capacities at high C-rates, thanks to the presence of CNFs matrix, which guarantees an easier electrolyte diffusion and good contact with $LiFePO_4$ particles, beneficial to reach lower polarization effects and higher reversibility.

The results suggest the applied electrospinning approach is suitable to synthesize self-standing cathodes performant at high C-rates, by loading lower amount of the active material than for the traditional tape-casted cathodes.

The NaSICON-type $Na_3MnZr(PO_4)_3$ and $Na_3MnTi(PO_4)_3$ compounds are chosen as active materials in self-standing cathodes for SIBs, as they provide good structural stability upon sodiation/desodiation, and high working potential. Both active materials are synthesized via sol-gel. The citric acid is added in different amount (citric acid/compound mole ratio: 8.8, 3, and 2), as both chelating agent and carbon source for active material's coating. Among the investigated compositions, the sample with the lower citric amount displays a thinner and homogeneous carbon coating, and higher graphitization degree, favourable to enhance the electrochemical performance: the cyclic voltammetry and charge/discharge cycling analysis confirm higher peak current intensity and specific capacity, compared to samples with higher amount of citric acid as chelating agent in the sol-gel synthesis.

The synthesized active materials with citric acid/compound mole ratio of 2 was used to synthesize the active material/CNF electrodes by dispersion method: 10 or 30 wt% of active material is dispersed into the polymeric solution, which is electrospun (horizontal or vertical setting) and graphitized. The active material/CNF electrodes are also synthesized by dip-drop method: the active material precursors' solution is dip-drop coated on pre-synthesized CNFs, and the active material is synthesized in-situ onto CNFs.

In the case of $Na_3MnZr(PO_4)_3$ /CNF self-standing cathodes, $Na_3MnZr(PO_4)_3$ displays the NaSICON-type structure, and is successfully loaded into CNFs, independently of the synthetic approach. However, the synthesis route influences the active material loaded amount, and the distribution within the carbon nanofibers sheets. Compared to the dip-drop coating approach, the dispersion method gives a homogeneous distribution of $Na_3MnZr(PO_4)_3$ particles along the thickness and into the CNFs sheets, and the aggregates link and coat the CNFs, but also are embedded into them: an intimate contact between active material and CNFs is achieved, that is beneficial for the electrochemical performance. Among the deposition setting, the vertical one is preferred, as the particles' settling is avoided, and the active material is quantitatively loaded into CNFs (29.8 wt%). Independently of the synthetic method, enhanced specific discharge capacities at different C-rates are achieved in the binder-free cathodes, compared to the tape-casted one. The enhancement is especially achieved at high C-rate, where the porous nature of the non-woven CNFs guarantees better electrolyte diffusion and easy contact with the active material. The best electrochemical performances are obtained for the v-30%MnZr/CNF electrode, which also displays promising long lifespan, compared to the tape-casted counterpart. The reported results suggest that the ex-situ synthesis of $Na_3MnZr(PO_4)_3$ and its addition (30 wt%) to the polymeric solution to be electrospun is a simple and feasible approach to obtain binder-free cathodes with improved electrochemical performances compared to the tape-casted ones (70 wt% of active material).

For the $Na_3MnTi(PO_4)_3$/CNF self-standing cathodes, only the 11.73 wt% of active material can be loaded into CNFs by dispersion method. For higher amount, $Na_3MnTi(PO_4)_3$particles agglomerate and settling accurs. In the dip-drop coating approach, impurity phases forms. The TEM, SEM and EDS analysis of the 10%MnTi/CNF sample demonstrate that the active material particles are homogeneously spread within and into CNFs, and along the sheet thickness. The loaded $Na_3MnTi(PO_4)_3$ powder display the NASICON-type structure, but cell shrinkage occurs, due to the sintering temperature of 750°C used for the carbonization process. Notwithstanding the low amount of loaded active material and the cell shrinkage make the redox activity sluggish, the charge/discharge cycling test at different C-rates and long cycling analysis confirm the promising electrochemical performance of the binder-free electrode, compared to the conventional tape-casted counterpart. The 10%MnTi/CNF cathode shows an initial discharge capacity of 124.38 mAh/g at 0.05C, completely recovered at the end of the measurement, and a coulombic efficiency ≥98%. The capacity value at 20C is 77.60 mAh/g. The self-standing electrode lifetime is better than the slurry one: cycled for 1350 cycles, it displays capacities ranging between 67.2 and 110.1 mAh/g at 1C, and can further be cycled at 5C, 10C and 20C after 1000 cycles at 1C, contrary to the slurry one, working only for 300 cycles and up to 5C. The porous non-woven CNFs permits an increased alkali metal-ion faradaic contribution to the total current, and an easier electrolyte diffusion.

Finally, we investigated self-standing anodes for SIBs. We chose ZnS-GO as active material, but we have also to take into account the CNFs themselves, as they are electrochemically active as anodes. We synthesized two ZnS-GO/CNF binder-free anodes with different active material loading (11.3 and 24.9 wt%) by deposition method. The loaded ZnS displays the sphalerite structure, and the ZnS–GO particles are spread between and within CNFs, and are homogeneously distributed on the surface and along the thickness of the CNFs sheet. The anodes were tested for both LIBs and SIBs. The electrochemical investigation demonstrates that both self-standing anodes display better electrochemical performance in terms of specific capacity at C-rates higher them 1 C, compared to the conventional tape-casted anode (69.93 and 92.59 mAh/g at 5 C for 10%ZnS–GO/CNF and 30%ZnS–GO/CNF samples, respectively, vs. 50 mAh/g for ZnS–GO) and CNFs alone. The best cycling performance is obtained for the 30%ZnS–GO/CNF sample, which exhibits capacity values in the 255–400 mAh/g range for 200 cycles at 0.5 C, coulombic efficiencies ≥99%, and capacities of 80–90 mAh/g for other 50 cycles at 5 C.

The aforementioned results demonstrate that the self-standing active material/CNFs electrodes are successfully synthesized by a simple, feasible and scalable technique: the electrospinning. Their fascinating properties, such as good electronic conductivity and high porosity, favor the electron migration and the electrolyte/active material intimate contact, essential to achieve the enhanced capacity values at high C-rates and the long cycle life, compared to the dense and poorly porous tape-casted counterparts. The improved electrochemical performances of the self-standing electrodes in terms of specific capacity at high C-rates and capacity retention are demonstrated by the results summarized in Table 4.1-4.4. The results reported in this PhD thesis suggest that the proposed self-standing manufacturing process acts as a technology *booster*, namely it improves performances of known active materials.

Table 4.1: Electrochemical performance of 30%$LiFePO_4$/CNF self-standing electrode vs $LiFePO_4$ tape-casted one.

	$LiFePO_4$	***30%$LiFePO_4$/CNF***
Specific capacity at 10C (mAh/g)	38.56	34.94
Specific capacity at 20C (mAh/g)	8.21	25.58
Capacity retention 50 cycles at 0.2C	74. 8%	77.4%
Capacity retention 1000 cycles at 1C	/	35.4%

Table 4.2: Electrochemical performance of v-30%$Na_3MnZr(PO_4)_3$/CNF self-standing electrode vs $Na_3MnZr(PO_4)_3$ tape-casted one.

	2-$Na_3MnZr(PO_4)_3$	***v-30%$Na_3MnZr(PO_4)_3$/CNF***
Specific capacity at 1C (mAh/g)	9.01	16.20
Specific capacity at 5C (mAh/g)	3.01	12.80
Specific capacity at 10C (mAh/g)	/	9.10
Capacity retention 50 cycles at 0.2C	15.8%	52.9%
Capacity retention 1000 cycles at 1C	/	22.6%

Table 4.3: Electrochemical performance of 10%$Na_3MnTi(PO_4)_3$/CNF self-standing electrode vs $Na_3MnTi(PO_4)_3$ tape-casted one.

	2-$Na_3MnTi(PO_4)_3$	***30%$Na_3MnTi(PO_4)_3$/CNF***
Specific capacity at 1C (mAh/g)	85.69	93.60
Specific capacity at 5C (mAh/g)	4.12	89.15
Specific capacity at 10C (mAh/g)	5.70	88.30
Capacity retention 50 cycles at 0.2C	77.6%	81.7%
Capacity retention 1000 cycles at 1C	/	59.6%

Table 4.4: Electrochemical performance of 30%ZnS-GO/CNF self-standing electrode vs ZnS-GO tape-casted one.

	ZnS-GO	***30%ZnS-GO/CNF***
Specific capacity at 1C (mAh/g)	51.72	113.83
Specific capacity at 5C (mAh/g)	36.76	80.80
Capacity retention 200 cycles at 0.5C	21.20%	69.57%

Bibliography

1. Lewis, N.S. Powering the Planet. *MRS Bulletin* **2007**, *32*, 808–820, doi:10.1557/mrs2007.168.
2. Hind Couzin; Anastasia Ioannou; Kristin Seyboth *RENEWABLES 2023 GLOBAL STATUS REPORT*; Uno enviroment origramme, 2023;
3. Causes of Climate Change - European Commission Available online: https://climate.ec.europa.eu/climate-change/causes-climate-change_en (accessed on 19 February 2024).
4. S. Collins, J. Feng, M. Vicente Garcia, K. Guerra, D. Hawila,; M. Jabbour, M. Abdul Kadir, Rodrigo Leme, G. Prakash, F. Rana, N. Wagner and; M. Xiao. World Energy Transitions Outlook 2023: 1.5°C Pathway. **2023**.
5. Consequences of Climate Change - European Commission Available online: https://climate.ec.europa.eu/climate-change/consequences-climate-change_en (accessed on 19 February 2024).
6. P. Ralon, M. Taylor and A. Ilas (IRENA), with H. Diaz-Bone V Electricity Storage and Renewables: Costs and Markets to 2030. **2017**.
7. Combustibile fossile. *Wikipedia* 2024.
8. L’impatto Dei Combustibili Fossili Sulla Terra Available online: https://www.nationalgeographic.it/l-impatto-dei-combustibili-fossili-sulla-terra (accessed on 13 February 2024).
9. Jacopo Celè Study of the Effect of Carbon Nanofibers Electrodes Morphology on Sodium-Ion Cells Electrochemical Performances.
10. Francisco Díaz-González, Andreas Sumper, Oriol Gomis-Bellmunt Energy Storage Technologies. In *Energy Storage in Power Systems*; John Wiley & Sons, Ltd, 2016; pp. 93–141 ISBN 978-1-118-97129-1.
11. Hannan, M.A. Review of Energy Storage Systems for Electric Vehicle Applications_ Issues and Challenges. *Renewable and Sustainable Energy Reviews* **2017**.
12. Broadhead, J.; Trumbore, F.A. Lithium-Niobium Selenide Secondary Battery. *J. Electrochem. Soc.; (United States)* **1973**, *120:3*.
13. Whittingham, M.S. Electrointercalation in Transition-Metal Disulphides. *J. Chem. Soc., Chem. Commun.* **1974**, 328–329, doi:10.1039/C39740000328.
14. Hwang, J.-Y.; Myung, S.-T.; Sun, Y.-K. Sodium-Ion Batteries: Present and Future. *Chem. Soc. Rev.* **2017**, *46*, 3529–3614, doi:10.1039/C6CS00776G.
15. The Nobel Prize in Chemistry 2019 Available online: https://www.nobelprize.org/prizes/chemistry/2019/press-release/ (accessed on 8 February 2024).
16. Ozawa, K. Lithium-Ion Rechargeable Batteries with LiCoO2 and Carbon Electrodes: The LiCoO2/C System. *Solid State Ionics* **1994**, *69*, 212–221, doi:10.1016/0167-2738(94)90411-1.
17. Blomgren, G.E. The Development and Future of Lithium Ion Batteries. *J. Electrochem. Soc.* **2016**, *164*, A5019, doi:10.1149/2.0251701jes.
18. Daniele Spada The Key Role of High-Performance Anode Materials in Li- and Na-Ion Batteries, 2022.
19. Alves, D.P.; Blagoeva, D.; Pavel, C.; Arvanitidis, N. Cobalt: Demand-Supply Balances in the Transition to Electric Mobility Available online: https://publications.jrc.ec.europa.eu/repository/handle/JRC112285 (accessed on 13 November 2023).
20. Vaalma, C.; Buchholz, D.; Weil, M.; Passerini, S. A Cost and Resource Analysis of Sodium-Ion Batteries. *Nat Rev Mater* **2018**, *3*, 1–11, doi:10.1038/natrevmats.2018.13.
21. Rajagopalan, R.; Zhang, Z.; Tang, Y.; Jia, C.; Ji, X.; Wang, H. Understanding Crystal Structures, Ion Diffusion Mechanisms and Sodium Storage Behaviors of NASICON Materials. *Energy Storage Materials* **2021**, *34*, 171–193, doi:10.1016/j.ensm.2020.09.007.
22. Survey, U.S.G. *Mineral Commodity Summaries 2023*; U.S. Geological Survey, 2023;

23. Survey, U.S.G. *Mineral Commodity Summaries 2020*; U.S. Geological Survey, 2020;
24. B. S. Gesine Ames. Critical Cobalt 2018.
25. Vikström, H.; Davidsson, S.; Höök, M. Lithium Availability and Future Production Outlooks. *Applied Energy* **2013**, *110*, 252–266, doi:10.1016/j.apenergy.2013.04.005.
26. Calisaya-Azpilcueta, D.; Herrera-Leon, S.; Cisternas, L.A. Current and Future Global Lithium Production Till 2025. *The Open Chemical Engineering Journal* **2020**, *14*, doi:10.2174/1874123102014010036.
27. Martin, G.; Rentsch, L.; Höck, M.; Bertau, M. Lithium Market Research – Global Supply, Future Demand and Price Development. *Energy Storage Materials* **2017**, *6*, 171–179, doi:10.1016/j.ensm.2016.11.004.
28. Yabuuchi, N.; Kubota, K.; Dahbi, M.; Komaba, S. Research Development on Sodium-Ion Batteries. *Chem. Rev.* **2014**, *114*, 11636–11682, doi:10.1021/cr500192f.
29. Stevens, D.A.; Dahn, J.R. High Capacity Anode Materials for Rechargeable Sodium-Ion Batteries. *J. Electrochem. Soc.* **2000**, *147*, 1271, doi:10.1149/1.1393348.
30. Okada, S.; Takahashi, Y.; Kiyabu, T.; Doi, T.; Yamaki, J.-I.; Nishida, T. Layered Transition Metal Oxides as Cathodes for Sodium Secondary Battery. *Meet. Abstr.* **2006**, *MA2006-02*, 201, doi:10.1149/MA2006-02/4/201.
31. Che, H.; Chen, S.; Xie, Y.; Wang, H.; Amine, K.; Liao, X.-Z.; Ma, Z.-F. Electrolyte Design Strategies and Research Progress for Room-Temperature Sodium-Ion Batteries. *Energy Environ. Sci.* **2017**, *10*, 1075–1101, doi:10.1039/C7EE00524E.
32. Li, L.; Zheng, Y.; Zhang, S.; Yang, J.; Shao, Z.; Guo, Z. Recent Progress on Sodium Ion Batteries: Potential High-Performance Anodes. *Energy Environ. Sci.* **2018**, *11*, 2310–2340, doi:10.1039/C8EE01023D.
33. Udod, I.A.; Orman, H.B.; Genchel, V.K. The Sodium-Graphite System under High-Pressure Conditions: The Comparison with the Lithium-Graphite System. *Carbon* **1994**, *32*, 101–106, doi:10.1016/0008-6223(94)90014-0.
34. Okoshi, M.; Yamad, Y.; Yamad, A.; Nakai, H. Theoretical Analysis on De-Solvation of Lithium, Sodium, and Magnesium Cations to Organic Electrolyte Solvents. *Journal of the Electrochemical Society* **2013**, *160*, A2160–A2165, doi:10.1149/2.074311jes.
35. Yamada, Y.; Koyama, Y.; Abe, T.; Ogumi, Z. Correlation between Charge−Discharge Behavior of Graphite and Solvation Structure of the Lithium Ion in Propylene Carbonate-Containing Electrolytes. *J. Phys. Chem. C* **2009**, *113*, 8948–8953, doi:10.1021/jp9022458.
36. Yamada, Y.; Iriyama, Y.; Abe, T.; Ogumi, Z. Kinetics of Lithium Ion Transfer at the Interface between Graphite and Liquid Electrolytes: Effects of Solvent and Surface Film. *Langmuir* **2009**, *25*, 12766–12770, doi:10.1021/la901829v.
37. Kuratani, K.; Uemura, N.; Senoh, H.; Takeshita, H.T.; Kiyobayashi, T. Conductivity, Viscosity and Density of MClO4 (M = Li and Na) Dissolved in Propylene Carbonate and γ-Butyrolactone at High Concentrations. *Journal of Power Sources* **2013**, *223*, 175–182, doi:10.1016/j.jpowsour.2012.09.039.
38. Guo, W.; Feng, T.; Li, W.; Hua, L.; Meng, Z.; Li, K. Comparative Life Cycle Assessment of Sodium-Ion and Lithium Iron Phosphate Batteries in the Context of Carbon Neutrality. *Journal of Energy Storage* **2023**, *72*, 108589, doi:10.1016/j.est.2023.108589.
39. Carvalho, M.L.; Cusenza, M.A.; Mela, G.; Temporelli, A.; Quinzeni, I.; Girardi, P. LCA and C-LCC Indicator as Tools for Sodium-Ion Batteries' Eco-Design. *Energies* **2023**, *16*, 6220, doi:10.3390/en16176220.
40. Muñoz-Márquez, M.Á.; Saurel, D.; Gómez-Cámer, J.L.; Casas-Cabanas, M.; Castillo-Martínez, E.; Rojo, T. Na-Ion Batteries for Large Scale Applications: A Review on Anode Materials and Solid Electrolyte Interphase Formation. *Advanced Energy Materials* **2017**, *7*, 1700463, doi:10.1002/aenm.201700463.
41. Shannon, R.D. Revised Effective Ionic Radii and Systematic Studies of Interatomic Distances in Halides and Chalcogenides. *Acta Cryst A* **1976**, *32*, 751–767, doi:10.1107/S0567739476001551.

42. Palomares, V.; Serras, P.; Villaluenga, I.; Hueso, K.B.; Carretero-González, J.; Rojo, T. Na-Ion Batteries, Recent Advances and Present Challenges to Become Low Cost Energy Storage Systems. *Energy Environ. Sci.* **2012**, *5*, 5884–5901, doi:10.1039/C2EE02781J.
43. Pu, X.; Wang, H.; Zhao, D.; Yang, H.; Ai, X.; Cao, S.; Chen, Z.; Cao, Y. Recent Progress in Rechargeable Sodium-Ion Batteries: Toward High-Power Applications. *Small* **2019**, *15*, 1805427, doi:10.1002/smll.201805427.
44. Jamesh, M.I.; Prakash, A.S. Advancement of Technology towards Developing Na-Ion Batteries. *Journal of Power Sources* **2018**, *378*, 268–300, doi:10.1016/j.jpowsour.2017.12.053.
45. Delmas, C.; Fouassier, C.; Hagenmuller, P. Structural Classification and Properties of the Layered Oxides. *Physica B+C* **1980**, *99*, 81–85, doi:10.1016/0378-4363(80)90214-4.
46. Wang, P.-F.; Xin, H.; Zuo, T.-T.; Li, Q.; Yang, X.; Yin, Y.-X.; Gao, X.; Yu, X.; Guo, Y.-G. An Abnormal 3.7 Volt O3-Type Sodium-Ion Battery Cathode. *Angewandte Chemie International Edition* **2018**, *57*, 8178–8183, doi:10.1002/anie.201804130.
47. Oh, S.-M.; Myung, S.-T.; Hwang, J.-Y.; Scrosati, B.; Amine, K.; Sun, Y.-K. High Capacity O3-Type $Na[Li_{0.05}(Ni_{0.25}Fe_{0.25}Mn_{0.5})_{0.95}]O_2$ Cathode for Sodium Ion Batteries. *Chem. Mater.* **2014**, *26*, 6165–6171, doi:10.1021/cm502481b.
48. Veerasubramani, G.K.; Subramanian, Y.; Park, M.-S.; Senthilkumar, B.; Eftekhari, A.; Kim, S.J.; Kim, D.-W. Enhanced Sodium-Ion Storage Capability of P2/O3 Biphase by Li-Ion Substitution into P2-Type $Na_{0.5}Fe_{0.5}Mn_{0.5}O_2$ Layered Cathode. *Electrochimica Acta* **2019**, *296*, 1027–1034, doi:10.1016/j.electacta.2018.11.160.
49. Wang, H.-G.; Yuan, S.; Ma, D.-L.; Zhang, X.-B.; Yan, J.-M. Electrospun Materials for Lithium and Sodium Rechargeable Batteries: From Structure Evolution to Electrochemical Performance. *Energy Environ. Sci.* **2015**, *8*, 1660–1681, doi:10.1039/C4EE03912B.
50. Guo, S.; Li, Q.; Liu, P.; Chen, M.; Zhou, H. Environmentally Stable Interface of Layered Oxide Cathodes for Sodium-Ion Batteries. *Nat Commun* **2017**, *8*, 135, doi:10.1038/s41467-017-00157-8.
51. Zhang, Y.; Zhang, R.; Huang, Y. Air-Stable NaxTMO2 Cathodes for Sodium Storage. *Frontiers in Chemistry* **2019**, *7*.
52. Nuti, M.; Spada, D.; Quinzeni, I.; Capelli, S.; Albini, B.; Galinetto, P.; Bini, M. From Tunnel NMO to Layered Polymorphs Oxides for Sodium Ion Batteries. *SN Appl. Sci.* **2020**, *2*, 1893, doi:10.1007/s42452-020-03607-z.
53. Leccardi, F.; Nodari, D.; Spada, D.; Ambrosetti, M.; Bini, M. Synergistic Effect of Polymorphs in Doped NaNi0.5Mn0.5O2 Cathode Material for Improving Electrochemical Performances in Na-Batteries. *Electrochem* **2021**, *2*, 335–346, doi:10.3390/electrochem2020024.
54. Barpanda, P.; Lander, L.; Nishimura, S.; Yamada, A. Polyanionic Insertion Materials for Sodium-Ion Batteries. *Advanced Energy Materials* **2018**, *8*, 1703055, doi:10.1002/aenm.201703055.
55. Zhou, Y.; Shao, X.; Lam, K.; Zheng, Y.; Zhao, L.; Wang, K.; Zhao, J.; Chen, F.; Hou, X. Symmetric Sodium-Ion Battery Based on Dual-Electron Reactions of NASICON-Structured $Na_3MnTi(PO_4)_3$ Material. *ACS Appl. Mater. Interfaces* **2020**, *12*, 30328–30335, doi:10.1021/acsami.0c05784.
56. Gao, H.; Seymour, I.D.; Xin, S.; Xue, L.; Henkelman, G.; Goodenough, J.B. Na3MnZr(PO4)3: A High-Voltage Cathode for Sodium Batteries. *J. Am. Chem. Soc.* **2018**, *140*, 18192–18199, doi:10.1021/jacs.8b11388.
57. Moreau, P.; Guyomard, D.; Gaubicher, J.; Boucher, F. Structure and Stability of Sodium Intercalated Phases in Olivine FePO4. *Chem. Mater.* **2010**, *22*, 4126–4128, doi:10.1021/cm101377h.
58. Liu, Y.; Zhou, Y.; Zhang, J.; Xia, Y.; Chen, T.; Zhang, S. Monoclinic Phase $Na_3Fe_2(PO_4)_3$: Synthesis, Structure, and Electrochemical Performance as Cathode Material in Sodium-Ion Batteries. *ACS Sustainable Chem. Eng.* **2017**, *5*, 1306–1314, doi:10.1021/acssuschemeng.6b01536.
59. Honma, T.; Togashi, T.; Ito, N.; Komatsu, T. Fabrication of $Na_2FeP_2O_7$ Glass-Ceramics for Sodium Ion Battery. *Journal of the Ceramic Society of Japan* **2012**, *120*, 344–346, doi:10.2109/jcersj2.120.344.
60. Barpanda, P.; Liu, G.; Avdeev, M.; Yamada, A. T-$Na_2(VO)P_2O_7$: A 3.8 V Pyrophosphate Insertion Material for Sodium-Ion Batteries. *ChemElectroChem* **2014**, *1*, 1488–1491, doi:10.1002/celc.201402095.

61. Nose, M.; Nakayama, H.; Nobuhara, K.; Yamaguchi, H.; Nakanishi, S.; Iba, H. $Na_4Co_3(PO_4)_2P_2O_7$: A Novel Storage Material for Sodium-Ion Batteries. *Journal of Power Sources* **2013**, *234*, 175–179, doi:10.1016/j.jpowsour.2013.01.162.
62. Kim, H.; Park, I.; Seo, D.-H.; Lee, S.; Kim, S.-W.; Kwon, W.J.; Park, Y.-U.; Kim, C.S.; Jeon, S.; Kang, K. New Iron-Based Mixed-Polyanion Cathodes for Lithium and Sodium Rechargeable Batteries: Combined First Principles Calculations and Experimental Study. *J. Am. Chem. Soc.* **2012**, *134*, 10369–10372, doi:10.1021/ja3038646.
63. Ben Smida, Y.; Guesmi, A.; Georges, S.; Avdeev, M.; Zid, M.F. Crystal Structure and Ionic Conductivity of the New Cobalt Polyphosphate $NaCo(PO_3)_3$. *Journal of Solid State Chemistry* **2016**, *234*, 15–21, doi:10.1016/j.jssc.2015.11.029.
64. Gond, R.; Meena, S.S.; Yusuf, S.M.; Shukla, V.; Jena, N.K.; Ahuja, R.; Okada, S.; Barpanda, P. Enabling the Electrochemical Activity in Sodium Iron Metaphosphate [$NaFe(PO_3)_3$] Sodium Battery Insertion Material: Structural and Electrochemical Insights. *Inorg. Chem.* **2017**, *56*, 5918–5929, doi:10.1021/acs.inorgchem.7b00561.
65. Kim, S.-W.; Seo, D.-H.; Kim, H.; Park, K.-Y.; Kang, K. A Comparative Study on Na_2MnPO_4F and Li_2MnPO_4F for Rechargeable Battery Cathodes. *Phys. Chem. Chem. Phys.* **2012**, *14*, 3299–3303, doi:10.1039/C2CP40082K.
66. Barker, J.; Saidi, M.Y.; Swoyer, J.L. A Sodium-Ion Cell Based on the Fluorophosphate Compound $NaVPO_4$ F. *Electrochem. Solid-State Lett.* **2002**, *6*, A1, doi:10.1149/1.1523691.
67. Essehli, R.; Belharouak, I.; Yahia, H.B.; Maher, K.; Abouimrane, A.; Orayech, B.; Calder, S.; Zhou, X.L.; Zhou, Z.; Sun, Y.-K. Alluaudite $Na_2Co_2Fe(PO_4)_3$ as an Electroactive Material for Sodium Ion Batteries. *Dalton Trans.* **2015**, *44*, 7881–7886, doi:10.1039/C5DT00971E.
68. Liu, D.; Palmore, G.T.R. Synthesis, Crystal Structure, and Electrochemical Properties of Alluaudite $Na_{1.702}Fe_3(PO_4)_3$ as a Sodium-Ion Battery Cathode. *ACS Sustainable Chem. Eng.* **2017**, *5*, 5766–5771, doi:10.1021/acssuschemeng.7b00371.
69. Wang, L.; Song, J.; Qiao, R.; Wray, L.A.; Hossain, M.A.; Chuang, Y.-D.; Yang, W.; Lu, Y.; Evans, D.; Lee, J.-J.; et al. Rhombohedral Prussian White as Cathode for Rechargeable Sodium-Ion Batteries. *J. Am. Chem. Soc.* **2015**, *137*, 2548–2554, doi:10.1021/ja510347s.
70. Yang, Y.; Zhou, J.; Wang, L.; Jiao, Z.; Xiao, M.; Huang, Q.; Liu, M.; Shao, Q.; Sun, X.; Zhang, J. Prussian Blue and Its Analogues as Cathode Materials for Na-, K-, Mg-, Ca-, Zn- and Al-Ion Batteries. *Nano Energy* **2022**, *99*, 107424, doi:10.1016/j.nanoen.2022.107424.
71. Du, G.; Pang, H. Recent Advancements in Prussian Blue Analogues: Preparation and Application in Batteries. *Energy Storage Materials* **2021**, *36*, 387–408, doi:10.1016/j.ensm.2021.01.006.
72. Peng, J.; Zhang, W.; Liu, Q.; Wang, J.; Chou, S.; Liu, H.; Dou, S. Prussian Blue Analogues for Sodium-Ion Batteries: Past, Present, and Future. *Advanced Materials* **2022**, *34*, 2108384, doi:10.1002/adma.202108384.
73. Perveen, T.; Siddiq, M.; Shahzad, N.; Ihsan, R.; Ahmad, A.; Shahzad, M.I. Prospects in Anode Materials for Sodium Ion Batteries - A Review. *Renewable and Sustainable Energy Reviews* **2020**, *119*, 109549, doi:10.1016/j.rser.2019.109549.
74. Conti, D.M.; Fusaro, C.; Bruni, G.; Galinetto, P.; Albini, B.; Milanese, C.; Berbenni, V.; Capsoni, D. ZnS–rGO/CNF Free-Standing Anodes for SIBs: Improved Electrochemical Performance at High C-Rate. *Nanomaterials* **2023**, *13*, 1160, doi:10.3390/nano13071160.
75. Spada, D.; Davino, S.; Girella, A.; Milanese, C.; Bini, M. Inside the Failure Mechanism of Tin Oxide as Anode for Sodium Ion Batteries. *J Solid State Electrochem* **2021**, *25*, 1401–1410, doi:10.1007/s10008-021-04919-9.
76. Liu, Y.; Yang, C.; Zhang, Q.; Liu, M. Recent Progress in the Design of Metal Sulfides as Anode Materials for Sodium Ion Batteries. *Energy Storage Materials* **2019**, *22*, 66–95, doi:10.1016/j.ensm.2019.01.001.
77. Divincenzo, D.P.; Mele, E.J. Cohesion and Structure in Stage-1 Graphite Intercalation Compounds. *Physical Review B* **1985**, *32*, 2538–2553, doi:10.1103/PhysRevB.32.2538.
78. Cabello, M.; Bai, X.; Chyrka, T.; Ortiz, G.F.; Lavela, P.; Alcántara, R.; Tirado, J.L. On the Reliability of Sodium Co-Intercalation in Expanded Graphite Prepared by Different Methods as Anodes for Sodium-Ion Batteries. *J. Electrochem. Soc.* **2017**, *164*, A3804, doi:10.1149/2.0211714jes.

79. Wen, Y.; He, K.; Zhu, Y.; Han, F.; Xu, Y.; Matsuda, I.; Ishii, Y.; Cumings, J.; Wang, C. Expanded Graphite as Superior Anode for Sodium-Ion Batteries. *Nature Communications* **2014**, *5*, doi:10.1038/ncomms5033.
80. Luo, X.-F.; Yang, C.-H.; Peng, Y.-Y.; Pu, N.-W.; Ger, M.-D.; Hsieh, C.-T.; Chang, J.-K. Graphene Nanosheets, Carbon Nanotubes, Graphite, and Activated Carbon as Anode Materials for Sodium-Ion Batteries. *Journal of Materials Chemistry A* **2015**, *3*, 10320–10326, doi:10.1039/c5ta00727e.
81. Jin, J.; Shi, Z.; Wang, C. Electrochemical Performance of Electrospun Carbon Nanofibers as Free-Standing and Binder-Free Anodes for Sodium-Ion and Lithium-Ion Batteries. *Electrochimica Acta* **2014**, *141*, 302–310, doi:10.1016/j.electacta.2014.07.079.
82. Chen, C.; Lu, Y.; Ge, Y.; Zhu, J.; Jiang, H.; Li, Y.; Hu, Y.; Zhang, X. Synthesis of Nitrogen-Doped Electrospun Carbon Nanofibers as Anode Material for High-Performance Sodium-Ion Batteries. *Energy Technol.* **2016**, *4*, 1440–1449, doi:10.1002/ente.201600205.
83. Li, D.; Zhang, L.; Chen, H.; Ding, L.; Wang, S.; Wang, H. Nitrogen-Doped Bamboo-like Carbon Nanotubes: Promising Anode Materials for Sodium-Ion Batteries. *Chem. Commun.* **2015**, *51*, 16045–16048, doi:10.1039/C5CC06266G.
84. Jo, J.; Lee, S.; Gim, J.; Song, J.; Kim, S.; Mathew, V.; Alfaruqi, M.H.; Kim, S.; Lim, J.; Kim, J. Facile Synthesis of Reduced Graphene Oxide by Modified Hummer's Method as Anode Material for Li-, Na- and K-Ion Secondary Batteries. *Royal Society Open Science* **2019**, *6*, 181978, doi:10.1098/rsos.181978.
85. Zheng, T.; Reimers, J.N.; Dahn, J.R. Effect of Turbostratic Disorder in Graphitic Carbon Hosts on the Intercalation of Lithium. *Physical Review B* **1995**, *51*, 734–741, doi:10.1103/PhysRevB.51.734.
86. Irisarri, E.; Ponrouch, A.; Palacin, M.R. Review—Hard Carbon Negative Electrode Materials for Sodium-Ion Batteries. *J. Electrochem. Soc.* **2015**, *162*, A2476, doi:10.1149/2.0091514jes.
87. Ingersoll, N.; Karimi, Z.; Patel, D.; Underwood, R.; Warren, R. Metal Organic Framework-Derived Carbon Structures for Sodium-Ion Battery Anodes. *Electrochimica Acta* **2019**, *297*, 129–136, doi:10.1016/j.electacta.2018.11.140.
88. Chen, Y.; Li, X.; Park, K.; Lu, W.; Wang, C.; Xue, W.; Yang, F.; Zhou, J.; Suo, L.; Lin, T.; et al. Nitrogen-Doped Carbon for Sodium-Ion Battery Anode by Self-Etching and Graphitization of Bimetallic MOF-Based Composite. *Chem* **2017**, *3*, 152–163, doi:10.1016/j.chempr.2017.05.021.
89. Hariharan, S.; Saravanan, K.; Ramar, V.; Balaya, P. A Rationally Designed Dual Role Anode Material for Lithium-Ion and Sodium-Ion Batteries: Case Study of Eco-Friendly Fe3O4. *Phys. Chem. Chem. Phys.* **2013**, *15*, 2945–2953, doi:10.1039/C2CP44572G.
90. Du, X.; Zhao, H.; Lu, Y.; Zhang, Z.; Kulka, A.; Świerczek, K. Synthesis of Core-Shell-like ZnS/C Nanocomposite as Improved Anode Material for Lithium Ion Batteries. *Electrochimica Acta* **2017**, *228*, 100–106, doi:10.1016/j.electacta.2017.01.038.
91. Lei, Y.; Chen, F.; Li, R.; Xu, J. A Facile Solvothermal Method to Produce Graphene-ZnS Composites for Superior Photoelectric Applications. *Applied Surface Science* **2014**, *308*, 206–210, doi:10.1016/j.apsusc.2014.04.135.
92. Li, J.; Yan, D.; Zhang, X.; Hou, S.; Lu, T.; Yao, Y.; Pan, L. ZnS Nanoparticles Decorated on Nitrogen-Doped Porous Carbon Polyhedra: A Promising Anode Material for Lithium-Ion and Sodium-Ion Batteries. *Journal of Materials Chemistry A* **2017**, *5*, 20428–20438, doi:10.1039/C7TA06180C.
93. Cao, Z.; Song, H.; Cao, B.; Ma, J.; Chen, X.; Zhou, J.; Ma, Z. Sheet-on-Sheet Chrysanthemum-like C/FeS Microspheres Synthesized by One-Step Solvothermal Method for High-Performance Sodium-Ion Batteries. *Journal of Power Sources* **2017**, *364*, 208–214, doi:10.1016/j.jpowsour.2017.08.018.
94. Yu, X.Y.; (David) Lou, X.W. Mixed Metal Sulfides for Electrochemical Energy Storage and Conversion. *Advanced Energy Materials* **2018**, *8*, doi:10.1002/aenm.201701592.
95. Ou, X.; Yang, C.; Xiong, X.; Zheng, F.; Pan, Q.; Jin, C.; Liu, M.; Huang, K. A New rGO-Overcoated Sb2Se3 Nanorods Anode for Na^+ Battery: In Situ X-Ray Diffraction Study on a Live Sodiation/Desodiation Process. *Advanced Functional Materials* **2017**, *27*, doi:10.1002/adfm.201606242.

96. Kim, Y.; Kim, Y.; Park, Y.; Jo, Y.N.; Kim, Y.-J.; Choi, N.-S.; Lee, K.T. SnSe Alloy as a Promising Anode Material for Na-Ion Batteries. *Chemical Communications* **2015**, *51*, 50–53, doi:10.1039/c4cc06106c.

97. Lu, Y.; Zhou, P.; Lei, K.; Zhao, Q.; Tao, Z.; Chen, J. Selenium Phosphide (Se_4P_4) as a New and Promising Anode Material for Sodium-Ion Batteries. *Advanced Energy Materials* **2017**, *7*, 1601973, doi:10.1002/aenm.201601973.

98. Liu, J.; Kopold, P.; Wu, C.; Van Aken, P.A.; Maier, J.; Yu, Y. Uniform Yolk-Shell Sn_4P_3@C Nanospheres as High-Capacity and Cycle-Stable Anode Materials for Sodium-Ion Batteries. *Energy and Environmental Science* **2015**, *8*, 3531–3538, doi:10.1039/c5ee02074c.

99. Ge, X.; Li, Z.; Yin, L. Metal-Organic Frameworks Derived Porous Core/shellCoP@C Polyhedrons Anchored on 3D Reduced Graphene Oxide Networks as Anode for Sodium-Ion Battery. *Nano Energy* **2017**, *32*, 117–124, doi:10.1016/j.nanoen.2016.11.055.

100. S. K. Park,.; J.K. Kim,; Y.C. Kang, Metal–Organic Framework-Derived $CoSe_2$/(NiCo)Se_2 Box-in-Box Hollow Nanocubes with Enhanced Electrochemical Properties for Sodium-Ion Storage and Hydrogen Evolution. *J. Mater. Chem. A* **2017**, *5*, 18823–18830, doi:10.1039/C7TA05571D.

101. Komaba, S.; Matsuura, Y.; Ishikawa, T.; Yabuuchi, N.; Murata, W.; Kuze, S. Redox Reaction of Sn-Polyacrylate Electrodes in Aprotic Na Cell. *Electrochemistry Communications* **2012**, *21*, 65–68, doi:10.1016/j.elecom.2012.05.017.

102. Ellis, L.D.; Wilkes, B.N.; Hatchard, T.D.; Obrovac, M.N. In Situ XRD Study of Silicon, Lead and Bismuth Negative Electrodes in Nonaqueous Sodium Cells. *J. Electrochem. Soc.* **2014**, *161*, A416, doi:10.1149/2.080403jes.

103. Liu, X.; Gao, Y.; Jin, R.; Luo, H.; Peng, P.; Liu, Y. Scalable Synthesis of Si Nanostructures by Low-Temperature Magnesiothermic Reduction of Silica for Application in Lithium Ion Batteries. *Nano Energy* **2014**, *4*, 31–38, doi:10.1016/j.nanoen.2013.12.002.

104. Baggetto, L.; Keum, J.K.; Browning, J.F.; Veith, G.M. Germanium as Negative Electrode Material for Sodium-Ion Batteries. *Electrochemistry Communications* **2013**, *34*, 41–44, doi:10.1016/j.elecom.2013.05.025.

105. Sun, J.; Lee, H.-W.; Pasta, M.; Sun, Y.; Liu, W.; Li, Y.; Lee, H.R.; Liu, N.; Cui, Y. Carbothermic Reduction Synthesis of Red Phosphorus-Filled 3D Carbon Material as a High-Capacity Anode for Sodium Ion Batteries. *Energy Storage Materials* **2016**, *4*, 130–136, doi:10.1016/j.ensm.2016.04.003.

106. Chen, S.; Wu, C.; Shen, L.; Zhu, C.; Huang, Y.; Xi, K.; Maier, J.; Yu, Y. Challenges and Perspectives for NASICON-Type Electrode Materials for Advanced Sodium-Ion Batteries. *Advanced Materials* **2017**, *29*, 1700431, doi:10.1002/adma.201700431.

107. Thirupathi, R.; Kumari, V.; Chakrabarty, S.; Omar, S. Recent Progress and Prospects of NASICON Framework Electrodes for Na-Ion Batteries. *Progress in Materials Science* **2023**, *137*, 101128, doi:10.1016/j.pmatsci.2023.101128.

108. Singh, B.; Wang, Z.; Park, S.; Gautam, G.S.; Chotard, J.-N.; Croguennec, L.; Carlier, D.; Cheetham, A.K.; Masquelier, C.; Canepa, P. A Chemical Map of NaSICON Electrode Materials for Sodium-Ion Batteries. *J. Mater. Chem. A* **2021**, *9*, 281–292, doi:10.1039/D0TA10688G.

109. Niu, Y.; Zhao, Y.; Xu, M. Manganese-based Polyanionic Cathodes for Sodium-ion Batteries. *Carbon Neutralization* **2023**, *2*, 150–168, doi:10.1002/cnl2.48.

110. Chen, Y.; Cheng, J.; Sun, S.; Wang, Y.; Guo, L. Coating a $Na_3V_2(PO_4)_3$ Cathode Material with Carbon to Improve Its Sodium Storage. *New Carbon Materials* **2021**, *36*, 1118–1126, doi:10.1016/S1872-5805(21)60098-7.

111. Chen, Y.; Xu, Y.; Sun, X.; Zhang, B.; He, S.; Li, L.; Wang, C. Preventing Structural Degradation from $Na_3V_2(PO_4)_3$ to $V_2(PO_4)_3$: F-Doped $Na_3V_2(PO_4)_3$/C Cathode Composite with Stable Lifetime for Sodium Ion Batteries. *Journal of Power Sources* **2018**, *378*, 423–432, doi:10.1016/j.jpowsour.2017.12.073.

112. Gao, R.; Tan, R.; Han, L.; Zhao, Y.; Wang, Z.; Yang, L.; Pan, F. Nanofiber Networks of $Na_3V_2(PO_4)_3$ as a Cathode Material for High Performance All-Solid-State Sodium-Ion Batteries. *J. Mater. Chem. A* **2017**, *5*, 5273–5277, doi:10.1039/C7TA00314E.

113. Ma, X.; Wu, X.; Liu, Y.; Wu, W.; Pan, Z.; Shen, P.K. Toward a High-Energy-Density Cathode with Enhanced Temperature Adaptability for Sodium-Ion Batteries: A Case Study of $Na_3MnZr(PO_4)_3$ Microspheres with Embedded Dual-Carbon Networks. *ACS Appl. Mater. Interfaces* **2021**, *13*, 21390–21400, doi:10.1021/acsami.1c03642.

114. Gao, H.; Goodenough, J.B. An Aqueous Symmetric Sodium-Ion Battery with NASICON-Structured $Na_3MnTi(PO_4)_3$. *Angewandte Chemie International Edition* **2016**, *55*, 12768–12772, doi:10.1002/anie.201606508.

115. Jiang, Y.; Liang, J.; Song, K.; Chen, K.; Li, X.; Zhao, L.; Dai, C.; Zhang, J.; Wang, Y. Benefits of Vanadium Doping in $Na_3MnTi(PO_4)_3$/C as a Potential Candidate for Sodium-Ion Batteries. *Materials Chemistry and Physics* **2022**, *282*, 125938, doi:10.1016/j.matchemphys.2022.125938.

116. Jiang, Y.; Wang, Y.; Li, X.; Zhang, J.; Chen, K.; Liang, J.; Zhao, L.; Dai, C. Chromium Doped NASICON-Structured $Na_3MnTi(PO_4)_3$/C Cathode for High-Performance Sodium-Ion Batteries. *Colloids and Surfaces A: Physicochemical and Engineering Aspects* **2022**, *649*, 129340, doi:10.1016/j.colsurfa.2022.129340.

117. Fanjat, N.; Lucazeau, G.; Dianoux, A.J. Study of $Na_3Fe_2(PO_4)_3$ and $Na_3Cr_2(PO_4)_3$ in Their Paramagnetic Phases by Neutron Scattering. *Journal of Physics and Chemistry of Solids* **1992**, *53*, 395–403, doi:10.1016/0022-3697(92)90174-C.

118. Kawai, K.; Asakura, D.; Nishimura, S.; Yamada, A. Stabilization of a 4.5 V Cr^{4+}/Cr^{3+} Redox Reaction in NASICON-Type $Na_3Cr_2(PO_4)_3$ by Ti Substitution. *Chem. Commun.* **2019**, *55*, 13717–13720, doi:10.1039/C9CC04860J.

119. Mamoor, M.; Lian, R.; Wang, D.; Dou, Y.; Wang, Y.; Yu, Y.; Wang, C.; Chen, G.; Wei, Y. Identification of the Structural, Electronic Properties, and Ionic Diffusion Kinetics of $Na_3Cr_2(PO_4)_3$ by First-Principles Calculations. *Electrochimica Acta* **2021**, *379*, 138157, doi:10.1016/j.electacta.2021.138157.

120. Li, Z.; Young, D.; Xiang, K.; Carter, W.C.; Chiang, Y.-M. Towards High Power High Energy Aqueous Sodium-Ion Batteries: The $NaTi_2(PO_4)_3/Na_{0.44}MnO_2$ System. *Advanced Energy Materials* **2013**, *3*, 290–294, doi:10.1002/aenm.201200598.

121. Park, S.I.; Gocheva, I.; Okada, S.; Yamaki, J. Electrochemical Properties of $NaTi_2(PO_4)_3$ Anode for Rechargeable Aqueous Sodium-Ion Batteries. *J. Electrochem. Soc.* **2011**, *158*, A1067, doi:10.1149/1.3611434.

122. Wang, D.; Liu, Q.; Chen, C.; Li, M.; Meng, X.; Bie, X.; Wei, Y.; Huang, Y.; Du, F.; Wang, C.; et al. NASICON-Structured $NaTi_2(PO_4)_3$@C Nanocomposite as the Low Operation-Voltage Anode Material for High-Performance Sodium-Ion Batteries. *ACS Appl. Mater. Interfaces* **2016**, *8*, 2238–2246, doi:10.1021/acsami.5b11003.

123. Ji, Y.; Honma, T.; Komatsu, T. Formation of Sodium Ion Conductive $NaZr_2(PO_4)_3$ Composite via Liquid Phase Sintering Method with Sodium Disilicate Glass. *Solid State Ionics* **2023**, *395*, 116213, doi:10.1016/j.ssi.2023.116213.

124. Kuganathan, N.; Chroneos, A. Defects, Diffusion, Dopants and Encapsulation of Na in $NaZr_2(PO_4)_3$. *Materialia* **2021**, *16*, 101039, doi:10.1016/j.mtla.2021.101039.

125. Wang, W.; Jiang, B.; Hu, L.; Jiao, S. Nasicon Material $NaZr_2(PO_4)_3$: A Novel Storage Material for Sodium-Ion Batteries. *J. Mater. Chem. A* **2013**, *2*, 1341–1345, doi:10.1039/C3TA14310D.

126. He, W.; Li, C.; Zhao, B.; Zhang, X.; San Hui, K.; Zhu, J. Metal Ti Quantum Chain-Inlaid 2D $NaSn_2(PO_4)_3$/H-Doped Hard Carbon Hybrid Electrodes with Ultrahigh Energy Storage Density. *Chemical Engineering Journal* **2021**, *403*, 126311, doi:10.1016/j.cej.2020.126311.

127. Hu, P.; Ma, J.; Wang, T.; Qin, B.; Zhang, C.; Shang, C.; Zhao, J.; Cui, G. NASICON-Structured $NaSn_2(PO_4)_3$ with Excellent High-Rate Properties as Anode Material for Lithium Ion Batteries. *Chem. Mater.* **2015**, *27*, 6668–6674, doi:10.1021/acs.chemmater.5b02471.

128. Palaniyandy, N.; Reddy, M.V.; Mamba, B.B. Unveiling the Electrochemistry Effect on Microsphere and Nanorod Morphology of $NaSn_2(PO_4)_3$ Anode for Lithium/Sodium Batteries. *J Solid State Electrochem* **2023**, *27*, 427–438, doi:10.1007/s10008-022-05324-6.

129. Avdeev, M. Crystal Chemistry of NaSICONs: Ideal Framework, Distortion, and Connection to Properties. *Chem. Mater.* **2021**, *33*, 7620–7632, doi:10.1021/acs.chemmater.1c02695.

130. Song, W.; Ji, X.; Wu, Z.; Zhu, Y.; Yang, Y.; Chen, J.; Jing, M.; Li, F.; Banks, C.E. First Exploration of Na-Ion Migration Pathways in the NASICON Structure $Na_3V_2(PO_4)_3$. *J. Mater. Chem. A* **2014**, *2*, 5358–5362, doi:10.1039/C4TA00230J.
131. Wang, Q.; Zhang, M.; Zhou, C.; Chen, Y. Concerted Ion-Exchange Mechanism for Sodium Diffusion and Its Promotion in $Na_3V_2(PO_4)_3$ Framework. *J. Phys. Chem. C* **2018**, *122*, 16649–16654, doi:10.1021/acs.jpcc.8b06120.
132. Hong, H.Y.-P. Crystal Structures and Crystal Chemistry in the System $Na_{1+x}Zr_2Si_xP_{3-x}O_{12}$. *Materials Research Bulletin* **1976**, *11*, 173–182, doi:10.1016/0025-5408(76)90073-8.
133. Goodenough, J.B.; Hong, H.Y.-P.; Kafalas, J.A. Fast Na+-Ion Transport in Skeleton Structures. *Materials Research Bulletin* **1976**, *11*, 203–220, doi:10.1016/0025-5408(76)90077-5.
134. Kreuer, K.-D.; Kohler, H.; Maier, J. Sodium Ion Conductors with Nasicon Framework Structure. In *High Conductivity Solid Ionic Conductors*; WORLD SCIENTIFIC, 1989; pp. 242–279 ISBN 978-9971-5-0750-3.
135. Wu, T.; Sun, J.; Jeremy Yap, Z.Q.; Ke, M.; Lim, C.Y.H.; Lu, L. Substantial Doping Engineering in $Na_3V_{2-x}Fe_x(PO_4)_3$ ($0 \leq x \leq 0.15$) as High-Rate Cathode for Sodium-Ion Battery. *Materials & Design* **2020**, *186*, 108287, doi:10.1016/j.matdes.2019.108287.
136. Zhang, B.; Zeng, T.; Liu, Y.; Zhang, J.-F. Effect of Ti-Doping on the Electrochemical Performance of Sodium Vanadium(Iii) Phosphate. *RSC Advances* **2018**, *8*, 5523–5531, doi:10.1039/c7ra12743j.
137. Huang, X.; Yi, X.; Yang, Q.; Guo, Z.; Ren, Y.; Zeng, X. Outstanding Electrochemical Performance of N/S Co-Doped Carbon/$Na_3V_2(PO_4)_3$ Hybrid as the Cathode of a Sodium-Ion Battery. *Ceramics International* **2020**, *46*, 28084–28090, doi:10.1016/j.ceramint.2020.07.303.
138. Wu, Q.; Yan, D.; Li, X.; Yu, C.; Yao, T. Promoting Electrochemical Performances of Vanadium Carbide Nanodots via N and P Co-Doped Carbon Nanosheets Wrapping. *Chemical Engineering Journal* **2020**, *393*, 123596, doi:10.1016/j.cej.2019.123596.
139. Wang, D.-W.; Zeng, Q.; Zhou, G.; Yin, L.; Li, F.; Cheng, H.-M.; Gentle, I.R.; Lu, G.Q.M. Carbon–Sulfur Composites for Li–S Batteries: Status and Prospects. *J. Mater. Chem. A* **2013**, *1*, 9382–9394, doi:10.1039/C3TA11045A.
140. Zhai, Y.; Dou, Y.; Zhao, D.; Fulvio, P.F.; Mayes, R.T.; Dai, S. Carbon Materials for Chemical Capacitive Energy Storage. *Advanced Materials* **2011**, *23*, 4828–4850, doi:10.1002/adma.201100984.
141. Yu, S.; Liu, Z.; Tempel, H.; Kungl, H.; Eichel, R.-A. Self-Standing NASICON-Type Electrodes with High Mass Loading for Fast-Cycling All-Phosphate Sodium-Ion Batteries. *J. Mater. Chem. A* **2018**, *6*, 18304–18317, doi:10.1039/C8TA07313A.
142. Meligrana, G.; Ferrari, S.; Lucherini, L.; Celè, J.; Colò, F.; Brugger, J.; Ricciardi, C.; Ruffo, R.; Gerbaldi, C. $Na_3V_2(PO_4)_3$-Supported Electrospun Carbon Nanofiber Nonwoven Fabric as Self-Standing Na-Ion Cell Cathode. *ChemElectroChem* **2020**, *7*, 1652–1659, doi:10.1002/celc.202000345.
143. Fang, J.; Wang, S.; Li, Z.; Chen, H.; Xia, L.; Ding, L.; Wang, H. Porous $Na_3V_2(PO_4)_3$@C Nanoparticles Enwrapped in Three-Dimensional Graphene for High Performance Sodium-Ion Batteries. *J. Mater. Chem. A* **2016**, *4*, 1180–1185, doi:10.1039/C5TA08869K.
144. Zhu, C.; Song, K.; van Aken, P.A.; Maier, J.; Yu, Y. Carbon-Coated $Na_3V_2(PO_4)_3$ Embedded in Porous Carbon Matrix: An Ultrafast Na-Storage Cathode with the Potential of Outperforming Li Cathodes. *Nano Lett.* **2014**, *14*, 2175–2180, doi:10.1021/nl500548a.
145. Conti, D.M.; Urru, C.; Bruni, G.; Galinetto, P.; Albini, B.; Milanese, C.; Pisani, S.; Berbenni, V.; Capsoni, D. Design of $Na_3MnZr(PO_4)_3$/Carbon Nanofiber Free-Standing Cathodes for Sodium-Ion Batteries with Enhanced Electrochemical Performances through Different Electrospinning Approaches. *Molecules* **2024**, *29*, 1885, doi:10.3390/molecules29081885.
146. Conti, D.M.; Urru, C.; Bruni, G.; Galinetto, P.; Albini, B.; Berbenni, V.; Girella, A.; Capsoni, D. $Na_3MnTi(PO_4)_3$/C Nanofiber Free-Standing Electrode for Long-Cycling-Life Sodium-Ion Batteries. *Nanomaterials* **2024**, *14*, 804, doi:10.3390/nano14090804.
147. Rui, X.; Sun, W.; Wu, C.; Yu, Y.; Yan, Q. An Advanced Sodium-Ion Battery Composed of Carbon Coated $Na_3V_2(PO_4)_3$ in a Porous Graphene Network. *Advanced Materials* **2015**, *27*, 6670–6676, doi:10.1002/adma.201502864.

148. Chen, M.; Kou, K.; Tu, M.; Hu, J.; Yang, B. Fabrication of Multi-Walled Carbon Nanotubes Modified $Na_3V_2(PO_4)_3$/C and Its Application to High-Rate Lithium-Ion Batteries Cathode. *Solid State Ionics* **2015**, *274*, 24–28, doi:10.1016/j.ssi.2015.02.021.
149. Huang, C.; Zuo, Z.; Deng, J.; Yao, Q.; Wang, Z.; Zhou, H. Electrochemical Properties of Hollow Spherical $Na_3V_2(PO_4)_3$/C Cathode Materials for Sodium-Ion Batteries. *International Journal of Electrochemical Science* **2017**, *12*, 9456–9464, doi:10.20964/2017.10.36.
150. Zhu, C.; Kopold, P.; van Aken, P.A.; Maier, J.; Yu, Y. High Power–High Energy Sodium Battery Based on Threefold Interpenetrating Network. *Advanced Materials* **2016**, *28*, 2409–2416, doi:10.1002/adma.201505943.
151. Jiang, Y.; Yang, Z.; Li, W.; Zeng, L.; Pan, F.; Wang, M.; Wei, X.; Hu, G.; Gu, L.; Yu, Y. Nanoconfined Carbon-Coated $Na_3V_2(PO_4)_3$ Particles in Mesoporous Carbon Enabling Ultralong Cycle Life for Sodium-Ion Batteries. *Advanced Energy Materials* **2015**, *5*, doi:10.1002/aenm.201402104.
152. Liu, Z.; Yuan, X.; Zhang, S.; Wang, J.; Huang, Q.; Yu, N.; Zhu, Y.; Fu, L.; Wang, F.; Chen, Y.; et al. Three-Dimensional Ordered Porous Electrode Materials for Electrochemical Energy Storage. *NPG Asia Mater* **2019**, *11*, 1–21, doi:10.1038/s41427-019-0112-3.
153. Ling, R.; Cai, S.; Xie, D.; Li, X.; Wang, M.; Lin, Y.; Jiang, S.; Shen, K.; Xiong, K.; Sun, X. Three-Dimensional Hierarchical Porous $Na_3V_2(PO_4)_3$/C Structure with High Rate Capability and Cycling Stability for Sodium-Ion Batteries. *Chemical Engineering Journal* **2018**, *353*, 264–272, doi:10.1016/j.cej.2018.07.118.
154. Wang, Q.; Zhao, B.; Zhang, S.; Gao, X.; Deng, C. Superior Sodium Intercalation of Honeycomb-Structured Hierarchical Porous $Na_3V_2(PO_4)_3$/C Microballs Prepared by a Facile One-Pot Synthesis. *J. Mater. Chem. A* **2015**, *3*, 7732–7740, doi:10.1039/C5TA00765H.
155. Yang, Q.; Li, Z.; Tian, H.; Su, Z. Synthesis and Characterization of NASICON-Structured $NaTi_2(PO_4)_3$/C as an Anode Material for Hybrid Li/Na-Ion Batteries. *Ceramics International* **2019**, *45*, 6291–6295, doi:10.1016/j.ceramint.2018.12.111.
156. Didwal, P.N.; Verma, R.; Min, C.-W.; Park, C.-J. Synthesis of 3-Dimensional Interconnected Porous $Na_3V_2(PO_4)_3$@C Composite as a High-Performance Dual Electrode for Na-Ion Batteries. *Journal of Power Sources* **2019**, *413*, 1–10, doi:10.1016/j.jpowsour.2018.12.018.
157. Xun, J.; Zhang, Y.; Xu, H. One Step Synthesis of Vesicular $Na_3V_2(PO_4)_2F_3$ and Network of $Na_3V_2(PO_4)_2F_3$@graphene Nanosheets with Improved Electrochemical Performance as Cathode Material for Sodium Ion Battery. *Inorganic Chemistry Communications* **2020**, *115*, 107884, doi:10.1016/j.inoche.2020.107884.
158. Huang, Z.; Liu, L.; Yi, L.; Xiao, W.; Li, M.; Zhou, Q.; Guo, G.; Chen, X.; Shu, H.; Yang, X.; et al. Facile Solvothermal Synthesis of $NaTi_2(PO_4)_3$/C Porous Plates as Electrode Materials for High-Performance Sodium Ion Batteries. *Journal of Power Sources* **2016**, *325*, 474–481, doi:10.1016/j.jpowsour.2016.06.066.
159. Väli, R.; Aruväli, J.; Härmas, M.; Jänes, A.; Lust, E. Glycine-Nitrate Process for Synthesis of $Na_3V_2(PO_4)_3$ Cathode Material and Optimization of Glucose-Derived Hard Carbon Anode Material for Characterization in Full Cells. *Batteries* **2019**, *5*, 56, doi:10.3390/batteries5030056.
160. Li, H.; Bai, Y.; Wu, F.; Li, Y.; Wu, C. Budding Willow Branches Shaped $Na_3V_2(PO_4)_3$/C Nanofibers Synthesized via an Electrospinning Technique and Used as Cathode Material for Sodium Ion Batteries. *Journal of Power Sources* **2015**, *273*, 784–792, doi:10.1016/j.jpowsour.2014.09.153.
161. Sun, H.; Liu, Z.; Lai, F.; Wang, X.; Wang, C.; Yu, N.; Geng, B. Freeze-Drying Assisted Biotemplated Route to 3D Mesoporous $Na_3V_2(PO_4)_3$@NC Composites as Cathodes with High Performance for Sodium-Ion Batteries. *Chem. Commun.* **2020**, *56*, 11961–11964, doi:10.1039/D0CC05217E.
162. Saravanan, K.; Mason, C.W.; Rudola, A.; Wong, K.H.; Balaya, P. The First Report on Excellent Cycling Stability and Superior Rate Capability of $Na_3V_2(PO_4)_3$ for Sodium Ion Batteries. *Advanced Energy Materials* **2013**, *3*, 444–450, doi:10.1002/aenm.201200803.
163. Zheng, W.; Gao, R.; Zhou, T.; Huang, X. Enhanced Electrochemical Performance of $Na_3V_2(PO_4)_3$ with Ni^{2+} Doping by a Spray Drying-Assisted Process for Sodium Ion Batteries. *Solid State Ionics* **2018**, *324*, 183–190, doi:10.1016/j.ssi.2018.07.006.

164. Li, S.; Ge, P.; Zhang, C.; Sun, W.; Hou, H.; Ji, X. The Electrochemical Exploration of Double Carbon-Wrapped $Na_3V_2(PO_4)_3$: Towards Long-Time Cycling and Superior Rate Sodium-Ion Battery Cathode. *Journal of Power Sources* **2017**, *366*, 249–258, doi:10.1016/j.jpowsour.2017.09.032.

165. Pu, X.; Wang, H.; Yuan, T.; Cao, S.; Liu, S.; Xu, L.; Yang, H.; Ai, X.; Chen, Z.; Cao, Y. $Na_4Fe_3(PO_4)_2P_2O_7$/C Nanospheres as Low-Cost, High-Performance Cathode Material for Sodium-Ion Batteries. *Energy Storage Materials* **2019**, *22*, 330–336, doi:10.1016/j.ensm.2019.02.017.

166. Kim, J.; Seo, D.-H.; Kim, H.; Park, I.; Yoo, J.-K.; Jung, S.-K.; Park, Y.-U.; Iii, W.A.G.; Kang, K. Unexpected Discovery of Low-Cost Maricite $NaFePO_4$ as a High-Performance Electrode for Na-Ion Batteries. *Energy Environ. Sci.* **2015**, *8*, 540–545, doi:10.1039/C4EE03215B.

167. Liu, Y.; Zhang, N.; Wang, F.; Liu, X.; Jiao, L.; Fan, L.-Z. Approaching the Downsizing Limit of Maricite $NaFePO_4$ toward High-Performance Cathode for Sodium-Ion Batteries. *Advanced Functional Materials* **2018**, *28*, 1801917, doi:10.1002/adfm.201801917.

168. Wood, S.M.; Eames, C.; Kendrick, E.; Islam, M.S. Sodium Ion Diffusion and Voltage Trends in Phosphates $Na_4M_3(PO_4)_2P_2O_7$ (M = Fe, Mn, Co, Ni) for Possible High-Rate Cathodes. *J. Phys. Chem. C* **2015**, *119*, 15935–15941, doi:10.1021/acs.jpcc.5b04648.

169. Sun, C.; Ni, Q.; Li, M.; Sun, Z.; Yuan, X.; Li, L.; Wang, K.; Jin, H.; Zhao, Y. Improving Rate Performance by Inhibiting Jahn–Teller Effect in Mn-Based Phosphate Cathode for Na-Ion Batteries. *Advanced Functional Materials n/a*, 2310248, doi:10.1002/adfm.202310248.

170. Boyadzhieva, T.; Koleva, V.; Zhecheva, E.; Nihtianova, D.; Mihaylov, L.; Stoyanova, R. Competitive Lithium and Sodium Intercalation into Sodium Manganese Phospho-Olivine $NaMnPO_4$ Covered with Carbon Black. *RSC Adv.* **2015**, *5*, 87694–87705, doi:10.1039/C5RA17299C.

171. Koleva, V.; Boyadzhieva, T.; Zhecheva, E.; Nihtianova, D.; Simova, S.; Tyuliev, G.; Stoyanova, R. Precursor-Based Methods for Low-Temperature Synthesis of Defectless $NaMnPO_4$ with an Olivine- and Maricite-Type Structure. *CrystEngComm* **2013**, *15*, 9080–9089, doi:10.1039/C3CE41545G.

172. Park, J.-S.; Kim, J.; Jo, J.H.; Myung, S.-T. Role of the Mn Substituent in $Na_3V_2(PO_4)_3$ for High-Rate Sodium Storage. *J. Mater. Chem. A* **2018**, *6*, 16627–16637, doi:10.1039/C8TA06162A.

173. Zhang, W.; Li, H.; Zhang, Z.; Xu, M.; Lai, Y.; Chou, S.-L. Full Activation of Mn4+/Mn3+ Redox in $Na_4MnCr(PO_4)_3$ as a High-Voltage and High-Rate Cathode Material for Sodium-Ion Batteries. *Small* **2020**, *16*, 2001524, doi:10.1002/smll.202001524.

174. Wang, Q.; Ling, C.; Li, J.; Gao, H.; Wang, Z.; Jin, H. Experimental and Theoretical Investigation of $Na_4MnAl(PO_4)_3$ Cathode Material for Sodium-Ion Batteries. *Chemical Engineering Journal* **2021**, *425*, 130680, doi:10.1016/j.cej.2021.130680.

175. Feltz, A.; Barth, S. Preparation and Conductivity Behaviour of $Na_3MIIZr(PO_4)_3$, (MII:Mn,Mg,Zn). *Solid State Ionics* **1983**, *9–10*, 817–821, doi:10.1016/0167-2738(83)90094-2.

176. Parejiya, A.; Essehli, R.; Amin, R.; Liu, J.; Muralidharan, N.; Meyer, H.M.; Wood, D.L.; Belharouak, I. $Na_{1+x}Mn_{x/2}Zr_{2-x/2}(PO_4)_3$ as a Li^+ and Na^+ Super Ion Conductor for Solid-State Batteries. *ACS Energy Lett.* **2021**, *6*, 429–436, doi:10.1021/acsenergylett.0c02513.

177. Kalnaus, S.; Amin, R.; Parish, C.; Parejiya, A.; Essehli, R.; Westover, A.; Tsai, W.-Y.; Nanda, J.; Belharouak, I. Effect of Composition on Mechanical Properties and Conductivity of the Dual-Ion Conductor $Na_{1+x}Mn_{x/2}Zr_{2-x/2}(PO_4)_3$ for Solid-State Batteries. *ACS Appl. Energy Mater.* **2021**, *4*, 11684–11692, doi:10.1021/acsaem.1c02414.

178. Li, H.; Zhang, W.; Han, Z.; Sun, K.; Gao, C.; Cheng, K.; Liu, Z.; Chen, Q.; Zhang, J.; Lai, Y.; et al. Pseudocapacitance Enhanced by N-Defects in $Na_3MnTi(PO_4)_3$/N-Doped Carbon Composite for Symmetric Full Sodium-Ion Batteries. *Materials Today Energy* **2021**, *21*, 100754, doi:10.1016/j.mtener.2021.100754.

179. Li, H.; Xu, M.; Gao, C.; Zhang, W.; Zhang, Z.; Lai, Y.; Jiao, L. Highly Efficient, Fast and Reversible Multi-Electron Reaction of $Na_3MnTi(PO_4)_3$ Cathode for Sodium-Ion Batteries. *Energy Storage Materials* **2020**, *26*, 325–333, doi:10.1016/j.ensm.2019.11.004.

180. Liu, J.; Huang, Y.; Zhao, Z.; Ren, W.; Li, Z.; Zou, C.; Zhao, L.; Tang, Z.; Li, X.; Wang, M.; et al. Yeast Template-Derived Multielectron Reaction NASICON Structure $Na_3MnTi(PO_4)_3$ for High-Performance Sodium-Ion Batteries. *ACS Appl. Mater. Interfaces* **2021**, *13*, 58585–58595, doi:10.1021/acsami.1c17700.

181. Lu, L.; Hu, P.; Xia, Y.; Tang, A. Effect of V3+ Doping on the Structure and Electrochemical Properties of Na$_3$MnTi(PO$_4$)$_3$ Cathode Material. *J. Phys.: Conf. Ser.* **2022**, *2351*, 012006, doi:10.1088/1742-6596/2351/1/012006.
182. Yan, X.; Zhou, Y.; Zhou, W.; Lam, K.; Hou, X. Na$_3$MnTi(PO$_4$)$_3$/C Composite as an Anode for Na-Ion Batteries with Superior Rate Performance and Long-Term Span. *Electrochimica Acta* **2022**, *429*, 140925, doi:10.1016/j.electacta.2022.140925.
183. Zhu, T.; Hu, P.; Wang, X.; Liu, Z.; Luo, W.; Owusu, K.A.; Cao, W.; Shi, C.; Li, J.; Zhou, L.; et al. Realizing Three-Electron Redox Reactions in NASICON-Structured Na$_3$MnTi(PO$_4$)$_3$ for Sodium-Ion Batteries. *Advanced Energy Materials* **2019**, *9*, 1803436, doi:10.1002/aenm.201803436.
184. Zhu, T.; Hu, P.; Cai, C.; Liu, Z.; Hu, G.; Kuang, Q.; Mai, L.; Zhou, L. Dual Carbon Decorated Na$_3$MnTi(PO$_4$)$_3$: A High-Energy-Density Cathode Material for Sodium-Ion Batteries. *Nano Energy* **2020**, *70*, 104548, doi:10.1016/j.nanoen.2020.104548.
185. Zhu, T.; Hu, P.; Wang, X.; Liu, Z.; Luo, W.; Owusu, K.A.; Cao, W.; Shi, C.; Li, J.; Zhou, L.; et al. Realizing Three-Electron Redox Reactions in NASICON- Structured Na$_3$MnTi(PO$_4$)$_3$ for Sodium-Ion Batteries. *Adv. Energy Mater.* **2019**.
186. Gao, H.; Li, Y.; Park, K.; Goodenough, J.B. Sodium Extraction from NASICON-Structured Na$_3$MnTi(PO$_4$)$_3$ through Mn(III)/Mn(II) and Mn(IV)/Mn(III) Redox Couples. *Chem. Mater.* **2016**, *28*, 6553–6559, doi:10.1021/acs.chemmater.6b02096.
187. Liu, J.; Huang, Y.; Chen, J.; Fu, L.; Zhao, L.; Zou, C.; Li, X.; Wang, M.; Lin, Y.; Cao, H. Architecture-Improved and Kinetics-Enhanced Nasicon-Type Na$_3$MnTi(PO$_4$)$_3$ Through Microbe Assisted and Structure Optimized for Boosting Sodium Ion Storage 2022.
188. Liu, J.; Lin, K.; Zhao, Y.; Zhou, Y.; Hou, X.; Liu, X.; Lou, H.; Lam, K.; Chen, F. Exceeding Three-Electron Reactions in Na$_{3+2x}$Mn$_{1+x}$Ti$_{1−x}$(PO$_4$)$_3$ NASICON Cathodes with High Energy Density for Sodium-Ion Batteries. *J. Mater. Chem. A* **2021**, *9*, 10437–10446, doi:10.1039/D1TA01148K.
189. Snarskis, G.; Pilipavičius, J.; Gryaznov, D.; Mikoliūnaitė, L.; Vilčiauskas, L. Peculiarities of Phase Formation in Mn-Based Na SuperIonic Conductor (NaSICON) Systems: The Case of Na$_{1+2x}$Mn$_x$Ti$_{2−x}$(PO$_4$)$_3$ (0.0≤*x*≤1.5). *Chem. Mater.* **2021**, *33*, 8394–8403, doi:10.1021/acs.chemmater.1c02775.
190. Li, J.; Yan, D.; Lu, T.; Qin, W.; Yao, Y.; Pan, L. Significantly Improved Sodium-Ion Storage Performance of CuS Nanosheets Anchored into Reduced Graphene Oxide with Ether-Based Electrolyte. *ACS Appl. Mater. Interfaces* **2017**, *9*, 2309–2316, doi:10.1021/acsami.6b12529.
191. Li, H.; Wang, Y.; Jiang, J.; Zhang, Y.; Peng, Y.; Zhao, J. CuS Microspheres as High-Performance Anode Material for Na-Ion Batteries. *Electrochimica Acta* **2017**, *247*, 851–859, doi:10.1016/j.electacta.2017.07.018.
192. Park, H.; Kwon, J.; Choi, H.; Shin, D.; Song, T.; Lou, X.W.D. Unusual Na+ Ion Intercalation/Deintercalation in Metal-Rich Cu$_{1.8}$S for Na-Ion Batteries. *ACS Nano* **2018**, *12*, 2827–2837, doi:10.1021/acsnano.8b00118.
193. Ma, J.; Wang, X.; Wang, H.; Wang, G.; Ma, S. Hollow ZnS Submicrospheres Encapsulated in Carbon Shells with Enhanced Lithium and Sodium Storage Properties. *Journal of Alloys and Compounds* **2018**, *735*, 51–61, doi:10.1016/j.jallcom.2017.11.046.
194. Tian, G.; Song, Y.; Luo, X.; Zhao, Z.; Han, F.; Chen, J.; Huang, H.; Tang, N.; Dsoke, S. ZnS Nanoparticles Embedded in N-Doped Porous Carbon Xerogel as Electrode Materials for Sodium-Ion Batteries. *Journal of Alloys and Compounds* **2021**, *877*, 160299, doi:10.1016/j.jallcom.2021.160299.
195. Wang, W.; Guan, M.; Wang, Q.; Chen, Y.; Chen, L.; Yin, H.; Zhu, Y.; Li, G.; Hou, Z. In Situ Embedment of ZnS Nanocrystals in High Porosity Carbon Fibers as an Advanced Anode Material for Efficient Lithium Storage. *Acta Metall. Sin. (Engl. Lett.)* **2023**, *36*, 167–176, doi:10.1007/s40195-022-01481-9.
196. Wei, X.; Yuan, H.; Wang, H.; Jiang, R.; Lan, J.; Yu, Y.; Yang, X. The Metal–Organic Framework Mediated Synthesis of Bell String-like Hollow ZnS–C Nanofibers to Enhance Sodium Storage Performance. *Materials Chemistry Frontiers* **2021**, *5*, 4712–4724, doi:10.1039/D1QM00423A.
197. Yang, K.; Guo, Q.; Li, H.; Hao, X.; Ma, Y.; Yang, M.; Zhai, T.; Savilov, S.V.; Lunin, V.V.; Xia, H. Highly Efficient Sol-Gel Synthesis for ZnS@N, S Co-Doped Carbon Nanosheets with Embedded

Heterostructure for Sodium Ion Batteries. *Journal of Power Sources* **2018**, *402*, 340–344, doi:10.1016/j.jpowsour.2018.09.046.

198. Zhang, R.; Wang, Y.; Jia, M.; Xu, J.; Pan, E. One-Pot Hydrothermal Synthesis of ZnS Quantum Dots/Graphene Hybrids as a Dual Anode for Sodium Ion and Lithium Ion Batteries. *Applied Surface Science* **2018**, *437*, 375–383, doi:10.1016/j.apsusc.2017.12.110.
199. Zhang, R.; Xu, J.; Jia, M.; Pan, E.; Zhou, C.; Jia, M. Ultrafine ZnS Quantum Dots Decorated Reduced Graphene Oxide Composites Derived from ZIF-8/Graphene Oxide Hybrids as Anode for Sodium-Ion Batteries. *Journal of Alloys and Compounds* **2019**, *781*, 450–459, doi:10.1016/j.jallcom.2018.11.122.
200. Ryu, H.-S.; Kim, J.-S.; Park, J.-S.; Park, J.-W.; Kim, K.-W.; Ahn, J.-H.; Nam, T.-H.; Wang, G.; Ahn, H.-J. Electrochemical Properties and Discharge Mechanism of Na/TiS_2 Cells with Liquid Electrolyte at Room Temperature. *J. Electrochem. Soc.* **2012**, *160*, A338, doi:10.1149/2.084302jes.
201. Lee, E.; Sahgong, S.; Johnson, C.S.; Kim, Y. Comparative Electrochemical Sodium Insertion/Extraction Behavior in Layered NaxVS2 and Na_xTiS_2. *Electrochimica Acta* **2014**, *143*, 272–277, doi:10.1016/j.electacta.2014.08.032.
202. Qu, B.; Zhang, M.; Lei, D.; Zeng, Y.; Chen, Y.; Chen, L.; Li, Q.; Wang, Y.; Wang, T. Facile Solvothermal Synthesis of Mesoporous Cu_2SnS_3 Spheres and Their Application in Lithium-Ion Batteries. *Nanoscale* **2011**, *3*, 3646–3651, doi:10.1039/C1NR10401B.
203. Wu, L.; Lu, H.; Xiao, L.; Qian, J.; Ai, X.; Yang, H.; Cao, Y. A Tin(II) Sulfide-Carbon Anode Material Based on Combined Conversion and Alloying Reactions for Sodium-Ion Batteries. *Journal of Materials Chemistry A* **2014**, *2*, 16424–16428, doi:10.1039/c4ta03365e.
204. Choi, S.H.; Kang, Y.C. Aerosol-Assisted Rapid Synthesis of SnS-C Composite Microspheres as Anode Material for Na-Ion Batteries. *Nano Res.* **2015**, *8*, 1595–1603, doi:10.1007/s12274-014-0648-z.
205. Zhang, S.; Zhao, H.; Wang, M.; Li, Z.; Mi, J. Low Crystallinity SnS Encapsulated in CNTs Decorated and S-Doped Carbon Nanofibers as Excellent Anode Material for Sodium-Ion Batteries. *Electrochimica Acta* **2018**, *279*, 186–194, doi:10.1016/j.electacta.2018.05.082.
206. Sun, R.; Wei, Q.; Li, Q.; Luo, W.; An, Q.; Sheng, J.; Wang, D.; Chen, W.; Mai, L. Vanadium Sulfide on Reduced Graphene Oxide Layer as a Promising Anode for Sodium Ion Battery. *ACS Appl. Mater. Interfaces* **2015**, *7*, 20902–20908, doi:10.1021/acsami.5b06385.
207. Zhu, L.; Li, Y.; Wang, J.; Zhu, X. Sodium Storage Performance and Mechanism of rGO-Wrapped Nanorod Vanadium Sulfide as an Anode Material for Sodium Ion Batteries. *Solid State Ionics* **2018**, *327*, 129–135, doi:10.1016/j.ssi.2018.10.022.
208. Cao, L.; Liang, X.; Ou, X.; Yang, X.; Li, Y.; Yang, C.; Lin, Z.; Liu, M. Heterointerface Engineering of Hierarchical Bi_2S_3/MoS_2 with Self-Generated Rich Phase Boundaries for Superior Sodium Storage Performance. *Advanced Functional Materials* **2020**, *30*, 1910732, doi:10.1002/adfm.201910732.
209. Cho, S.-H.; Kim, J.-H.; Kim, I.-G.; Park, J.-H.; Jung, J.-W.; Kim, H.-S.; Kim, I.-D. Reduced Graphene-Oxide-Encapsulated MoS_2/Carbon Nanofiber Composite Electrode for High-Performance Na-Ion Batteries. *Nanomaterials* **2021**, *11*, 2691, doi:10.3390/nano11102691.
210. Chen, D.; Ji, G.; Ding, B.; Ma, Y.; Qu, B.; Chen, W.; Lee, J.Y. In Situ Nitrogenated Graphene–Few-Layer WS_2 Composites for Fast and Reversible Li^+ Storage. *Nanoscale* **2013**, *5*, 7890–7896, doi:10.1039/C3NR02920D.
211. Chen, R.; Zhao, T.; Wu, W.; Wu, F.; Li, L.; Qian, J.; Xu, R.; Wu, H.; Albishri, H.M.; Al-Bogami, A.S.; et al. Free-Standing Hierarchically Sandwich-Type Tungsten Disulfide Nanotubes/Graphene Anode for Lithium-Ion Batteries. *Nano Lett.* **2014**, *14*, 5899–5904, doi:10.1021/nl502848z.
212. Cheng, Y.; Wang, Y.; Jia, C.; Bao, F. MnS Hierarchical Hollow Spheres with Novel Shell Structure. *J. Phys. Chem. B* **2006**, *110*, 24399–24402, doi:10.1021/jp063698x.
213. Kim, D.S.; Lee, J.Y.; Na, C.W.; Yoon, S.W.; Kim, S.Y.; Park, J.; Jo, Y.; Jung, M.-H. Synthesis and Photoluminescence of Cd-Doped α-MnS Nanowires. *J. Phys. Chem. B* **2006**, *110*, 18262–18266, doi:10.1021/jp063965z.
214. Wang, Q.; Zhang, W.; Guo, C.; Liu, Y.; Wang, C.; Guo, Z. In Situ Construction of 3D Interconnected FeS@Fe_3C@Graphitic Carbon Networks for High-Performance Sodium-Ion Batteries. *Advanced Functional Materials* **2017**, *27*, doi:10.1002/adfm.201703390.

215. Li, Q.; Wei, Q.; Zuo, W.; Huang, L.; Luo, W.; An, Q.; Pelenovich, V.O.; Mai, L.; Zhang, Q. Greigite Fe_3S_4 as a New Anode Material for High-Performance Sodium-Ion Batteries. *Chemical Science* **2016**, *8*, 160–164, doi:10.1039/c6sc02716d.

216. Han, F.; Lv, T.; Sun, B.; Tang, W.; Zhang, C.; Li, X. In Situ Formation of Ultrafine CoS_2 Nanoparticles Uniformly Encapsulated in N/S-Doped Carbon Polyhedron for Advanced Sodium-Ion Batteries. *RSC Adv.* **2017**, *7*, 30699–30706, doi:10.1039/C7RA03628K.

217. Du, Y.; Zhu, X.; Zhou, X.; Hu, L.; Dai, Z.; Bao, J. Co3S4 Porous Nanosheets Embedded in Graphene Sheets as High-Performance Anode Materials for Lithium and Sodium Storage. *J. Mater. Chem. A* **2015**, *3*, 6787–6791, doi:10.1039/C5TA00621J.

218. Xia, X.; Wang, Q.; Zhu, Q.; Xie, J.; Wang, J.; Zhuang, D.; Zhang, S.; Cao, G.; Zhao, X. Improved Na-Storage Cycling of Amorphous-Carbon-Sheathed Ni_3S_2 Arrays and Investigation by in Situ TEM Characterization. *Materials Today Energy* **2017**, *5*, 99–106, doi:10.1016/j.mtener.2017.05.003.

219. Wang, J.; Xu, Z. Environmental Friendly Technology for Aluminum Electrolytic Capacitors Recycling from Waste Printed Circuit Boards. *Journal of Hazardous Materials* **2017**, *326*, 1–9, doi:10.1016/j.jhazmat.2016.10.039.

220. Sun, W.; Rui, X.; Zhang, D.; Jiang, Y.; Sun, Z.; Liu, H.; Dou, S. Bismuth Sulfide: A High-Capacity Anode for Sodium-Ion Batteries. *Journal of Power Sources* **2016**, *309*, 135–140, doi:10.1016/j.jpowsour.2016.01.092.

221. Xiao, Y.; Lee, S.H.; Sun, Y.-K. The Application of Metal Sulfides in Sodium Ion Batteries. *Advanced Energy Materials* **2017**, *7*, 1601329, doi:10.1002/aenm.201601329.

222. Isah, I.; Isah, M. First-Principle Study of Zinc Sulfide (Zinc Blende, Rock Salt and Wurtzite): Stability, Phase Transition and Structural Parameters. **2020**.

223. Ulian, G.; Moro, D.; Valdrè, G. Thermodynamic and Thermoelastic Properties of Wurtzite-ZnS by Density Functional Theory. *American Mineralogist* **2020**, *105*, 1212–1222, doi:10.2138/am-2020-7330.

224. Qin, W.; Li, D.; Zhang, X.; Yan, D.; Hu, B.; Pan, L. ZnS Nanoparticles Embedded in Reduced Graphene Oxide as High Performance Anode Material of Sodium-Ion Batteries. *Electrochimica Acta* **2016**, *191*, 435–443, doi:10.1016/j.electacta.2016.01.116.

225. Hu, L.; Hu, X.; Lin, Z.; Wen, Z. 3D Graphene Network Encapsulating Mesoporous ZnS Nanospheres as High-Performance Anode Material in Sodium-Ion Batteries. *ChemElectroChem* **2018**, *5*, 1552–1558, doi:10.1002/celc.201800412.

226. Ciobanu, M.; Wilburn, J.P.; Krim, M.L.; Cliffel, D.E. 1 - Fundamentals. In *Handbook of Electrochemistry*; Zoski, C.G., Ed.; Elsevier: Amsterdam, 2007; pp. 3–29 ISBN 978-0-444-51958-0.

227. Berndt, D. *Maintenance-Free Batteries: Lead-Acid, Nickel/Cadmium, Nickel/Metal Hydride : A Handbook of Battery Technology*; Electronic & electrical engineering research studies; 2nd ed.; Research Studies Press ; John Wiley & Sons: Somerset, England, New York, 1997; ISBN 978-0-86380-198-3.

228. Tosaka *English: Electric Double-Layer (BMD Model) No Text*; 2008;

229. Helmholtz, H. Studien Über Electrische Grenzschichten. *Annalen der Physik* **1879**, *243*, 337–382, doi:10.1002/andp.18792430702.

230. Gouy, M. Sur la constitution de la charge électrique à la surface d'un électrolyte. *J. Phys. Theor. Appl.* **1910**, *9*, 457–468, doi:10.1051/jphystap:019100090045700.

231. Chapman, D.L. LI. A Contribution to the Theory of Electrocapillarity. *The London, Edinburgh, and Dublin Philosophical Magazine and Journal of Science* **1913**, *25*, 475–481, doi:10.1080/14786440408634187.

232. Otto Stern The Theory of the Electrolytic Double-Layer. *Z . Elektrochem 30.508* **1924**, 1014–1020.

233. Grahame, D.C. The Electrical Double Layer and the Theory of Electrocapillarity. *Chem. Rev.* **1947**, *41*, 441–501, doi:10.1021/cr60130a002.

234. Keith Oldham, Jan Myland, Alan Bond *Electrochemical Science and Technology: Fundamentals and Applications*; Wiley, 2011; ISBN 978-0-470-71085-2.

235. Van der Ven, A.; Bhattacharya, J.; Belak, A.A. Understanding Li Diffusion in Li-Intercalation Compounds. *Acc. Chem. Res.* **2013**, *46*, 1216–1225, doi:10.1021/ar200329r.

236. Morgan, D.; Ven, A.V. der; Ceder, G. Li Conductivity in Li_xMPO_4 (M = Mn , Fe , Co , Ni) Olivine Materials. *Electrochem. Solid-State Lett.* **2003**, *7*, A30, doi:10.1149/1.1633511.

237. Zhang, Q.; White, R.E. Comparison of Approximate Solution Methods for the Solid Phase Diffusion Equation in a Porous Electrode Model. *Journal of Power Sources* **2007**, *165*, 880–886, doi:10.1016/j.jpowsour.2006.12.056.

238. Li, W.; Zeng, L.; Wu, Y.; Yu, Y. Nanostructured Electrode Materials for Lithium-Ion and Sodium-Ion Batteries via Electrospinning. *Sci. China Mater.* **2016**, *59*, 287–321, doi:10.1007/s40843-016-5039-6.

239. Zhang, L.; Aboagye, A.; Kelkar, A.; Lai, C.; Fong, H. A Review: Carbon Nanofibers from Electrospun Polyacrylonitrile and Their Applications. *J Mater Sci* **2014**, *49*, 463–480, doi:10.1007/s10853-013-7705-y.

240. Zhou, Z.; Liu, T.; Khan, A.U.; Liu, G. Block Copolymer–Based Porous Carbon Fibers. *Science Advances* **2019**, *5*, eaau6852, doi:10.1126/sciadv.aau6852.

241. Heiner Hans Heimes, Achim Kampker, Christoph Lienemann, Marc Locke, Christian Offermanns, Sarah Michaelis, Ehsan Rahimzei *LITHIUM-ION BATTERY CELL PRODUCTION PROCESS*; PEM of RWTH Aachen and VDMA, 2018;

242. Singh, M.; Kaiser, J.; Hahn, H. A Systematic Study of Thick Electrodes for High Energy Lithium Ion Batteries. *Journal of Electroanalytical Chemistry* **2016**, *782*, 245–249, doi:10.1016/j.jelechem.2016.10.040.

243. Zheng, H.; Li, J.; Song, X.; Liu, G.; Battaglia, V.S. A Comprehensive Understanding of Electrode Thickness Effects on the Electrochemical Performances of Li-Ion Battery Cathodes. *Electrochimica Acta* **2012**, *71*, 258–265, doi:10.1016/j.electacta.2012.03.161.

244. Vu, A.; Qian, Y.; Stein, A. Porous Electrode Materials for Lithium-Ion Batteries – How to Prepare Them and What Makes Them Special. *Advanced Energy Materials* **2012**, *2*, 1056–1085, doi:10.1002/aenm.201200320.

245. Goodenough, J.B.; Kim, Y. Challenges for Rechargeable Li Batteries. *Chem. Mater.* **2010**, *22*, 587–603, doi:10.1021/cm901452z.

246. Nelson, P.; Bloom, I.; Amine, K.; Henriksen, G. Design Modeling of Lithium-Ion Battery Performance. *Journal of Power Sources* **2002**, *110*, 437–444, doi:10.1016/S0378-7753(02)00209-4.

247. Lu, W.; Jansen, A.; Dees, D.; Nelson, P.; Veselka, N.R.; Henriksen, G. High-Energy Electrode Investigation for Plug-in Hybrid Electric Vehicles. *Journal of Power Sources* **2011**, *196*, 1537–1540, doi:10.1016/j.jpowsour.2010.08.117.

248. Singh, M.; Kaiser, J.; Hahn, H. Thick Electrodes for High Energy Lithium Ion Batteries. *J. Electrochem. Soc.* **2015**, *162*, A1196, doi:10.1149/2.0401507jes.

249. Wang, J.S.; Liu, P.; Sherman, E.; Verbrugge, M.; Tataria, H. Formulation and Characterization of Ultra-Thick Electrodes for High Energy Lithium-Ion Batteries Employing Tailored Metal Foams. *Journal of Power Sources* **2011**, *196*, 8714–8718, doi:10.1016/j.jpowsour.2011.06.071.

250. Habedank, J.B.; Günter, F.J.; Billot, N.; Gilles, R.; Neuwirth, T.; Reinhart, G.; Zaeh, M.F. Rapid Electrolyte Wetting of Lithium-Ion Batteries Containing Laser Structured Electrodes: In Situ Visualization by Neutron Radiography. *Int J Adv Manuf Technol* **2019**, *102*, 2769–2778, doi:10.1007/s00170-019-03347-4.

251. Singh, M.; Kaiser, J.; Hahn, H. Effect of Porosity on the Thick Electrodes for High Energy Density Lithium Ion Batteries for Stationary Applications. *Batteries* **2016**, *2*, 35, doi:10.3390/batteries2040035.

252. Du, Z.; Wood, D.L.; Daniel, C.; Kalnaus, S.; Li, J. Understanding Limiting Factors in Thick Electrode Performance as Applied to High Energy Density Li-Ion Batteries. *J Appl Electrochem* **2017**, *47*, 405–415, doi:10.1007/s10800-017-1047-4.

253. Habedank, J.B.; Kraft, L.; Rheinfeld, A.; Krezdorn, C.; Jossen, A.; Zaeh, M.F. Increasing the Discharge Rate Capability of Lithium-Ion Cells with Laser-Structured Graphite Anodes: Modeling and Simulation. *J. Electrochem. Soc.* **2018**, *165*, A1563, doi:10.1149/2.1181807jes.

254. Wu, M.-S.; Liao, T.-L.; Wang, Y.-Y.; Wan, C.-C. Assessment of the Wettability of Porous Electrodes for Lithium-Ion Batteries. *Journal of Applied Electrochemistry* **2004**, *34*, 797–805, doi:10.1023/B:JACH.0000035599.56679.15.
255. Liu, S.; Wan, K.; Zhang, C.; Liu, T. Polyaniline-Decorated 3D Carbon Porous Network with Excellent Electrolyte Wettability and High Energy Density for Supercapacitors. *Composites Communications* **2021**, *24*, 100610, doi:10.1016/j.coco.2020.100610.
256. Sheng, Y. Investigation of Electrolyte Wetting in Lithium Ion Batteries: Effects of Electrode Pore Structures and Solution. *Theses and Dissertations* **2015**.
257. Sheng, Y.; Fell, C.R.; Son, Y.K.; Metz, B.M.; Jiang, J.; Church, B.C. Effect of Calendering on Electrode Wettability in Lithium-Ion Batteries. *Front. Energy Res.* **2014**, *2*, doi:10.3389/fenrg.2014.00056.
258. Ogihara, N.; Kawauchi, S.; Okuda, C.; Itou, Y.; Takeuchi, Y.; Ukyo, Y. Theoretical and Experimental Analysis of Porous Electrodes for Lithium-Ion Batteries by Electrochemical Impedance Spectroscopy Using a Symmetric Cell. *J. Electrochem. Soc.* **2012**, *159*, A1034, doi:10.1149/2.057207jes.
259. Ye, J.; Baumgaertel, A.C.; Wang, Y.M.; Biener, J.; Biener, M.M. Structural Optimization of 3D Porous Electrodes for High-Rate Performance Lithium Ion Batteries. *ACS Nano* **2015**, *9*, 2194–2202, doi:10.1021/nn505490u.
260. Ji, L.; Guo, Z.; Zhang, Y. Electrochemomechanical Performance of Porous Electrode Incorporating Binder Network. *Sci. China Technol. Sci.* **2019**, *62*, 1331–1340, doi:10.1007/s11431-018-9480-8.
261. Su, B.-L. Hierarchically Structured Porous Materials for Energy Conversion and Storage. In *Hierarchically Structured Porous Materials*; John Wiley & Sons, Ltd, 2011; pp. 577–600 ISBN 978-3-527-63958-8.
262. Lu, A.-H.; Schüth, F. Nanocasting: A Versatile Strategy for Creating Nanostructured Porous Materials. *Advanced Materials* **2006**, *18*, 1793–1805, doi:10.1002/adma.200600148.
263. Polarz, S.; Antonietti, M. Porous Materials via Nanocasting Procedures: Innovative Materials and Learning about Soft-Matter Organization. *Chem. Commun.* **2002**, 2593–2604, doi:10.1039/B205708P.
264. Frank Caruso (Editor) *Colloids and Colloid Assemblies: Synthesis, Modification, Organization and Utilization of Colloid Particles*; Wiley, 2006; ISBN 978-3-527-60610-8.
265. R. C. Schroden , A. Stein, A.S., F. Li ,.N.R. Denny Colloids and Colloid Assemblies: Synthesis, Modifi Cation, Organization and Utilization of Colloid Particles. *(Ed.: F. Caruso), Wiley-VCH ,Chem. Mater* **2004**, *20*, 465–649.
266. Kotobuki, M.; Okada, N.; Kanamura, K. Design of a Micro-Pattern Structure for a Three Dimensionally Macroporous Sn–Ni Alloy Anode with High Areal Capacity. *Chem. Commun.* **2011**, *47*, 6144–6146, doi:10.1039/C1CC10781J.
267. Zhou, H.; Fan, T.; Zhang, D. Biotemplated Materials for Sustainable Energy and Environment: Current Status and Challenges. *ChemSusChem* **2011**, *4*, 1344–1387, doi:10.1002/cssc.201100048.
268. Yu, Y.; Gu, L.; Zhu, C.; Tsukimoto, S.; van Aken, P.A.; Maier, J. Reversible Storage of Lithium in Silver-Coated Three-Dimensional Macroporous Silicon. *Advanced Materials* **2010**, *22*, 2247–2250, doi:10.1002/adma.200903755.
269. Bao, Z.; Weatherspoon, M.R.; Shian, S.; Cai, Y.; Graham, P.D.; Allan, S.M.; Ahmad, G.; Dickerson, M.B.; Church, B.C.; Kang, Z.; et al. Chemical Reduction of Three-Dimensional Silica Micro-Assemblies into Microporous Silicon Replicas. *Nature* **2007**, *446*, 172–175, doi:10.1038/nature05570.
270. Sandhage, K. h.; Dickerson, M. b.; Huseman, P. m.; Caranna, M. a.; Clifton, J. d.; Bull, T. a.; Heibel, T. j.; Overton, W. r.; Schoenwaelder, M. e. a. Novel, Bioclastic Route to Self-Assembled, 3D, Chemically Tailored Meso/Nanostructures: Shape-Preserving Reactive Conversion of Biosilica (Diatom) Microshells. *Advanced Materials* **2002**, *14*, 429–433, doi:10.1002/1521-4095(20020318)14:6<429::AID-ADMA429>3.0.CO;2-C.

271. Ke, F.-S.; Huang, L.; Wei, H.-B.; Cai, J.-S.; Fan, X.-Y.; Yang, F.-Z.; Sun, S.-G. Fabrication and Properties of Macroporous Tin–Cobalt Alloy Film Electrodes for Lithium-Ion Batteries. *Journal of Power Sources* **2007**, *170*, 450–455, doi:10.1016/j.jpowsour.2007.04.019.
272. Kim, J.M.; Huh, Y.S.; Han, Y.-K.; Cho, M.S.; Kim, H.J. Facile Synthesis Route to Highly Crystalline Mesoporous γ-MnO_2 Nanospheres. *Electrochemistry Communications* **2012**, *14*, 32–35, doi:10.1016/j.elecom.2011.10.023.
273. Ha, H.-W.; Kim, T.W.; Choy, J.-H.; Hwang, S.-J. Relationship between Electrode Performance and Chemical Bonding Nature in Mesoporous Metal Oxide-Layered Titanate Nanohybrids. *J. Phys. Chem. C* **2009**, *113*, 21941–21948, doi:10.1021/jp910091y.
274. Lee, K.-H.; Song, S.-W. One-Step Hydrothermal Synthesis of Mesoporous Anatase TiO_2 Microsphere and Interfacial Control for Enhanced Lithium Storage Performance. *ACS Appl. Mater. Interfaces* **2011**, *3*, 3697–3703, doi:10.1021/am200872c.
275. Feng, L.; Xie, N.; Zhong, J. Carbon Nanofibers and Their Composites: A Review of Synthesizing, Properties and Applications. *Materials* **2014**, *7*, 3919–3945, doi:10.3390/ma7053919.
276. Ji, D.; Lin, Y.; Guo, X.; Ramasubramanian, B.; Wang, R.; Radacsi, N.; Jose, R.; Qin, X.; Ramakrishna, S. Electrospinning of Nanofibres. *Nat Rev Methods Primers* **2024**, *4*, 1–21, doi:10.1038/s43586-023-00278-z.
277. Tebyetekerwa, M.; Ramakrishna, S. What Is Next for Electrospinning? *Matter* **2020**, *2*, 279–283, doi:10.1016/j.matt.2020.01.004.
278. Peng, S.; Ilango, P.R. *Electrospinning of Nanofibers for Battery Applications*; Springer: Singapore, 2020; ISBN 9789811514272.
279. Robert Ilango, P.; Peng, S. Electrospinning Techniques for Li, Na and K-Ion Batteries. *Current Opinion in Electrochemistry* **2019**, *18*, 106–112, doi:10.1016/j.coelec.2019.10.016.
280. Geoffrey R Mitchell, Ben Zhong Tang. *Polymer Chemistry: Electrospinning: Principles, Practice and Possibilities (Hardcover)*; RCS. RSC Poly- mer Chemistry Series Editor-in-Chief, 2014; ISBN 978-1-84973-556-8.
281. Huang, Z.-M.; Zhang, Y.-Z.; Kotaki, M.; Ramakrishna, S. A Review on Polymer Nanofibers by Electrospinning and Their Applications in Nanocomposites. *Composites Science and Technology* **2003**, *63*, 2223–2253, doi:10.1016/S0266-3538(03)00178-7.
282. Inagaki, M.; Yang, Y.; Kang, F. Carbon Nanofibers Prepared via Electrospinning. *Advanced Materials* **2012**, *24*, 2547–2566, doi:10.1002/adma.201104940.
283. Zhang, B.; Kang, F.; Tarascon, J.-M.; Kim, J.-K. Recent Advances in Electrospun Carbon Nanofibers and Their Application in Electrochemical Energy Storage. *Progress in Materials Science* **2016**, *76*, 319–380, doi:10.1016/j.pmatsci.2015.08.002.
284. Munajat, N.A.; Nurfaizey, A.H.; Husin, M.H.M.; Fadzullah, S.H.S.M.; Omar, G.; Salim, M.A. The Effects of Different Carbonization Temperatures on the Properties of Electrospun Carbon Nanofibre from Polyacrylonitrile (PAN) Precursor. *Journal of Advanced Research in Fluid Mechanics and Thermal Sciences* **2018**, *49*, 85–91.
285. Faccini, M.; Borja, G.; Boerrigter, M.; Morillo Martín, D.; Martinez Crespiera, S.; Vázquez-Campos, S.; Aubouy, L.; Amantia, D. Electrospun Carbon Nanofiber Membranes for Filtration of Nanoparticles from Water. *Journal of Nanomaterials* **2015**, *2015*, e247471, doi:10.1155/2015/247471.
286. Arshad, S.N.; Naraghi, M.; Chasiotis, I. Strong Carbon Nanofibers from Electrospun Polyacrylonitrile. *Carbon* **2011**, *49*, 1710–1719, doi:10.1016/j.carbon.2010.12.056.
287. Raimondo, M.; Guadagno, L.; Vertuccio, L.; Naddeo, C.; Barra, G.; Spinelli, G.; Lamberti, P.; Tucci, V.; Lafdi, K. Electrical Conductivity of Carbon Nanofiber Reinforced Resins: Potentiality of Tunneling Atomic Force Microscopy (TUNA) Technique. *Composites Part B: Engineering* **2018**, *143*, 148–160, doi:10.1016/j.compositesb.2018.02.005.
288. Gogotsi, Y.; Gogotsi, Y. *Nanotubes and Nanofibers*; 1st ed.; CRC Press, 2006; ISBN 978-1-4200-0938-5.
289. *Nanomaterials in Advanced Batteries and Supercapacitors*; Ozoemena, K.I., Chen, S., Eds.; Nanostructure Science and Technology; Springer International Publishing: Cham, 2016; ISBN 978-3-319-26080-8.

290. Chen, R.; Hu, Y.; Shen, Z.; Pan, P.; He, X.; Wu, K.; Zhang, X.; Cheng, Z. Facile Fabrication of Foldable Electrospun Polyacrylonitrile-Based Carbon Nanofibers for Flexible Lithium-Ion Batteries. *J. Mater. Chem. A* **2017**, *5*, 12914–12921, doi:10.1039/C7TA02528A.
291. Wu, Y.; Reddy, M.V.; Chowdari, B.V.R.; Ramakrishna, S. Long-Term Cycling Studies on Electrospun Carbon Nanofibers as Anode Material for Lithium Ion Batteries. *ACS Appl. Mater. Interfaces* **2013**, *5*, 12175–12184, doi:10.1021/am404216j.
292. Chen, T.; Liu, Y.; Pan, L.; Lu, T.; Yao, Y.; Sun, Z.; Chua, D.H.C.; Chen, Q. Electrospun Carbon Nanofibers as Anode Materials for Sodium Ion Batteries with Excellent Cycle Performance. *J. Mater. Chem. A* **2014**, *2*, 4117–4121, doi:10.1039/C3TA14806H.
293. De Vrieze, S.; Van Camp, T.; Nelvig, A.; Hagström, B.; Westbroek, P.; De Clerck, K. The Effect of Temperature and Humidity on Electrospinning. *J Mater Sci* **2009**, *44*, 1357–1362, doi:10.1007/s10853-008-3010-6.
294. Cono di Taylor. *Wikipedia* 2020.
295. Shao, D.; Wang, J.; Dong, X.; Yu, W.; Liu, G.; Zhang, F.; Wang, L. Coaxial Electrospinning Fabrication and Electrochemical Properties of $LiFePO_4/C/Ag$ Composite Hollow Nanofibers. *J Mater Sci: Mater Electron* **2013**, *24*, 4718–4724, doi:10.1007/s10854-013-1465-y.
296. Sun, G.; Sun, L.; Xie, H.; Liu, J. Electrospinning of Nanofibers for Energy Applications. *Nanomaterials* **2016**, *6*, 129, doi:10.3390/nano6070129.
297. Joshi, B.; Samuel, E.; Kim, Y.; Yarin, A.L.; Swihart, M.T.; Yoon, S.S. Progress and Potential of Electrospinning-Derived Substrate-Free and Binder-Free Lithium-Ion Battery Electrodes. *Chemical Engineering Journal* **2022**, *430*, 132876, doi:10.1016/j.cej.2021.132876.
298. Bhardwaj, N.; Kundu, S.C. Electrospinning: A Fascinating Fiber Fabrication Technique. *Biotechnology Advances* **2010**, *28*, 325–347, doi:10.1016/j.biotechadv.2010.01.004.
299. Bin Ding, Xianfeng Wang, Jianyong Yu *Electrospinning: Nanofabrication and Applications*; Elsevier, 2019; ISBN 978-0-323-51270-1.
300. Eda, G.; Shivkumar, S. Bead-to-Fiber Transition in Electrospun Polystyrene. *Journal of Applied Polymer Science* **2007**, *106*, 475–487, doi:10.1002/app.25907.
301. Nie, G.; Zhao, X.; Luan, Y.; Jiang, J.; Kou, Z.; Wang, J. Key Issues Facing Electrospun Carbon Nanofibers in Energy Applications: On-Going Approaches and Challenges. *Nanoscale* **2020**, *12*, 13225–13248, doi:10.1039/D0NR03425H.
302. Farsani, R.E.; Shokuhfar, A.; Sedghi, A. Stabilization of Commercial Polyacrylonitrile Fibres for Fabrication of Low-Cost Medium-Strength Carbon Fibres. *e-Polymers* **2006**, *6*, doi:10.1515/epoly.2006.6.1.1.
303. Dalton, S.; Heatley, F.; Budd, P.M. Thermal Stabilization of Polyacrylonitrile Fibres. *Polymer* **1999**, *40*, 5531–5543, doi:10.1016/S0032-3861(98)00778-2.
304. Fitzer, E.; Frohs, W.; Heine, M. Optimization of Stabilization and Carbonization Treatment of PAN-Fibers and Structural Characterization of the Resulting Carbon Fibers. *Carbon* **1986**, *24*, 387–395.
305. Rahaman, M.S.A.; Ismail, A.F.; Mustafa, A. A Review of Heat Treatment on Polyacrylonitrile Fiber. *Polymer Degradation and Stability* **2007**, *92*, 1421–1432, doi:10.1016/j.polymdegradstab.2007.03.023.
306. Khayyam, H.; Jazar, R.N.; Nunna, S.; Golkarnarenji, G.; Badii, K.; Fakhrhoseini, S.M.; Kumar, S.; Naebe, M. PAN Precursor Fabrication, Applications and Thermal Stabilization Process in Carbon Fiber Production: Experimental and Mathematical Modelling. *Progress in Materials Science* **2020**, *107*, 100575, doi:10.1016/j.pmatsci.2019.100575.
307. Konstantopoulos, G.; Soulis, S.; Dragatogiannis, D.; Charitidis, C. Introduction of a Methodology to Enhance the Stabilization Process of PAN Fibers by Modeling and Advanced Characterization. *Materials* **2020**, *13*, 2749, doi:10.3390/ma13122749.
308. Cristina Fusaro Ottimizzazione Elettrochimica Del Materiale Anodico ZnS per Batterie Agli Ioni Sodio, Università degli studi di Pavia, 2020.
309. Dai, Q.; Shen, J. Lithium Iron Phosphate Cathode Material 2010.
310. Bruker AXS *TOPAS V3.0: General Profile and Structural Analysis Software for Powder Diffraction Data. User Manual Bruker AXS.*; 2005;

311. Kern, A.; Coelho, A.A.; Cheary, R.W. Convolution Based Profile Fitting. In *Diffraction Analysis of the Microstructure of Materials*; Mittemeijer, E.J., Scardi, P., Eds.; Springer: Berlin, Heidelberg, 2004; pp. 17–50 ISBN 978-3-662-06723-9.
312. Cheary, R.W.; Coelho, A.A. Fundamental Parameters Line Profile Fitting in Laboratory Diffractometers. *Journal of Research of the National Institute of Standards and Technology* **2004**, *109*.
313. Cheary, R.W.; Coelho, A. A Fundamental Parameters Approach to X-Ray Line-Profile Fitting. *J Appl Cryst* **1992**, *25*, 109–121, doi:10.1107/S0021889891010804.
314. Contact Angle Measurement, Theory & Relation to Surface Energy Available online: https://www.ossila.com/pages/contact-angle-theory-measurement (accessed on 3 January 2024).
315. Kwok, D.Y.; Neumann, A.W. Contact Angle Measurement and Contact Angle Interpretation. *Advances in Colloid and Interface Science* **1999**, *81*, 167–249, doi:10.1016/S0001-8686(98)00087-6.
316. Dung, L.-R.; Chen, C.-E.; Yuan, H.-F. A Robust, Intelligent CC-CV Fast Charger for Aging Lithium Batteries. In Proceedings of the 2016 IEEE 25th International Symposium on Industrial Electronics (ISIE); June 2016; pp. 268–273.
317. Liu, H.; Naqvi, I.H.; Li, F.; Liu, C.; Shafiei, N.; Li, Y.; Pecht, M. An Analytical Model for the CC-CV Charge of Li-Ion Batteries with Application to Degradation Analysis. *Journal of Energy Storage* **2020**, *29*, 101342, doi:10.1016/j.est.2020.101342.
318. Li, G.; Ma, H. A Hybrid IPT System With High-Misalignment Tolerance and Inherent CC–CV Output Characteristics for EVs Charging Applications. *IEEE Journal of Emerging and Selected Topics in Power Electronics* **2022**, *10*, 3152–3160, doi:10.1109/JESTPE.2021.3112969.
319. Chen, M.; Rincon-Mora, G.A. Accurate, Compact, and Power-Efficient Li-Ion Battery Charger Circuit. *IEEE Transactions on Circuits and Systems II: Express Briefs* **2006**, *53*, 1180–1184, doi:10.1109/TCSII.2006.883220.
320. Lin, C.-H.; Hsieh, C.-Y.; Chen, K.-H. A Li-Ion Battery Charger With Smooth Control Circuit and Built-In Resistance Compensator for Achieving Stable and Fast Charging. *IEEE Transactions on Circuits and Systems I: Regular Papers* **2010**, *57*, 506–517, doi:10.1109/TCSI.2009.2023830.
321. Zhang, Z.; Li, X.; Wang, C.; Fu, S.; Liu, Y.; Shao, C. Polyacrylonitrile and Carbon Nanofibers with Controllable Nanoporous Structures by Electrospinning. *Macromolecular Materials and Engineering* **2009**, *294*, 673–678, doi:10.1002/mame.200900076.
322. Qanati, M.V.; Rasooli, A.; Rezvani, M. Main Structural and Mechanical Properties of Electrospun PAN-Based Carbon Nanofibers as a Function of Carbonization Maximum Temperature. *Polym. Bull.* **2022**, *79*, 331–355, doi:10.1007/s00289-020-03520-w.
323. Liu, C.-K.; Feng, Y.; He, H.-J.; Zhang, J.; Sun, R.-J.; Chen, M.-Y. Effect of Carbonization Temperature on Properties of Aligned Electrospun Polyacrylonitrile Carbon Nanofibers. *Materials & Design* **2015**, *85*, 483–486, doi:10.1016/j.matdes.2015.07.021.
324. Kumar, P.S.; Sahay, R.; Aravindan, V.; Sundaramurthy, J.; Ling, W.C.; Thavasi, V.; Mhaisalkar, S.G.; Madhavi, S.; Ramakrishna, S. Free-Standing Electrospun Carbon Nanofibres—a High Performance Anode Material for Lithium-Ion Batteries. *J. Phys. D: Appl. Phys.* **2012**, *45*, 265302, doi:10.1088/0022-3727/45/26/265302.
325. Conti, D.M.; Urru, C.; Bruni, G.; Galinetto, P.; Albini, B.; Berbenni, V.; Capsoni, D. High C-Rate Performant Electrospun $LiFePO_4$/Carbon Nanofiber Self-Standing Cathodes for Lithium-Ion Batteries. *Electrochem* **2024**, *5*, 223–242, doi:10.3390/electrochem5020014.
326. Bini, M.; Ferrari, S.; Capsoni, D.; Mustarelli, P.; Spina, G.; Giallo, F.D.; Lantieri, M.; Leonelli, C.; Rizzuti, A.; Massarotti, V. Pair Distribution Function Analysis and Mössbauer Study of Defects in Microwave-Hydrothermal LiFePO4. *RSC Adv.* **2011**, *2*, 250–258, doi:10.1039/C1RA00525A.
327. Belharouak, I.; Johnson, C.; Amine, K. Synthesis and Electrochemical Analysis of Vapor-Deposited Carbon-Coated $LiFePO_4$. *Electrochemistry Communications* **2005**, *7*, 983–988, doi:10.1016/j.elecom.2005.06.019.
328. Hamelet, S.; Gibot, P.; Casas-Cabanas, M.; Bonnin, D.; Grey, C.P.; Cabana, J.; Leriche, J.-B.; Rodriguez-Carvajal, J.; Courty, M.; Levasseur, S.; et al. The Effects of Moderate Thermal Treatments

under Air on $LiFePO_4$-Based Nano Powders. *J. Mater. Chem.* **2009**, *19*, 3979–3991, doi:10.1039/B901491H.

329. Delaporte, N.; Trudeau, M.L.; Bélanger, D.; Zaghib, K. Protection of $LiFePO_4$ against Moisture. *Materials* **2020**, *13*, 942, doi:10.3390/ma13040942.
330. K. Zaghib, A. Mauger, J.B. Goodenough, F. Gendron and C.M. Julien Design and Properties of $LiFePO_4$ Positive Electrode Materials for Li-Ion Batteries. In; Sheng Shui Zhang, 2007 ISBN 978-81-7895-279-6.
331. Kumar, A.; Thomas, R.; Karan, N.K.; Saavedra-Arias, J.J.; Singh, M.K.; Majumder, S.B.; Tomar, M.S.; Katiyar, R.S. Structural and Electrochemical Characterization of Pure $LiFePO_4$ and Nanocomposite C-$LiFePO_4$ Cathodes for Lithium Ion Rechargeable Batteries. *Journal of Nanotechnology* **2010**, *2009*, 176517, doi:10.1155/2009/176517.
332. Ferrari, A.C.; Robertson, J. Interpretation of Raman Spectra of Disordered and Amorphous Carbon. *Phys. Rev. B* **2000**, *61*, 14095–14107, doi:10.1103/PhysRevB.61.14095.
333. Padhi, A.K.; Nanjundaswamy, K.S.; Goodenough, J.B. Phospho-olivines as Positive-Electrode Materials for Rechargeable Lithium Batteries. *J. Electrochem. Soc.* **1997**, *144*, 1188, doi:10.1149/1.1837571.
334. Malik, R.; Abdellahi, A.; Ceder, G. A Critical Review of the Li Insertion Mechanisms in $LiFePO_4$ Electrodes. *J. Electrochem. Soc.* **2013**, *160*, A3179, doi:10.1149/2.029305jes.
335. Bachtin, K.; Kramer, D.; Chakravadhanula, V.S.K.; Mu, X.; Trouillet, V.; Kaus, M.; Indris, S.; Ehrenberg, H.; Roth, C. Activation and Degradation of Electrospun $LiFePO_4$ Battery Cathodes. *Journal of Power Sources* **2018**, *396*, 386–394, doi:10.1016/j.jpowsour.2018.06.051.
336. Yu, D.Y.W.; Donoue, K.; Inoue, T.; Fujimoto, M.; Fujitani, S. Effect of Electrode Parameters on LiFePO4 Cathodes. *J. Electrochem. Soc.* **2006**, *153*, A835, doi:10.1149/1.2179199.
337. Franger, S.; Cras, F.L.; Bourbon, C.; Rouault, H. $LiFePO_4$ Synthesis Routes for Enhanced Electrochemical Performance. *Electrochem. Solid-State Lett.* **2002**, *5*, A231, doi:10.1149/1.1506962.
338. Hu, Y.; Gu, D.; Jiang, H.; Wang, L.; Sun, H.; Wang, J.; Shen, L. Electrochemical Performance of $LiFePO_4$/C via Coaxial and Uniaxial Electrospinning Method. *Advances in Chemical Engineering and Science* **2016**, *6*, 149–157, doi:10.4236/aces.2016.62017.
339. Chen, Q.; Qiao, X.; Peng, C.; Zhang, T.; Wang, Y.; Wang, X. Electrochemical Performance of Electrospun $LiFePO_4$/C Submicrofibers Composite Cathode Material for Lithium Ion Batteries. *Electrochimica Acta* **2012**, *78*, 40–48, doi:10.1016/j.electacta.2012.05.143.
340. Stenina, I.; Minakova, P.; Kulova, T.; Yaroslavtsev, A. Electrochemical Properties of $LiFePO_4$ Cathodes: The Effect of Carbon Additives. *Batteries* **2022**, *8*, 111, doi:10.3390/batteries8090111.
341. Wang, Y.; Zhang, J.; Xue, J.; Zhang, K.; Wen, L.; Liang, G. Effect of Particle Dispersion on the Properties of $LiFePO_4$ Slurry and the Electrochemical Properties of the Battery. *Ionics* **2022**, *28*, 1547–1558, doi:10.1007/s11581-021-04412-3.
342. Zhang, C.; Yao, L.; Qiu, Y. Synthesis and Characterization of $LiFePO_4$–Carbon Nanofiber–Carbon Nanotube Composites Prepared by Electrospinning and Thermal Treatment as a Cathode Material for Lithium-Ion Batteries. *Journal of Applied Polymer Science* **2016**, *133*, doi:10.1002/app.43001.
343. Dominko, R.; Bele, M.; Gaberscek, M.; Remskar, M.; Hanzel, D.; Pejovnik, S.; Jamnik, J. Impact of the Carbon Coating Thickness on the Electrochemical Performance of $LiFePO_4$ / C Composites. *J. Electrochem. Soc.* **2005**, *152*, A607, doi:10.1149/1.1860492.
344. Bachtin, K.; Kaus, M.; Pfaffmann, L.; Indris, S.; Knapp, M.; Roth, C.; Ehrenberg, H. Comparison of Electrospun and Conventional $LiFePO_4$/C Composite Cathodes for Li-Ion Batteries. *Materials Science and Engineering: B* **2016**, *213*, 98–104, doi:10.1016/j.mseb.2016.04.006.
345. Shao, D.; Wang, J.; Dong, X.; Yu, W.; Liu, G.; Zhang, F.; Wang, L. Electrospinning Fabrication and Electrochemical Properties of $LiFePO_4$/C Composite Nanofibers. *J Mater Sci: Mater Electron* **2013**, *24*, 4263–4269, doi:10.1007/s10854-013-1395-8.
346. Toprakci, O.; Ji, L.; Lin, Z.; Toprakci, H.A.K.; Zhang, X. Fabrication and Electrochemical Characteristics of Electrospun $LiFePO_4$/Carbon Composite Fibers for Lithium-Ion Batteries. *Journal of Power Sources* **2011**, *196*, 7692–7699, doi:10.1016/j.jpowsour.2011.04.031.

347. Rao Penki, T.; Kishore; N. Munichandraiah, B.; Shanmughasundaram, D. High Rate Capability Of Coconut Kernel Derived Carbon As An Anode Material For Lithium-Ion Batteries. *Advanced Materials Letters* **2014**, *5*, 184–190, doi:10.5185/amlett.2013.8530.

348. Rangan, K.K.; Gopalakrishnan, J. AMVMIII(PO_4)$_3$: New Mixed-Metal Phosphates Having NASICON and Related Structures. *Inorg. Chem.* **1995**, *34*, 1969–1972, doi:10.1021/ic00111a055.

349. Patoux, S.; Rousse, G.; Leriche, J.-B.; Masquelier, C. Structural and Electrochemical Studies of Rhombohedral $Na_2TiM(PO_4)_3$ and $Li_{1.6}Na_{0.4}TiM(PO_4)_3$ (M = Fe, Cr) Phosphates. *Chem. Mater.* **2003**, *15*, 2084–2093, doi:10.1021/cm020479p.

350. Zhu, C.; Song, K.; van Aken, P.A.; Maier, J.; Yu, Y. Carbon-Coated $Na_3V_2(PO_4)_3$ Embedded in Porous Carbon Matrix: An Ultrafast Na-Storage Cathode with the Potential of Outperforming Li Cathodes. *Nano Lett.* **2014**, *14*, 2175–2180, doi:10.1021/nl500548a.

351. Jian, Z.; Zhao, L.; Pan, H.; Hu, Y.-S.; Li, H.; Chen, W.; Chen, L. Carbon Coated $Na_3V_2(PO_4)_3$ as Novel Electrode Material for Sodium Ion Batteries. *Electrochemistry Communications* **2012**, *14*, 86–89, doi:10.1016/j.elecom.2011.11.009.

352. Kawai, K.; Zhao, W.; Nishimura, S.; Yamada, A. High-Voltage Cr^{4+}/Cr^{3+} Redox Couple in Polyanion Compounds. *ACS Appl. Energy Mater.* **2018**, *1*, 928–931, doi:10.1021/acsaem.7b00105.

353. Bachtin, K.; Kramer, D.; Chakravadhanula, V.S.K.; Mu, X.; Trouillet, V.; Kaus, M.; Indris, S.; Ehrenberg, H.; Roth, C. Activation and Degradation of Electrospun $LiFePO_4$ Battery Cathodes. *Journal of Power Sources* **2018**, *396*, 386–394, doi:10.1016/j.jpowsour.2018.06.051.

354. Hung, T.-F.; Lan, W.-H.; Yeh, Y.-W.; Chang, W.-S.; Yang, C.-C.; Lin, J.-C. Hydrothermal Synthesis of Sodium Titanium Phosphate Nanoparticles as Efficient Anode Materials for Aqueous Sodium-Ion Batteries. *ACS Sustainable Chem. Eng.* **2016**, *4*, 7074–7079, doi:10.1021/acssuschemeng.6b01962.

355. Liu, Y.; Rong, X.; Zhao, J. Unlocking the Muti-Electron Transfer Reaction in NASICON-Type Cathode Materials. *Mater. Futures* **2023**, doi:10.1088/2752-5724/acc7bb.

356. Kalluri, S.; Seng, K.H.; Guo, Z.; Liu, H.K.; Dou, S.X. Electrospun Lithium Metal Oxide Cathode Materials for Lithium-Ion Batteries. *RSC Adv.* **2013**, *3*, 25576–25601, doi:10.1039/C3RA45414B.

357. Liu, J.; Huang, Y.; Chen, J.; Fu, L.; Zhao, L.; Zou, C.; Li, X.; Wang, M.; Lin, Y.; Cao, H. Architecture-Improved and Kinetics-Enhanced Nasicon-Type Na3mnti(Po4)3 Through Microbe Assisted and Structure Optimized for Boosting Sodium Ion Storage 2022.

358. Liu, Y.; Rong, X.; Bai, R.; Xiao, R.; Xu, C.; Zhang, C.; Xu, J.; Yin, W.; Zhang, Q.; Liang, X.; et al. Identifying the Intrinsic Anti-Site Defect in Manganese-Rich NASICON-Type Cathodes. *Nat Energy* **2023**, *8*, 1088–1096, doi:10.1038/s41560-023-01301-z.

359. Liu, J.; Huang, Y.; Zhao, Z.; Ren, W.; Li, Z.; Zou, C.; Zhao, L.; Tang, Z.; Li, X.; Wang, M.; et al. Yeast Template-Derived Multielectron Reaction NASICON Structure $Na_3MnTi(PO_4)_3$ for High-Performance Sodium-Ion Batteries. *ACS Appl. Mater. Interfaces* **2021**, *13*, 58585–58595, doi:10.1021/acsami.1c17700.

360. Cheng, Y.C.; Jin, C.Q.; Gao, F.; Wu, X.L.; Zhong, W.; Li, S.H.; Chu, P.K. Raman Scattering Study of Zinc Blende and Wurtzite ZnS. *Journal of Applied Physics* **2009**, *106*, 123505, doi:10.1063/1.3270401.

361. Kaniyoor, A.; Ramaprabhu, S. A Raman Spectroscopic Investigation of Graphite Oxide Derived Graphene. *AIP Advances* **2012**, *2*, 032183, doi:10.1063/1.4756995.

362. Jorio, A.; Saito, R. Raman Spectroscopy for Carbon Nanotube Applications. *Journal of Applied Physics* **2021**, *129*, 021102, doi:10.1063/5.0030809.

363. Zhang, J.; Qi, L.; Ran, J.; Yu, J.; Qiao, S.Z. Ternary NiS/$Zn_xCd_{1-x}S$/Reduced Graphene Oxide Nanocomposites for Enhanced Solar Photocatalytic H_2-Production Activity. *Advanced Energy Materials* **2014**, *4*, 1301925, doi:10.1002/aenm.201301925.

364. Li, W.; Bi, R.; Liu, G.; Tian, Y.; Zhang, L. 3D Interconnected MoS_2 with Enlarged Interlayer Spacing Grown on Carbon Nanofibers as a Flexible Anode Toward Superior Sodium-Ion Batteries. *ACS Appl. Mater. Interfaces* **2018**, *10*, 26982–26989, doi:10.1021/acsami.8b05825.

365. Xia, J.; Jiang, K.; Xie, J.; Guo, S.; Liu, L.; Zhang, Y.; Nie, S.; Yuan, Y.; Yan, H.; Wang, X. Tin Disulfide Embedded in N-, S-Doped Carbon Nanofibers as Anode Material for Sodium-Ion Batteries. *Chemical Engineering Journal* **2019**, *359*, 1244–1251, doi:10.1016/j.cej.2018.11.053.

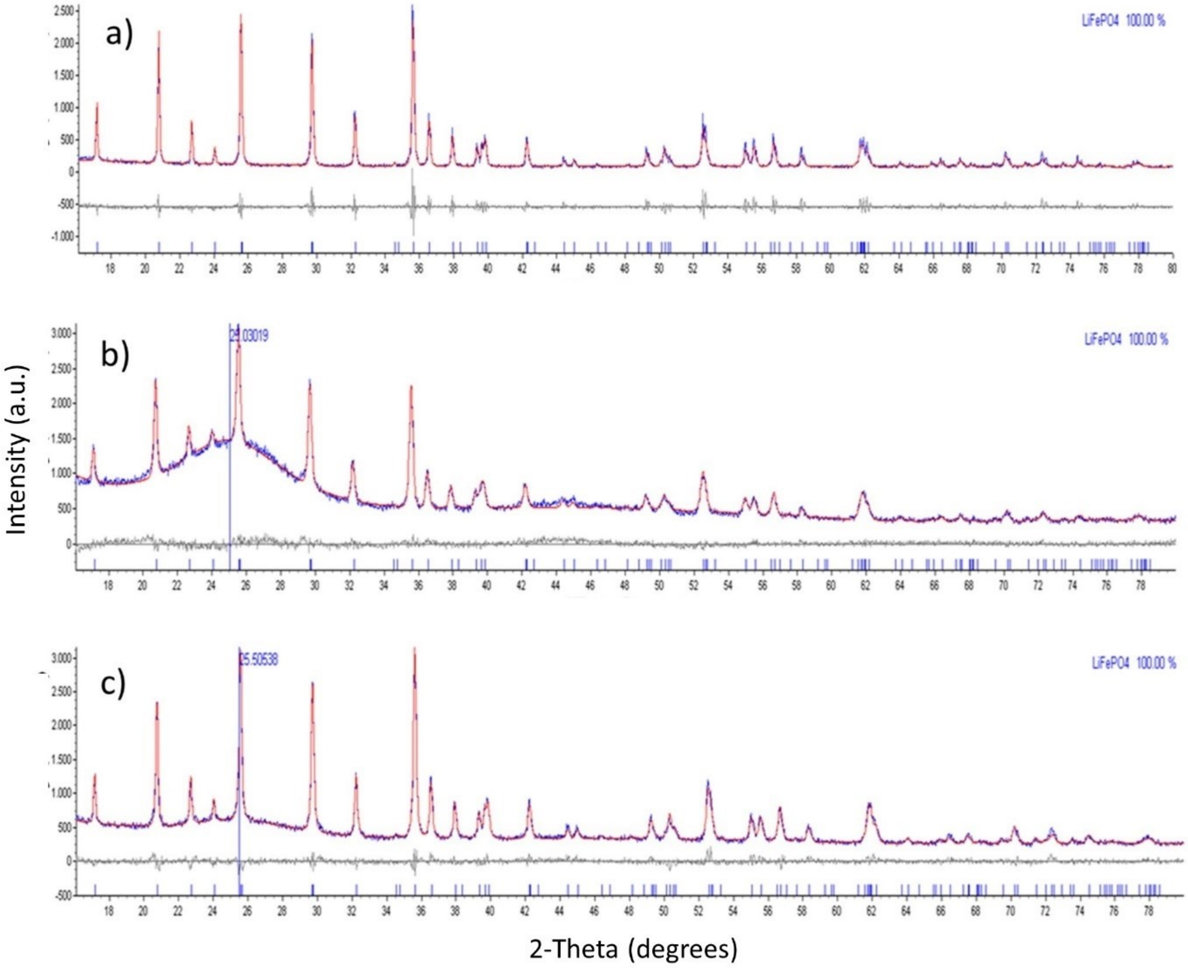

Figure S. 1: Rietveld refinement of X-Ray patterns of a) $LiFePO_4$, b) 10%$LiFePO_4$/CNF carb, and c) 30%$LiFePO_4$/CNF carb samples. Experimental pattern (blue line), calculated pattern (red line), difference curve (grey line). Peaks position of the $LiFePO_4$ phase (blue bars on the bottom). The refined position of the broad peak of the amorphous CNF phase is indicated by the blue vertical line.

Table S. 1: $LiFePO_4$ lattice parameters, cell volume, discrepancy factor and goodness of fit obtained by the Rietveld refinement of the $LiFePO_4$ and $LiFePO_4$/CNF samples.

Lattice parameters	***$LiFePO_4$***	***10%$LiFePO_4$/CNF***	***30%$LiFePO_4$/CNF***
a (Å)	10.3141(5)	10.3181(10)	10.3074(6)
b (Å)	6.0002(3)	6.0012(5)	5.9979(3)
c (Å)	4.6886(3)	4.6925(5)	4.6914(3)
V (Å^3)	290.16	290.56	290.04
R_{wp}	13.84	5.20	6.27
S	1.78	1.33	1.34

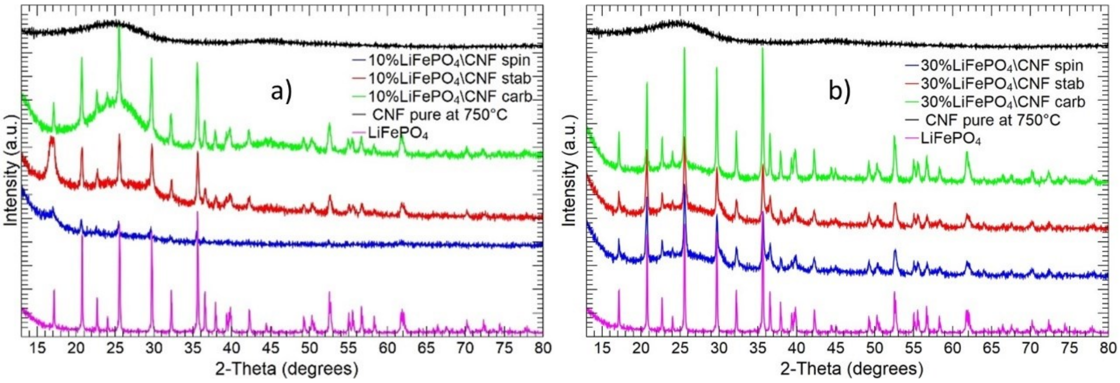

Figure S. 2: X-Ray patterns of a) 10%$LiFePO_4$/CNF spin (blue), stab (red), carb (green), and b) 30%$LiFePO_4$/CNF spin (blue), stab (red), carb (green). In both figures the X-Ray patterns of CNF pure carbonized at 750°C (black) and $LiFePO_4$ commercial powder (purple) are also shown.

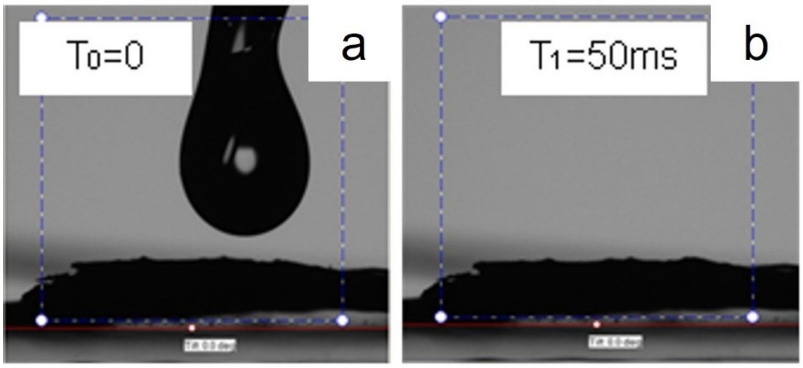

Figure S. 3: The electrolyte permeation in 30%$LiFePO_4$/CNF after carbonization.

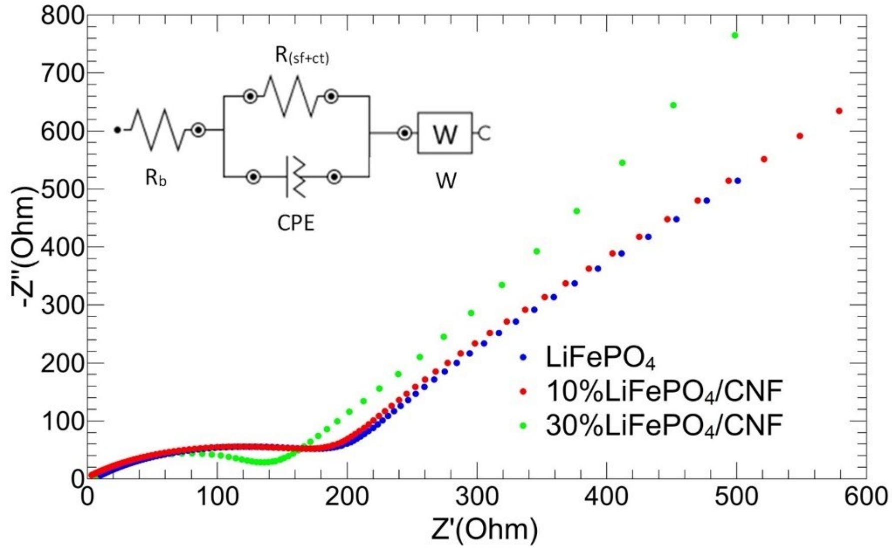

Figure S. 4: Nyquist plot of the 30%$LiFePO_4$/CNF and $LiFePO_4$ cathodes. The equivalent circuit is shown in the inset. Rb: electrolyte resistance; R(sf+ct): surface and charge transfer resistance; W: Warburg impedance.

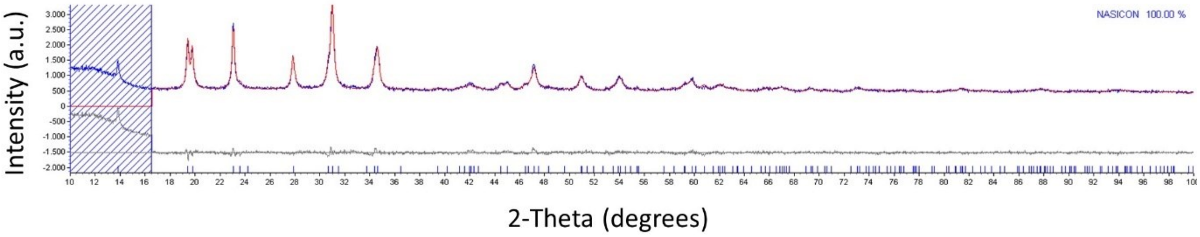

Figure S. 5: Rietveld refinement of 2-MnZr sample. Experimental pattern (blue line), calculated pattern (red line), difference curve (grey line). Peaks position of the the $Na_3MnZr(PO_4)_3$ phase (blue bars on the bottom).

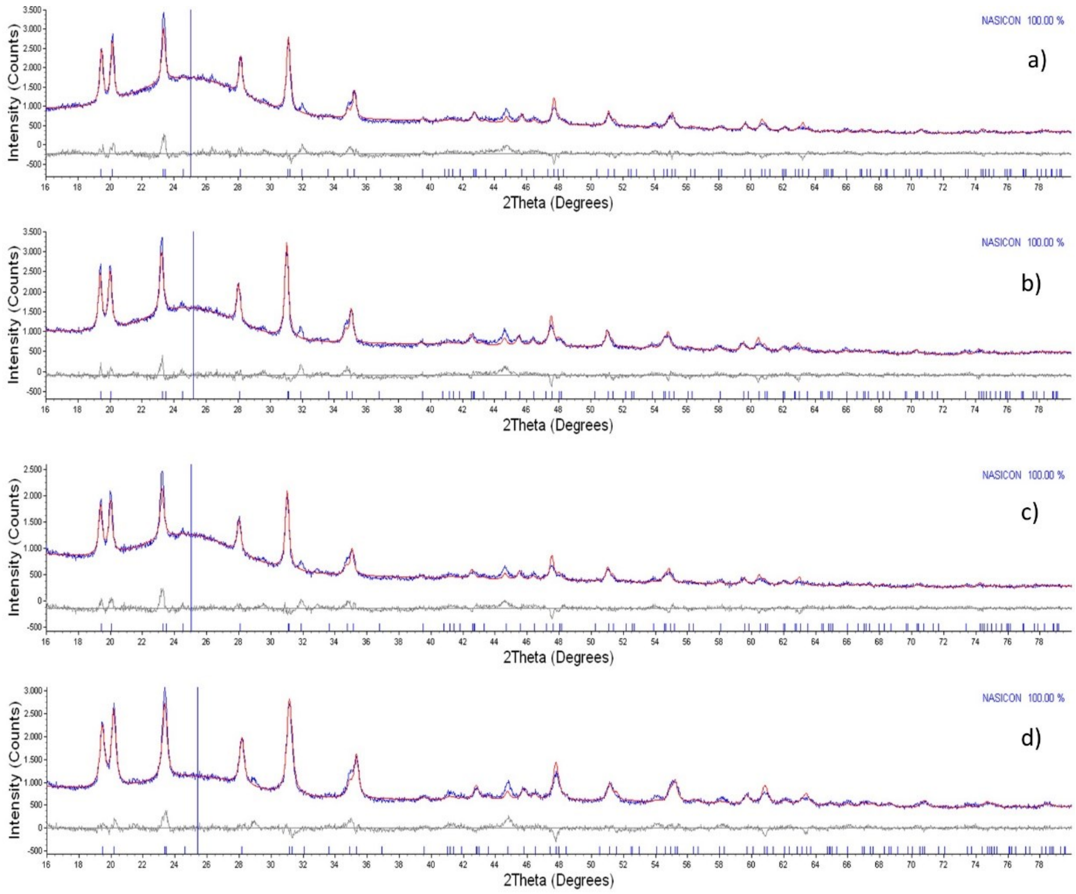

Figure S. 6: Rietveld refinement of the X-ray diffraction data of the a) h-10%MnZr/CNF, b) h-30%MnZr/CNF c) v-30%MnZr/CNF and d) dd-MnZr/CNF samples. Experimental pattern (blue line), calculated pattern (red line), difference curve (grey line). Peaks position of the $Na_3MnZr(PO_4)_3$ phase (blue bars on the bottom). The refined position of the broad peak of the amorphous CNF phase is indicated by the blue vertical line.

Table S. 2: Refined lattice parameters, cell volume, crystallite size, weighted-pattern discrepancy factor and Goodness of Fit of the *NaSICON*-structured $Na_3MnZr(PO_4)_3$ phase obtained by Rietveld refinement of 2-MnZr and MnZr/CNF samples.

Samples	***2-MnZr***	***dd-MnZr/CNF***	***h-10%MnZr/CNF***	***h-30%MnZr/CNF***	***v-30%MnZr/CNF***
a (Å)	8.970(1)	8.794(1)	8.818(1)	8.844(1)	8.840(1)
c (Å)	22.585 (5)	22.742(4)	22.740(4)	22.705(4)	22.709(4)
V ($Å^3$)	175.45	173.20	173.66	173.90	173.85
c/a	2.518	2.586	2.578	2.567	2.569
Crystallite size (nm)	30(1)	28(1)	40(1)	37(1)	36(1)
R_{wp}	5.51	6.26	6.67	6.13	6.79
S	1.41	1.75	1.83	1.76	1.62

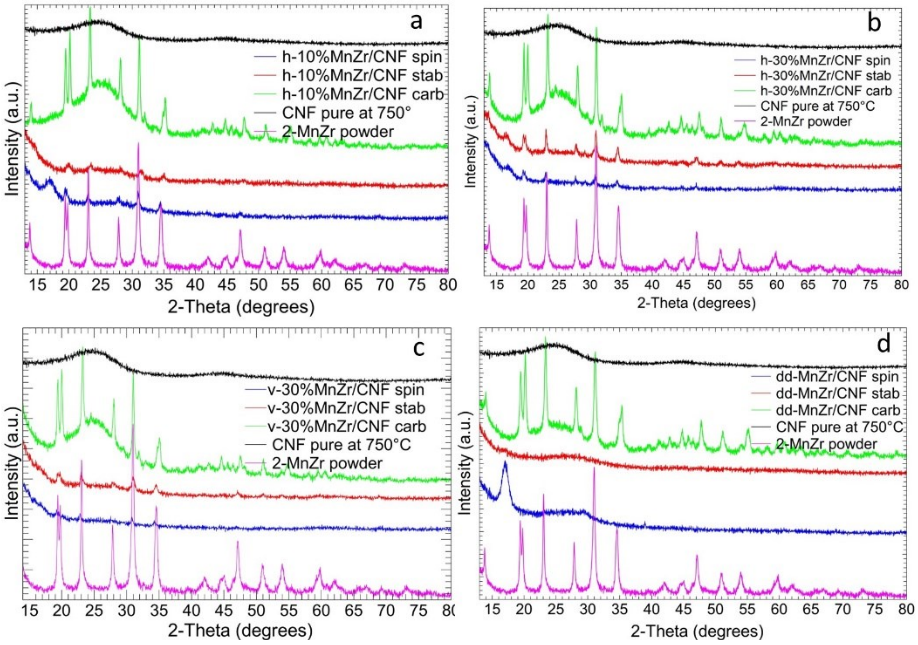

Figure S. 7: Diffraction patterns of electrospun (blue), stabilized (red) and carbonized (green) samples of a) h-10%MnZr/CNF, b) h-30%MnZr/CNF, c) v-30%MnZr/CNF and d) dd-MnZr/CNF samples. The X-ray pattern of 2-MnZr powder sample (purple) and CNF (black) are also reported.

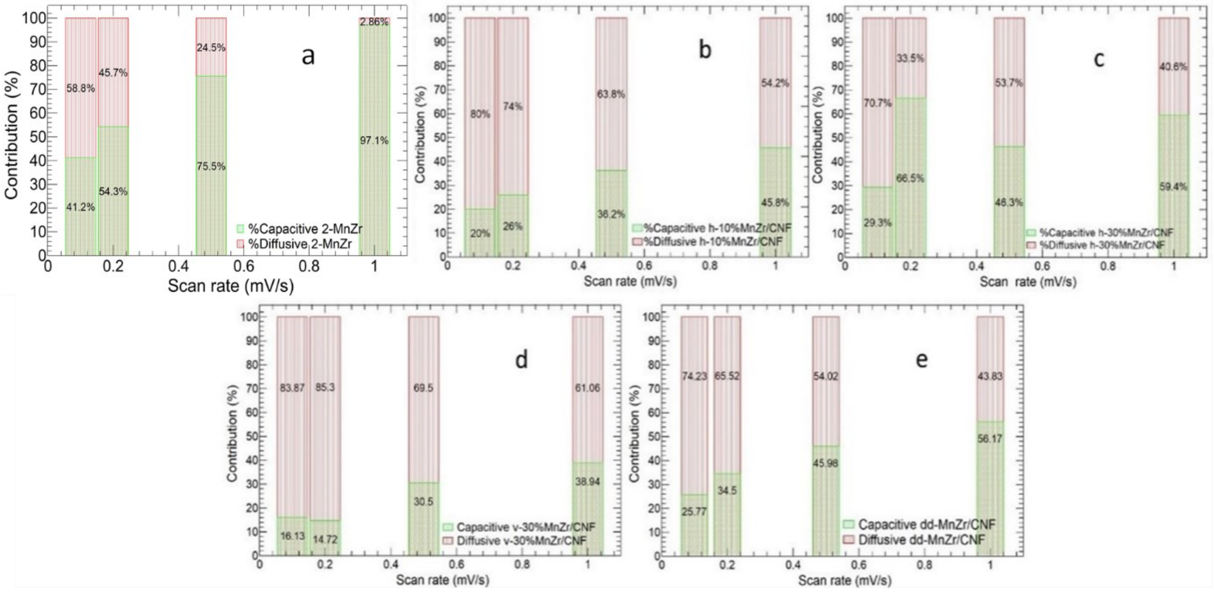

Figure S. 8: Capacitive and diffusive contribution obtained by CV at different scan rate of a) 2-MnZr, b) h-10%MnZr/CNF, c) h-30%MnZr/CNF, d) v-30%MnZr/CNF, and e) dd-MnZr/CNF.

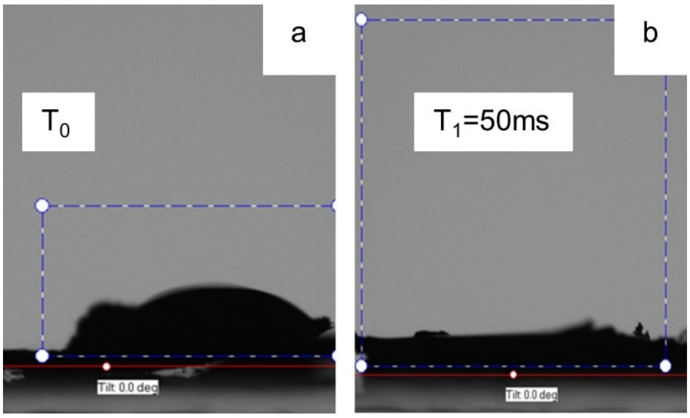

Figure S. 9: The electrolyte permeation in v-30%MnZr/CNF after carbonization.

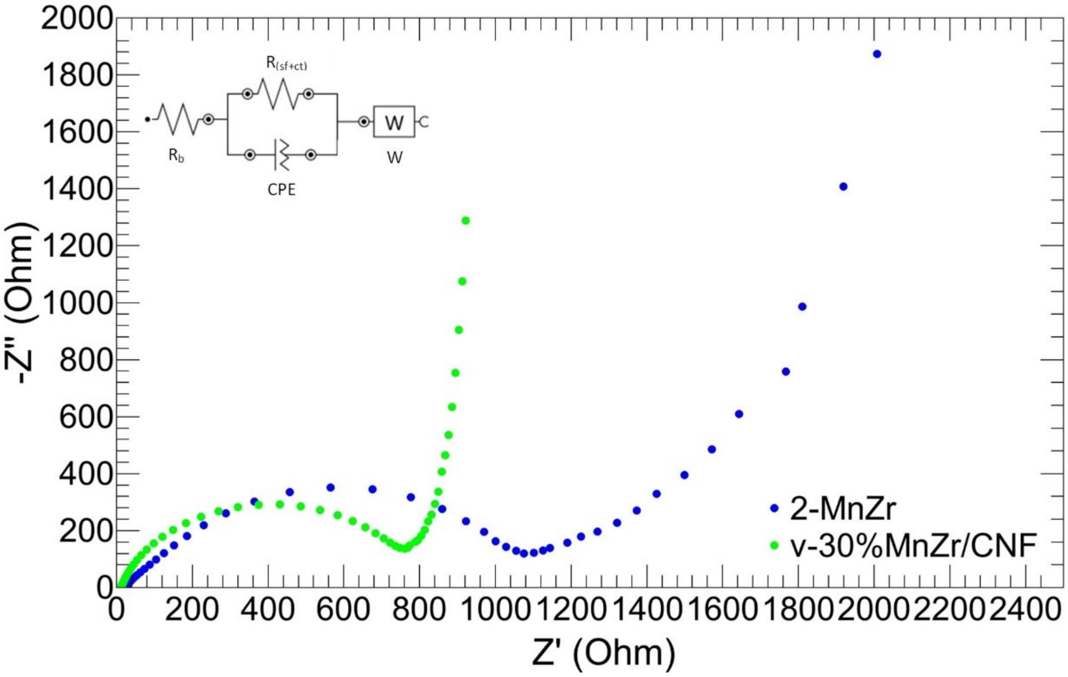

Figure S. 10: Nyquist plot of the v-30%MnZr/CNF and 2-MnZr cathodes. The equivalent circuit is shown in the inset. R b : electrolyte resistance; R (sf+ct) : surface and charge transfer resistance; W: Warburg impedance.

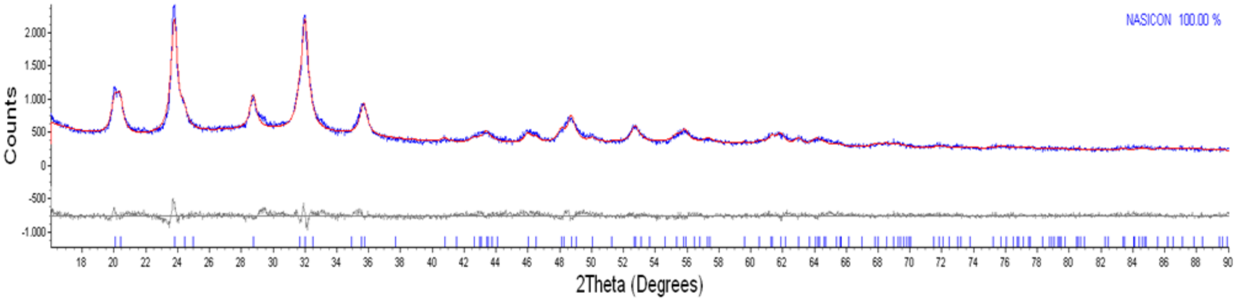

Figure S. 11: Rietveld refinement of the X-ray diffraction data of the 2-MnTi sample. Peaks position of the $Na_3MnTi(PO_4)_3$ phase (blue bars on the bottom).

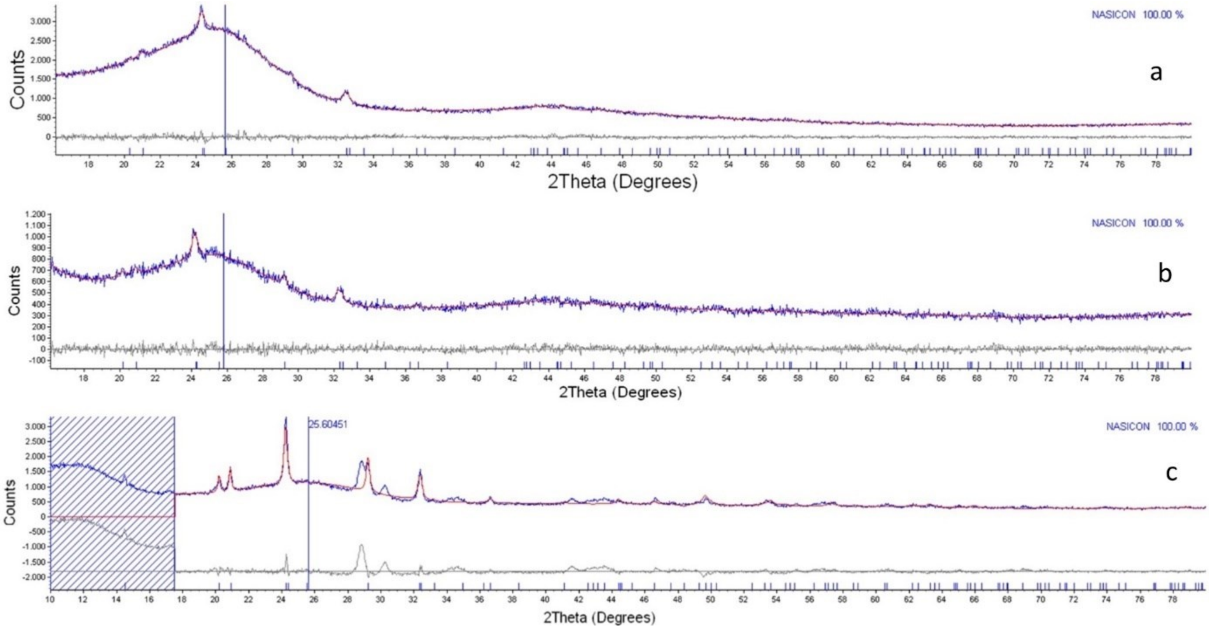

Figure S. 12: Rietveld refinement of the X-ray diffraction data of the a) 10% MnTi/CNF, b) 30%MnTi/CNF c) dd-MnTi/CNF samples. Experimental pattern (blue line), calculated pattern (red line), difference curve (grey line). Peaks position of the $Na_3MnTi(PO_4)_3$ phase (blue bars on the bottom). The refined position of the broad peak of the amorphous CNF phase is indicated by the blue vertical line.

Table S. 3: $Na_3MnTi(PO_4)_3$ lattice parameters, crystallite size, crystallinity degree, discrepancy factor and goodness of fit obtained by the Rietveld refinement of the 2-MnTi and MnTi/CNF samples. Cell volumes and c/a ratios are also reported.

Samples	***2-MnTi***	***10%MnTi/CNF***	***30%MnTi/CNF***
a (Å)	8.696(2)	8.441(6)	8.462(8)
c (Å)	21.851 (5)	21.834(19)	21.911(29)
V (Å^3)	1431.00	1347.26	1358.75
c/a	2.51	2.59	2.59
Crystallite size (nm)	18.7	19.0(1.4)	25.2(2.3)
Degree of crystallinity (%)	-	9.25	8.1
R_{wp}	6.26	4.20	5.13
GoF	1.34	1.10	1.07

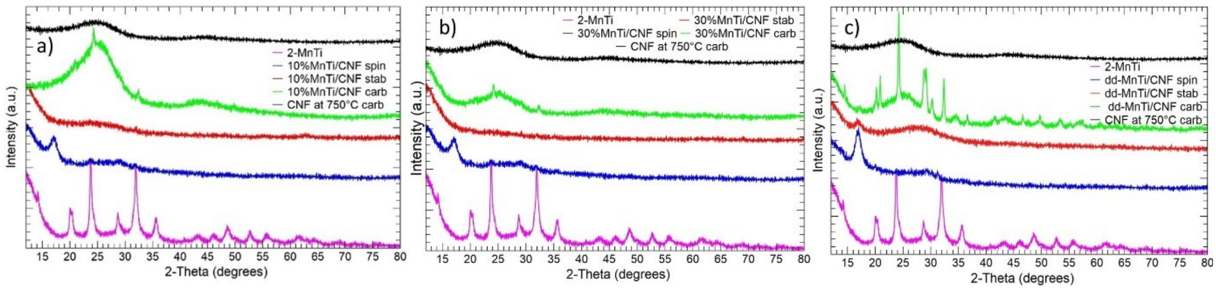

Figure S. 13: X-Ray diffraction pattern of electrospun (blue), stabilized (red) and carbonized (green) samples of a) 10%MnTi/CNF, b) 30%MnTi/CNF, and c) dd-MnTi/CNF samples. The X-ray pattern of 2-MnTi powder sample (purple) and CNF (black) are also reported.

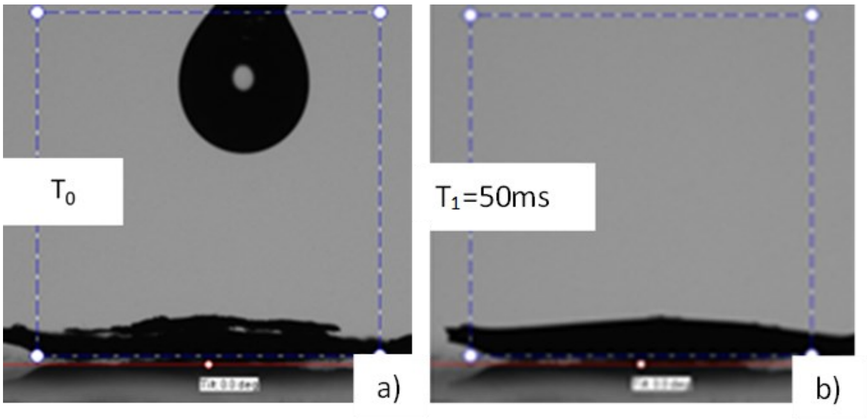

Figure S. 14: The electrolyte permeation in 10%MnTi/CNF after carbonization.

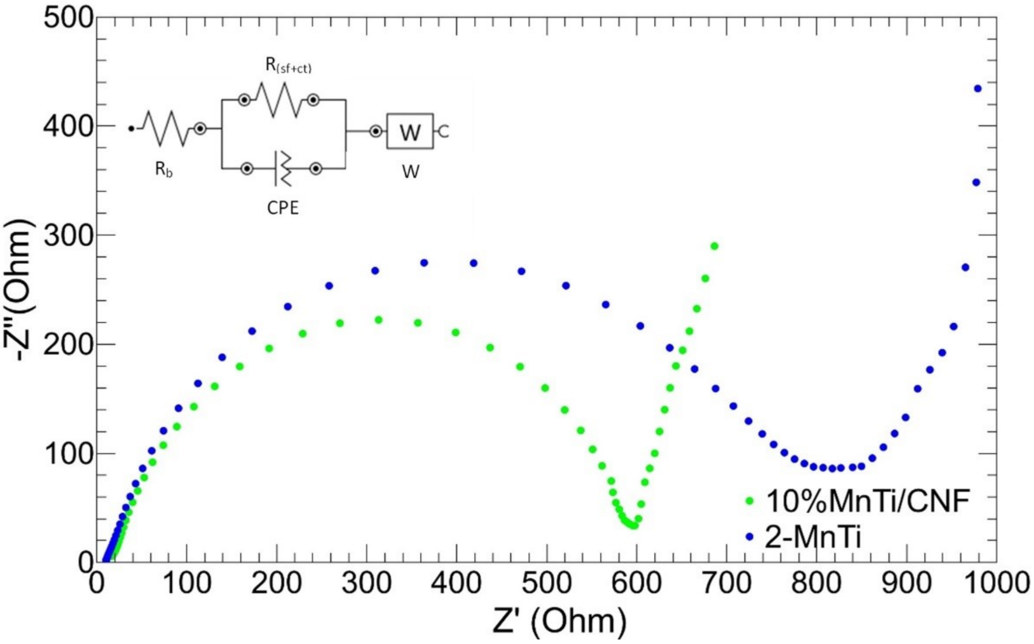

Figure S. 15: Nyquist plot of the 10%MnTi/CNF and 2-MnTi electrodes. The equivalent circuit is shown in the inset. Rb: electrolyte resistance; R(sf+ct): surface and charge transfer resistance; W: Warburg impedance.

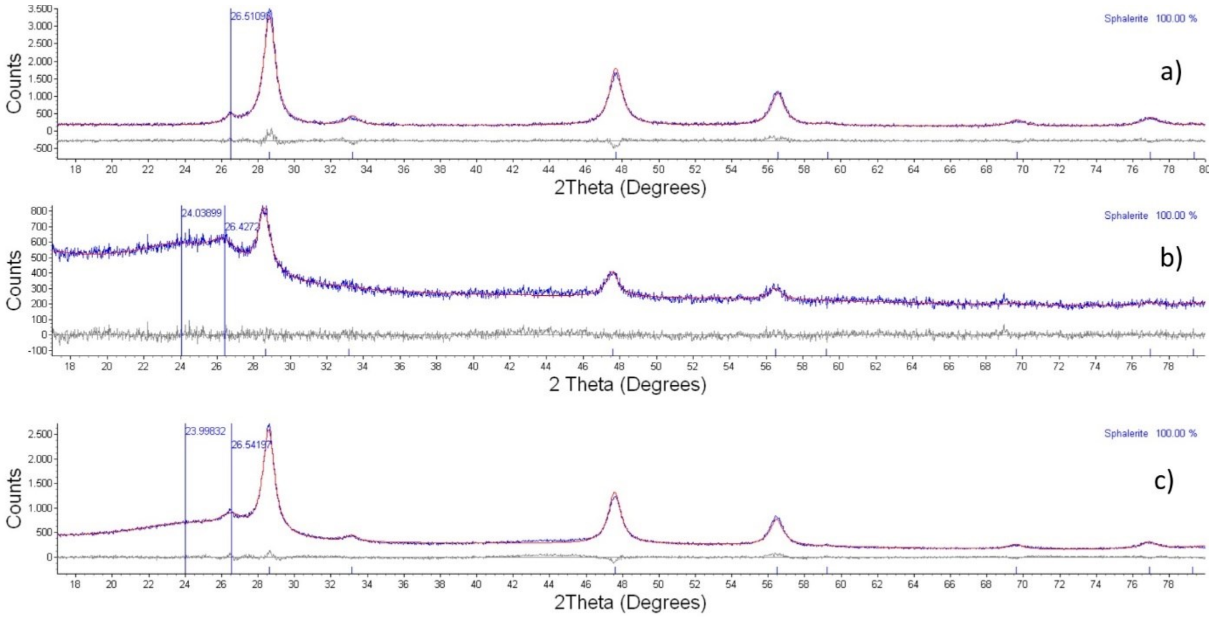

Figure S. 16: Rietveld refinement of the X-ray diffraction data of the a) ZnS-GO, b) 10%ZnS-GO/CNF and c) 30%ZnS-GO/CNF samples. Experimental pattern (blue line), calculated pattern (red line), difference curve (gray line). Peaks position of the sphalerite phase (bottom: blue bars). Peaks position of the (0 0 2) plane of graphene and of the amorphous carbon (blue vertical lines).

Table S. 4 Lattice parameters, crystallite size, weighted discrepancy factor and Goodness of Fit obtained by the Rietveld refinement of the diffraction data of the ZnS-GO, 10%ZnS-GO/CNF, 30%ZnS-GO/CNF samples.

Samples	***ZnS-GO***	***10%ZnS-GO/CNF***	***30% ZnS-GO /CNF***
a (Å)	5.3947(7)	5.3961(32)	5.3986(8)
Crystallite size (nm)	11.8	11.7	11.7
R_{wp}	9.7	6.2	5.4
GoF	1.7	1.1	1.1

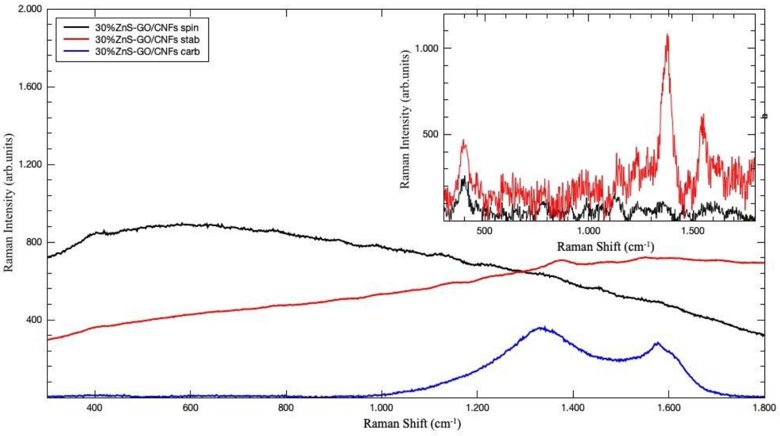

Figure S. 17: Room temperature Raman spectra for the sample 30%ZnS-GO/CNF as obtained after electrospinning (black line), after stabilization (red line) e post carbonization process (blue line). The inset shows the first two spectra as derived after baseline subtraction using a polynomial curve.

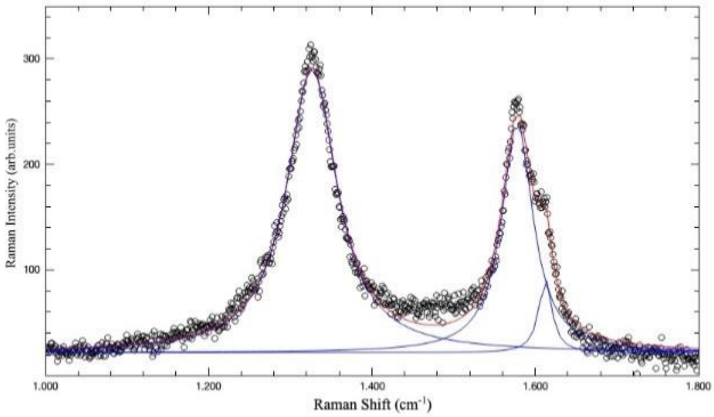

Figure S. 18: Result from best-fitting procedure (red line) performed in the range 1000-1800 cm^{-1} on the Raman data (empty circle) from Zn-GO sample using a sum of 3 lorentzian curves (blue lines). From the fitting parameters the values for (I_G/I_D) have been derived.

Figure index

Table index

Acronyms

BES = energy storage
CAES = Compressed Air Energy Storage
CC = constant current
CCCV = constant current and constant potential
CCV = Close Circuit Voltage
CNFs = carbon nanofibers
CNTs = carbon nanotubes
C-Rate = Current Rating
CV = Cyclic voltammetry
DFT = Density functional theory
DMAc = Dimethylacetamide
DOD = Depth of Discharge
DRC = Democratic Republic of Congo
EC = ethylene carbonate
ECS = Energy Chemical Storage
EDS = Energy Dispersive X-ray spectroscopy
EES = electrochemical energy storage
ESW = electrochemical stability window
FEC = fluoroethylene carbonate
GCD = Galvanostatic charge/discharge cycles
GHGs = greenhouse gases
IHP = Inner Helmotz plane
JT = Jahn Teller
LCO = lithium-cobalt oxide $LiCoO_2$
LFP = Lithium-Iron-Phosphate
LIB = Lithium-ion battery
LMOs = lithium layered oxides
MW = molecular weight
NaSICON = Sodium (Na) Super Ionic Conductors
NCA = Lithium-Nickel-Cobalt-Aluminum oxide
NMC = Lithium-Nickel-Manganese-Cobalt oxide
NMP = N-methyl-2-pirrolidone
OCV = Open Circuit Voltage
OHP = Outer Helmotz plane
PA = Polyamide
PAN = Polyacrylonitrile
PANI = Polyaniline
PBAs = Prussian Blue Analogues
PBI = Polybenzimidazole
PC = propylene carbonate
PEO = Polyethylene oxide
PHS = Pumped Hydroelectric Storage
PI = Polyimide

PS = Polystyrene
PVA = Polyvinyl alcohol
PVC = Polyvinyl chloride PMMA = Polymethyl methacrylate
PVdF = Polyvinylidene fluoride
PVK = Polyvinyl carbazole
RB = rechargeable batteries
RE = renewable energy
r-GO = graphene oxide
RRs = renewable resources
SEI = solid electrolyte interphase
SEM = Scanning Electron Microscopy
SIB = Sodium-ion battery
SOC = battery's state-of-charge
TEM = Transmission Electron Microscopy
TES = Thermal Energy Storage
TGA = Thermogravimetric analysis
V(SOB) = Voltage profile